Mechanisms of Stress Corrosion Cracking and Mechanical Property Degradation of X80 Steel Caused by Sulfate Reducing Bacteria

A dissertation presented to

the faculty of

the Russ College of Engineering and Technology of Ohio University

In partial fulfillment

of the requirements for the degree

Doctor of Philosophy

Zhong Li

August 2023

This dissertation titled

Mechanisms of Stress Corrosion Cracking and Mechanical Property Degradation of X80 Steel Caused by Sulfate Reducing Bacteria

by

ZHONG LI

has been approved for

the Department of Chemical and Biomolecular Engineering

and the Russ College of Engineering and Technology by

Tingyue Gu

Professor of Chemical and Biomolecular Engineering

Maj Mirmirani

Interim Dean, Russ College of Engineering and Technology

Abstract

LI, ZHONG, Ph.D., August 2023, Chemical Engineering

Mechanisms of Stress Corrosion Cracking and Mechanical Property Degradation of X80 Steel Caused by Sulfate Reducing Bacteria

Director of Dissertation: Tingyue Gu

Awareness of microbiologically influenced corrosion (MIC), which threatens assets in the marine, oil and gas, water utilities, power generation, and various other industries, is growing. At least 20% of all corrosion losses can be attributed to MIC. MIC can also cause mechanical property degradation, resulting in metal fracturing, rupturing, collapsing, and cracking that reduce equipment service life and threaten safety.

Sulfate reducing bacteria (SRB) such as *Desulfovibrio vulgaris* and *Desulfovibrio ferrophilus* (strain IS5) are a major type of microbe that cause MIC. The latter is several times more corrosive. SRB are anaerobic bacteria that can use sulfate as the terminal electron acceptor in their respiration. Unlike soluble organic carbon, elemental iron releases electrons extracellularly, and then the electrons are used in sulfate reduction inside the SRB cytoplasm under bio-catalysis, which requires extracellular electron transfer (EET). Thus, this type of MIC is labeled as “EET-MIC”, which is the result of the demand for energy by sessile cells in biofilms that can perform EET.

In practical applications, mechanical property degradation and stress corrosion cracking (SCC) caused by MIC can result in disastrous consequences such as pipeline

ruptures and support beam collapses. In the past, most studies on MIC only investigated the MIC mechanisms that lead to pinhole leaks. The effects of microbes and MIC on mechanical property degradation and SCC are also important, if not more. In this work X80 carbon steel was used as an example of pipeline steel.

The following topics and results are reported in this dissertation:

(1) The relationship between tensile stress and *D. vulgaris* MIC was explored to study biotic SCC. In the presence of an applied tensile stress most pronounced in the outer bottom of an X80 U-bend, *D. vulgaris* MIC initiated crack formation in the ATCC 1249 culture medium at 37ºC in an anaerobic bottle. The biotic corrosion weight loss of the X80 U-bend coupon was found to be lower than that of the X80 square coupon after a 14-d SRB incubation, which was supported by electrochemical measurements. Moreover, after a 6-week incubation in the presence of *D. vulgaris*, a pre-cracked U-bend coupon caused SCC failure.

(2) *D. ferrophilus* grown in enriched artificial seawater (EASW) at 28ºC and *D. vulgaris* grown in ATCC 1249 culture medium at 37ºC were used to investigate the MIC impact on X80 U-bend (with stress) and square (without stress) coupons. The weight loss and pit depth of the X80 U-bend coupon were larger than those of the X80 square coupon, suggesting that the mechanical stress accelerated the *D. ferrophilus* MIC for X80 steel. After a 14-d incubation, *D. vulgaris* caused significant cracks, whereas *D. ferrophilus* did not. This was attributed to the fact that the much faster

corrosion rate caused by *D. ferrophilus* prevented or dissolved crack tips, whereas the much slower *D. vulgaris* MIC rate did not. For the first time, the abiotic SCC phenomenon that fast corrosion does not necessarily cause more severe SCC has been expanded to biotic SCC.

(3) Carbon source starvation was used to vary MIC severity for studying microbial degradation of X80 carbon steel mechanical properties. Pre-grown biofilms (after 3-d of *D. vulgaris* incubation) on X80 coupons were moved to new ATCC 1249 culture media with varied caron source levels (with the original strength being 100% carbon source) for additional 14-d of incubation. After the 14-d starvation incubation, the sequence of sessile cell count (cells cm^{-2}) on dogbone coupons in the anaerobic bottles was 0% < 10% < 50% < 100% of carbon source levels. The sequence of weight loss and pit depth on X80 dogbone coupons were both 0% < 10% < 100% < 50%. The 50% carbon source level resulted in carbon source starvation but without suffering excessive sessile cell loss. Thus, its weight loss and pit depth were both the highest. In addition, the results showed that even in the 17-d short-term test, mechanical properties were significantly degraded, and more severe MIC pitting caused more severe degradation in terms of ultimate strength and ultimate strain losses, which were 22% and 24%, respectively for 50% carbon source starvation compared to the fresh dogbone coupons.

(4) X80 pipeline steel dogbone coupons and square coupons were immersed in 150 mL *D. vulgaris* broths for 14 d to test the impact of headspace volume change on

X80 mechanical properties degradation. The headspace volumes in the anaerobic bottles were increased from 150 mL to 200 mL and 300 mL to increase MIC severity. After the 14-d of SRB incubation, the sessile cell counts were 6.5×10^7 cells cm^{-2} for 150 mL, 2.3×10^8 cells cm^{-2} for 200 mL, and 1.4×10^9 cells cm^{-2} for 300 mL headspace volumes, respectively, owing to reduce the H_2S cytotoxicity in the broth with a larger headspace because it allowed more biogenic H_2S to escape from the broth. The sessile cell count results were in agreement with the weight loss results of 1.7 mg cm^{-2}, 1.9 mg cm^{-2} and 2.3 mg cm^{-2} for 150 mL, 200 mL, and 300 mL headspace volumes, respectively. Moreover, the results show that more severe MIC pitting led to a higher ultimate strain loss of up to 23% (300 mL headspace) compared to the abiotic control dogbone, which means SRB MIC made the X80 dogbone less ductile. The ultimate strength losses for all headspace volumes were relatively small (3% and lower).

(5) The *D. ferrophilus* MIC rate of X80 carbon steel was investigated with different incubation times. The corrosion rate of the coupons was the fastest for the first 7-d incubation. For 14 d and 21 d, the corrosivity of *D. ferrophilus* gradually decreased due to sessile cell starvation loss, resulting in corrosion rate decreasing. The ultimate strength and strain degraded noticeably with increasing incubation time. After the 21-d incubation, the weight loss was 24.8 mg cm^{-2} with a pit depth of 30.6 μm, which resulted in the ultimate strength and ultimate strain losses of 9% and 18%, respectively compared to the fresh X80 dogbone coupon without incubation.

(6) Tetrakis hydroxymethyl phosphonium sulfate (THPS), a green biocide, was used to mitigate the MIC caused by *D. ferrophilus* in EASW for the purpose of reducing SRB degradation of X80 mechanical properties. The weight loss of X80 square coupons decreased from 19.5 mg cm^{-2} for the no treatment control to 1.1 mg cm^{-2} with 100 ppm (w/w) THPS in EASW after 7 d of incubation. There were clear differences in pit depth and pit (surface) diameter of no treatment (maximum pit depth of 13.5 μm and maximum pit diameter of 36.7 μm) and with 100 ppm THPS treatment (no apparent corrosion pit). The sessile cell count and planktonic cell count with 100 ppm THPS mitigation declined by 3-log and 4-log, respectively compared with the untreated control. After the 7-d SRB incubation, 100 ppm THPS mitigation led to lower ultimate strength loss (0% vs. 6%) and ultimate strain loss (3% vs. 13%) compared to the abiotic control. This work demonstrated that mitigating SRB led to MIC mitigation and also alleviation in microbial degradation of mechanical properties.

Dedication

To

All the people who motivated and supported me during my PhD degree life

Especially to my husband: Jike Yang,

To my children, Hanyu (Vivian) Yang and Hanming (Vincent) Yang,

To my father, Xiaogang Li, my mother, Dongmei Fu,

Without their endless love encouragement, selfless contribution, I could not finish my degree.

Acknowledgments

I wish to express my sincere gratitude to my outstanding adviser Prof. Tingyue Gu. His support, patience and encouragement were essential throughout my whole Ph.D. life. His meticulous mentoring motivated me to become a mature researcher in the MIC field. He put a lot of time and effort into advancing my projects, and technical writings. Without his steady and rigorous mentoring, I would not have been able to complete my dissertation. I appreciate his efforts throughout the years of my professional development.

I am also appreciative that Prof. Sumit Sharma, Prof. Peter Coschigano, Prof. Marc Singer and Prof. Xiaozhuo Chen serving on my dissertation committee. I would want to take this opportunity to thank them for their time and help. I also appreciate Prof. Marc Singer's kind support in the tensile testing of dogbone samples. I especially appreciate the academic education I received from Prof. Douglas Goetz, Prof. John Staser, Prof. Monica Burdick, Prof. Srdjan Nesic, and Prof. Valerie Young, who provided me with years of expert expertise in chemical engineering learning and technical skill development. My sincere gratitude goes out to each and every one of the Ohio University MIC group members, both present and past, who supported me over the years, including: Dr. Dake Xu, Dr. Yingchao Li, Dr. Ru Jia, Dongqing Yang, Dr. Di Wang, Dr. Tuba Unsal, Dr. Jielong Tan, Dr. Wenwen Dou, Jialin Liu, Jike Yang, Dr. Junlei Wang, Purch Kijkla, and Lingjun Xu. I want to thank Joey Boyle and James

Caesar for their enthusiasm and technical assistance in setting up part of my lab work. For their assistance with the administrative matters, Carrie Carpenter, Jyl Steinberg, and Rachel Meyer are also appreciated.

Additional gratitude goes to Prof. Xiaogang Li, Prof. Dawei Zhang, Prof. Zhiyong Liu, Prof. Cuiwei Du, Dr. Wei Wu, Dr. Yuntian Lou, Jingzhi Yang, Huihua Guo, Shihang Lu, and other staff and students at Corrosion & Protection Center, University of Science & Technology Beijing where I spent two years for my Ph.D. internship. Their friendship provided a welcoming environment with constant encouragement in my academic career. Their informative suggestions and guidance were a huge assistance to me as I moved forward with my research and experiments.

For their financial support of my projects, I would like to sincerely thank the Chinese Society for Corrosion and Protection, Saudi Aramco, PTTEP and Pioneer Natural Resources.

Finally, but most importantly, my heartfelt thanks to my dearest husband, Jike Yang. Because of his constant love and numerous sacrifices, I have been able to persevere with my research to this final point. I would also like to express my deepest appreciation to my parents and other family members for their unwavering support and confidence throughout my long and arduous but fulfilling Ph.D. journey.

Table of Contents

List of Tables

List of Figures

Chapter 1: Introduction

Corrosion is the deterioration of a material (usually a metal) because of its chemical interactions with its surroundings. This definition is applicable to any material. However, it is typically used for metals and metal alloys. Microbiologically influenced corrosion (MIC), also known as biocorrosion, is one of the common reasons for materials failure in the oil and gas industry, chemical and petrochemical industry, and water utilities. NACE International (now AMPP) estimated that the annual total cost of corrosion is around US$2.5 trillion globally, and MIC accounts for 20%–40% of that (Beavers & Thompson, 2006; Salgar-Chaparro et al., 2020; Wolodko et al., 2018). The Aliso Canyon (near Los Angeles, CA) gas leak between 2015 and 2016 led to a serious environmental disaster with a huge emission of methane gas, which is a greenhouse gas many times more potent than carbon dioxide. The leak was caused by a metal well casing that failed due to soil MIC (CPUC and DOGGR, 2019).

Corrosion processes also affect the chemical characteristics of a metal or metal alloy, its physical qualities, and its mechanical behavior. The in-bulk metal deterioration of pipe materials was a crucial factor in the long-term loss of serviceability of main pipelines and other structures. Severe operating conditions, such as long-term contact with the stressed metal in an MIC environment and under pressure, accelerate the degradation processes of oil and gas pipeline steels.

The overwhelming majority of MIC literature deals with MIC pitting and the threat of pinhole leaks (Sharma et al., 2018; Su et al., 2014). It is well known that corrosion, both uniform corrosion and pitting corrosion, degrades mechanical properties of a metal, which can be measured by the loss in ultimate strength and ultimate strain (Li et al., 2021c). The latter reflects a metal's ductility. It is important to address MIC degradation of mechanical properties. This will fill an important knowledge gap. Apart from the mechanical damages by MIC uniform corrosion and MIC pitting corrosion, microbes produce metabolites such as H_2S and H_2 that can potentially impact a metal's mechanical properties (Wang et al., 2021a; Wang et al., 2020). Thus, microbial degradation of mechanical properties needs a holistic approach.

Simultaneously, stress corrosion cracking (SCC) causes ruptures in industrial fields such as pipelines or storage tanks, leading to severe economic losses. In addition to direct and indirect economic damage, pipeline and storage tank catastrophes impose extensive environmental costs and pose a safety risk to operators. The initiation and propagation of metal fractures require both a corrosive environment, which corrosive bacteria may supply, and a source of stress, which is derived through internal transport and external soil and fluid components. If SCC occurs, ductile metals will encounter unexpected sudden failure (Skovhus & Lee, 2017). When SCC occurs to a metal, for example, X80 steel, which is commonly used in oil pipelines worldwide, it will reduce its service lifespan.

The MIC of underground pipes may be attributed to the circumstances around the pipelines, which are continuously buried in soil containing corrosive microorganisms in a moist environment. The risk of MIC grows with pipeline age. Decades of investigations have been devoted to this issue with many exciting progresses made in the past decades. However, considerable uncertainty remains regarding MIC because it requires multidisciplinary knowledge in several research fields, including corrosion engineering, microbiology, molecular biology, chemical engineering, and electrochemistry.

The stress factor in SCC is primarily because of the internal operating pressure or pressure fluctuation in oil and gas pipelines. The movement of soil also provides longitudinal stress and strain, which is a causal factor in the initiation and propagation of SCC in pipelines. The liquid/gas pressure from inside the pipeline and the soil pressure from outside apply tensile stress to the pipeline, which is a source of stress for SCC formation (Rosenfeld & Kiefner, 2006). Small stresses, typically below the macroscopic yield strength of a metal, can cause SCC. This means SCC can easily occur if corrosive bacteria are present in the soil because MIC is sufficient (Wasim, 2018). Therefore, the combination of stress and MIC causes crack formation, and the cost of addressing pipeline integrity issues and pipeline management should pay attention to MIC in addition to abiotic corrosion as a cause of SCC. By applying electrochemical and mechanical techniques, this research will obtain new insight into the mechanism of

SCC caused by corrosive bacteria. This information will assist in the development of SCC mechanism caused by microbial activities, improving the SCC mitigation and increasing the service life and safety of pipelines.

Previous research on metal degradation and failure has rarely focused on the cooperative formation mechanisms of both MIC and stress. This study investigated the different corrosive bacteria under continuous stress with several specific coupons to determine mechanical properties and electrochemistry to investigate the mechanism and behaviors of SCC caused by MIC. The research gap can be closed by determining the destruction mechanisms for X80 steel, such as SCC and mechanical deterioration in the MIC environment. These results will improve the integrity management of pipelines, which contributes to significant economic benefits and environmental protection.

Chapter 2: Literature Review

This chapter elaborates on background knowledge to demonstrate the systematic approach for research used in follow-up chapters. The literature review covers a wide range of topics, including corrosive microorganisms such as *D. vulgaris* and *D. ferrophilus* (strain IS5, MIC). SCC mechanism, the characteristic and influence factors of mechanical properties of metal degradation and SCC, microbiology techniques to visualize and quantify microbes, techniques applied to the study of mechanical properties and SCC, and electrochemical techniques used to study MIC and its biocide mitigation.

2.1 Biofilms

Most microbes in nature live in biofilms, usually synergistic mixed-culture biofilms for nutritional benefits and for better protection (Aslan et al., 2022). Figure 2-1 shows the five stages of the biofilm formation process (Abu Bakar et al., 2018). First, planktonic cells reversibly adhere to a surface in an initial attachment (Thomas et al., 2004). Second, irreversible attachment is promoted by more and more cells adhering to each other (Flemming & Wingender, 2010). Third, cells become adsorbent on the surface and develop into microcolonies with physical dimensions ranging from tens to hundreds of microns facilitated by the production of extracellular polymeric substances (EPS) (Borlee et al., 2010). Fourth, as cells proliferate and EPS accumulate, the microbial community forms a three-dimensional (3D) structure and settles as a mature

biofilm (Alpkvist et al., 2006). Fifth, some sessile cells separate from the biofilm and disperse into the bulk fluid, floating freely and creating new biofilms (Hall-Stoodley et al., 2004; Hall-Stoodley & Stoodley, 2005).

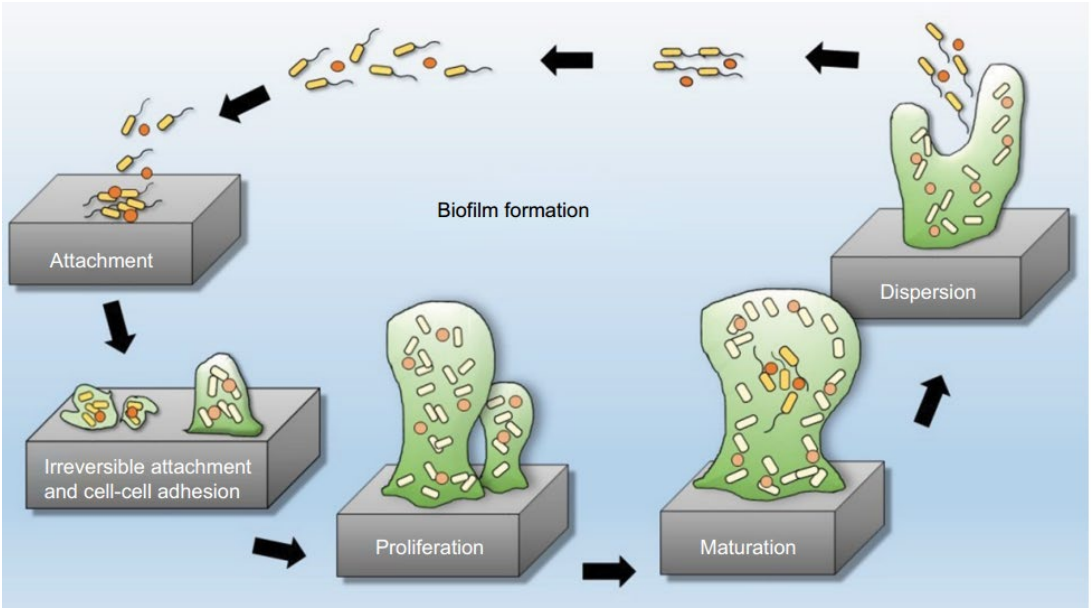

Figure 2-1. Five stages of biofilm formation (Abu Bakar et al., 2018). (Permission is not needed.)

The formation of the biofilm matrix creates a one-of-a-kind habitat for microbes, allowing them to live in a dynamic biofilm mode. Biofilms and the resultant lifestyle are produced through specific processes, resulting in a temporally and spatially diverse bacterial community (Funari & Shen, 2022). EPS are microbiological biopolymers in which biofilm microbes are embedded. Archaeal, bacterial, and eukaryotic microbes generate biopolymers. Contrary to widespread assumption, EPS are more than just

polysaccharides. They also contain a diverse range of proteins, glycoproteins, glycolipids, and significant quantities of extracellular DNA (e-DNA), as shown in Figure 2-2 (Flemming et al., 2007; Flemming & Wingender, 2010).

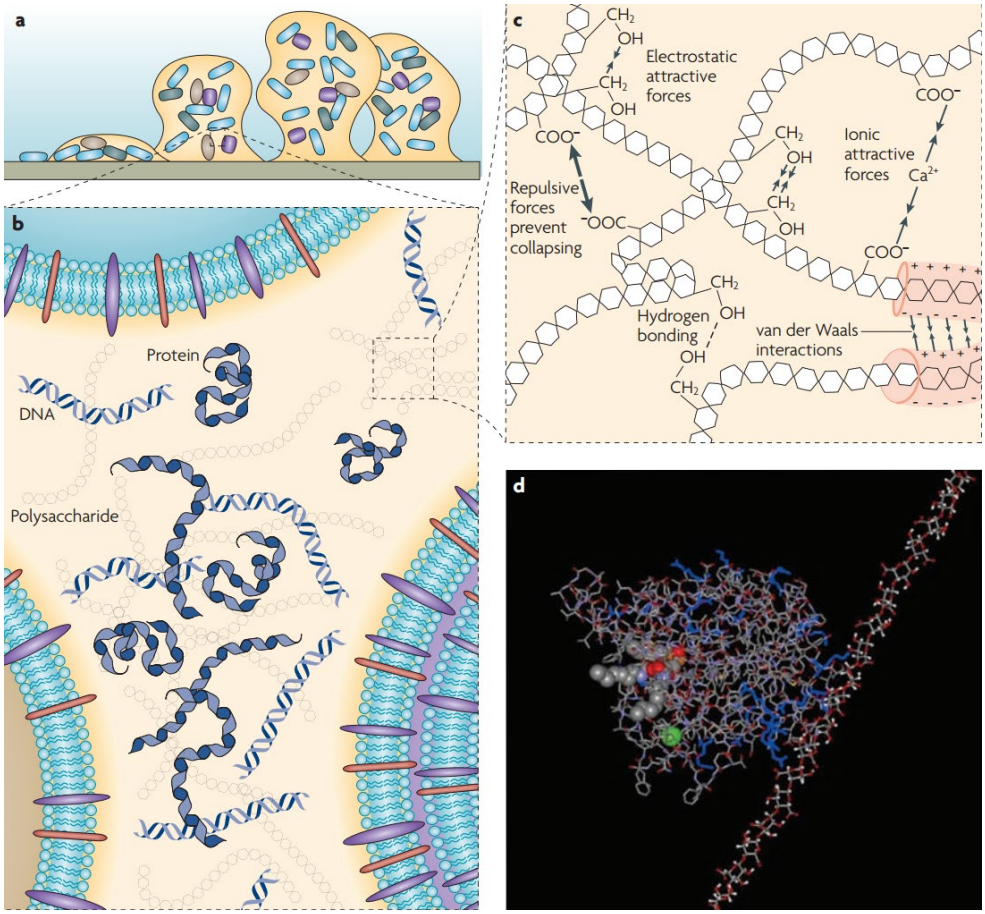

Figure 2-2. EPS matrix at different dimensions: (a) Model of a bacterial biofilm, (b) major matrix components (polysaccharides, proteins, and e-DNA), (c) weak physicochemical interactions and the entanglement of biopolymers in the EPS matrix, and, (d) molecular simulation of the interactions (Flemming & Wingender, 2010). (Reproduced with permission from the publisher.)

Dispersal in bacteria is typically a final event that occurs just as the biofilm reaches maturity, indicating the completion of the biofilm life cycle, as shown in Figure 2-3 (Uppuluri & Lopez-Ribot, 2016) for the purpose of propagation of microbes. Biofilms experience cell detachment and dispersion into the environment, a crucial process for bacterial survival, reproduction, and virulence (Kostakioti et al., 2013). Because of their complicated organizational structure, biofilms contain a variety of microenvironments with varying pH levels, oxygen availability, nutrition availability, and biocide stress, which causes metabolic variability across cell populations in various biofilm sites (Rumbaugh & Sauer, 2020).

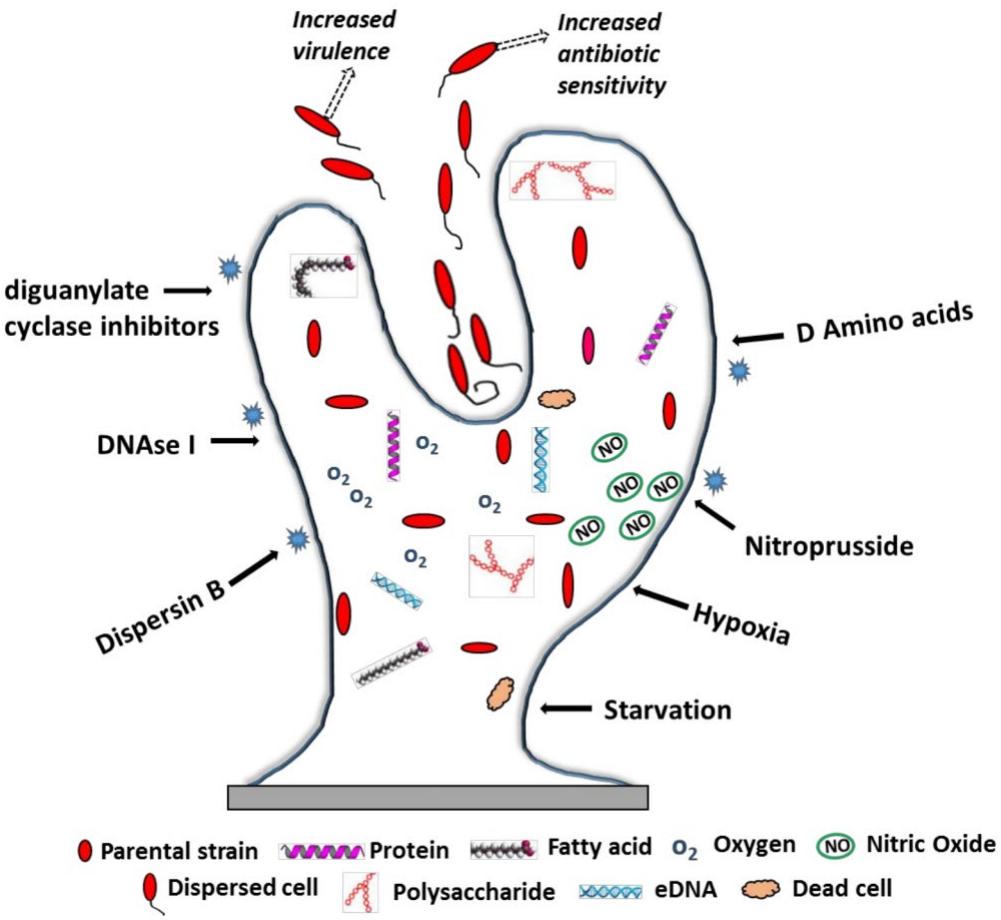

Figure 2-3. Biofilm dispersion process and the influence factors impacting the biofilm dispersion process (Uppuluri & Lopez-Ribot, 2016). (Permission is not needed.)

2.2 Sulfate Reducing Bacteria

SRB are corrosive bacteria that can acquire energy by oxidizing organic substances (or dissolved hydrogen gas) while reducing sulfate (SO_4^{2-}) to hydrogen sulfide (H_2S) (Lovley & Phillips, 1994). SRB are anaerobic microbes; however, they can survive when exposed to oxygen, which means they are aerotolerant. SRB are tenacious organisms that are abundant in nature. Some highly oxygen-tolerant SRB

biofilms could survive in atmospheric oxygen for up to 72 h (Bade et al., 2000). The pH range for SRB growth is 5-8 (Virpiranta et al., 2022). The highest temperature for specific thermophilic species of SRB is approximately 90°C (Ollivier et al., 2007), and the highest pressure is 500 atm (Reza, 2008). Uncontrolled SRB activities can have disastrous consequences in industrial fields. SRB contaminate stored gas and oil, threatens industrial assets, and is a primary reason for MIC. Good SRB management can prevent the formation of the corrosive gas H_2S (also the cause for reservoir souring), extend the service life of industrial utilities, and reduce the incidence of MIC.

2.2.1 Desulfovibrio vulgaris

D. vulgaris is an SRB species widely used in MIC investigations (Figure 2-4) (Barton & Fauque, 2009; Černoušek et al., 2021). Many cases indicate that *D. vulgaris* is involved in corrosion activities and mechanical damages such as mechanical degradation and SCC of iron (Chen et al., 2015; Enning & Garrelfs, 2014). *D. vulgaris* can attach to metal surfaces, such as oil steel pipeline surfaces, the inner rust layer of pipeline steel, and the seawater pipeline, and then it corrodes metal materials by harvesting electrons from stainless steel (SS) or other metal materials (Li et al., 2018c; Li & Ning, 2019; Liu & Cheng, 2020).

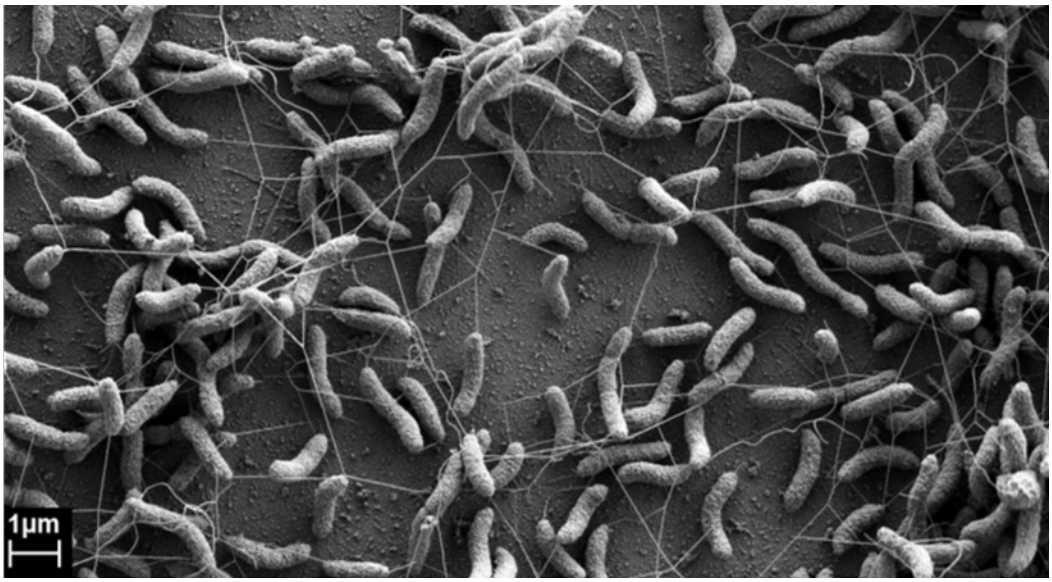

Figure 2-4. *D. vulgaris* biofilm from continuous culture (5,420X) (Brileya et al., 2014). (Permission is not needed.)

2.2.2 Desulfovibrio ferrophilus

D. ferrophilus (strain IS5), shown in Figure 2-5, is known to cause truly very severe MIC in marine environments. It is another strain SRB rapidly gaining popularity in MIC research. *D. ferrophilus* is a novel iron-corroding SRB species that can use elemental iron as the sole electron donor (Chatterjee et al., 2021; Deng et al., 2015), but it likely uses the $2H^+/H_2$ electron shuttle just like *D. vulgaris* (Woodard Trevor et al., 2023). The earlier researchers who tested *D. ferrophilus* did not delete the hydrogenase genes before they drew the conclusion. *D. ferrophilus* corrodes steel 10X faster than common SRB such as *D. vulgaris* (Wang et al., 2021a).

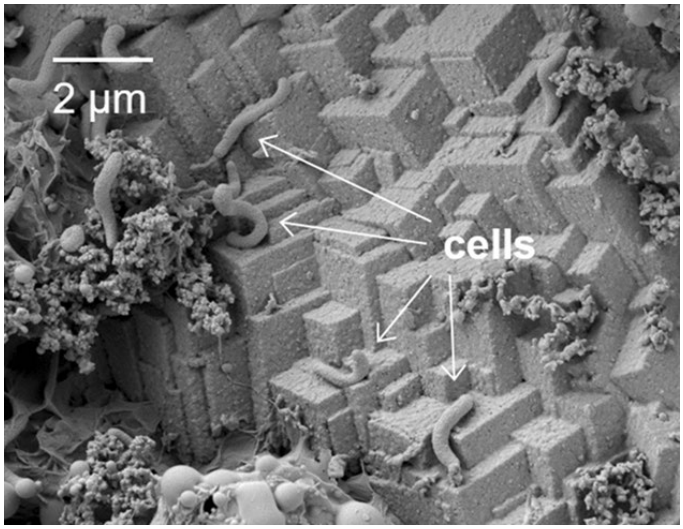

Figure 2-5. *D. ferrophilus* attached to carbon steel surface (Chatterjee et al., 2021). (Permission is not needed.)

2.3 Mechanisms of SRB MIC

MIC is an electrochemical process in which microorganisms initiate, facilitate, and accelerate various corrosion reactions (Videla, 2018). MIC is a serious problem in the oil and gas industry and many other industrial fields, such as water utilities and power generation. MIC causes pipeline leakage, and injection well plugging, which jeopardize oil production and cause safety issues (Skovhus et al., 2017).

Microorganisms may exist in reservoirs since geological times (Rosnes Jan et al., 1991). The ecosystem of a mixed-culture corrosive biofilm is shown in Figure 2-6. Microorganisms such as SRB and nitrate reducing bacteria (NRB) are common corrosive bacteria that cause MIC and biodegradation (Lou et al., 2021). Acid producing bacteria (APB) also cause MIC (Dong et al., 2018). However, many

uncertainties remain regarding MIC because its study requires multidisciplinary knowledge in several research fields, including corrosion engineering, microbiology, molecular biology, chemical engineering, and electrochemistry.

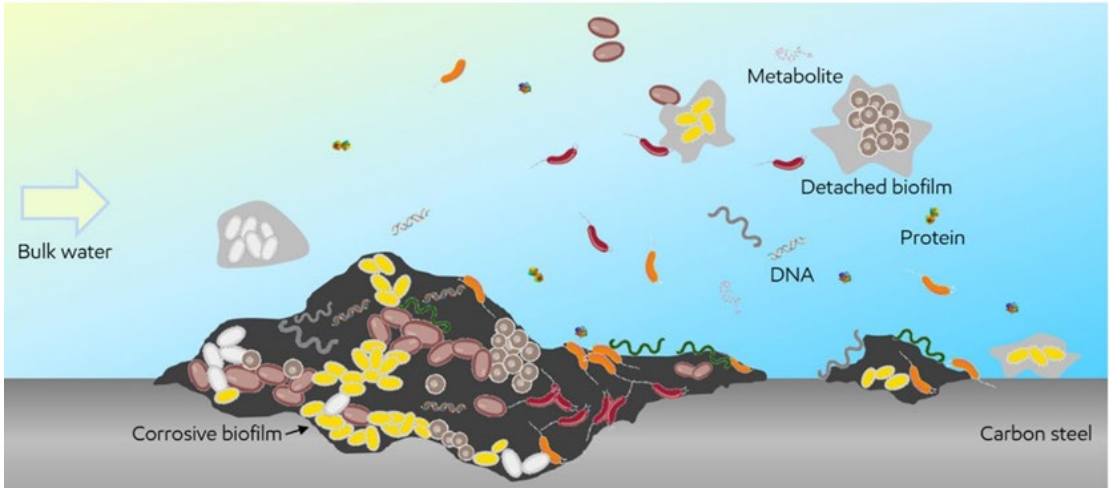

Figure 2-6. Schematic of corrosive biofilm and potential biomarkers (e.g., proteins, DNA, and metabolites) associated with MIC (Chatterjee et al., 2021). (Permission is not needed.)

SRB have been investigated extensively in the MIC field because sulfate is a ubiquitous electron acceptor (oxidant) in many natural and industrial environments (Gu et al., 2019). SRB are prevalent in anaerobic environments because they utilize this electron acceptor for respiration (Wang et al., 2020). Moreover, SRB produce biogenic H_2S that may accelerate localized corrosion and it is the cause of reservoir souring (Al-

Abbas et al., 2013; Jia et al., 2018a). Even in aerobic environments, SRB can grow underneath an aerobic biofilm that provides an anerobic local environment.

When lactate is the organic carbon for growth as in the ATCC 1249 culture medium, *D. vulgaris* first oxidizes it to yield pyruvate. Pyruvate is subsequently oxidized to acetate with concomitant production of molecular hydrogen (H_2) and energy molecule ATP (adenosine 5'-triphosphate). H_2 is used for cytoplasmic reduction of sulfate. Some H_2 escapes from the liquid phase to the headspace in an anaerobic vial in a typical lab test. As lactate is consumed, the bacteria will in turn consume H_2 (Su et al., 2022) in the headspace. Thus, SRB metabolism involves hydrogen cycling, which is actually a cyclic transfer of electrons using $2H^+/H_2$ shuttle (Wang et al., 2020), as shown in Figure 2-7.

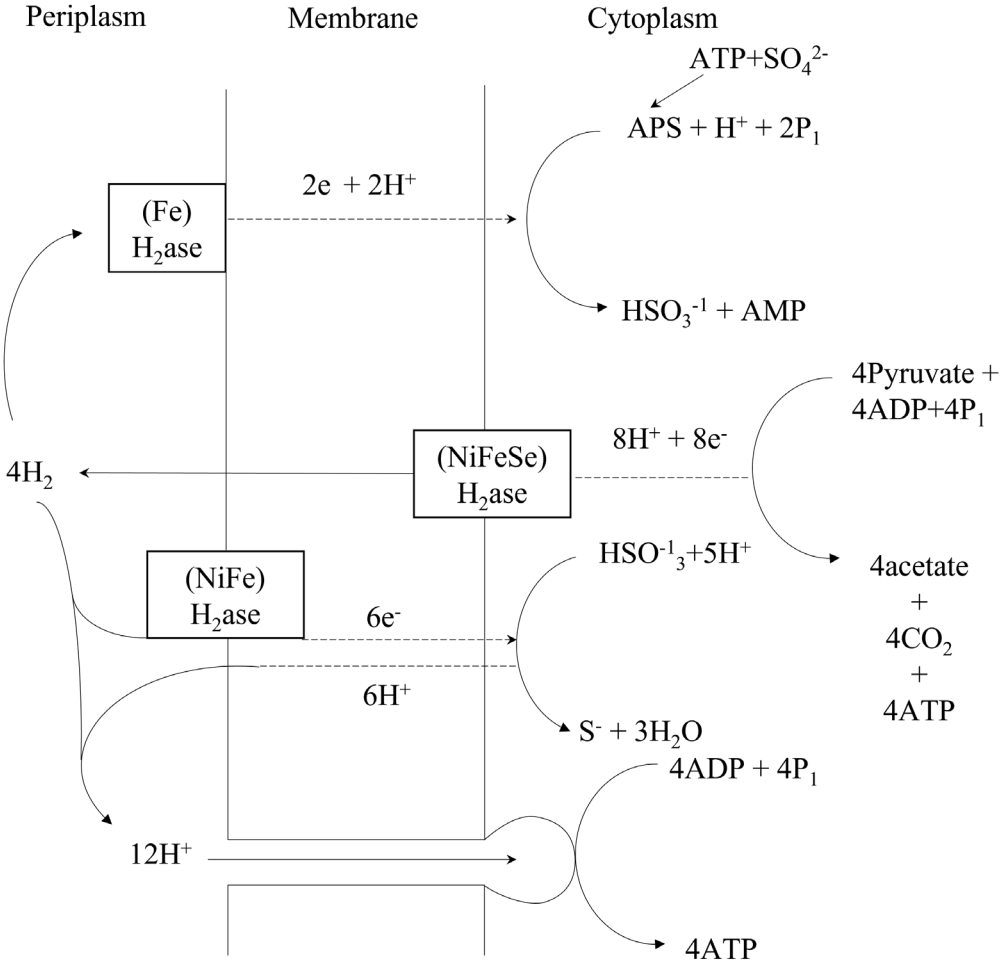

Figure 2-7. Bioenergetics of hydrogen cycling using $2H^+/H_2$ shuttle (Odom & Singleton, 1993). (Reproduced with permission from the publisher.)

The redox reaction of lactate and corresponding reduction reaction are shown below with potential using SHE (standard hydrogen electrode) as reference: (Dou et al., 2019; Gu et al., 2019; Li et al., 2018d; Reza, 2008; Xu & Gu, 2011, 2014).

$$2CH_3CHOHCOO^- + 2H_2O \rightarrow 2CH_3COO^- + 2CO_2 + 8H^+ + 8e^- \quad (E^{o'} = -430 \text{ mV}) \quad (2\text{-}1)$$

$$SO_4^{2-} + 9H^+ + 8e^- \rightarrow HS^- + 4H_2O \qquad (E^{o'} = -217 \text{ mV}) \quad (2\text{-}2)$$

The modified standard conditions used in bioelectrochemistry are 1 M of each substance (1 bar gas), 25°C, and pH 7. The cell potential ($\Delta E^{o'}$) of the redox reaction coupling Reactions 2-1 and 2-2 is 213 mV (–217 mV – (–430 mV)) at the modified standard conditions. The corresponding Gibbs free energy change ($\Delta G^{o'}$) can be calculated using the equation below:

$$\Delta G^{o'} = -zF\Delta E^{o'} \quad (2\text{-}3)$$

where z is the number of electrons in the redox reaction (z = 8 here), and F Faraday constant (96.485 kJ mol^{-1} V^{-1}). It gives $\Delta G^{o'}$ = −164 kJ mol^{-1} sulfate, which means lactate produces energy for SRB metabolism.

Elemental iron is almost equally as energetic and as lactate when comparing the reduction potential below with that in lactate oxidation reaction.

$$Fe \rightarrow Fe^{2+} + 2e^{-} \quad (E^{o} = -447 \text{ mV}) \quad (2\text{-}4)$$

The first example of MIC was reported more than one hundred years ago (Enning & Garrelfs, 2014). However, cathodic depolarization theory (CDT) is still considered the first to explain MIC caused by hydrogenase-positive SRB (Li et al., 2018d). Furthermore, Gu et al. proposed a new MIC theory known as “biocatalytic cathodic sulfate reduction (BCSR)” (Gu et al., 2009), which is the first MIC theory to systematically consider bioenergetics and cover all types of SRB including those that are not hydrogenase-positive.

2.3.1 Cathodic Depolarization Theory

CDT is the first widely recognized theory that explains how SRB MIC occurs. Figure 2-8 shows that SRB cathodic depolarization at an iron surface is the cause of MIC. This theory is summarized in the following reactions:

Anodic reaction (iron dissolution)	$4Fe \rightarrow 4Fe^{2+} + 8e^-$	(2-5)
Dissociation of water	$8H_2O \rightarrow 8H^+ + 8OH^-$	(2-6)
Cathodic reaction	$8H^+ + 8e^- \rightarrow 8H_{ads}$	(2-7)
Cathodic depolarization by hydrogenase	$8H_{ads} \rightarrow 4H_2$	(2-8)
Sulfate reduction by SRB	$SO_4^{2-} + 9H^+ + 8e^- \rightarrow HS^- + 4H_2O$	(2-9)
Corrosion product formation	$Fe^{2+} + HS^- \rightarrow FeS + 2H^+$	(2-10)
Corrosion product formation	$3Fe^{2+} + 6OH^- \rightarrow 3Fe(OH)_2$	(2-11)
Overall reaction	$4Fe + SO_4^{2-} + 4H_2O \rightarrow 3Fe(OH)_2 + FeS + 2OH^-$	(2-12)

Cathodic depolarization is the process that H atoms adsorbed onto a cathode surface are removed to facilitate electron removal from the cathode. H_{ads} is removed by either of the following reactions (Booth & Tiller, 1960):

Chemical desorption	$2H_{ads} \rightarrow H_2$	(2-13)
Electrochemical desorption	$H_{ads} + H^+ + e^- \rightarrow H_2$	(2-14)

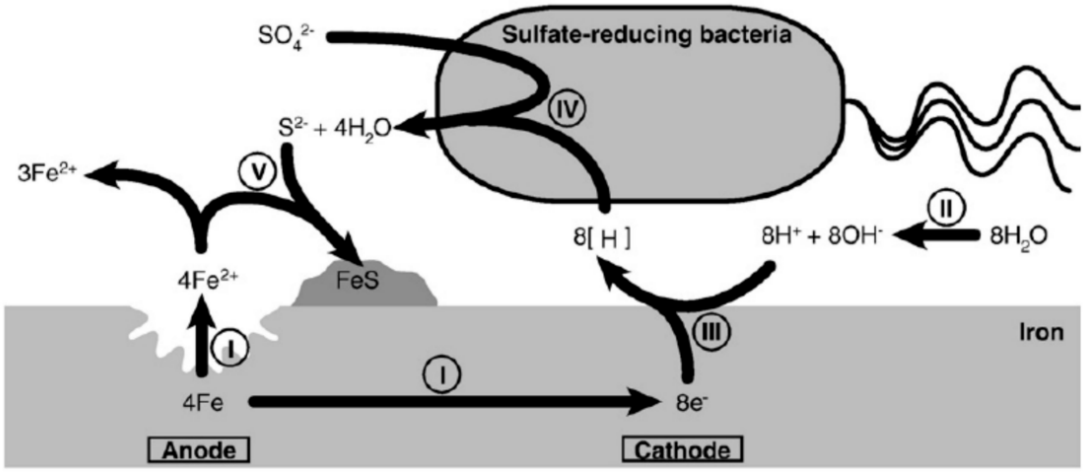

Figure 2-8. Schematic of MIC caused by SRB cathodic depolarization at an iron electrode (Mori et al., 2010). (Reproduced with permission from the publisher.)

However, CDT has some limitations. First, it does not specifically indicate the role of microbial biofilms. It is known that SRB biofilms influence the corrosion process. Second, CDT is inapplicable to hydrogenase-negative SRB and strains that do not use hydrogen gas in their metabolism (Gu et al., 2019).

2.3.2 Anodic Depolarization Theory

Anodic depolarization has also been investigated as a mechanism of MIC in metals. As indicated in the below reactions, the electrochemical processes for iron dissolution to Fe^{2+}, water dissociation to H^+, and formation of a protective layer of H_2 gas remain the same as in the concept of cathodic depolarization (Araujo-Jorge et al., 1992; Coetser & Cloete, 2005; Obuekwe et al., 1981).

Anodic reaction $4Fe \rightarrow 4Fe^{2+} + 8e^-$ (2-115)

Water dissociation	$8H_2O \rightarrow 8H^+ + 8OH^-$	(2-116)
Cathodic reaction	$8H^+ + 8e^- \rightarrow 8H_{ads}/4H_2$	(2-117)
Anodic depolarization	$3Fe^{2+} + 6OH^- \rightarrow 3Fe(OH)_2$	(2-118)
Hydrogen oxidation	$SO_4^{2-} + 4H_2 \rightarrow H_2S + 2H_2O + 2OH^-$	(2-119)
Dissociation of hydrogen sulfide	$H_2S \rightarrow S^{2-} + 2H^+$	(2-20)
Anodic depolarization	$3Fe^{2+} + S^{2-} \rightarrow 3FeS$	(2-21)
Overall reaction	$4Fe + SO_4^{2-} + 4H_2O \rightarrow 3Fe(OH)_2 + FeS + 2OH^-$	(2-22)

This theory is not popular because it is widely observed that electron utilization by biofilms in SRB MIC of carbon steel is the bottleneck as evidenced by electron mediator acceleration biofilm electron uptake (Wang et al., 2020; Wang et al., 2022c). This means that it is the cathodic reaction, rather than the anodic reaction that is rating limiting, which is consistent with CDT.

2.3.3 Iron Sulfides and Volatile Phosphorous Compound

In the absence of SRB biofilms, where pits were discovered, one group of researchers hypothesized that an iron surface acted as the anodic site, while the region passivated by FeS film and covered with the SRB biofilm acted as the cathodic site (King & Miller, 1971). The protective Mackinawite coating degrades when the solution has more Fe^{2+} ions, significantly accelerating the corrosion process. Figure 2-9 shows the hypothesized galvanic-effect corrosion mechanism proposed by King and Miller. This is consistent with experimental findings in pitting corrosion (Xu et al., 2023b).

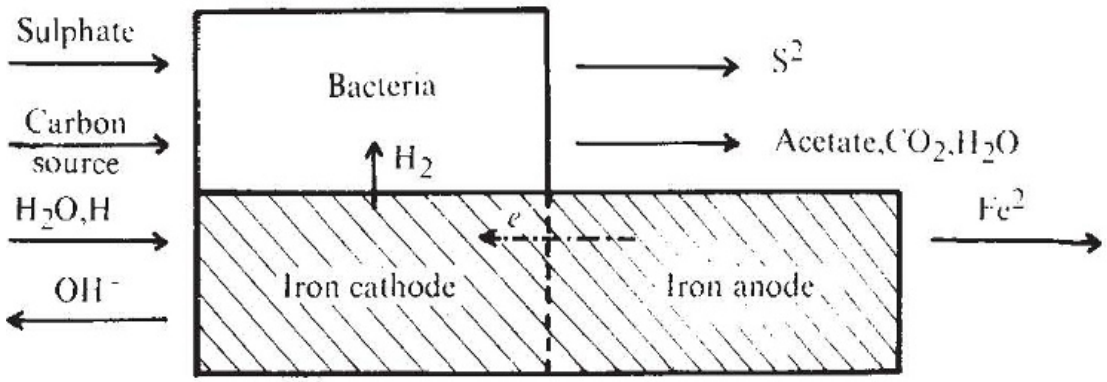

Figure 2-9. King's mechanism of MIC process induced by SRB (King & Miller, 1971). (Reproduced with permission from the publisher.)

Iverson and Olson established a unique theory of biocorrosion, according to which SRB accelerates the corrosion process by generating corrosion products such as phosphine (H_3P) and iron phosphide (Fe_2P) (Iverson & Olson, 1983). Yeast extract was selected to collect phosphorus compounds, which may be the source of the corrosive phosphorus compounds (Iverson, 2001). This theory is not consistent with SRB MIC experiments performed by many researchers, especially the carbon source starvation and electron mediator studies (Wang et al., 2020). One should realize that corrosion is a stoichiometric process. An oxidant molecule is no longer corrosive once it takes up electrons during corrosion. Thus, any corrosive metabolite (an oxidant) cannot sustain corrosion if it is low in quantity.

2.3.4 Biocatalytic Cathodic Sulfate Reduction (BCSR) Theory

According to the BCSR theory, also called the biocathode theory for MIC (Li et al., 2018d), the electrons released in Reaction (2-23) by lactate oxidation can be utilized by cytoplasmic sulfate reduction in Reaction (2-24) to produce energy for SRB intracellularly. SRB sessile cells residing at the bottom of a biofilm harvest e^- from elemental iron for cytoplasmic sulfate reduction when there is a local shortage of electrons supplied by organic carbon electron donor. Fe(0) is almost as energetic as lactate as an energy source: $E^{o'}$ values −447 mV in Reaction (2-4) vs. −430 mV) (Thauer et al., 2007).

Oxidation Reaction:

$$CH_3CHOHCOO^- + H_2O \rightarrow CH_3COO^- + CO_2 + 4H^+ + 4e^- \ (E^{\circ\prime} = -430 \text{ mV}) \quad (2\text{-}23)$$

Reduction reaction:

$$SO_4^{2-} + 9H^+ + 8e^- \rightarrow HS^- + 4H_2O \qquad (E^{\circ\prime} = -217 \text{ mV}) \quad (2\text{-}24)$$

$$E_e\,(SO_4^{2-}/\,HS^-) = 0.249 \text{ V} - \frac{2.591RT}{F}pH + \frac{RT}{8F}ln\frac{[SO_4^{2+}]}{[HS^-]} \qquad \text{(vs. SHE)} \quad (2\text{-}25)$$

In the Nernst equation above, R denotes the universal gas constant, T the absolute temperature (in Kelvin), and F the Faraday constant (96,485 C mol^{-1}). Standard hydrogen electrode (SHE) is typically used in bioenergetics. Because of mass transfer resistance, SRB cells at the bottom of biofilms are more likely to experience a lack of organic carbon as an electron donor for SRB respiration. Thus, SRB sessile cells obtain electrons from the oxidation of elemental iron instead of the organic carbon source, as

shown in Figure 2-10(a). This theory was proven by Xu et al. using organic carbon starvation tests (Xu & Gu, 2014). The pre-grown mature *D. vulgaris* biofilm was more corrosive in starving condition because the sessile cells obtained more electrons from elemental Fe for sessile cell survival (Xu & Gu, 2014).

Oxidation reaction: $Fe \rightarrow Fe^{2+} + 2e^{-}$ (2-26)

$$E_e(V) = -0.447 + \frac{RT}{2F} ln[Fe^{2+}] \quad \text{(vs. SHE)} \quad (2\text{-}27)$$

Sulfate reduction occurs in the cytoplasm of SRB cells; hence, no physical cathode (like a metal surface) exists inside the cytoplasm (Li et al., 2015), but we can treat the biofilm covered metal surface as the biocathode as in microbial fuel cell research.

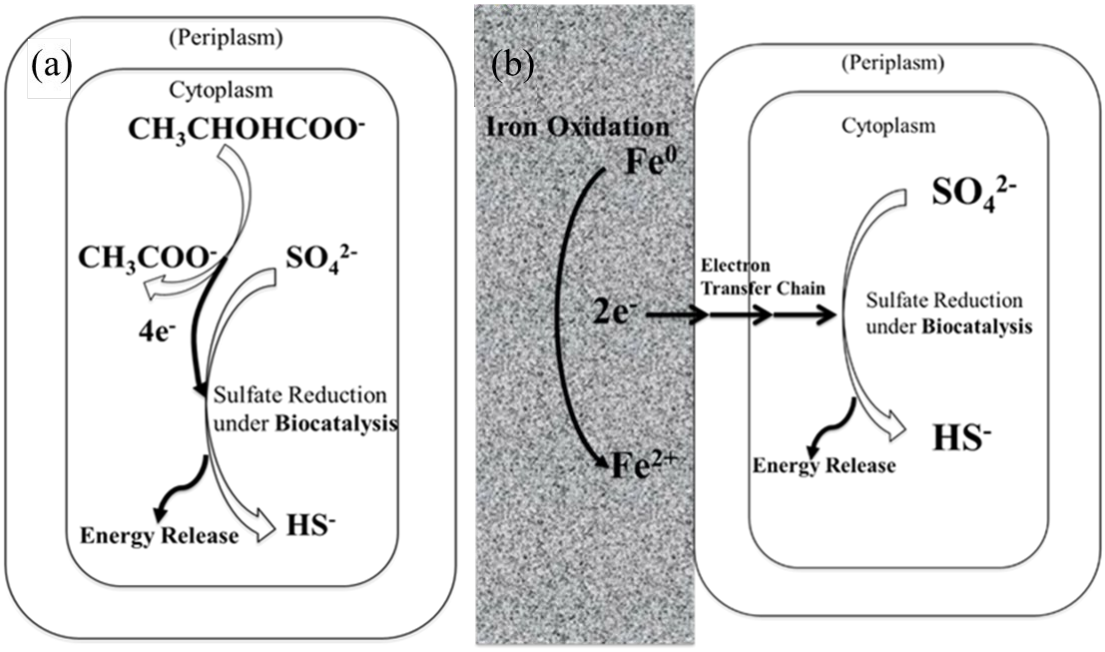

Figure 2-10. Schematic of SRB respiration using (a) lactate and (b) elemental iron as electron donor (Li et al., 2018d). (Reproduced with permission from the publisher.)

In Figure 2-10(b), electron transfer is required to transfer electrons from outside the cell to the SRB cytoplasm because electrons cannot "swim" like ions in water liquid. Therefore, an electroactive biofilm (defined broadly as any biofilm that performs electron transfer across a cell wall) is needed to facilitate the electrons moving through the outside the cell wall to the cytoplasm of the cell. This action is termed extracellular electron transfer (EET), which is known bidirectional (Li et al., 2018d). In MIC, EET is broadly defined as cross-cell electron transfer, which includes $2H^+/H_2$ shuttling of electrons.

2.3.5 Classification of Mechanisms of Fe MIC Caused by SRB

The EET depends on a biofilm's need for energy from the electrons released extracellular by an energetic metal to maintain the metabolic activities. Figure 2-11 shows the two electron transfer methods involved in EET-MIC. One is direct electron transfer (DET), indicating that direct contact between microorganisms and the iron (or steel) surface is required. This method also includes the scenario that protein-based cellular structures such as electron-conductive pili (e-pili) or *c*-type cytochromes attach to the metal surface to perform DET (Li et al., 2015; Xie et al., 2021). The other is mediated electron transfer (MET), involving soluble redox mediators (Aulenta et al., 2007; Usher et al., 2014). In MIC, $2H^+/H_2$ shuttling belongs to MET. Riboflavin is another rather universal electron mediator for MET (Wang et al., 2020).

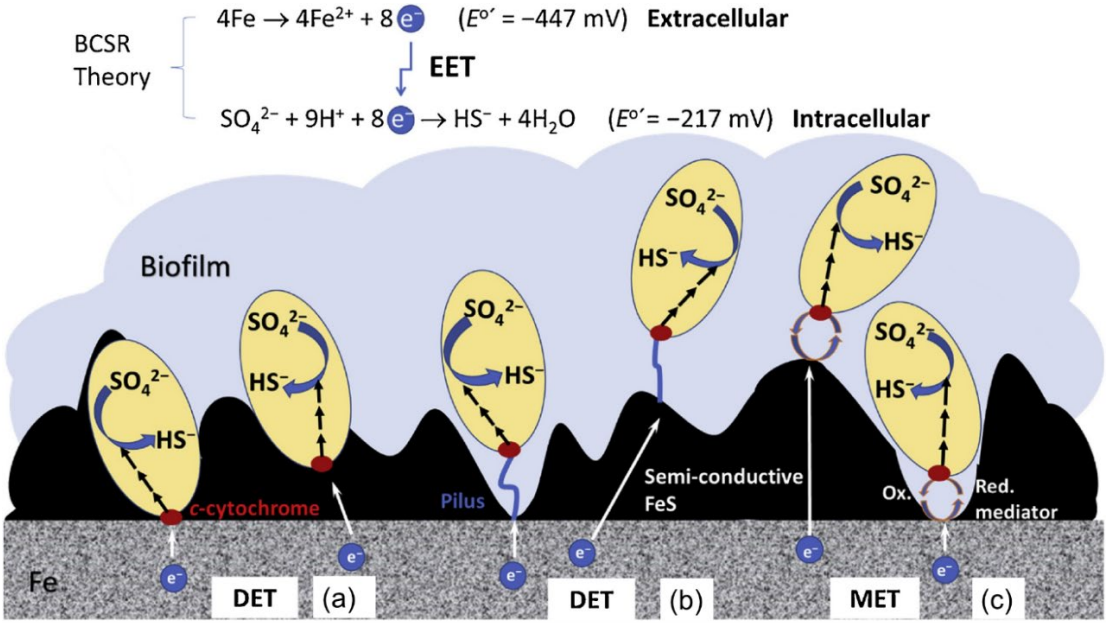

Figure 2-11. EET in SRB MIC of carbon steel to transport extracellularly released electrons from Fe oxidation to SRB cytoplasm for sulfate reduction: (a) DET relying on *c*-cytochrome contact with Fe or a semi-conductive FeS film surface, (b) DET with a Type IV conductive pilus, and (c) MET with electron mediator including $2H^+/H_2$ (Gu et al., 2019). (Reproduced with permission from the publisher.)

In DET, sessile cells need to make direct contact with a steel surface. The *c*-type cytochrome that is membrane-bound makes the EET possible. Conducive nanowires (pili) may be produced by a sessile cell to attach to a steel surface for EET if the distance between the sessile cell and the steel surface is relatively close (Li et al., 2015; Xu & Gu, 2014). However, pili do not always appear. In one study, it was found that SRB only produced pili to attach to a carbon steel surface when organic carbon source was

missing in the culture medium (Sherar et al., 2011). By utilizing the pili, the SRB cells made capturing electrons from elemental iron easier.

According to the definition of MET, flavins, melanin, phenazines, and quinines can be used as soluble electron transporters in MET for different microbial systems. Electron mediators can promote SRB MIC of stainless steel (SS) by MET in biofilms (Zhang et al., 2015). Electron mediators involved in SRB MIC consistently resulted in more severe MIC and deeper corrosion pits on carbon steel and SS coupons (Khan et al., 2022). Note that in addition to the electron mediators secreted by bacteria that can transport the electrons released by Fe(0) into the cytoplasm for bio-catalytic reduction reactions, $2H^+/H_2$ shuttling is also a common form for MET (Unsal et al., 2023).

2.4 Characteristics of Microbial Degradation of Mechanical Properties and SCC

2.4.1 Characteristics of Mechanical Properties of Metals and Their Degradation

Mechanical properties are the behaviors of metals when subjected to external forces or loads, ultimately resulting in the degradation or failure of metals. These mechanical properties are determined by the type of materials that comprise the fundamental characteristics of the metals.

Stress is the first critical mechanical property parameter widely used in corrosion research. The relationship between stress and strain is found using tensile test machine. During the tensile test process, a steadily increasing axial force is exerted on a dogbone coupon to plot a load-deflection curve by the machine's computer. The deflection is

determined by both the elastic modulus of the metal material and the geometry of the specimen (cross-section area and effective length). The concept formula of stress is expressed as follows:

$$\sigma = \lim_{\partial A \to 0} \frac{\partial F}{\partial A} \tag{2-28}$$

where σ is stress (MPa or N m^{-2}), F force (N or kN), and A the area (m^2 or mm^2).

Strain is the second critical mechanical property parameter widely used in corrosion research. When a metal material is subjected to a load or stress, it will be deformed or distorted. If the load is small, the distortion or deformation will probably disappear when removed, indicating elastic strain. However, when the load is large, the distortion or deformation cannot return to the original situation, indicating plastic strain. The definition equation for strain is as follows:

$$\varepsilon = \lim_{L \to 0} \frac{\Delta L}{L} \tag{2-29}$$

where ε is the strain, Δl the length change of the metal, and L the original length of the metal. Strain is expressed in percentage, which is dimensionless (Courtney, 2005).

The third critical parameter for mechanical properties is yield strength. It is defined as a stress value in MPa or N m^{-2}, located before the plastic deformation of a metal specimen under a tensile test. The material type determines the yield strength. It is a fundamental material property that cannot change because of the surrounding conditions (Luecke et al., 2005).

The fourth critical parameter of mechanical properties is the elastic region. The elastic region indicates that the metal material can return to its original state after a period of time when applied forces are removed. In the elastic region, metal deformation can be reversible. The critical stress value is the yield stress (Terzopoulos & Fleischer, 1988).

The plastic region is the fifth mechanical property parameter. The plastic region is found in an irreversible process while the elastic region is found in a reversible process. Therefore, when the applied stress exceeds the yield strength, the metal material cannot return to its original state permanently (Ren & Ren, 2018).

2.4.2 Characteristic of SCC

Corrosion can induce the deterioration of a steel's mechanical properties if the specimen has a stress loading. SCC is a major concern when metals are exposed to aggressive environments under stress. Various definitions of SCC exist. According to a commonly accepted definition, SCC is the cracking induced by the combined effects of tensile stress and a corrosive environment (Cheng & Chen, 2017). As shown in Figure 2-12, a sensitized material, a corrosive environment, and sufficient tensile stress are generally required for SCC formation (Cheng, 2013). A corrosive environment that causes SCC is usually aqueous and it can be either a condensed layer of moisture or a bulk liquid. Either a permanent environment, such as seawater around a marine structure, or a temporary environment attributed to a particular operation, such as

electrolyte residue left behind after rust removal from a metallic structure, can fulfill the requirements for SCC formation. MIC can also serve as the corrosive environment to cause SCC.

In the laboratory and field, the stress required to initiate SCC is small, typically below the macroscopic yield strength of the metal. When the stress is excessive, direct mechanical fracturing occurs rather than SCC. The application of tensile stress that exceeds the critical stress value to a susceptible material can result in unexpected and sudden failure of typically ductile metals but not SCC, particularly at elevated temperatures. When the corrosion rate is excessively high, cracking does not occur because a high corrosion rate results in fast uniform corrosion which prevents the formation of SCC. SCC needs a “tip”, such as a corrosion tip, to propagate (Abedi et al., 2007). Figure 2-13(a) presents an example of a pipeline ruptured due to SCC. Figure 2-13(b) and (c) show SCC cracks on the exterior of a high-pressure gas pipeline (Zvirko et al., 2016).

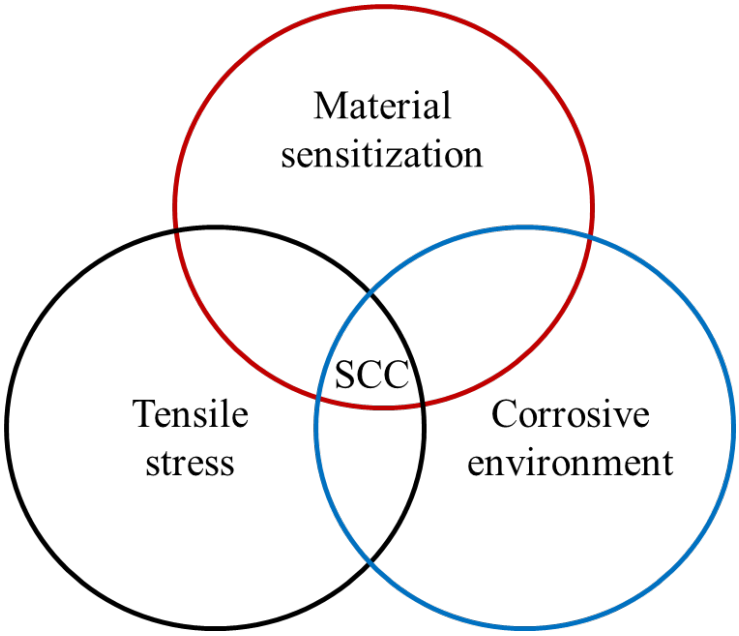

Figure 2-12. Essential factors required for SCC (Khalifeh, 2019). (Permission is not needed.)

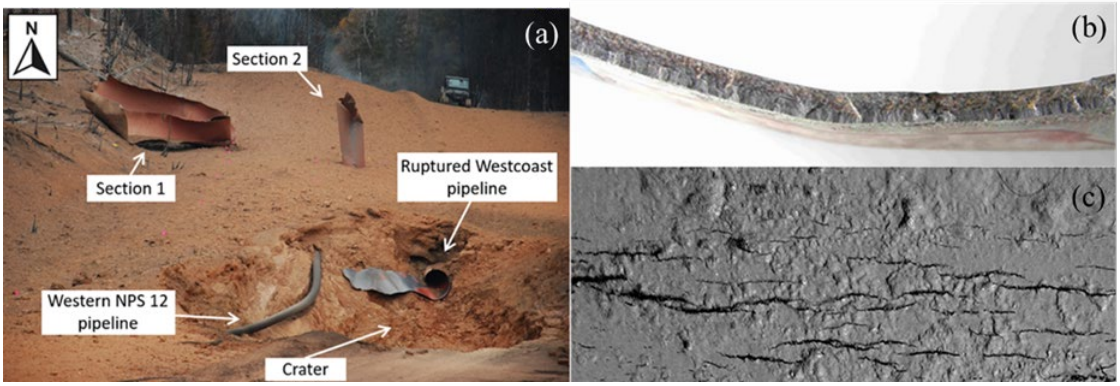

Figure 2-13. (a) Pipeline ruptured by SCC (Khan, 2016), (b) cracks found on the first section of the ruptured pipe in (a) (Materials Performance, 2020), and (c) a region of SCC on the outside surface of a high-pressure gas pipeline (Zvirko et al., 2016). (Permission is not needed.)

2.5 Influencing Factors of Mechanical Property Degradation and SCC

In this study, the primary objective was to investigate SCC of X80 carbon steel under SRB MIC condition and SRB degradation of X80 mechanical properties. The first aspect influencing mechanical properties degradation and SCC is a specific environment. The specific chemical composition provided by the specific environment is mandatory to promote mechanical degradation and SCC and then induce failure or fracture of the steel. In general, this specific environment is corrosion. In this study, the specific environment was provided by corrosive SRB rather than an abiotic corrosive agent such as an acid.

Time is the second aspect involved in the mechanical property degradation and SCC of steel. Mechanical degradation is aggravated in a specific environment as time passes. In contrast, SCC may only have tiny cracks for a short time and then fracture after a long enough time. Therefore, time is a critical parameter in the mechanical property degradation and SCC phenomena.

The last factor, tensile stress, is crucial to distinguishing mechanical degradation from SCC of steel. If the specimen is not subjected to applied stress in the specific circumstance, the drop in steel performance is called mechanical properties degradation, not SCC, owing to the “stress” factor being missing. The mechanical properties degradation of steel reflects on the deterioration of mechanical properties such as yield point, elongation, and type of fracture; however, no cracks are formed. In contrast, if

the specimen is subjected to an applied stress in a specific corrosive environment, the typical SCC occurs, ultimately resulting in cracks and fracture formation in steel.

2.5.1 Materials

SCC and mechanical properties degradation of carbon steels have been identified as the primary causes of pipeline leakage and rupture events. Carbon steels have shown SCC and mechanical properties degradation in corrosive environments and under internal or external pressures. The environments in which carbon steels become susceptible to SCC are sulfates, carbonates, and high-pH caustic solutions (Cheng, 2013).

X80 carbon steel is a very popular steel for pipelines. Different types of carbon steel have different SCC resistances because the mechanical properties such as ultimate strength, ultimate strain, and corrosive resistance are different, as listed in Table 2-1 and Table 2-2 (Zhang et al., 2022a).

Table 2-1. Elemental compositions of X20, X60, and X80 steels (mass% with Fe as balance) (Zhang et al., 2022a).

Metal	Mn	Si	P	Mo	C	S	Ni	Cr	Cu
X20	1.71	0.218	0.009	0.23	0.057	0.001	0.016	0.228	0
X60	1.28	0.276	0.008	0.002	0.115	<0.001	<0.001	<0.001	0.017
X80	1.70	0.207	0.01	<0.001	0.056	0.002	0.085	0.22	0.194

Table 2-2. Average time to crack growth and maximum crack depth of the X20, X60, and X80 steels (Zhang et al., 2022a).

Metal	Time to crack growth (d)	Maximum crack depth (μm)
X20	2.57	12.22
X60	4.32	8.99
X80	2.84	12.89

2.5.2 Environmental Conditions

(1) pH

Depending on pH, SCC can be classified into near-neutral pH SCC (NN-pH SCC) and high pH SCC, indicating that different pH values correspond to different SCC behaviors (Batte et al., 2012). Among these three types of SCC, researchers have primarily focused on NN-pH SCC, which covers MIC-induced SCC.

High pH SCC is a typical SCC identified in Louisiana, USA, first identified in 1965 in a gas transmission pipeline (Leis et al., 1996). The pH value of high pH SCC ranges from 9 to 13 (Song, 2010). High pH SCC typically happens in a relatively narrow cathodic potential range (–600 to –750 mV vs. $Cu/CuSO_4$) (Manfredi & Otegui, 2002). A corroded spot can act as a crack tip when the oxide film breaks down by loading or cyclic loading and the crack extends because of corrosion. Cracks attributed to high pH SCC move along the grain boundaries and are named intergranular SCC (IGSCC) (Niazi et al., 2021). High pH SCC is not as prevalent as NN-pH SCC owing to the

relatively stringent environmental requirements for initiation of this type of SCC. In addition, the passive film is easier to form in a high-pH solution, which can act as a protective film that diminishes corrosion and thus crack propagation (Cheng, 2013; Zheng et al., 2011).

Near-neutral pH SCC (NN-pH SCC) was first reported on Canadian pipelines in 1986 (Beavers & Bubenik, 2017). Since then, NN-pH SCC has been considered a threat to pipeline integrity in the industrial field. The pH value of NN-pH SCC is approximately 5.5–7.5, the common pH value range of typical MIC. NN-pH SCC can occur at –760 and –790 mV (vs. $Cu/CuSO_4$) (Hagarová et al., 2015). Cracking is attributed to NN-pH SCC moving across grain boundaries, called transgranular (TGSCC) (Yan et al., 2015). The NN-pH SCC is the most destructive of these three types of SCC. At NN-pH value, the corrosion rate of steel is not as fast as when immersed in an acidic environment (pH 4–6), which can dissolve crack tips more easily, as shown in Figure 2-14. Without efficient crack tips, inefficient cracks have longer fracture times because the crack growth rate (CGR) is slower.

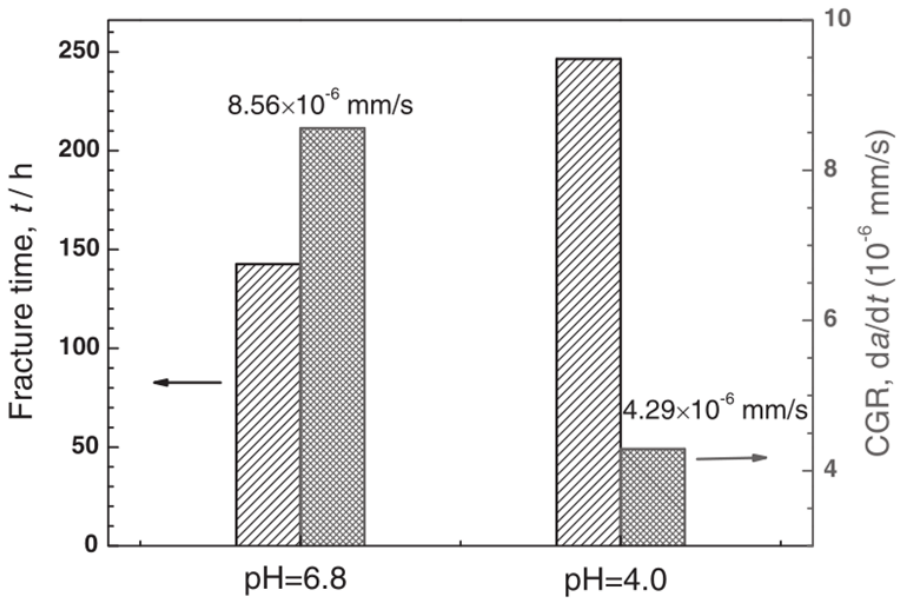

Figure 2-14. Fracture time (left column) and the mean CGR (right column) of X70 steel in NN-pH and acidic solution (Cui et al., 2015). (Permission is not needed.)

(2) Temperature

Temperature always has a significant effect on SCC and mechanical properties degradation behavior. It was found that increasing temperature always corresponds with an increasing CGR in A537 steel, as shown in Figure 2-15. (Sridhar et al., 2016). The SCC susceptibility increases with increasing temperature (Cheng et al., 2022; Manfredi & Otegui, 2002).

In high-pH SCC, higher temperature-induced SCC is more likely to occur, because under the higher temperature, the oxide film is easier to break, and thus cannot act as a

protective film to reduce the crack growth (Jack et al., 2000). However, higher temperature can produce a higher corrosion rate that can dissolve crack tips.

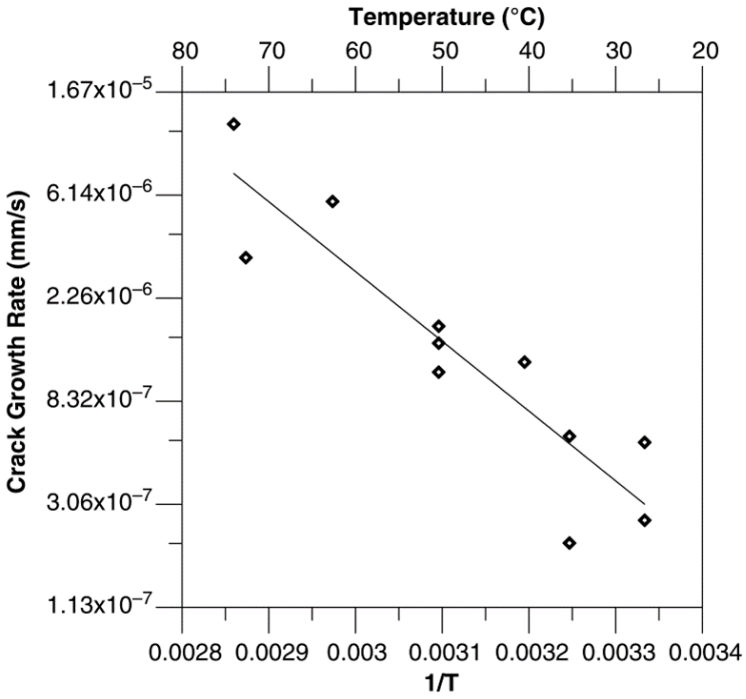

Figure 2-15. Effect of temperature on the CGR of the A537 steel specimens (Sridhar et al., 2016). (Reproduced with permission from the publisher.)

2.5.3 Exposure Time

The effect of exposure time has been researched by Rahimi et al. and is presented in Figure 2-16 (Rahimi et al., 2016). The severe cracks of 304 austenitic SS developed with longer exposure times without applied tensile bending stress and under 200 MPa of applied tensile bending stress. In NN-pH and acidic solution environments of X70 steel, another group of researchers showed that the crack length increases gradually

with increasing test time, as shown in Figure 2-17; longer exposure time induced deeper crack propagation as expected (Cui et al., 2015).

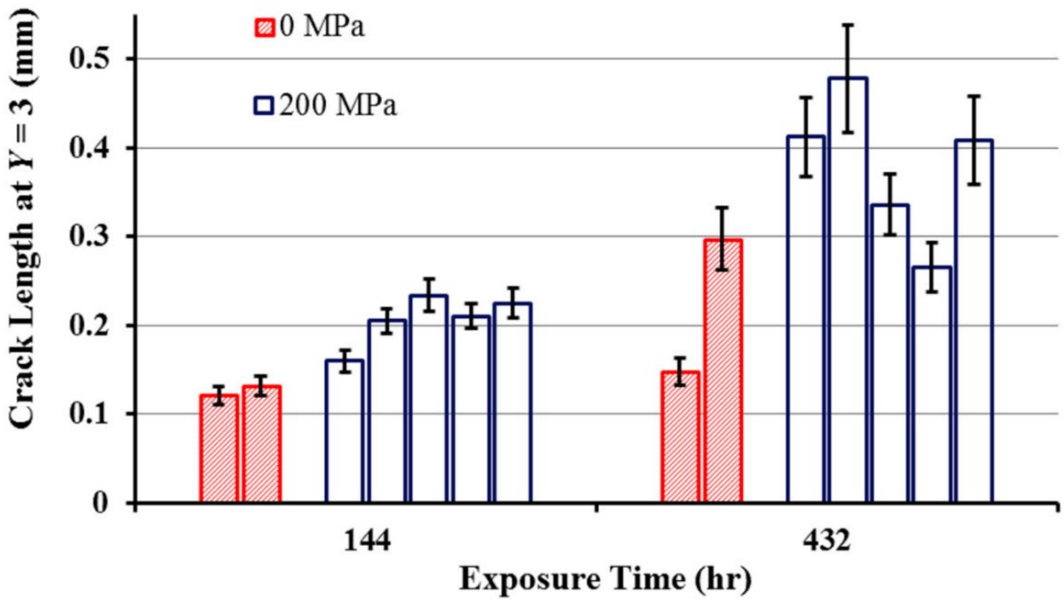

Figure 2-16. Effect of applied load and exposure time on the crack development of 304 austenitic SS: after 144 h and 432 h (Rahimi et al., 2016). (Permission is not needed.)

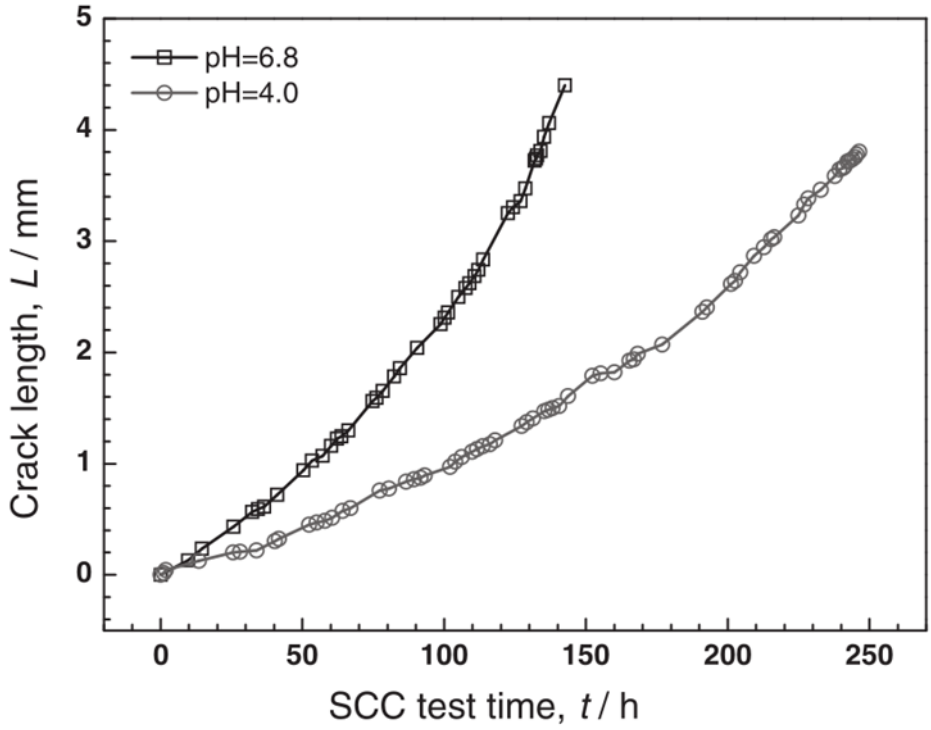

Figure 2-17. Crack length of the X70 steel during the crack growth tests in near-neutral pH and acidic solution (Cui et al., 2015). (Permission is not needed.)

2.6 Mechanisms of SCC

SCC can be attributed to several different mechanisms. Four major theories control SCC: anodic dissolution, film rupture, stress sorption, and (atomic) hydrogen embrittlement mechanisms. These four mechanisms can be classified as dissolution effects (first two mechanisms), and mechanical effects (last two).

2.6.1 Anodic Dissolution Mechanism

This anodic dissolution mechanism is also named the electrochemical mechanism of SCC or the active path mechanism in SCC. Anodic dissolution-assisted cracking is a characteristic intergranular mode of failure in which cracks propagate along the grain

boundaries (Zhu et al., 2014b). According to the electrochemical theory, anodic dissolution-assisted cracking requires a condition that makes the grain boundaries or adjacent regions anodic to the rest of the microstructure such that the dissolution will proceed selectively along the grain boundaries. Moreover, cracking occurs at the grain boundary in synergy with the applied stress (Yavas et al., 2018). The passive film covering the crack tip breaks after the tensile stress acts at the tip. Hence, the crack tip (exposing bare metal) starts to dissolve and act as an anode while re-passivation co-occurs, as shown in Figure 2-18 (Lazzari, 2019).

The anodic dissolution mechanism has two limitations. First, it cannot explain the transgranular SCC that cracks or faults across the crystals of metals and alloys rather than at the grain boundaries. Second, the anodic dissolution involved in the electrochemical theory, also cannot depict the SCC case in the aluminum-titanium alloy in the presence of CCl_4, which is a solvent, rather than an electrolyte (Galvele, 1995).

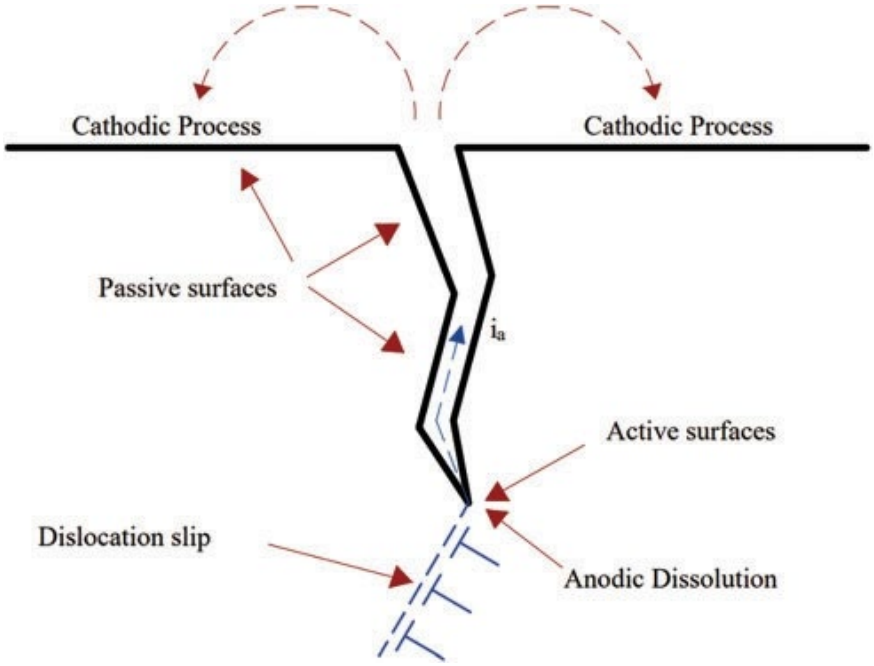

Figure 2-18. Schematic representation of the anodic dissolution mechanism for SCC (Lazzari, 2019). (Permission is not needed.)

2.6.2 Film Rupture Mechanism

In this mechanism, the passive oxide film or corrosion product layer on the cracks is ruptured by the applied stress in the film and around the crack tips. Then, the bare metal around the crack tips is exposed to the corrosion media within the cracks. The cracks propagate by the combined effect of anodic dissolution and applied stress (δ), as shown in Figure 2-19. The cracking process can be continuous or discontinuous depending on whether or not the passive film reformation on the rupture occurs (Zhu et al., 2014a).

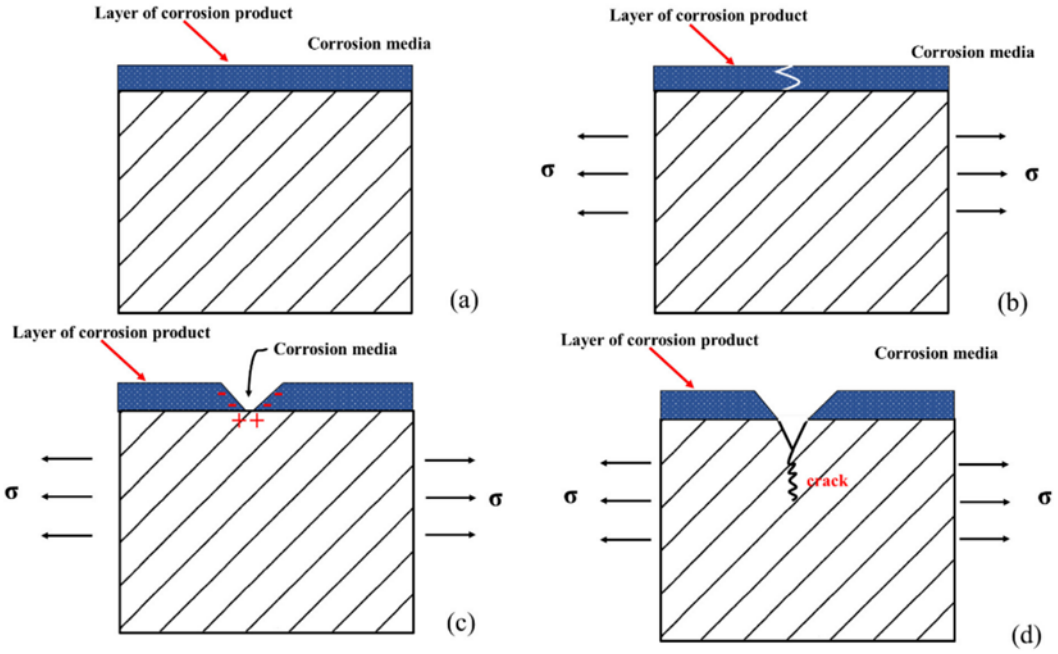

Figure 2-19. Illustration of the film rupture mechanism for SCC (Zhang et al., 2019). (Reproduced with permission from the publisher.)

2.6.3 Stress-Sorption Mechanism

Uhlig and Cook proposed the stress-sorption cracking mechanism (Uhlig & Cook, 1969). This mechanism describes that the chemisorption effect between specific chemical species and the metal surface can reduce the surface energy of the defects at the crack tip. The reduced iron atom affinities reduce the energy required for crack propagation. The defects provide sites for adsorption at the crack tip. The stress-sorption process of SCC occurs in three steps, as shown in Figure 2-20: (1) electrochemical corrosion occurs at grain boundaries that supply the micro-cracks in the iron; (2) ions adsorb on the sites of the micro-crack and the defects at the crack tip;

and (3) owing to the decreased energy for cracking progress, the brittle fracture occurs by the weakening of the interatomic bond at the tip of the tracks, resulting in the breaking of the bond by the applied stress. For a crack in a thin sheet, the required stress for fracture can be calculated by the Griffith criterion as shown below (Wool, 2005):

$$\sigma_F = \sqrt{\frac{2\gamma E}{\pi a}} \tag{2-30}$$

where σ_F is the required stress for the brittle fracture, γ the material's surface energy density, E Young's modulus, and a the half-crack length. The chemisorption effect reduces γ with the consequence that σ is decreased.

This mechanism assumes that the crack should propagate continuously at a rate dictated by the embrittling chemical species absorbed at the crack tip. Uhlig and Cook demonstrated that the driving force of this mechanism is not the chemical or electrochemical dissolution of metal at the crack tip but instead the reduction of surface energy by weakening strained metal atom bonds through adsorption of stress (Uhlig & Cook, 1969).

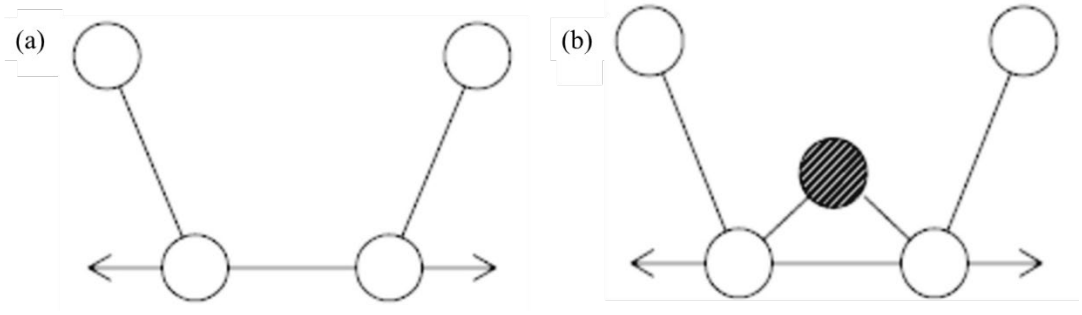

Figure 2-20. Stress-sorption mechanism for SCC: (a) chemisorption of the ion at the tip of the crack and (b) weakening of interatomic bonds at the tip of the tracks so that applied stress results in the breaking of this bond (Loto, 2017). (Reproduced with permission from the publisher.)

2.6.4 Hydrogen Embrittlement Mechanism

Hydrogen embrittlement (HE) is also named hydrogen-assisted cracking (HAC). The definition of HE is that because the material is exposed to atomic hydrogen and the hydrogen penetrates or adsorbs on the material, metallic materials have mechanical degradation, such as loss of ductility and tensile strength (Djukic et al., 2015). The cathodic reaction of hydrogen ions produces hydrogen atoms. Depending on the diffusion and enrichment of hydrogen atoms, hydrogen atoms adsorb on the crack tips to induce initiation and propagation of the crack (Ohaeri et al., 2018). The first step is as follows:

$$Fe \rightarrow Fe^{2+} + 2e^{-} \qquad \text{(anodic reaction)} \qquad (2\text{-}31)$$

Followed by chemical reaction,

$$2H_{ads} \rightarrow H_2\ (g) \qquad (2\text{-}32)$$

or electrochemical reaction,

$$2H^+ + 2e^- \rightarrow 2H_{ads} \quad \text{(cathodic reaction)} \qquad (2\text{-}33)$$

The process includes Reaction $2Hads \rightarrow H_2$ (g) and $2H^+ + 2e^- \rightarrow 2H_{ads}$ (cathodic reaction) which is known as the combination mechanism of hydrogen evolution (Cheng & Niu, 2007; Elboujdaini & Revie, 2009), whereas the process includes Reactions (2-32) and (2-33), which is known as the electrochemical mechanism of hydrogen evolution (Shiraz et al., 2021).

The HE mechanism process does not have an exact final theory; however, it can be expressed, as shown in Figure 2-21 and Figure 2-22, as follows:

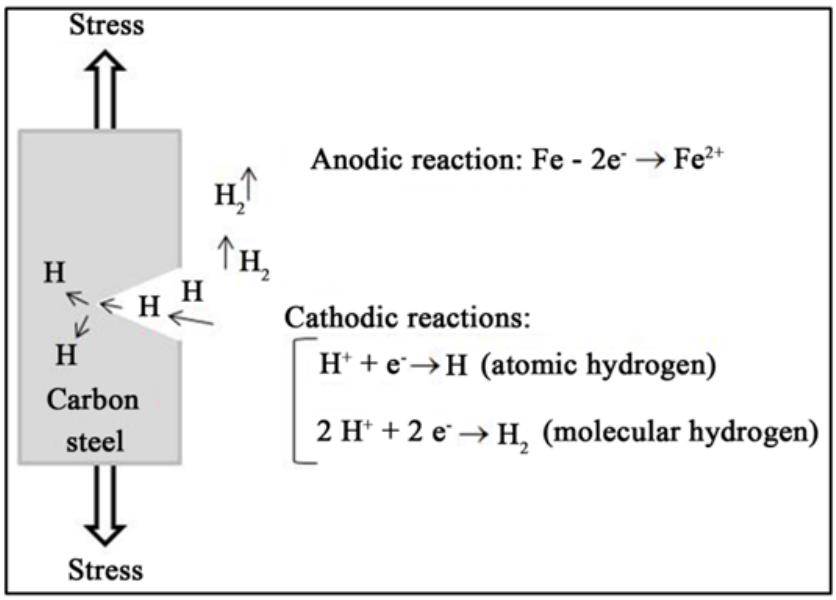

Figure 2-21. HE mechanism for SCC (Mainier et al., 2015). (Permission is not needed.)

(1) The hydrogen atoms are generated by the polarization in the cathodic reaction (Cheng & Niu, 2007).

(2) Hydrogen permanent diffusion and redistribution of inside materials, such as vacancies, dislocations, precipitates, grain boundaries, phase interfaces, triple points, microcracks, voids, and other defects that limit hydrogen and accelerate its movement. The tiny hydrogen atoms fill in the voids, and flaws in the iron induce an internal pressure in iron, forming the brittle region or path as crack tips in steel. Hydrogen adsorbs on the crack tips, reducing the surface free energy of steel and decreasing the time of fracture. In addition, the concentrated hydrogen ions that dissolve in the steel enrich the crack tip, which results from the acidification near the crack tip. This induces the plastic deformation of steel in advance of cracks and decreases the time of fracture (Venezuela et al., 2016).

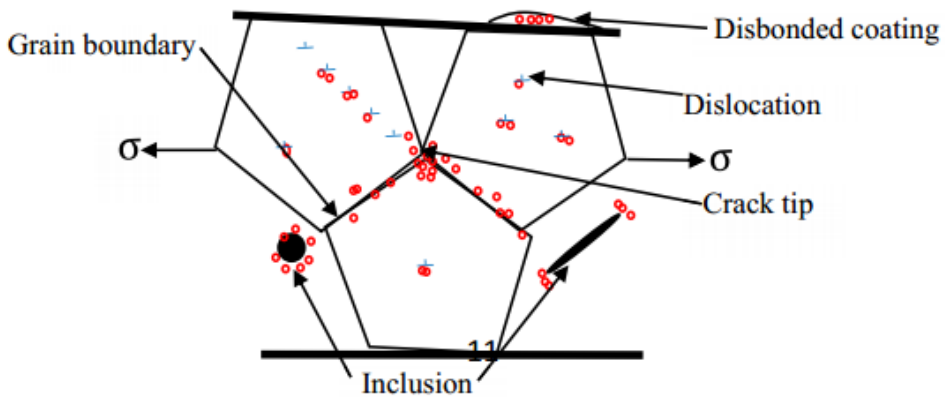

Figure 2-22. Diagram of hydrogen atoms trapped at several locations in steel (Ohaeri et al., 2018). (Reproduced with permission from the publisher.)

2.7 SCC Initiation and Propagation Mechanisms

An SCC process is classified into four stages: pit formation, pit growth, crack initiation, and crack propagation induced final crack, as shown in Figure 2-23. The SCC initiation process has three steps (Figure 2-23 (a)–(c)), always called a pit-to-crack process, whereas, as shown in Figure 2-23 (d), crack propagation and final failure belong to the SCC propagation process.

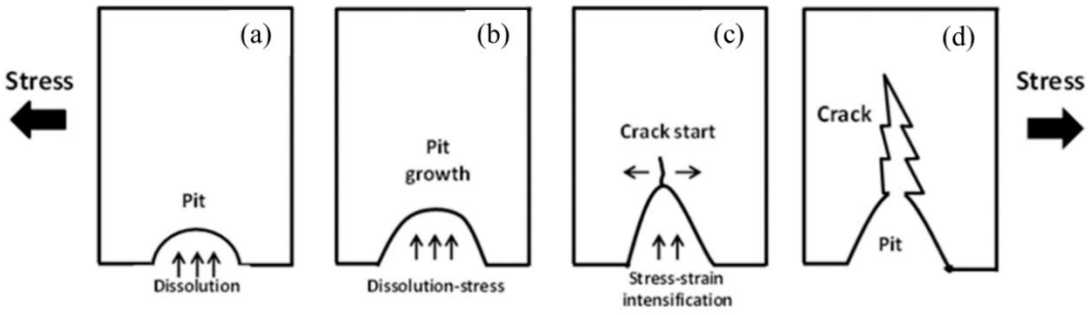

Figure 2-23. Pit-to-crack transition: (a) pit initiation, (b) pit growth, (c) crack initiation, and (d) crack propagation and final crack (Quej-Ake et al., 2020). (Permission is not needed.)

2.7.1 SCC Initiation Mechanisms

In the SCC initiation process, a corrosion pit transfers to a crack tip as a result of specific conditions, particularly stress, shown in Figure 2-24(a)–(c).

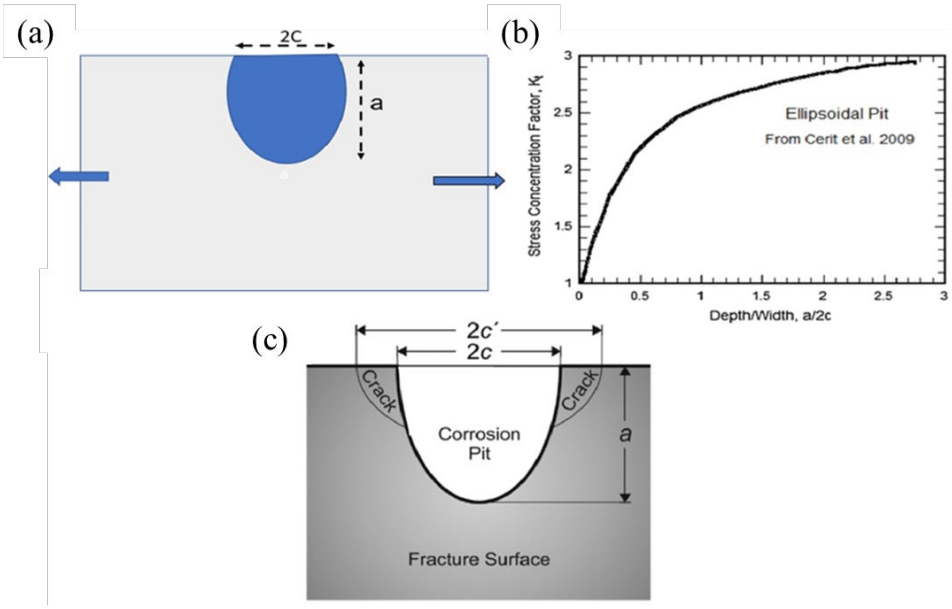

Figure 2-24. (a) Pit modeled as a semi-ellipsoid notch, (b) stress concentration factor as a function of its aspect ratio, and (c) crack growth from a pit starting from its surface (Sadananda & Vasudevan, 2020). (Reproduced with permission from the publisher.)

When a corrosion pit transitions to a crack, it appears as a semi-elliptical crack of the same length as the pit depth. The stress intensity factor (SIF) ΔK is used to depict the magnitude of stress. The general expression of the coefficient ΔK of the SIF is shown below:

$$\Delta K = Y\sigma\sqrt{\pi a} \tag{2-34}$$

Here, Y is the shape coefficient, σ the nominal stress, and a the crack depth (Etube et al., 2000). The range of the value at the moment of pit-to-crack tip transition is equal to the threshold value for the propagation of fatigue or corrosion fatigue crack (ΔK_{th}) (Jakubowski, 2015):

$$\Delta K = \Delta K_{th} \tag{2-35}$$

SCC initiation mechanisms have three different types, as illustrated below (Raja, 2011):

First, cracks initiate at surface discontinuities. Discontinuities on a metal surface can have several types, including grooves, scratches, and dents, which can be caused by corrosion or other physical forces. They can lead to environments with localized electrochemical activities detrimental to the protective film.

Second, cracks initiate at metallurgical defects. Metallurgical defects can have many forms, including voids, inclusions, and grain boundaries. Galvanic corrosion can occur. This can cause preferential dissolution.

Third, cracks initiate at corrosion pits. Localized stress or strain at the pits enhances local dissolution with the possibility of some pits transition into cracks.

Fracture mechanics provide a critical pit dimension, a threshold for pit-to-crack transition (Roylance, 2001):

$$a_0 = \frac{1}{\pi}\left(\frac{\Delta K_{th}}{c\Delta\sigma_0}\right)^2 \tag{2-36}$$

where a_0 is the critical crack depth, ΔK_{th} the stress intensity threshold, c a constant, and $\Delta\sigma_0$ the alternating surface stress. Notably, this model lacks supporting data for predicting the pit-crack transition because it assumes that pitting corrosion conditions are equal to metal surface conditions. This model cannot explain the corrosion pit-to-

crack transition. This model can only describe a critical crack depth proportional to the stress intensity threshold and an inverse relationship with the alternating surface stress.

2.7.2 SCC Propagation Mechanisms

The cracks can initiate at stress concentration points when the pits form on the surface. Once a crack is initiated in a corrosion pit, growth continues intergranularly via a combination of anodic dissolution and film cleavage. In all SCC propagation mechanisms for metals in aqueous solutions, the fundamental principle is that the crack tip grows faster than its sides such that the crack site will not dull into a notch (Ford, 1982).

Two different SCC propagation mechanisms exist: dissolution-based and mechanical fracture-based.

(1) Dissolution-based SCC propagation

The occurrence of cracks preferentially occurs upon dissolution at the tip. In intergranular cracking, the grain boundaries exist as segregated solutes or precipitated phases, which can lead to local electrochemical heterogeneity. In an appropriate environment, preferential dissolution occurs in a limited area. If the stress is minimal, the corrosion may not go far owing to film formation and the lack of stress to rupture the protective film. In the presence of stress, a stress point opens up a crack because of corrosion. The repetitive rupturing of films can maintain the dissolution reaction that enables continued crack growth, typically at grain boundaries (Ford, 1996).

A significant parameter in the SCC propagation process for a pure metal, the crack propagation rate (CPR), can be calculated under controlled dissolution conditions (Ford, 1996):

$$CPR = \frac{i_a \cdot M}{z \cdot F \cdot \rho} \tag{2-37}$$

where i_a is the dissolution current density, M the atomic weight of Fe (55.845), z the valence of solvated species, F the Faraday constant (96,485 C mol^{-1}), and ρ the density of steel (7.874 g cm^{-3} for most carbon steels).

Figure 2-25 shows the schematic of SCC failure governed by the anodic dissolution mechanism when the material is steel. During the anodic dissolution process, corrosion pits form on the surface of the specimen and generate stress concentration at the pit bottom. Consequently, external stress starts and spreads microcracks. Therefore, the fracture surface exhibits a quasi-cleavage characteristic.

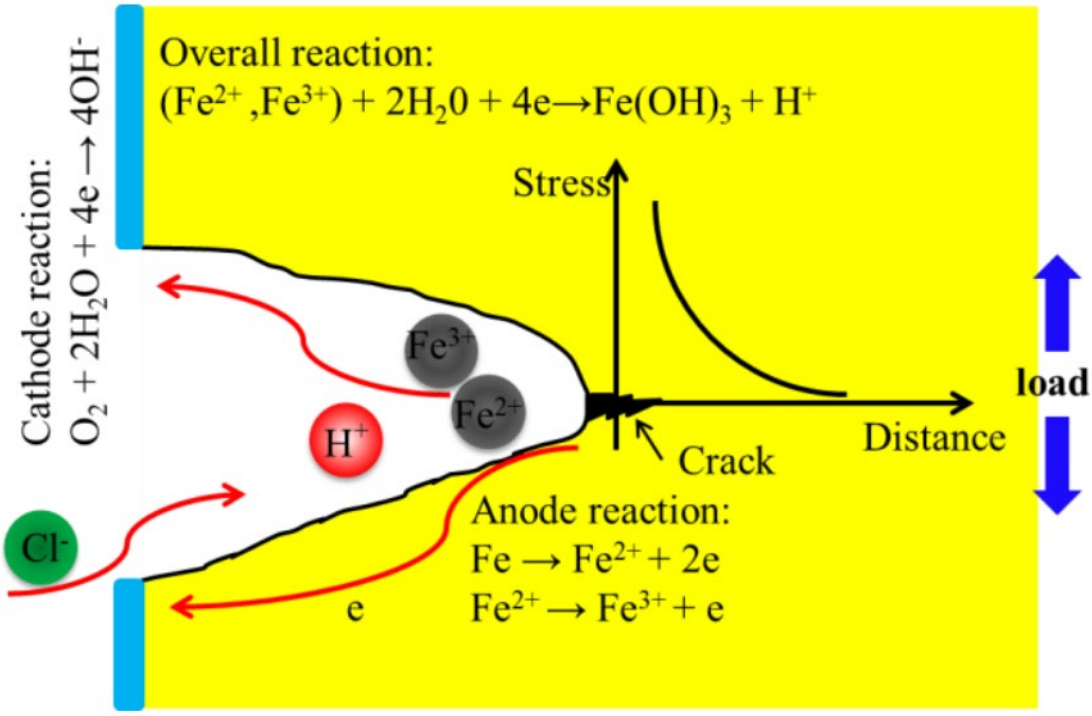

Figure 2-25. Illustration of SCC failure following anodic dissolution mechanism (Zeng et al., 2020). (Reproduced with permission from the publisher.)

The dissolution current density can be abiotic, or biotic, which means corrosion current caused by corrosive microorganisms such as SRB, NRB, and APB. However, much work needs to be done to prove biotic cases experimentally. This work proved SRB SCC against X80 carbon steel.

(2) Mechanical fracture-based SCC propagation

The fracture can be classified into two modes, intergranular and transgranular fractures. Figure 2-26 illustrates the two mechanisms (Ghiasi et al., 2010; Zhu, 2022).

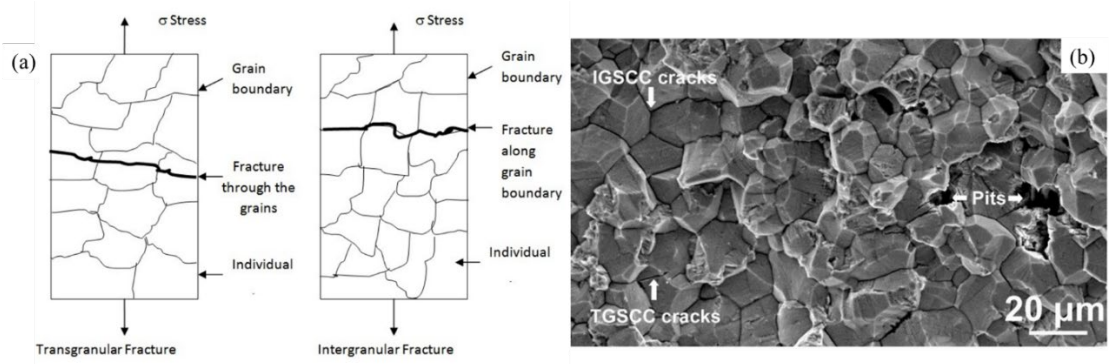

Figure 2-26. (a) Mechanism of IGSCC (Intergranular stress corrosion cracking) and TGSCC (Transgranular Stress Corrosion Cracking). (b) IGSCC cracks, TGSCC cracks, and pits of type 316L non-sensitized austenitic SS (Ghiasi et al., 2010; Zhu, 2022). (Permission is not needed.)

A mechanical fracture occurs when the concentrated stress accumulated at the tips of corrosion pits or mechanical defects increases to reach metal fracture. Concentrated stress at corrosion pits generates SCC. The K value quantifies the effect of stress concentration on mechanical fracturing. A mechanical fracture occurs when a critical stress concentration, K_{crit}, is reached. When the stress concentration does not exceed the critical value ($K_{scc} < K_{crit}$), mechanical fracture of the material does not occur. Corrosion in the absence of stress does not result in apparent crack propagation phenomena, whereas exposure to simultaneous environmental and applied stress results in time-dependent crack propagation (Burt, 2015).

2.8 SCC Thermodynamics and Kinetics

2.8.1 Thermodynamic Conditions Determine Whether Cracking Is Feasible

Thermodynamic conditions are a key consideration when deciding whether or not cracking occurs. The thermodynamic requirements for anodic dissolution-induced SCC involve two aspects: thermodynamically feasible metal dissolution or oxidation in the electrolyte, and thermodynamically stable protective film produced on the crack wall.

2.8.2 Protective Films on the Crack Wall Must Be Thermodynamically Stable

If the thermodynamic properties of a protective film are not stable, the protective film itself cannot be stable, and the layer cannot play a protective role in reducing corrosion. The dissolution rate of a crack wall can only be reduced by the formation of a passive layer when a crack tip is present on a bare steel surface.

2.8.3 Kinetics Dictates the Rate of Crack Propagation

The crack-tip reactions and rate-determining steps control the crack propagation rate (CPR). CPR is a function of the total charge transfer at a crack tip, which is provided the current density at the crack tip (Cheng, 2013):

$$\frac{da}{dt} = \frac{i_a M}{nF\rho} \tag{2-38}$$

where a is the crack length, t the time, $\frac{da}{dt}$ the crack propagation rate, i_a the anodic dissolution current density at the crack tip, M the atomic weight of the Fe (55.845), n the number of electrons exchanged, F the Faraday constant (96,485 C mol^{-1}), and ρ the density of steel.

2.9 Mechanical Techniques for Quantifying Mechanical Properties and SCC

2.9.1 U-Bend Test

Stress can be achieved by bending a metal strip to form a U-bend for SCC investigations. A bolt is used to convert the U shape to a D shape for testing. A U-bend can provide stable strain during immersion time, which leads to SCC, as shown in Figure 2-27. The following equation can calculate the applied strain (ε).

$$\varepsilon = \frac{t}{2r} \qquad (t << r) \tag{2-39}$$

where t is the thickness of the specimen and r the radius of curvature. Test details can be found in the standard method ASTM G30 (ASTM G30, 2000). It is easy to cause cracks at the outer bottom surface of U-bend specimens. Moreover, the U-bend can exhibit electrochemical activity when the material is subjected to both longitudinal tensile stress and corrosive conditions.

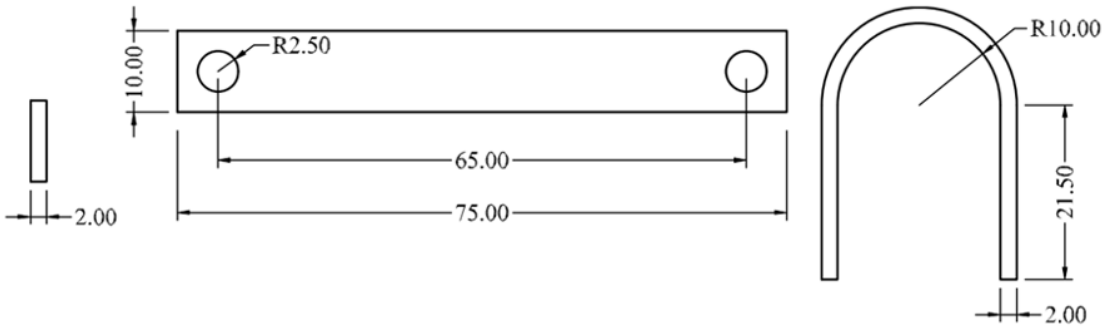

Figure 2-27. U-bend sample (dimensions in mm) (ASTM G30, 2000). (Permission is not needed.)

2.9.2 Tensile Test

The X80 SCC susceptibility in anaerobic bottles containing SRB broth with different headspace volumes (and fixed broth volume) were investigated in Chapter 7 by using the slow strain rate tensile test (SSRT). Tests were performed using dogbone coupons with dimensions shown in Figure 2-28. The specimens were dogbone coupons that had been exposed to corrosive SRB environment. After immersion, the dogbone samples were subjected to tensile testing to determine the changes in mechanical properties. The gage length was modified to meet ASTM E9 standard (ASTM E9, 2000).

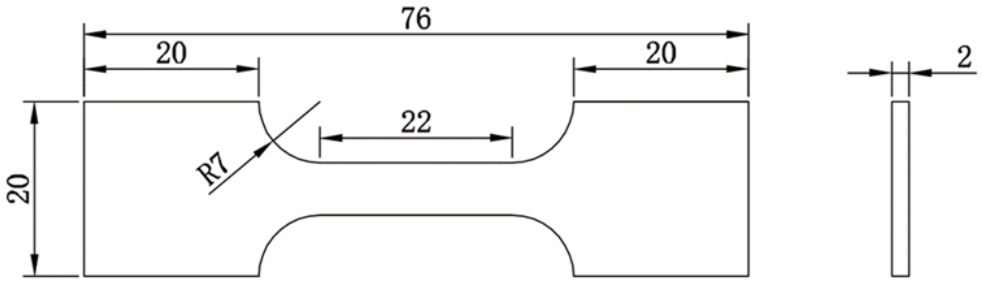

Figure 2-28. Tensile test dogbone specimen (dimensions in mm) (ASTM E9, 2000). (Permission is not needed.)

In recent years, dogbone specimens have been widely used to test the mechanical properties of metal materials immersed in various corrosive media. Tensile testing can produce mechanical property data such as yield point and elongation, which can indicate how microbes and MIC can degrade the mechanical properties of a material.

The stress-strain curve can be obtained from the tensile test. A typical stress-strain curve is shown in Figure 2-29. Yield strength is an indication of the maximum stress developed in a material without plastic deformation, which is the stress at which point that a material shows a degree of permanent deformation and is close to the elastic limit. Ultimate strength and ultimate strain are the two parameters used in this work to quantify mechanical properties. A lower ultimate strain means the metal is less ductile.

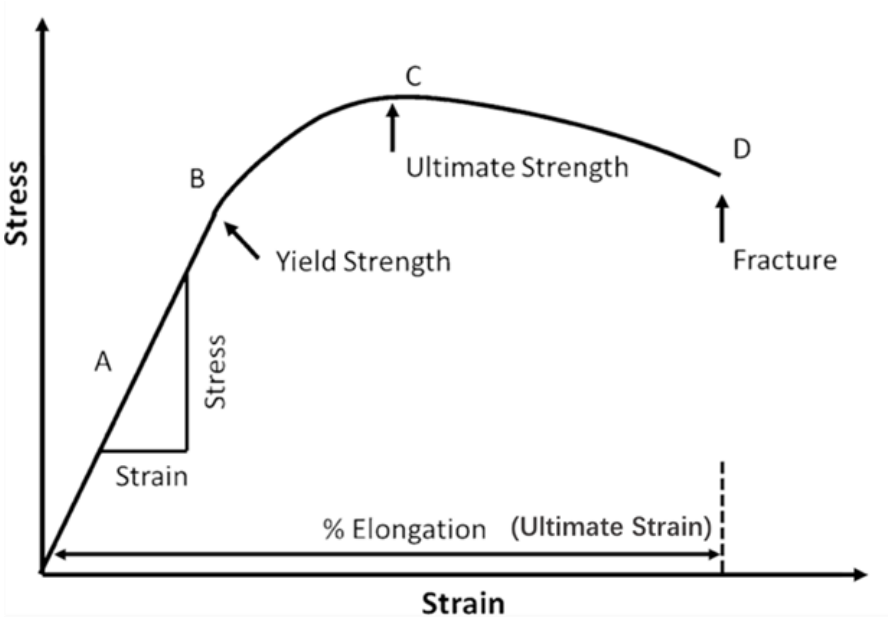

Figure 2-29. Diagram of the stress-strain curve (Lim & Hoag, 2013). (Reproduced with permission from the publisher.)

2.10 Electrochemical Corrosion Testing Techniques for MIC

Several non-destructive electrochemical methods have been applied to investigate MIC behavior, including open circuit potential (OCP), linear polarization resistance

(LPR) (R_p), and electrochemical impedance spectroscopy (EIS) (Jia et al., 2018b; Little & Lee, 2007). Potentiodynamic polarization (PDP) curves are also generally used to study MIC in a wide potential range; however, they are used only once for the working electrode because the wide potential range alters the electrode surface properties (Jia et al., 2018a).

2.10.1 OCP

OCP, denoted as E_{ocp}, describes an electrode potential without any load. OCP is typically measured relative to a stable reference electrode not covered by a biofilm. At E_{oc}, the current is zero because the circuit is open (Dubey et al., 1999). OCP has been used in biocorrosion systems for many years. Theoretically, a lower OCP means the working electrode is more eager to give up electrons, i.e., a higher tendency to be corroded. With a protective coating, OCP typically shifts to a much higher position (Gabrielli et al., 1979). The corrosion tendency does not equal the actual corrosion rate. A large thermodynamic driving force can be offset by very slow reaction kinetics. It was found that for complicated SRB MIC systems, OCP is often inaccurate in predicting actual corrosion outcomes (Jia et al., 2018a). Kinetic electrochemical data are far more reliable. They include LPR, EIS, and PDP, which can be used to judge qualitative corrosion trends. Because different MIC systems have very different corrosive environments, cross comparison using electrochemical data is unreliable and should be avoided. It is unacceptable to use i_{corr} from PDP or R_p from LPR to calculate

actual corrosion rate for complicated MIC systems. Such practice is only permitted in simple corrosion cases such as abiotic acid corrosion with charge transfer control (McCafferty, 2005).

2.10.2 LPR

The polarization resistance (R_P) is defined as the slope of the potential (E) vs. the current density (i) at corrosion potential (E_{corr}). E_{corr} comes from the interception point of cathodic and anodic slopes in Tafel analysis. It is close to the measured OCP (open circuit potential) if there is no OCP drift and the Tafel scans start at OCP. Therefore, R_P is expressed as follows:

$$R_p = (\frac{dE}{di})\ around\ E = E_{corr} \tag{2-40}$$

Corrosion current density (i_{corr}) and R_p are related via Stern–Geary equation:

$$i_{corr} = (\frac{1}{2.3R_p})(\frac{\beta_a\beta_c}{\beta_a+\beta_c}) \tag{2-41}$$

The i_{corr} calculation requires measurements of R_p and the anodic and cathodic Tafel slopes (β_a and βc, respectively). Here, β_c is the absolute value of the Tafel slope for the cathodic reaction. Computer programs have been developed to determine the corrosion current density (Gerchakov et al., 1981). Because Tafel slopes scan vary greatly for different testing conditions and at different incubation times even for the same MIC system, unlike traditional CO_2 corrosion, Equation (2-41) is only helpful with constant Tafel slopes. Thus, R_p is often used qualitatively without calculating i_{corr} to study corrosion trends (Jia et al., 2018b). A lower R_p corresponds to a higher corrosion rate.

LPR is a fast and non-destructive electrochemical method to study abiotic corrosion. It has been widely used in MIC (Jia et al., 2018a; Jia et al., 2019b; Xu et al., 2017). A small DC voltage (e.g., ±10 mV) is typically measured at a scan rate of 0.0167 mV s^{-1}. The solution resistance is also lumped into R_P. Significant errors in corrosion rates can occur in low-conductivity electrolytes without correcting for the solution resistance (Little & Lee, 2007). This is not a problem for MIC systems, where charge transfer resistance often dominates based on EIS (Jia et al., 2017a; Jia et al., 2017b; Xu et al., 2017), and LPR data are only used qualitatively.

2.10.3 EIS

EIS can be applied to all types of corrosion, including studying MIC. EIS can monitor corrosion processes by measuring the impedance of an electrochemical system as a function of frequency in electrolytes with low conductivity (Cesiulis et al., 2016). EIS has been widely applied to investigate MIC of carbon steel exposed to SRB (Jia et al., 2017a). The small-amplitude (e.g., 10 mV) AC signals applied in EIS are one of the advantages of MIC studies (Dubey et al., 1999). Repeated use of EIS analysis does not damage biofilms and causes no major change in OCP (Sasser et al., 1984). Franklin et al. confirmed that the use of EIS to study MIC mechanisms causes almost damage to the biofilms (Franklin et al., 1991). Unlike LPR, EIS can differentiate among solution resistance, biofilm/corrosion product film resistance, and charge transfer resistance, thus providing more information on the corrosion process.

2.10.4 Tafel Scan

PDP scan is also known as Tafel scan. It employs a large DC (direct current) voltage scan. The corrosion current density (i_{corr}) can be derived from polarization curves by Tafel analysis. Unlike LPR, Tafel analysis can provide i_{corr} value. It is usually done at the end of a corrosion test. Thus, one must be careful when using i_{corr} to calculate weight loss because the weight loss is for the entire corrosion period (Dou et al., 2018). Many researchers have applied polarization curves to characterize corrosion processes resulting from microbes attached to a metal surface, such as carbon steel. For example, Jia et al. used it to obtain i_{corr} in mechanistic studies of the SRB MIC of carbon steel (Jia et al., 2018a). A disadvantage of this technique is that the high potential used on the surface is feared to cause irreversible changes to the working electrode surface. After Tafel extrapolation, the specimen cannot be subjected to other electrochemical tests. Recently, our group demonstrated that if the anodic curve and cathodic curve were both scanned from OCP, PDP scans (Tafel scans) can be repeated without altering the working electrode (Wang et al., 2022b). In comparison, continuous upward scan with OCP in the middle is harsher because the biofilm is immediately exposed to the most negative voltage. This provides no time for the biofilm to adapt, which causes Tafel curve skews and last i_{corr} deviations.

For corrosion inhibitor studies, it is essential to know that a cathodic scan can substantially enhance the adsorption of inhibitor molecules on the working electrode

surface and thus alter the anodic scan outcome, making the inhibitor appear more protective (Wang et al., 2019a). Thus, a single cathodic curve or anodic curve in sometimes used to obtain i_{corr} to avoid the problem.

2.11 Mitigation of Biofilms

MIC is caused by biofilms because they can perform EET or provide locally high concentrations of corrosive metabolites, or they can damage passive films (Li et al., 2018d). MIC mitigation is about biofilm mitigation. The most common practice is still the age-old "spray and scrub" approach. Biocides are typically used to treat biofilms in industrial fields. In M-MIC, planktonic cells can also contribute to MIC, but planktonic cells are usually far easier to treat than biofilms.

Tetrakis hydroxymethyl phosphonium sulfate (THPS) is a very popular non-oxidizing green biocide to mitigate biocorrosion in oilfields because of its excellent broad-spectrum efficacy and biodegradability (Jia et al., 2019a). It is also compatible with other oilfield chemicals. It inhibits cell growth or kill microbes by damaging the outer membrane of the cell and inhibiting enzymes (Wang et al., 2022d). In addition, THPS provides high-temperature tolerance and H_2S scavenging ability for downhole conditions. The injection of THPS at 300 ppm (w/w) by mass every 3 d in a high-temperature (80–84°C) oil reservoir controlled H_2S levels to less than 20 ppm (v/v) for 17 months (Jurelevicius et al., 2021).

Sessile cells in biofilms are far more resistant to biocide treatment than free-floating planktonic cells in the bulk fluid (Costerton et al., 1995). When a biocide kills previous dwellers, resistant microbes readily move in from the surrounding environment to take over the niche. A biocide is not recommended for use in the same system for a very long time, because it may lead to problems like escalation of biocide dosage, increased cost, and adverse environmental impact (Zuo, 2007). Thus, it is beneficial to enhance the efficacy of current biocides using biocide enhancers rather than waiting for a blockbuster new green biocide to come to the market, which is very uncertain.

THPS is defined by the US Environmental Protection Agency (EPA) as a green chemical in 1997 (Li et al., 2016). THPS disrupts disulfide bonds in bacterial proteins and enzymes, while glutaraldehyde, a popular readily biodegradable biocide, is a crosslinking agent that reacts with peptides and proteins in the cell wall. Sessile cells in biofilms are far more challenging to kill than planktonic cells. Thus, high doses of biocides are required in the field to eliminate sessile cells because of the protectiveness of biofilms. The THPS concentration required to mitigate sessile cells can be 10 or more times greater than that for planktonic cells (Videla, 2018). In addition, the resistance of bacteria to THPS is increasing owing to natural selection. Therefore, a high dosage of THPS is required to maintain a biocidal effect, because after interacting with bacteria, THPS is converted to trishydroxymethyl phosphine oxide (Ballantyne & Jordan, 2003),

which is not active as a biocide. This means biocide killing can be a stoichiometric reaction problem with biocide attribution. High doses of biocides in large-scale applications have raised environmental concerns and increased costs.

2.12 Finite Element Method Simulation for U-Bend Stress Distribution

Finite Element Method (FEM) is a powerful numerical method to solve complicated partial different equations. It is a computational technique applied to get numerical solutions to boundary value problems in engineering (Ashcroft & Mubashar, 2011). ABAQUS is a commercial software package using FEM for various simulations. ABAQUS has three core products: ABAQUS/Standard, ABAQUS/Explicit, and ABAQUS/CAE. ABAQUS/Explicit can be used in U-bend simulation.

In Chapter 4, FEM simulation of the U-bend coupon was performed to find the most critical region (i.e., the location most likely to fail first due to highest stress). This region was the focus of the studies on the MIC SCC. A finite element model was used to estimate stress levels and distributions in U-bend coupons. Figure 2-30 shows a 3D representation of the final geometry of a bent specimen overlaid with von Mises stress. The highest stress occurs at the outer bottom, whereas the flat regions at the two ends (legs) have the lowest stress.

The modeling of the U-bend specimen was performed using the FEM software package. First, the uncracked U-bend was modeled with FEM to locate the most vulnerable region for cracking (the most stressed region).

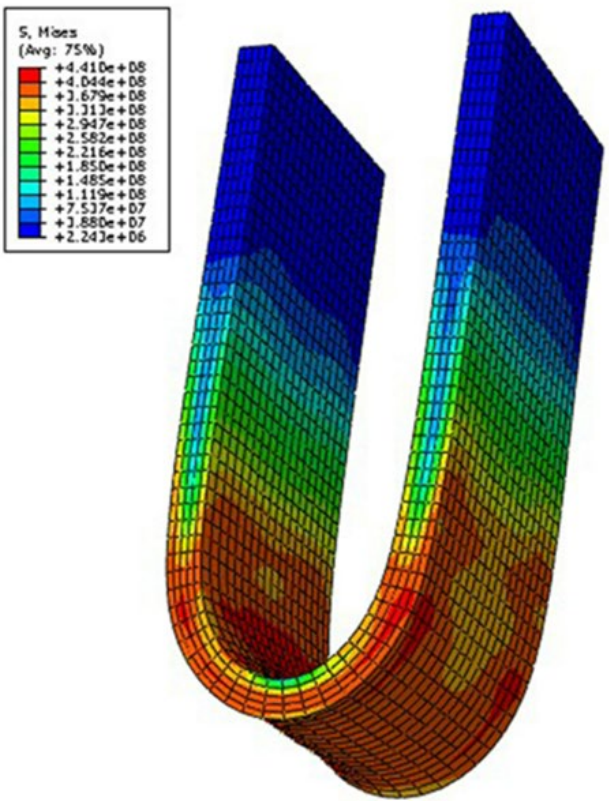

Figure 2-30. von Mises stress in pascals overlaid on the final deformed shape of a U-bend specimen from FEM simulation (Brandal & Lawrence Yao, 2017). (Permission is not needed.)

The equations that used for FEM simulation was a three-dimensional force system with the necessary equations shown below (Megson, 2016),

The direct stress, σ, defined as

$$\sigma = \lim_{\partial A \to 0} \frac{\partial F_D}{\partial A} \tag{2-42}$$

where F is applied stress, A is area that suffered stress. The direct stress acting on the x plane is σ_x, on the y plane σ_y, on the z plane σ_z.

The shear stress, τ, is defined as,

$$\tau = \lim_{\partial A \to 0} \frac{\partial F_s}{\partial A} \tag{2-43}$$

in which, subscript s indicates plane xy, plane xz, plane yz. τ acting on a plane is written as τ_{xy}, τ_{xz}, τ_{yz}.

The equations of force equilibrium in a 3D force system like that in Figure 2-31 are shown in below (Megson, 2016):

$$\frac{\partial \sigma_x}{\partial x} + \frac{\partial \tau_{xy}}{\partial y} + \frac{\partial \tau_{xz}}{\partial z} + X = 0 \tag{2-44a}$$

$$\frac{\partial \sigma_y}{\partial y} + \frac{\partial \tau_{yx}}{\partial x} + \frac{\partial \tau_{yz}}{\partial z} + Y = 0 \tag{2-44b}$$

$$\frac{\partial \sigma_z}{\partial z} + \frac{\partial \tau_{zx}}{\partial x} + \frac{\partial \tau_{zy}}{\partial y} + Z = 0 \tag{2-44c}$$

in which X, Y, Z are the components of body force per unit volume for the axes X, Y, and Z which spread across the volume of body.

The strain, ε, is defined as:

$$\varepsilon = \lim_{L \to 0} \frac{\Delta L}{L} \tag{2-45}$$

And $\varepsilon_x = \frac{\partial u}{\partial x}$, $\varepsilon_y = \frac{\partial v}{\partial y}$, $\varepsilon_z = \frac{\partial w}{\partial z}$, as shown in Figure 2-32.

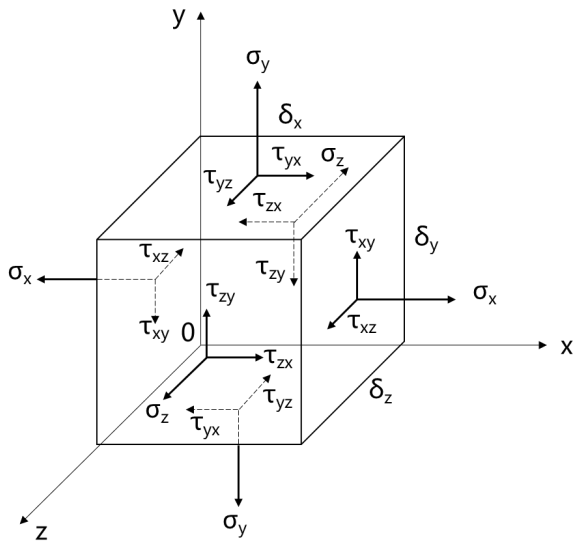

Figure 2-31. c in a 3D body (Megson, 2016). (Reproduced with permission from the publisher.)

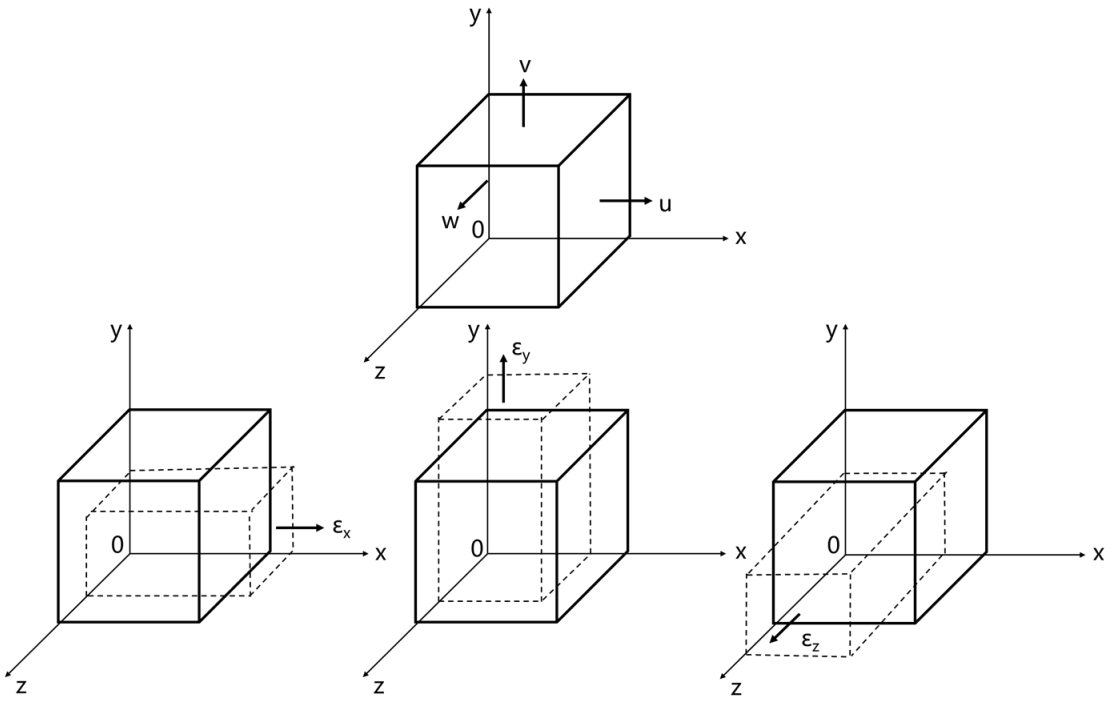

Figure 2-32. Sign guidelines and mathematical expression for strain in a 3D body (Megson, 2016). (Reproduced with permission from the publisher.)

The direct strains ε_x, ε_y, ε_z in a 3D body and the direct stress σ_x, σ_y, σ_z in a linearly elastic, isotropic body (steel is belong to this) are shown in below (Megson, 2016),

$$\varepsilon_x = \frac{1}{E}\left[\sigma_x - v\left(\sigma_y + \sigma_z\right)\right] \tag{2-46a}$$

$$\varepsilon_y = \frac{1}{E}\left[\sigma_y - v(\sigma_x + \sigma_z)\right] \tag{2-46b}$$

$$\varepsilon_z = \frac{1}{E}\left[\sigma_z - v\left(\sigma_x + \sigma_y\right)\right] \tag{2-46c}$$

$$\sigma_x = \frac{v}{(1+v)}\left(\varepsilon_x + \varepsilon_y + \varepsilon_z\right) + \frac{E}{(1+v)}\varepsilon_x \tag{2-47a}$$

$$\sigma_y = \frac{v}{(1+v)}\left(\varepsilon_x + \varepsilon_y + \varepsilon_z\right) + \frac{E}{(1+v)}\varepsilon_y \tag{2-47b}$$

$$\sigma_z = \frac{v}{(1+v)}\left(\varepsilon_x + \varepsilon_y + \varepsilon_z\right) + \frac{E}{(1+v)}\varepsilon_z \tag{2-47c}$$

where E denotes a constant known as the Young's modulus and v the Poisson's ratio of a steel.

X80 carbon steel possesses plasticity. This means it can be deformed. When the bending process occurs, generally using von Mises stress as a failure criterion to describe the stress value that suffered by the bending. The von Mises stress, σ_{vm} , can be defined as (Wang et al., 2021c),

$$\sigma_{vm} = \sqrt{\frac{1}{2}\left[\left(\sigma_x - \sigma_y\right)^2 + \left(\sigma_y - \sigma_x\right)^2 + (\sigma_z - \sigma_x)^2\right]} \tag{2-48}$$

in which the yield criterion is $\sigma_{vm} < \sigma_{yield\ stress}$.

The ABAQUS software requires a stress-strain curve in input data. All stress-strain curves in this dissertation are engineering stress-strain curves, which can be obtained from tensile test machines. The data can be transferred into the ABAQUS software.

Based on this, the transfer formulas between engineering stress-strain and true stress-strain should be list below (Choung & Cho, 2008),

$$\sigma_{true} = \sigma_{engineering} \times (1 + \varepsilon_{engineering}) \quad (2\text{-}49a)$$

$$\varepsilon_{true} = ln(1 + \varepsilon_{engineering}) \quad (2\text{-}49b)$$

Chapter 3: Objectives and Hypotheses

3.1 Research Objectives

The following objectives were achieved in this work to gain insights into biotic SCC mechanisms and microbial degradation of mechanical properties.

3.1.1 SCC Failure of X80 U-Bend Caused by D. vulgaris MIC

Pitting is the primary corrosion form of SRB MIC of carbon steel because the corrosion products iron sulfides are partially passivating and semi-conductive, which are the two pre-requisites for classical pitting (Xu et al., 2023b). In the presence of stress, pitting pits tend to develop into more harmful SCC crack tips (Biezma, 2001; Li et al., 2021b; Li et al., 2022b). Furthermore, H_2 is produced by *D. vulgaris* during the degradation of lactate. When the hydrogen atoms in the environment diffuse into steel, the ductility and strength of the material are significantly reduced, resulting in cracking and brittle fracture (Mukhopadhyay et al., 2001). Therefore, MIC caused by *D. vulgaris* can cause SCC failure of materials under stress. To accelerate SCC failure, X80 U-bend coupons were pre-cracked to examine SCC failure in the presence of *D. vulgaris.* X80 (flat) square coupons were also used as control to investigate the impact of SCC on MIC. This study would provide sights in the role of MIC in SCC.

3.1.2 SCC Crack Tip Dissolution by Fast D. ferrophilus MIC

It is known in abiotic SCC that fast corrosion does not necessarily lead to more severe SCC because fast corrosion can dissolve crack tips and convert them into less

harmful corrosion tips (Dinh et al., 2004). *D. ferrophilus* is a super corrosive SRB species, which is several times more corrosive than *D. vulgaris* (Wang et al., 2021a). This provided a unique opportunity to study the differences in SCC caused by relatively corrosive SRB vs. super corrosive SRB. This would provide useful insight into the relationship of MIC and SCC

3.1.3 Effect of Carbon Source Starvation on D. vulgaris MIC Degradation of Mechanical Properties

Starved sessile cells are more eager to harvest extracellular electrons for energy production in order to survive, which can result in more severe MIC provided that the sessile cell count is not decreased too much. Moreover, carbon starvation also affects the concentrations of dissolved H_2S and headspace H_2. The effect of carbon source starvation on the degradation of mechanical properties of steel is not yet known. Therefore, this study explored the effect of *D. vulgaris* MIC on the mechanical properties of X80 steel at different carbon source levels.

3.1.4 Effect of Headspace on D. vulgaris MIC Degradation of Mechanical Properties

In SRB MIC of carbon steel, a larger headspace allows more H_2S to escape from the broth. This reduces the H_2S cytotoxicity in the broth, leading to better planktonic and sessile SRB growth, resulting in a more severe MIC. Therefore, the headspace test provided another way to vary MIC severity in the study of how microbes degrade mechanical properties of a metal.

3.1.5 Effect of Incubation Time on Mechanical Degradation Caused by D. ferrophilus MIC

Longer incubation time will cause higher cumulative weight loss, but the corrosion rate will decrease if the biofilm is weakened due to nutrient exhaustion. This provided yet another way to vary MIC severity for the investigation of MIC severity on microbial degradation of mechanical properties in this work.

3.1.6 Mitigating D. ferrophilus MIC Degradation of Mechanical Properties Using THPS Biocide

MIC causes the degradation of mechanical properties of steels, such as deteriorations in tensile strength and strain. Because biofilms cause MIC and locally high concentrations of harmful metabolites. Thus, to mitigate MIC degradation of mechanical properties, THPS biocide was chosen to demonstrate that it could mitigate *D. ferrophilus* degradation of mechanical properties.

3.2 Hypotheses and Experimental Plans to Prove Them

(1) SCC Failure Can Be Caused by SRB MIC

X80 U-bend coupons were pre-cracked at the outer bottom of the U-shape using abiotic acid corrosion and then exposed to *D. vulgaris* broth to show that an X80 U-bend could fail completely, while the abiotic control suffered no crack deterioration.

(2) Relatively Slow MIC Causes SCC of X80 Steel While Fast MIC Does not Because of Crack Tip Dissolution

To prove this hypothesis, *D. vulgaris* and *D. ferrophilus* were employed, the latter being several times more corrosive. The experiment was designed to show that *D. vulgaris* would cause MIC pits and more harmful SCC, while *D. ferrophilus* would only cause MIC pits in X80 U-bends.

(3) More Severe MIC Causes More Severe Microbial Degradation of Mechanical Properties

To prove this hypothesis intensively, three different ways to vary *D. ferrophilus* MIC severity were employed. The first was to use carbon source starvation which increased corrosivity of each sessile cell but with some loss of sessile cells due to starvation. The second way was headspace variation. A larger headspace allowed more H_2S to escape from the SRB broth which promoted sessile cell grow and thus increased MIC severity. The third way was to increase incubation time, which increased cumulative weight loss, but the corrosivity decreased over time due to nutrient exhaustion. All these three ways produced MIC outcomes, allowing various parameters to be investigated. The degradation of mechanical properties was assessed through tensile testing X80 dogbones after exposure to SRB.

(4) Biocide Can Mitigate MIC and Alleviate Microbial Degradation of Mechanical Properties

MIC and harmful metabolites degrade mechanical properties, while MIC itself is caused by microbial biofilms. Thus, the key to mitigate the degradation is to treat biofilms which is usually done using a biocide. To prove the hypothesis, THPS biocide was used to assess its impact on *D. ferrophilus* biofilm on X80 dogbones and *D. ferrophilus* MIC. Finally, the dogbones were tested using a tensile machine to assess ultimate strength and ultimate strain losses with and without THPS in the culture medium.

Chapter 4: Stress Corrosion Cracking failure of X80 Carbon Steel U-Bend Caused by *D. vulgaris* Biocorrosion

4.1. Introduction

MIC is caused by microbial metabolic activities or metabolites. Because biofilm offer high concentrations of chemicals underneath it and the ability to transfer electrons (Xu et al., 2023a), biofilms are often responsible for MIC (Cheng et al., 2021; Lu et al., 2023a; Zhang et al., 2022b). In the past two decades, many cases of pipeline failure and leakage caused by MIC which resulted in economic losses and environmental pollution were reported (Jacobson, 2007; Li et al., 2018d). MIC is an electrochemical process, and the main form of corrosion on steels is pitting (Li et al., 2020; Li et al., 2021d; Tang et al., 2021; Zhou et al., 2022b), because some MIC products such as iron sulfides are partially passive and semi-conductive, which leads to large cathode-small anode situation (Xu et al., 2023b). However, the occurrence of pitting corrosion damages a steel's mechanical properties, leading to crack initiation, which can eventually result in the material's failure and catastrophic consequences (Biezma, 2001; Li et al., 2021b; Li et al., 2022b). Thus, this should also be a focus in MIC investigations.

SCC is defined as the cracking caused by the interaction between tensile stress and a corrosive environment (Zeitvogel et al., 2014). SCC can lead to premature failures of metal materials. Weakened pipeline integrity including pipe rupture can occur (Syah Putri et al., 2022). The general consensus on the SCC mechanism is that there are

mainly three factors: mechanical stress, corrosion environment and metal properties (Asahi et al., 1999; Liu et al., 2012; Tang & Cheng, 2009). SCC usually occurs when a metal is subjected to mechanical stress in a corrosive environment (Nyrkova, 2020). The SCC process consists of three stages: crack germination, crack aggregation and crack rapid development to failure (Syah Putri et al., 2022). Crack germination is an important stage in the SCC process. The formation of corrosion pits is generally considered to be the main factor leading to the crack germination under applied stress (Rokkam et al., 2019).

Several studies showed that microbial metabolic activities promoted SCC. A synergistic effect of elastic stress and MIC on SCC failures of steels was observed in a lab investigation (Wu et al., 2014). MIC pits was found to cause the failure of stainless steel due to SCC under the action of vibration stress (El Hosary & Saleh, 1993). A X52 pipeline in northern Iran failed in 2004 due to a combination of SRB MIC and stress (Abedi et al., 2007).

SRB are widely present in oil pipeline systems because deaerated water which contains sulfate is often used for reservoir flooding to increase well pressure. SRB are the most widely studied bacteria in MIC due to their prevalence and corrosivity (Gu et al., 2019; Jia et al., 2019a; Su et al., 2022). SRB MIC can significantly reduce the strength and plasticity of X80 pipeline steel (Li et al., 2021b; Li et al., 2022b). In addition, In addition, H_2 can be produced by SRB during the degradation organic carbon

(Smith et al., 2019) and corrosion. When the hydrogen atoms in the environment diffuse into a steel matrix, the ductility and strength of the steel significantly are reduced, resulting in cracking and brittle fracture. This is an important factor inducing SCC (Mukhopadhyay et al., 2001). Therefore, MIC caused by SRB is hypothesized to lead to SCC failure of metals under stress, but the mechanism for it is still largely unknown.

U-bend coupons have been commonly employed to evaluate the SCC resistance of different metals in various corrosive environments (Syah Putri et al., 2022). In this work, modeling using FEM implemented in the commercial ABAQUS 2022 software package was used to find the distribution of tensile stress in X80 U-bend coupons. In this work this was used to determine the most susceptible region on the coupons for SCC. Corrosion surface analysis and electrochemical corrosion measurements were used to characterize the differences between the corrosion behaviors of X80 U-bend coupons (with stress) and (flat) X80 square coupons (without stress). Furthermore, U-bend coupons were pre-cracked slightly to simulate the initiation of a structural failure. The SCC sensitivity of X80 U-bends under the combined effects of tensile stress and SRB MIC was investigated to prove the aforementioned hypothesis about SRB MIC impact on SCC.

4.2. Materials and Methods

4.2.1 Materials Preparation

Table A-1 lists the elemental composition of X80 pipeline steel. The square coupon size was 1 cm × 1 cm × 0.3 cm. All surfaces were sealed with Epoxy except one work surface (1 cm^2 on top). The U-bend coupon dimensions are described in Figure 4-1(a, b) (ASTM G30, 2000). The U-bend coupons were also painted with Epoxy, leaving only one 1 cm^2 outer bottom surface for the electrochemical tests (Figure 4-1(c)). The completely unpainted U-bend coupons with a total of 1 cm^2 surface area were used in immersion tests to find weight loss, sessile cell count and SCC observation by SEM coupons were sequentially polished with 180, 400, and 600 grit sandpapers. Before exposure to the SRB culture medium, the coupons were cleaned with pure isopropanol and dried under ultraviolet light for 20 min.

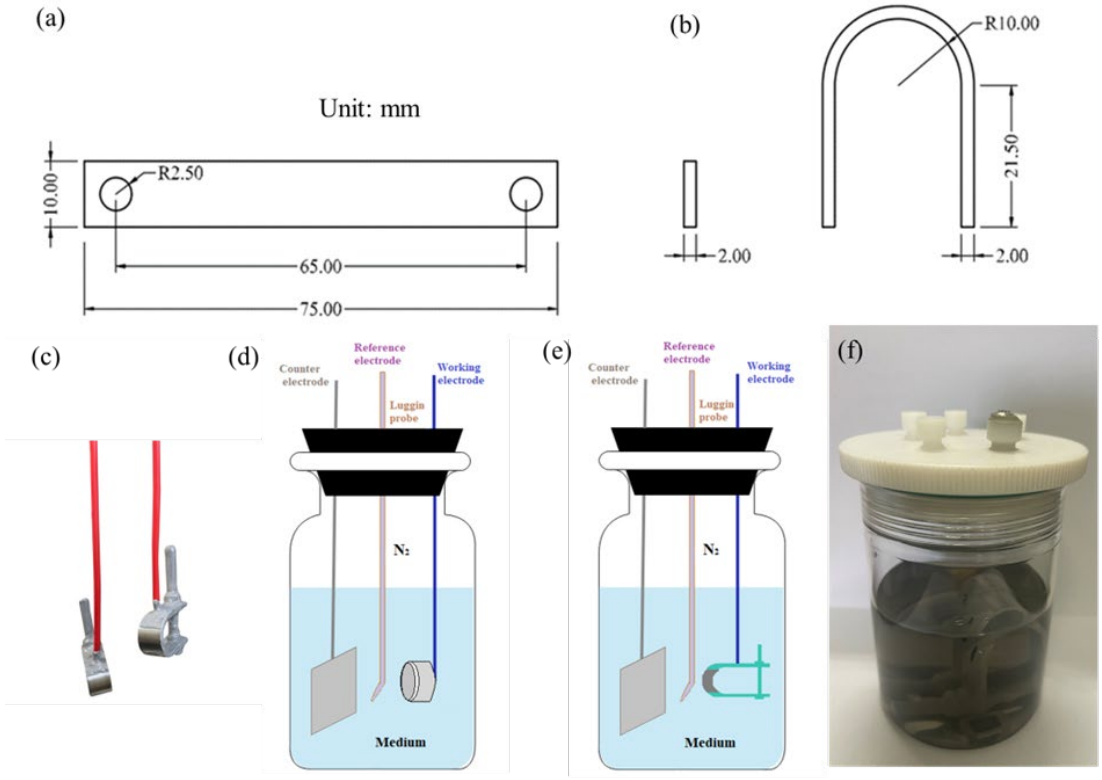

Figure 4-1. Schematic diagram of coupons and devices: (a) dimensions of unpainted X80 U-bend coupon before bending (mm), (b) dimensions of X80 U-bend coupon after bending (mm), (c) X80 U-bend coupon after Epoxy painting, (d) electrolytic tank containing coupons X80 square coupon) and culture medium with *D. vulgaris*, (e) electrolytic tank containing X80 U-bend coupon and culture medium with *D. vulgaris*, and (f) anaerobic bottle containing X80 U-bend and X80 square coupons upon inoculation.

4.2.2 Microbe and Culture Medium Preparation

D. vulgaris (ATCC 7757) was used in this research with 450 mL anaerobic bottles containing 200 mL culture medium. The culture medium was ATCC 1249 medium with

(g L^{-1}): yeast extract 1.0, tri-sodium citrate 5.0, sodium lactate 3.5, $CaSO_4 \cdot 2H_2O$ 1.0, NH_4Cl 1.0, $MgSO_4$ 2.0, $Fe(NH_4)_2(SO_4)_2$ 1.0, and K_2HPO_4 0.5 (Jia et al., 2018a). The initial pH in the medium was adjusted to 7.0 ± 0.1 using 1 M NaOH and 1 M HCl solutions. After the medium was autoclaved at 121°C for 20 min, filter-sterilized N_2 was used to deoxygenate for more than 45 min. Then, 100 ppm (w/w) L-cysteine was added to further remove the dissolved oxygen in the medium (Dou et al., 2019). Finally, each anaerobic bottle containing 300 mL of medium was inoculated with 3 mL of 3-d-old *D. vulgaris* seed culture before incubation at 37°C for 14 d.

4.2.3 FEM

To characterize the stress distributions of the X80 U-bend coupon, FEM modeling was carried out using the commercial ABAQUS 2022 software. First, the software needed to know the basic mechanical properties of X80 carbon steel. A stress-strain curve was fed to ABAQUS 2022, to provide the material properties of fresh X80 steel. The density of X80 steel (7.86 g cm^{-3}) was also required by ABAQUS 2022 (Li et al., 2021a). The input data for X80 material properties (ASTM E8, 2013; Choung & Cho, 2008; Liu et al., 2019b) are shown in Supplemental Materials.

4.2.4 X80 U-Bend SCC Analyses

Two X80 U-bend coupons (stressed by bending and bolt fixing) without artificial pre-cracking were immersed in an anaerobic bottle with freshly inoculated SRB broth (200 mL broth and 250 mL headspace) for 14 d. Another two fresh X80 U-bend coupons

were pre-cracked with microscopic cracks. This was achieved by immersing them in a bottle containing a simulated soil solution called NS4 ($NaHCO_3$ 0.483 g/L, $CaCl_2 \cdot 2H_2O$ 0.181 g/L, $MgSO_4 \cdot 7H_2O$, 0.131 g/L, KCl 0.122 g/L) (López-Celvera et al., 2018) with a pH of 3 for 14 d. The NS4 solution pH was around 8 (López-Celvera et al., 2018); however, in this work, the pH of the NS4 solution was adjusted with hydrochloric acid to reach a pH of 3 to accelerate cracking as was done by other researchers in the literature (Liu et al., 2017). The soil solution was used because SCC can occur in external pipeline corrosion in the field.

After 14 d of NS4 immersion to pre-crack the X80 U-bend coupons, the coupons were retrieved and cleaned with a freshly prepared Clarke's solution (ASTM G1-03, 2003). And then, the pre-cracked X80 U-bend coupons were washed with 100% isopropanol and dried before being placed into two separate 450 mL anaerobic bottles that contained 200 mL culture medium, one inoculated with SRB and one not (control). Several (flat) X80 square coupons (without stress) were immersed in the same 450 mL anaerobic bottles with 200 mL medium with and without *D. vulgaris* for comparison.

A field emission scanning electron microscope (FESEM) (Carl Zeiss Ultra plus, Carl Zeiss, Oberkochen, Germany) was used to examine the biofilm morphology on the surface of the square coupons and microcracks on X80 U-bend coupons. Before the FESEM examination, the flat coupons were gently rinsed with a phosphate-buffered saline (PBS) solution (pH 7) for 15 s, then immersed in a 2.5% (w/w) glutaraldehyde

biocide at 10 °C for 8 h to kill and fix the biofilms on the coupons. Afterwards, the coupons were dehydrated with 50%, 70%, 80%, 90%, 95%, and 100% ethanol (v/v) sequentially for 10 min at each of the 6 concentrations. Finally, the coupon surfaces were sputter-coated with Au.

To observe the microcracks, a U-bend coupon's bottom section was cut and molded into an Epoxy cake with the 2 mm side surface exposed (Fig. S4). The metal surface was polished on a 600-grit abrasive paper to remove a very thin outer layer, and then further polished on 800 and 2000 grit sandpapers sequentially. Finally, the surface was abraded using 2.5 μm and 0.25 μm diamond polishing pastes, sequentially to reveal the microcracks better (Zhang et al., 2022a).

4.2.5 Sessile Cell Count, Weight Loss, XRD and Headspace Gas Measurement

For sessile cell counting, X80 U-bend coupons and X80 square coupons were taken out from anaerobic bottles after 14-d incubation. The sessile cells on the coupons were scraped into 10 mL PBS using a tiny brush. Then, the coupon, the brush and the PBS solution were vortexed in a 50 mL test tube for 30 s. Under an optical microscope, each cell suspension was enumerated using a hemocytometer at 400 × magnification.

At the end of the 14-d incubation, X80 U-bend coupons and X80 square coupons were cleaned with a fresh Clarke's solution to remove the biofilms and corrosion products before weighing. For the square coupons, each weight loss data point came from the average of three replicate coupons in the same anaerobic bottle. The corrosion

products on the X80 square and U-bend coupon surfaces were identified using an X-ray diffractometer (XRD; Bruker D8 Discovery model, Bruker AXS GmbH, Karlsruhe, Germany).

A portable H_2S sensor (GAXT-H-DL, BW Technologies, Calgary, Alberta, Canada) and a digital manometer (Xplorer GLX-PS-2002, PASCO Scientific, Roseville, CA, USA) were used to measure the concentration of H_2S and total pressure in each anaerobic bottle's headspace.

4.2.6 Electrochemical Corrosion Measurements

Electrochemical measurements were performed using a classical three-electrode system in a 450 mL anaerobic glass cell filled with 200 mL culture medium. A potentiostat (Model VersaSTAT 3, Princeton Applied Research, Oak Ridge, TN, USA) was used to perform OCP, LPR, EIS, and PDP analyses. The X80 coupons (either U-bend or square) were used as the working electrodes (1 cm^2 surface). A saturated calomel electrode (SCE) and a thin platinum plate (10 mm × 10 mm × 1 mm) were used as the reference electrode and the counter electrode, respectively (Figure 4-1(d, e)). LPR was scanned at a rate of 0.1667 mV s^{-1} in the range of −10 mV to +10 mV vs. OCP each day. EIS was performed at OCP by applying a sinusoidal signal of 10 mV (amplitude) at a frequency ranging from 10^5 to 10^{-2} Hz each day. Potentiodynamic polarization curves were scanned from OCP to −200 mV vs. OCP and from OCP to +200 mV vs. OCP at a rate of 0.1667 mV s^{-1} once at the end of the 14-d incubation.

The corrosion potential (E_{corr}), corrosion current density (i_{corr}), and anodic and (absolute) cathodic Tafel slopes (β_a and β_c) were determined from a Tafel analysis of the polarization curves.

4.3 Results and Discussion

4.3.1 X80 U-Bend SCC Analyses

(1) Stress distribution on X80 U-bend

Figure 4-2 from FEM modeling shows the 3-D representation of the stress distribution on the two legs of an X80 U-bend coupon. The highest stress occurred at the outer bottom section at the 2 mm-wide side edge of the U-bend coupon with a value of 731 MPa. Thus, SCC will preferentially occur at this spot. Additional modeling details are shown in Supplemental Materials.

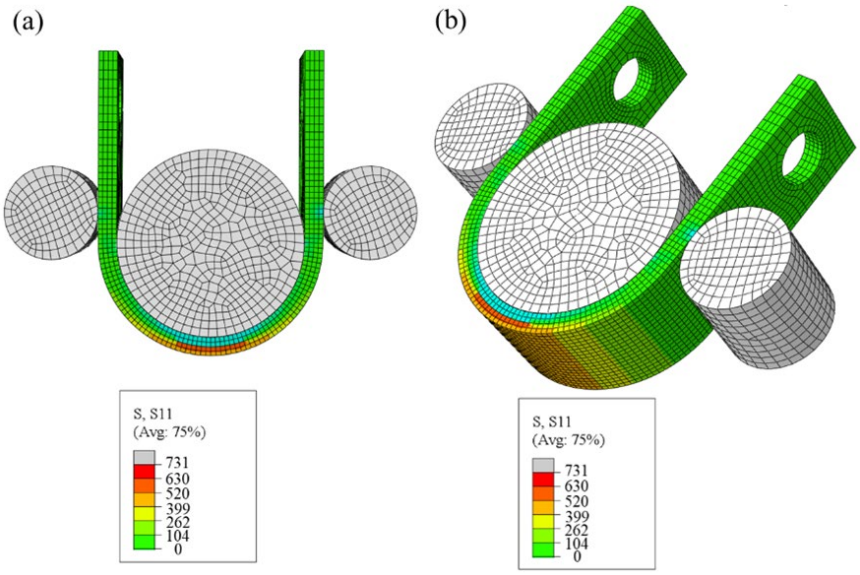

Figure 4-2. FEM simulation results of stress distribution on X80 U-bend.

(2) Biofilm and SCC observations

Figure 4-3(a, b) shows FESEM images of the biofilms and microbial corrosion products on the X80 square coupon and U-bend coupon surfaces after the 14-d incubation with *D. vulgaris*. No significant differences in the biofilms on the two types of coupons are visible. After removing the film containing biofilm biomass and microbial corrosion products, several shallow corrosion pits were found on the cross-section of the biotic square coupon, while sharp cracks and corrosion pits were both present on the biotic U-bend coupon (Figure 4-3(c, d)). No pits or cracks were on the cross-section of the abiotic square and U-bend coupons (Figure 4-3(e, f)). These FESEM images clearly indicate that the *D. vulgaris* MIC on square coupons primarily caused pitting corrosion. In comparison, it caused both SCC microcracks and pitting corrosion, but pits were much smaller than those on the square coupons. The microcracks could be explained by arguing that corrosion pits caused by MIC developed into cracks under the action of tensile stress. Pitting corrosion is an important factor in crack germination, which is the early stage of SCC (Rokkam et al., 2019). Thus, the data here indicate that the *D. vulgaris* MIC increased the SCC sensitivity of X80 in the presence of stress.

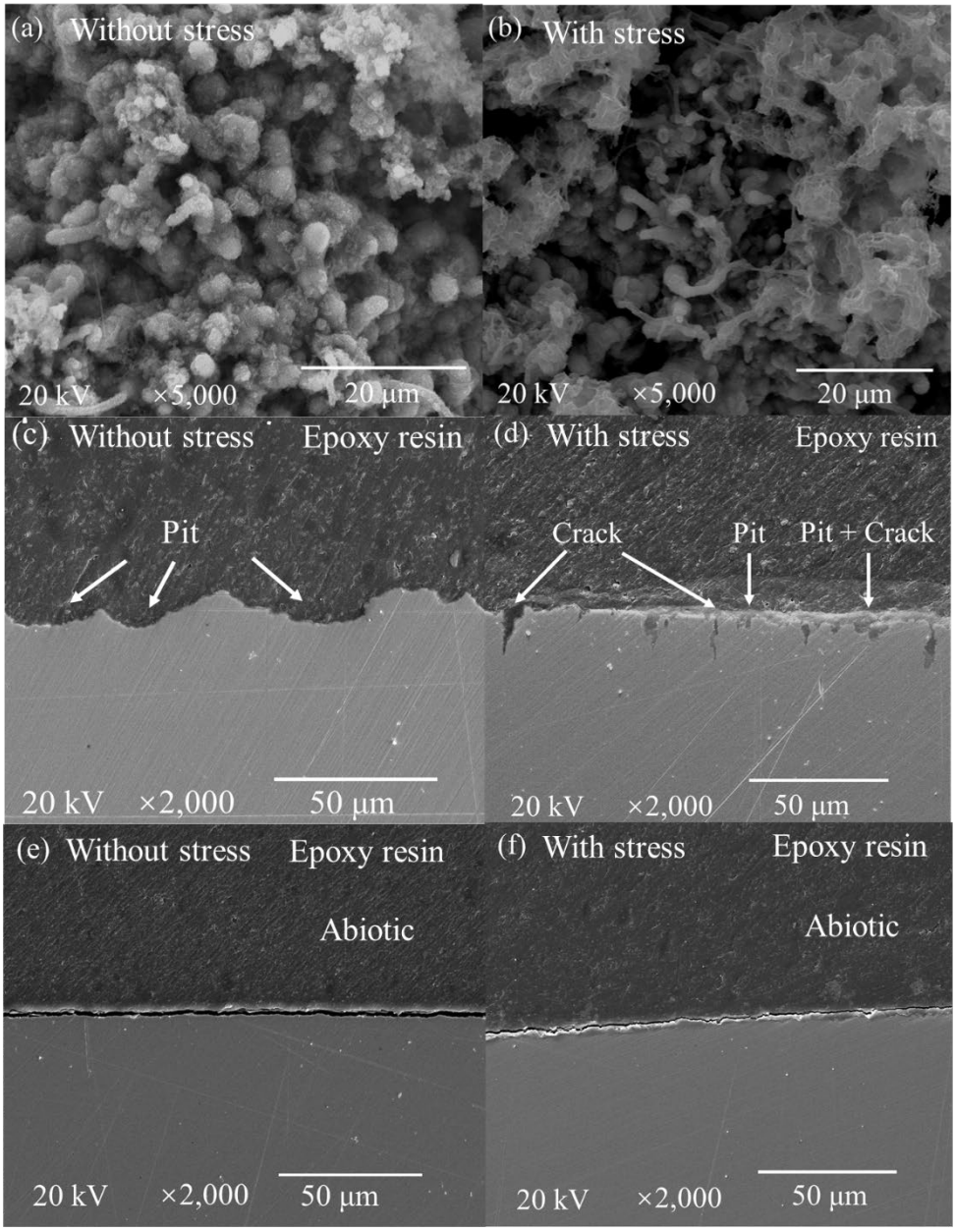

Figure 4-3. SEM images of (a) biofilms and corrosion products on X80 square and (b) U-bend coupon surfaces after a 14-d incubation in an anaerobic culture medium with *D. vulgaris*. Cross-sectional SEM images of (c) square and (d) U-bend coupons in the medium with *D. vulgaris* and (e) square and (f) U-bend coupons in the medium without *D. vulgaris* after removing biofilm and corrosion products at end of 14-d incubation.

Figure 4-4 shows the FESEM images of the cross sections of U-bend coupons without pre-cracking after a 12-week immersion in abiotic and biotic ATCC 1249 culture medium. Compared with the abiotic control, many adjacent microcracks were present on the biotic X80 U-bend coupon. This indicates that the presence of *D. vulgaris* accelerated the formation of cracks during the 12-week SRB incubation (no culture medium change).

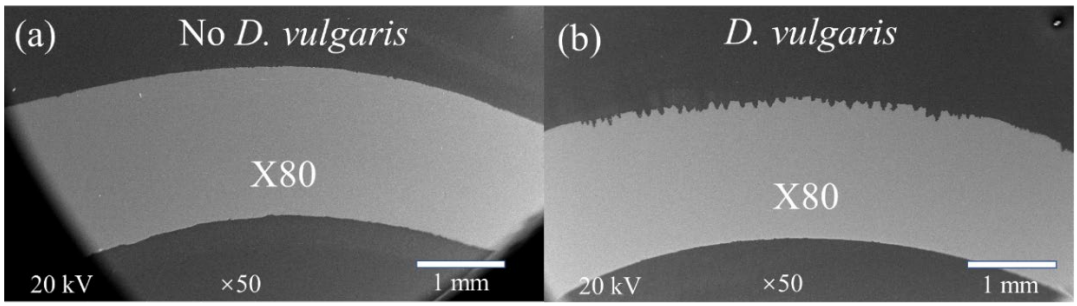

Figure 4-4. Cross-sectional SEM images of X80 U-bend coupons after a 12-week incubation in an anaerobic medium (a) without and (b) with *D. vulgaris*.

To study a case in which SRB MIC actually led to SCC failure, X80 U-bend coupons were pre-cracked with a deep crack before incubation (Figure 4-5). The crack morphology of the pre-crack on the X80 U-bend coupon after 6-week immersion in the abiotic culture medium was similar to that of a replicate unsoaked coupon (Figure 4-5(a, b)), indicating that the abiotic incubation did not promote crack growth. In comparison, the 6-week SRB incubation caused the failure of the pre-cracked X80 U-

bend which was broken at the pre-crack position after the pre-crack was expanded due to MIC (Figure 4-5(c)). It can be clearly seen in Figure 4-5(d) that *D. vulgaris* sessile cells lined the inner crack surfaces.

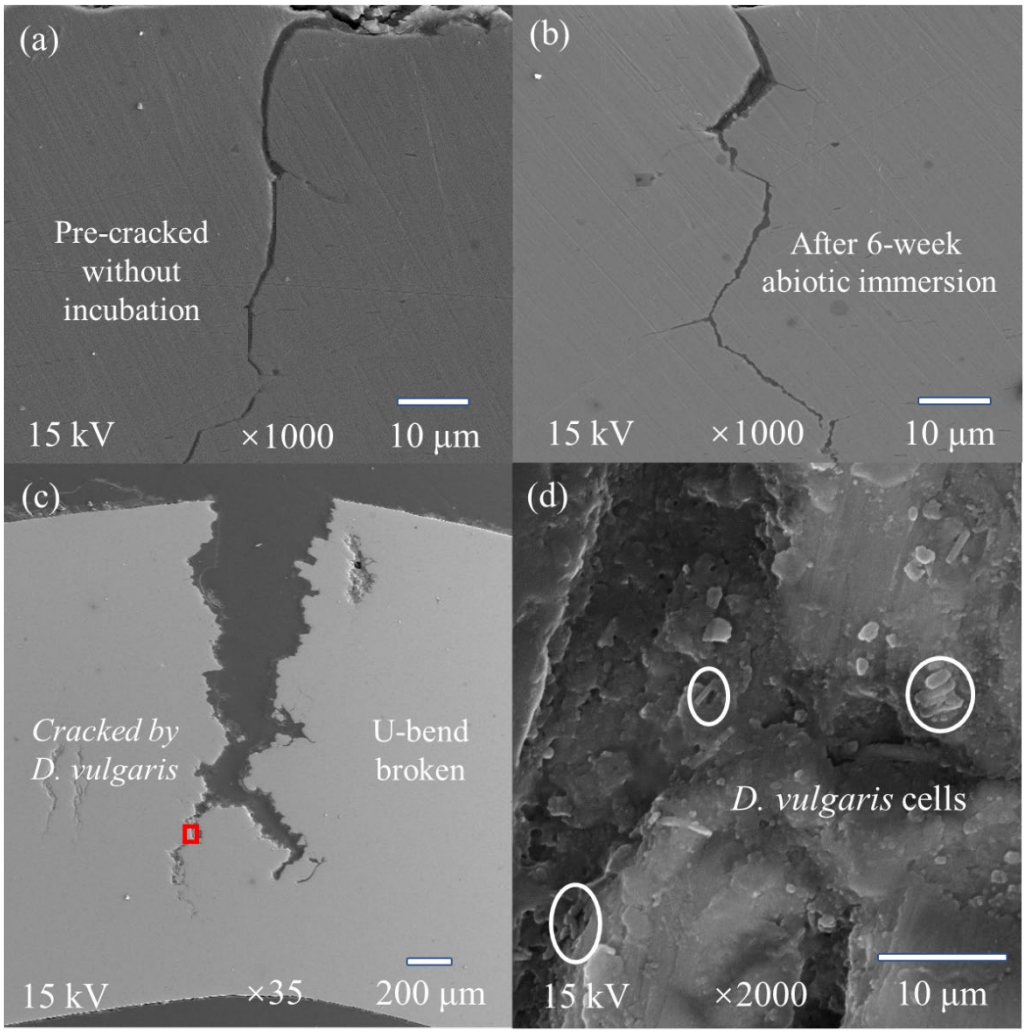

Figure 4-5. (a) SEM images of the cross-section of a pre-cracked X80 U-bend coupon without incubation. SEM images of the cross-section of pre-cracked coupon in an anaerobic medium (b) without and (c) with *D. vulgaris* after a 6-week incubation in ATCC 1249 medium. (d) SEM enlarged image of the red box area in (c).

The *D. vulgaris* MIC increased the SCC sensitivity of X80 U-bend coupons primarily for two reasons. *D. vulgaris* accelerated the X80 steel corrosion as evidenced by the corrosion pits generated by MIC in Figure 4-3(c, d). SRB MIC reduced ultimate tensile strength as well as ultimate tensile strain of X80 carbon steel as demonstrated previously (Li et al., 2021b). Because SRB MIC of X80 manifested itself as primarily pitting corrosion, it germinated cracks under tensile stress (Figure 4-3). Another contributing factor was also possible. The metabolic activity of *D. vulgaris* produced H_2 and HS^- as shown in Reactions (4-1) for lactate oxidation to acetate, and (4-2) for sulfate reduction (Dou et al., 2019; Smith et al., 2019). HS^- and Fe^{2+} combine to form FeS and H^+ (Reaction 4-3). H^+ can be reduced to form H atom that is adsorbed on the metal M (in this work Fe) and eventually become dissolved H atom in the metallic lattice as denoted by H_M in Reaction (4-4) (Biezma, 2001).

$$CH_3CHOHCOO^- + H_2O \rightarrow CH_3COO^- \text{(acetate)} + 2H_2 + CO_2 \quad (4\text{-}1)$$

$$SO_4^{2-} + 9H^+ + 8e^- \rightarrow HS^- + 4H_2O \quad (4\text{-}2)$$

$$Fe^{2+} + HS^- \rightarrow FeS + H^+ \quad (4\text{-}3)$$

$$M + H^+ + e^- \rightarrow M - H_{ads} \rightarrow M - H_M \quad (4\text{-}4)$$

The diffusion of hydrogen atoms into metal materials causes stress concentration on the bottom of the pit and crack tip, which reduces the plasticity of a metal and leads to failure (Raman, 2003). A schematic diagram of hydrogen atom penetration and stress corrosion cracking is shown in Figure 4-6. Because of its small size, hydrogen atoms

can easily penetrate the metal lattice during the diffusion process. As the coupon is exposed to a continuous stress in the X80 U-bend, the stress distribution in the metal is unequal (Figure 4-2), and stress concentration occurs at internal defects and microcracks of the metal (Li et al., 2018a). The stress gradient causes the H atoms to flow into the lattice or follow dislocation migration to the stress concentration zone. The interaction of hydrogen atoms with metal atoms decreases the binding force of metal atoms, causing cracks and crack expansion in the hydrogen-enriched area, resulting in brittle fracture. Furthermore, the diffused hydrogen atoms will concentrate in grain boundaries, phase boundaries, dislocations, and other structures, becoming trapped hydrogen atoms. When the quantity of trapped hydrogen atoms grows, the hydrogen atoms link together to create hydrogen molecules, creating high pressure at the traps (Huang et al., 2010). When the hydrogen molecule pressure equals the bonding force of metal atoms, the atomic bonds for certain locations break up and produce microcracks. With the growth of diffused hydrogen atoms with time, the fracture pressure will increase, resulting in a new cycle of crack propagation and generating more cracks (Ohaeri et al., 2018).

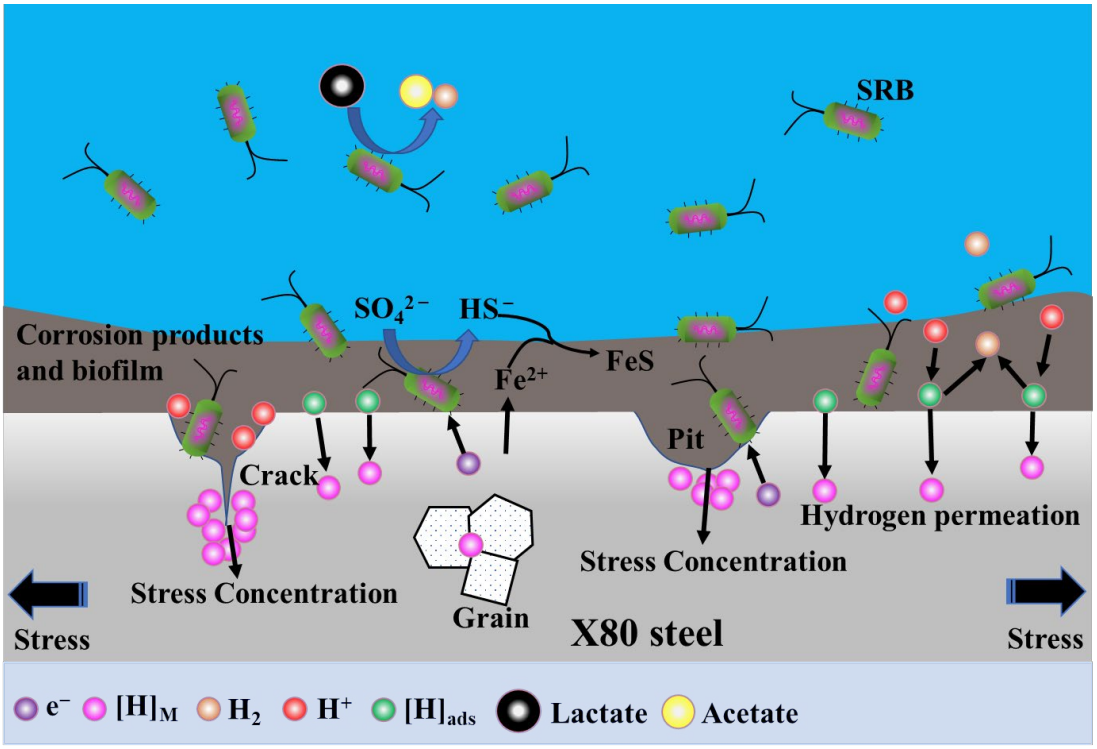

Figure 4-6. Schematic diagram of hydrogen penetration and stress corrosion cracking.

4.3.2 Weight Loss, Sessile Cell Count, and Headspace Gas Analyses

Figure 4-7(a) shows the sessile cell counts on the X80 U-bend and square coupons after the 14-d SRB incubation. The sessile cell counts on the X80 U-bend and square coupons were 2.4×10^8 cells cm^{-2} and 4.2×10^8 cells cm^{-2}, respectively. The sessile cell count for the X80 U-bend was 57% of that for the X80 square coupons. The reason why the stress on X80 U-bend caused a lower sessile cell count needs to be further investigated. The orientation and depth of the X80 U-bend coupon in the anaerobic bottle could be the factors too. Replicate X80 U-bend coupons should be used in the future.

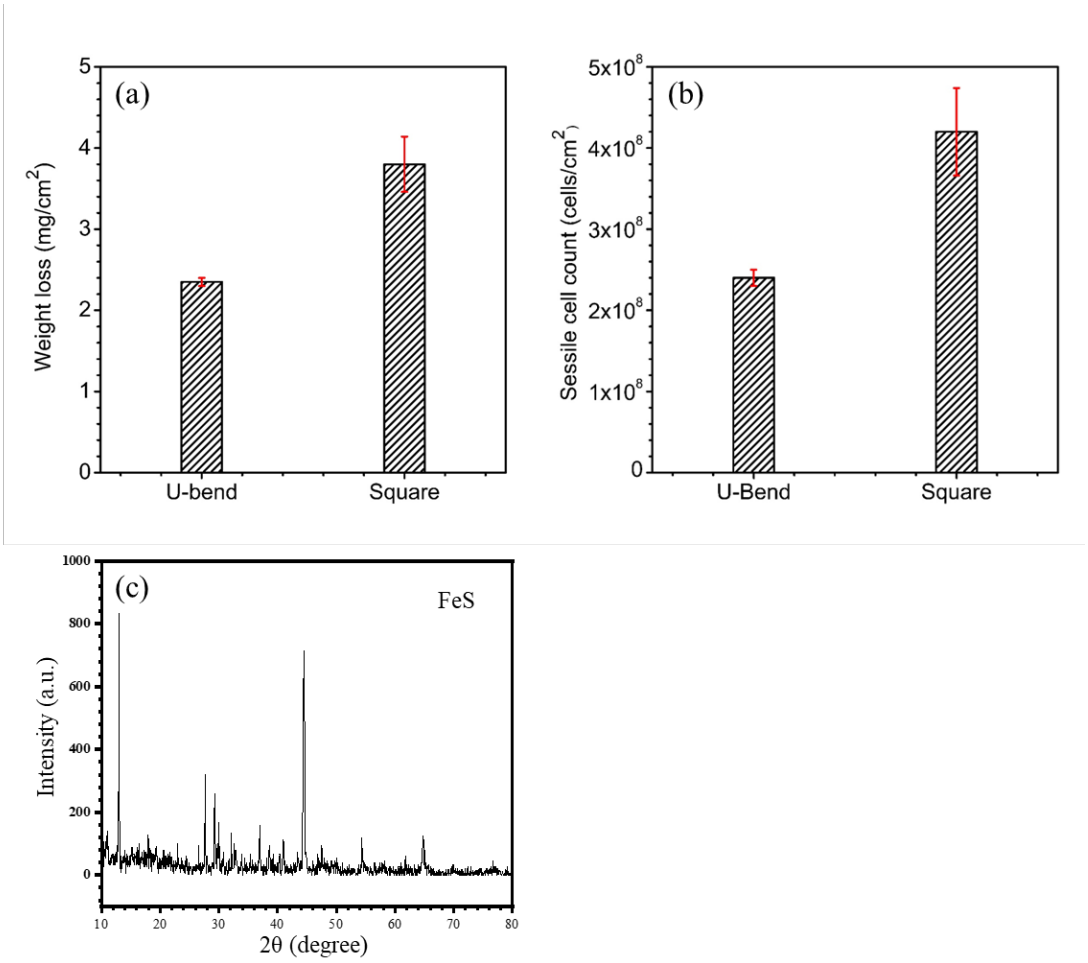

Figure 4-7. (a) Sessile cell counts, (b)weight losses, and (c) XRD spectrum of X80 square coupon after a 14-d incubation in an anaerobic culture medium with *D. vulgaris.* (The X80 U-bend coupon had similar patterns.)

The weight losses of X80 U-bend and square coupons after the 14-d incubation are shown in Figure 4-7(b). After the 14-d incubation, the weight losses of U-bend and square coupons were 2.35 mg cm^{-2} and 3.83 mg cm^{-2}, respectively. The weight loss-based uniform corrosion rate of the X80 U-bend coupon (stressed due to bending) was approximately 61% of that of the square coupon (no stress) after the 14-d incubation,

indicating that the stress affected the MIC rate. This could be explained by the 57% lower sessile cell count on the X80 U-bend coupon.

The XRD results in Figure 4-7(c) indicate that the X80 steel corrosion products were primarily FeS. The X80 square and U-bend coupons had similar XRD patterns, suggesting that the stress on the U-bend did not affect the nature of the SRB MIC.

Table 4-1 lists the headspace gas concentrations, total pressure, and broth pH after the 14-d incubation. The total pressure, H_2 amount, and H_2S amount in the headspace were 1.42 bar, 2.5×10^3 ppm, and 6.2×10^3 ppm, respectively. H_2 was produced by SRB during pyruvate (a product of lactate oxidation) oxidation to acetate, whereas H_2S was produced by HS^- combination with H^+ (Dou et al., 2019; Smith et al., 2019). *D. vulgaris* first oxidizes lactate to produce pyruvate, followed by the oxidation of pyruvate to acetate with concomitant production of H_2 and ATP (adenosine 5'-triphosphate), which are energy molecules for microbes. H_2 acts as an electron donor for the reduction of sulfate (Peck, 1993). Some H_2 escapes to the headspace of an SRB culture. Thus, H_2 can come from SRB metabolism in addition to H^+ reduction in Fe corrosion. It was argued that $2H^+/H_2$ electron shuttling is the primarily means for SRB utilization of the electrons released by Fe^0 in the SRB MIC (Xu et al., 2023a).

Note that the U-bend and square coupons were incubated in the same anaerobic bottle. Therefore, the 60% weight loss difference in corrosion rates of X80 U-bend and square coupons was unlikely because of the variations in culture conditions.

Table 4-1. H_2 and H_2S concentrations, total pressure, and broth pH after 14-d incubation in ATCC 1249 culture medium with *D. vulgaris*.

Total pressure in headspace (bar)	H_2 headspace (ppm) (v/v)	H_2S in headspace (ppm) (v/v)	Dissolved [H_2S] in broth (M)	Final broth pH
1.42	2.5×10^3	6.2×10^3	7.9×10^{-4}	7.2

4.3.3 Electrochemical Corrosion Measurements

The variations of OCP vs. time for X80 U-bend and square coupons are shown in Figure 4-8. The abiotic OCP values of the U-bend and square coupons were almost identical and they remained stable. The biotic OCP values of the U-bend and square coupons were much higher than the abiotic values, and they fluctuated with the incubation time. Although a higher OCP value indicates a lower corrosion tendency, the actual corrosion outcome for a corroding electrode is determined by the corrosion kinetics. Due to the complexity of SRB MIC systems, OCP often fails to reflect the actual MIC outcome, unlike in simple abiotic corrosion cases. Instead, LPR, EIS, and Tafel scans should be relied upon (Jia et al., 2019b; Zhou et al., 2022a).

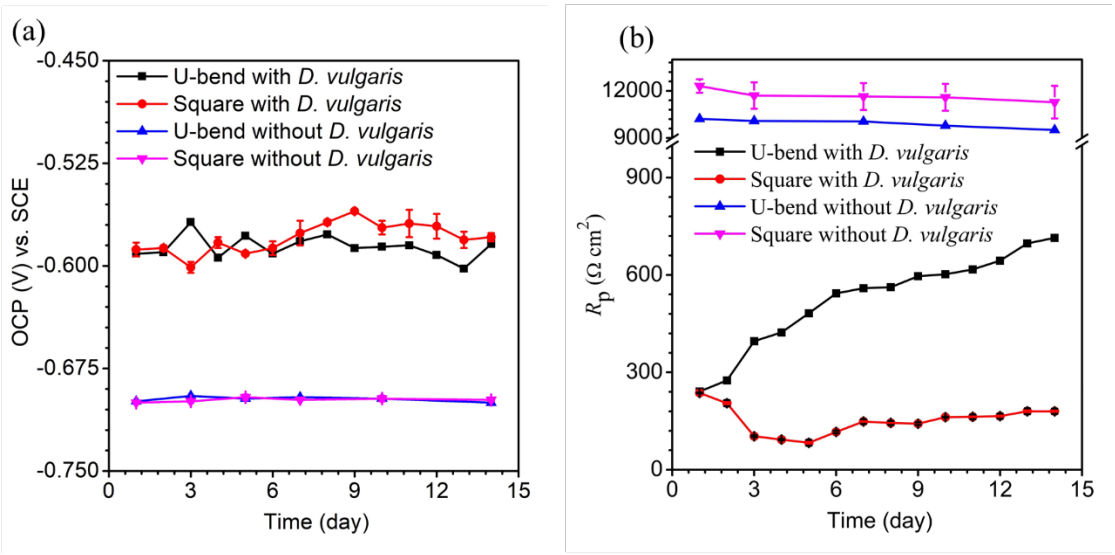

Figure 4-8. Variations of OCP vs. time (a) and LPR vs. time (b) of X80 U-bend and square coupons during a 14-d incubation in an anaerobic culture medium with and without *D. vulgaris*.

Figure 4-8(b) shows the variations of LPR vs. time for X80 U-bend and square coupons during the 14-d SRB incubation. The abiotic R_p values of the U-bend and square coupons were significantly higher than biotic values. A higher R_p value indicates a lower corrosion rate. Therefore, the biotic X80 corrosion rate was higher than the abiotic corrosion rate. In the presence of SRB, the R_p values of the U-bend coupon were much higher than that of the square coupon, suggesting that the *D. vulgaris* MIC rate of the U-bend coupon was lower than that of the square coupon. The biotic R_p values of the square coupon first decreased and then increased gradually after stabilizing. In comparison, the R_p values of U-bend coupons increased with incubation time. The R_p results were consistent with weight loss results.

The Nyquist and Bode plots of X80 U-bend and square coupons are plotted in Figure 4-9. The diameter of the impedance semi-circle of the biotic U-bend was much lower than the abiotic one, indicating that the SRB corrosion rate was faster than the abiotic corrosion rate. The diameter of the impedance semi-circle of the biotic U-bend coupon was larger than that of the biotic square coupon, suggesting that the MIC rate of the U-bend coupon was lower than that of the biotic square coupon.

D. vulgaris accelerated corrosion, resulting in a corrosion product film forming on the coupon surfaces. Therefore, a two-time constant circuit model with biofilm/corrosion product film resistance (R_f) and charge transfer resistance (R_{ct}) was needed. However, in the absence of SRB, only one time constant was needed with R_{ct}. In the Nyquist plots of the biotic U-bend and square coupons, a diffusion resistance Warburg element (W) was needed to model EIS data accurately. This could be attributed to the presence of the SRB biofilm and corrosion products that hindered the ion migration on the X80 working electrode surface, which slowed down mass transfer (Yin et al., 2018). However, no diffusion hindrance phenomenon was found for the biotic U-bend coupon on the 10^{th} and 14^{th} days. This could be attributed to the restrictions of nutrients in the medium, which resulted in the decrease of the sessile cell counts, and the thinning of the biofilm, and the weakening of mass transfer resistance at the later stage of incubation.

For the abiotic EIS spectra, a simple one-time constant circuit model was sufficient, unlike the biotic case that needed a two-constant circuit model (Figure 4-9). Table 4-2 lists the electrochemical parameters from equivalent circuit modeling, in which Q is the constant phase element (CPE) with its impedance calculated from the following equation,

$$Z_Q = {Y_0}^{-1}(i\omega)^{-n} \tag{4-5}$$

where ω, i, Y_0, and n are angular frequency in rad s^{-1}, unit imaginary number, CPE parameter related to capacitance, and dispersion exponent related to the electrode surface state, respectively (Chen et al., 2021; Lu et al., 2023b). The biotic R_{ct} was found lower than abiotic R_{ct}. This suggests that *D. vulgaris* accelerated the corrosion reaction on the X80 surface. Moreover, the R_{ct} values of the U-bend coupon were higher than those of the square coupon, indicating that the MIC rate of the U-bend coupon was lower than that of the square coupon. Thus, the EIS fitting results supported the weight loss results (Figure 4-7(b)).

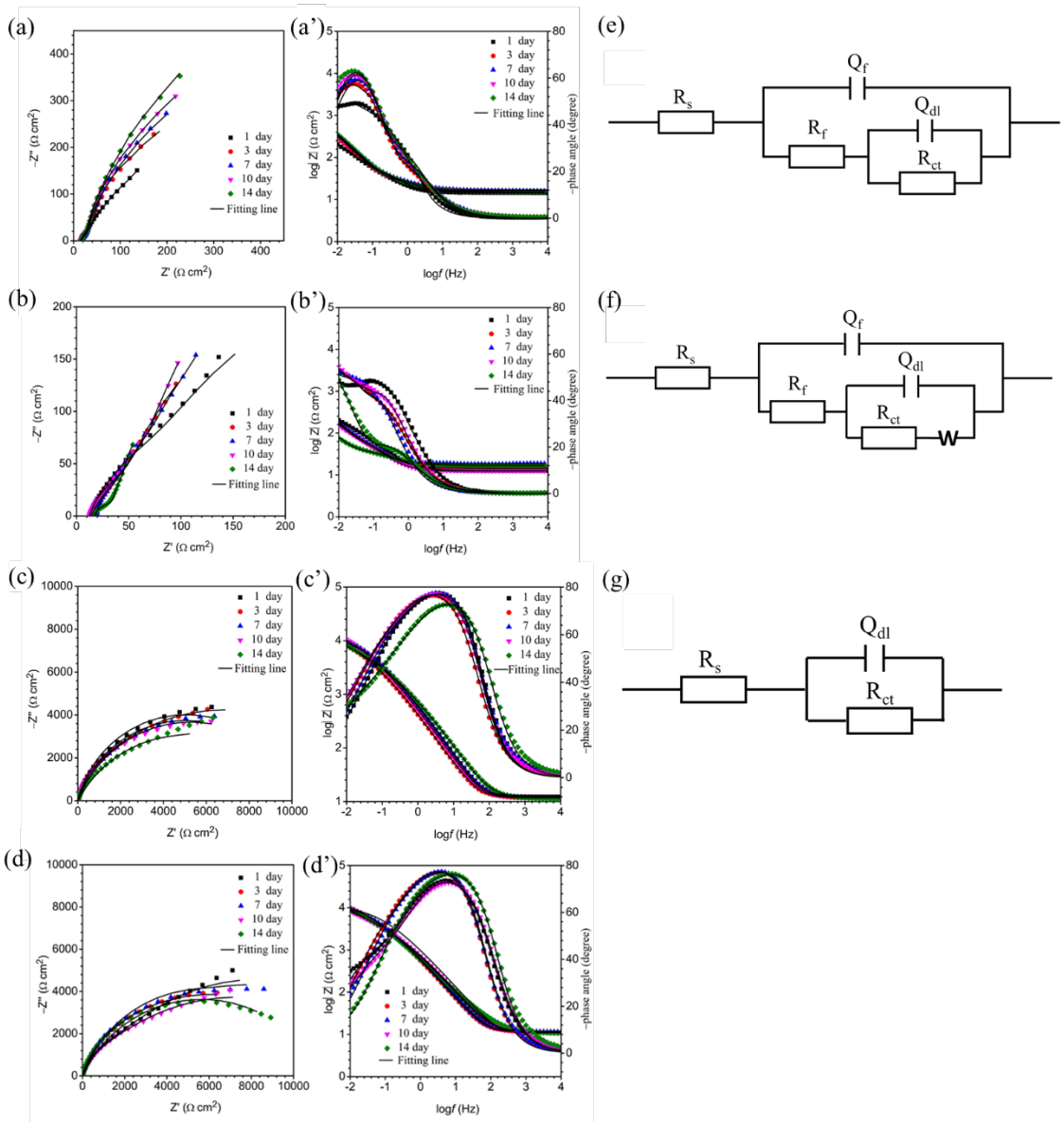

Figure 4-9. Nyquist and Bode plots of (a, a') X80 U-bend coupon with *D. vulgaris*, (b, b') square coupon with *D. vulgaris*, (c, c') U-bend coupon without *D. vulgaris*, (d, d') square coupon without *D. vulgaris*, (e) equivalent circuit model for fitting EIS data with two-time constants without W for biotic condition, (f) two-time constants with W for biotic condition, and (g) one-time constants for abiotic condition.

Table 4-2. Electrochemical parameters obtained from fitting EIS spectra in Figure 4-9.

	t (d)	R_s (Ω cm^2)	Q_{dl} (Ω^{-1} cm^{-2} s^n)	n_1	R_f (Ω cm^2)	Q_{dl} (Ω^{-1} cm^{-2} s^n)	n_2	R_{ct} (Ω cm^2)	W (Ω^{-1} cm^{-2} s$^{1/2}$)
Biotic	1	14.2	2.58×10^{-2}	0.72	263	2.36×10^{-2}	0.99	387	0.47
U-bend	3	16.9	1.31×10^{-2}	0.99	46.6	3.10×10^{-2}	0.99	468	0.47
	7	16.2	1.27×10^{-2}	0.78	36.1	1.57×10^{-2}	0.99	652	0.39
	10	15.1	1.18×10^{-3}	0.81	39.2	1.38×10^{-2}	0.99	680	
	14	15.3	1.07×10^{-2}	0.84	39.6	1.39×10^{-2}	0.99	732	0.44
	1	12.5	2.25×10^{-2}	0.78	226	5.99×10^{-2}	0.99	357	0.43
Abiotic	3	18.9	2.47×10^{-2}	0.83	122	7.86×10^{-2}	0.75	162	0.46
Square	7	13.7	4.06×10^{-2}	0.70	148	1.79×10^{-2}	0.77	305	0.50
	10	12.4	2.38×10^{-2}	0.85	70.4	2.95×10^{-2}	0.99	372	0.54
	14	14.3	2.59×10^{-2}	0.83	38.7	2.52×10^{-2}	0.64	434	
Abiotic	1	10.4	6.32×10^{-4}	0.77				1.05×10^4	
U-bend	3	11.2	7.52×10^{-4}	0.81				1.02×10^4	
	7	11.9	8.01×10^{-4}	0.85				1.01×10^4	
	10	10.5	8.36×10^{-4}	0.70				1.00×10^4	
	14	11.3	8.11×10^{-4}	0.82				1.00×10^4	
	1	11.5	6.64×10^{-4}	0.79				1.20×10^4	
Abiotic	3	11.2	9.31×10^{-4}	0.83				1.18×10^4	
Square	7	11.2	9.22×10^{-4}	0.79				1.16×10^4	
	10	10.3	4.53×10^{-4}	0.75				1.13×10^4	
	14	10.6	3.26×10^{-3}	0.73				1.13×10^4	

Figure 4-10 shows the PDP curves at the end of the 14-d incubation. Table 4-3 lists the electrochemical parameters fitted from the Tafel curves. The i_{corr} values of the abiotic U-bend and square coupons were 45 μA cm^{-2} and 79 μA cm^{-2}, respectively, indicating that the square coupon had a higher MIC rate, corroborating the weight loss data. These values were many times larger than the two very close abiotic values (1.6 μA cm^{-2} for the U-bend coupon and 1.7 μA cm^{-2} for the square coupon). Thus, the Tafel analysis data supported the weight loss data.

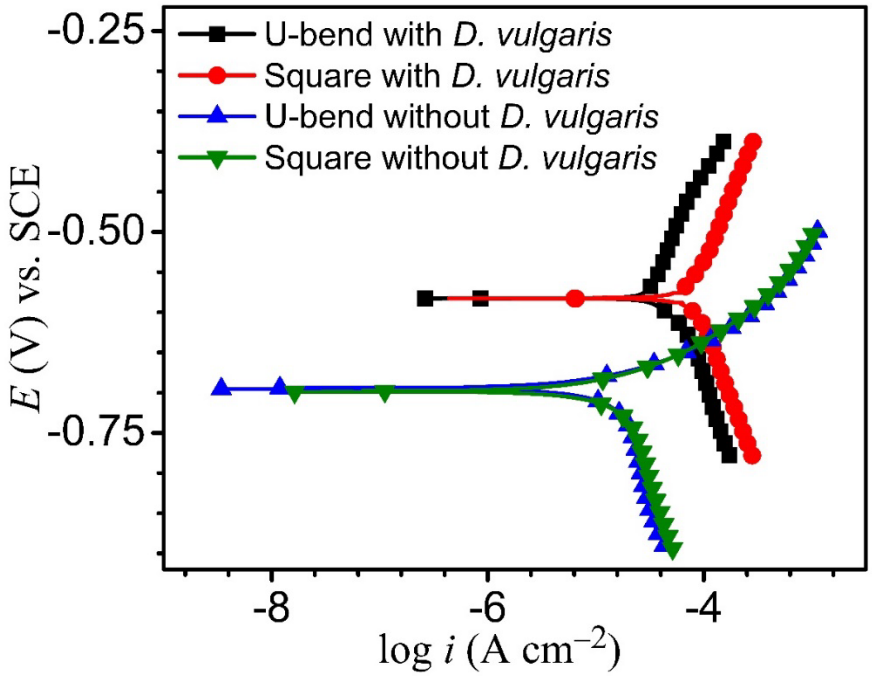

Figure 4-10. Potentiodynamic polarization curves of X80 U-bend and square coupons at the end of a 14-d incubation in an anaerobic culture medium with and without *D. vulgaris*.

Table 4-3. Electrochemical parameters fitted from Tafel curves for X80 U-bend and square coupons exposed to ATCC 1249 culture medium after 14-d incubation.

	Sample	i_{corr} (μA cm^{-2})	E_{corr} (V) vs. SCE	β_a (V dec^{-1})	β_c (V dec^{-1})
With *D. vulgaris*	U-bend	45	–0.53	0.352	–0.434
	Square	79	–0.58	0.345	–0.378
Without *D. vulgaris*	U-bend	1.6	–0.70	0.084	–0.295
	Square	1.7	–0.68	0.063	–0.213

All the data in this work coherently supported SRB acceleration of X80 corrosion which enhanced SCC. It is known that sessile *D. vulgaris* cells can obtain energy from steel as an electron donor and transfer the electrons from the extracellular steel surface to the cytoplasm for biocatalytic sulfate reduction in the SRB cytoplasm, thus accelerating corrosion (Wang et al., 2021a):

$$4Fe \rightarrow 4Fe^{2+} + 8e^{-} \text{ (extracellular)} \quad (4\text{-}6a)$$

$$SO_4^{2-} + 9H^{+} + 8e^{-} \rightarrow HS^{-} + 4H_2O \text{ (intracellular)} \quad (4\text{-}7a)$$

$$E_e\,(Fe^{2+}/Fe^0) = -\,0.447\ V + \frac{RT}{2F} ln[Fe^{2+}] \quad \text{(vs. SHE)} \quad (4\text{-}6b)$$

$$E_e\,(SO_4^{2-}/\,HS^{-}) = 0.249\ V - \frac{2.591RT}{F} pH + \frac{RT}{8F} ln\frac{[SO_4^{2+}]}{[HS^{-}]} \quad \text{(vs. SHE)} \quad (4\text{-}7b)$$

At 25 °C, 1 M solutes (except H^+) and 1 bar gases, and pH 7, the equilibrium potential E_e values from Equations (4-6b) and (4-7b) are –447 mV and 217 mV (vs. standard hydrogen electrode or SHE). The cell potential for the reaction coupling Equations (4-6a) and (4-7a) is +230 mV. This positive cell potential indicates that SRB MIC of Fe^0 is thermodynamically favorable (i.e., energy released). The results in this work show that MIC rates were much higher than biotic corrosion rates.

It is worthwhile to note that the overall corrosion rate of the U-bend coupon was less than that of the square coupon. Some researchers claimed that micro-cracks filled with corrosion products generated on the surface of X80 U-bend coupons. The corrosion products can effectively operate as a barrier against general corrosion of base steel coupons by significantly reducing the anodic and cathodic reaction rates (Asawa

et al., 2004). In this work, X80 U-bend had a considerably lower sessile cell count. Further investigations are needed to prove that stress affects sessile cell count.

4.4. Conclusion

D. vulgaris, a common SRB strain, accelerated the corrosion of X80 square and U-bend coupons in an anaerobic environment. The combined effects of tensile stress and *D. vulgaris* MIC increased the SCC sensitivity of X80 carbon steel. MIC pitting germinated sharp SCC microcracks in 2-week and 12-week SRB immersion tests. A pre-cracked U-bend coupon suffered SCC failure after a 6-week SRB incubation. It is interesting to find that stressed X80 steel suffered lower weight loss compared with unstressed X80 and this observation was supported by LPR, EIS and PDP results.

Chapter 5: SCC of X80 Carbon Steel U-Bend Caused by *D. ferrophilus*

5.1 Introduction

Sulfate is widely distributed in many environments such as the marine environment. Most oil and gas systems contain sulfate as well because seawater is frequently used in enhanced oil recovery through seawater injection downhole to increase reservoir pressure (Basafa & Hawboldt, 2019; Mohammed et al., 2022; Xu et al., 2023a). SRB are ubiquitous in many environments especially under anaerobic conditions. They are aerotolerant anaerobes that can even grow underneath aerobic biofilms that provide a locally anoxic condition (Li et al., 2018b). SRB are intensively investigated in MIC because of their ubiquitous presence and corrosivity in field operations (Liu et al., 2022a; Wang et al., 2021e; Wasim & Djukic, 2020; Xu et al., 2023a).

D. vulgaris is the most widely used SRB species in the investigations of SRB MIC mechanisms (Wang et al., 2021a; Yang et al., 2023). Recently, a super-corrosive SRB strain, namely *D. ferrophilus* (strain IS5), has been gaining popularity because it can produce double-digit weight losses in mg cm^{-2} after only 7 d incubation, with pits that are visible even in images taken by common smartphone cameras (Xu et al., 2023b). It was originally isolated from the North Sea in northern Germany (Enning et al., 2012). *D. vulgaris* MIC in ATCC 1249 culture medium at 37ºC (optimal for growth) caused a pit depth of 18.2 μm and a weight loss of 2.1 mg cm^{-2} against C1018 carbon steel after

a 7-d incubation (Jia et al., 2018a). In comparison, these values were 26.9 μm, and 15.6 mg cm^{-2} (7.4X higher), respectively for *D. ferrophilus* MIC in EASW at 28ºC (optimal for growth) (Wang et al., 2021a). In both cases, abiotic corrosion control showed negligible corrosion in the deoxygenated culture medium. Thus, *D. ferrophilus* is a far more corrosive SRB species than *D. vulgaris*.

In carbon steel MIC, both *D. vulgaris* and *D. ferrophilus* were found to follow the EET-MIC mechanism, because riboflavin, an electron mediator, accelerated their MIC weight losses (Wang et al., 2021a; Wang et al., 2020). The much higher corrosivity of *D. ferrophilus* can be attributed to its better sessile growth and higher EET ability per sessile cell (Wang et al., 2021a).

Most MIC studies have focused on the threat of pinhole leaks caused by MIC pitting (Gopi et al., 2007; Ramesh et al., 2003; Sharma et al., 2018; Su et al., 2014). However, microbial degradation of mechanical properties can be more damaging because they can lead to catastrophic failures costing huge losses economically and even losses in human lives (Cui et al., 2022; Li et al., 2021c; Zhang et al., 2023). Stress corrosion cracking (SCC) is the growth of crack formation under stress in corrosive condition (Hwang et al., 2015; Shi et al., 2019; Weng et al., 2022). Failures due to SCC leading to pipe ruptures and structural support collapses are major concerns in corrosion research (Wasim & Djukic, 2022). Some researchers have started to investigate MIC impact on SCC. It was found that The SCC susceptibility was greatly elevated by the

combination of stress and SRB MIC (Sun et al., 2023), and SCC was also related to H_2S metabolite produced by SRB (Chen et al., 2022a).

In abiotic SCC investigations such as SCC in acid corrosion environment (Pal et al., 2022), researchers observed that fast corrosion does not necessarily lead to more severe SCC because fast corrosion can dissolve SCC crack tips and converted them to less harmful pits (Pal et al., 2022; Parkins, 1980). This important phenomenon in SCC has never been demonstrated in biotic systems in lab investigations because MIC rates are usually very low.

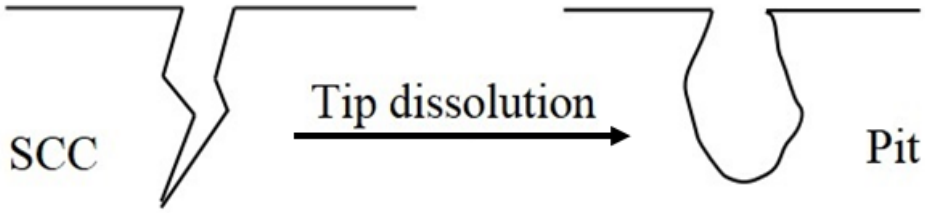

Figure 5-1. Schematic diagram of crack tip dissolution leading to SCC development to pits.

This work hypothesized that in biotic SCC, the same crack tip dissolution can also occur. The comparison of *D. vulgaris* SCC and *D. ferrophilus* SCC can offer a unique advantage because the latter is super corrosive.

U-bend is commonly used to investigate SCC in lab tests. A metal strip is bent to form a U shaped to apply stress. The outer bottom of the U-bend suffers from the highest stress. X80 carbon steel is a popular pipeline steel in oil and gas transportation due to its high strength and affordable price. The two SRB species were incubated in anaerobic bottles containing X80 U-bend coupons (stressed) and square coupons (no stress for comparison). H_2, H_2S, broth pH, sessile cell count, weight loss, and pit depth were measured. U-bend SCC cracks were examined. Corrosion results were corroborated using various electrochemical measurements.

5.2 Materials and Methods

The composition of X80 carbon steel is listed in Table A-1. X80 square coupon and X80 U-bend coupon dimensions are in Figure A-2 and Figure A-3, respectively. Each X80 square coupon (1 cm^2 top surface exposed) and X80 U-bend coupon for electrochemical test and immersion test were prepared as described in Appendix A (Figure A-1, Figure A-2, Figure A-3, Figure A-4). Coupon surface polishing, cleaning, drying, and culture medium the sterilization and deoxygenation procedures are illustrated in Appendix A.

D. ferrophilus (strain IS5) was incubated in an EASW at 28°C (optimal temperature) in this study. The chemical composition of EASW (Wang et al., 2021a) was listed in Table A-1. It was incubated in 450 mL anaerobic bottles with 200 mL EASW at 28ºC as described in Appendix A. At the end of a 14-d incubation, the

coupons were cleaned with a fresh Clarke's solution to remove the biofilms and corrosion products before a weight measurement was taken (ASTM G1-03, 2003). Each weight loss data point was derived from three replicate coupons in the same anaerobic bottle. The sessile cells on the surface of the coupons were counted using a hemocytometer under a 400X microscope as shown in Appendix A (Wang et al., 2021a). The concentration of H_2S, H_2 and total pressure in each anaerobic bottle were measured followed the Appendix A (Figure A-7) (Li et al., 2021c; Li et al., 2022b). The corrosion products on the X80 square and U-bend coupon surfaces were identified using an X-ray diffractometer (XRD; Bruker D8 Discovery model, Bruker AXS GmbH, Karlsruhe, Germany).

Electrochemical tests were conducted in 450 mL anaerobic bottles containing 200 mL EASW and 2 mL *D. ferrophilus* seed. X80 square coupon and U-bend coupon were used as the working electrode. OCP, LPR, EIS and Tafel scan were measured by an electrochemical station (Gamry, Reference 600 Plus). The parameters and set up of the electrochemical anaerobic bottles were shown in Appendix A.

Infinite Focus Microscope (IFM) (Model ALC13, Alicona Imaging GmbH, Graz, Austria) was used to obtain pit depth profiles and scanning electron microscopy. A scanning electron microscopy (SEM; FEI Quanta 250, Hillsboro, OR, USA) was used to observe the biofilm morphology on the coupon surface, which flowed the methods

by Chapter 4. Both preparation processes were shown in Appendix A. The test matrix of SCC of X80 U-bend steel caused by *D. ferrophilus* is illustrated in Table 5-1.

Table 5-1. Test matrix for stress corrosion cracking of X80 U-bend steel caused by *D. ferrophilus.*

Parameter	Condition
Bacterium	*D. ferrophilus* (strain IS5) and *D. vulgaris*
Culture medium	EASW for *D. ferrophilus* and ATCC 1249 for *D. vulgaris*
Coupon	X80 U-bend coupons and X80 square coupons
Temperature	28°C for *D. ferrophilus* and 37°C for *D. vulgaris*
Anaerobic bottle volume	450 mL
Culture medium	200 mL (plus 2 mL seed culture)
Incubation time	14 d (U-bends and square coupons), and 3 months (U-bends only)
Analysis	Weight loss, sessile cell count, gas measurements, broth pH, electrochemical measurements, pit depth, SCC visualization at 25X and 1000X.

5.3 Results and Discussion

5.3.1 Weight Loss, Sessile Cell Count, pH and Headspace Gas Measurements

The weight losses and sessile cell counts of X80 U-bend coupons (with stress) and (flat) square coupons (without stress) in EASW with *D. ferrophilus* after the 14-d incubation are presented. The weight losses of U-bend coupon and square coupon were 30.2 mg cm^{-2} and 23.9 mg cm^{-2}, respectively with the X80 U-bend having 26% higher weight loss. These values are larger than the 2.1 mg cm^{-2} (X80 U-bend) and 3.5 mg

cm^{-2} (X80 square) values for *D. vulgaris* (3.7 mg cm^{-2} (Li et al., 2021c)) in ATCC 1249 culture medium at 37ºC, confirming that *D. ferrophilus* was far more corrosive. In addition, it is interesting to note that the weight loss for the U-bend coupon caused by *D. ferrophilus* was significantly higher than that of the square coupon after the 14-d incubation. However, the situation was opposite in *D. vulgaris* MIC of X80.

In EET-MIC, the EET rate typically is the limiting step in the MIC process (Yin et al., 2018). More sessile *D. ferrophilus* cells harvested more electrons from elemental iron via EET, leading to a higher weight loss. Furthermore, it was found that *D. ferrophilus* had a higher EET ability (Wang et al., 2021a). The sessile cell counts on the U-bend coupon and square coupon were 8.8×10^8 cells cm^{-2} and 6.1×10^8 cells cm^{-2}, respectively (Figure 5-2), reflecting a 41% higher sessile cell count for the U-bend which explained its 26% higher weight loss. In *D. vulgaris* MIC, the sessile cell count on the U-bend was 13% lower, which explained its lower weight loss.

Table 5-2 lists the H_2 and H_2S concentrations, and total pressure in the headspace of each anaerobic bottle, as well as broth pH after the 14-d incubation in the *D. ferrophilus* medium. The H_2 and H_2S concentrations in the headspace were 3.4×10^{-5} M and 7.0×10^{-6} M, respectively, and the total pressure in the headspace was 1.04 bar. The [H_2S] concentration in the *D. ferrophilus* broth was 1.3×10^{-5} M based on Henry's law (Ning et al., 2014), which is close to 1.4×10^{-3} M reported for *D. vulgaris* (Li et al., 2021c), demonstrating that the far more aggressive *D. ferrophilus* MIC for X80 steel was not due to H_2S corrosion, consistent with the same finding for C1018 carbon steel MIC by *D. vulgaris* previously (Jia et al., 2018a). In addition, the final pH 6.9 was near neutral and close to the initial pH 7 in the *D. ferrophilus* broth, suggesting that acid corrosion could not be a significant contributing factor in this study.

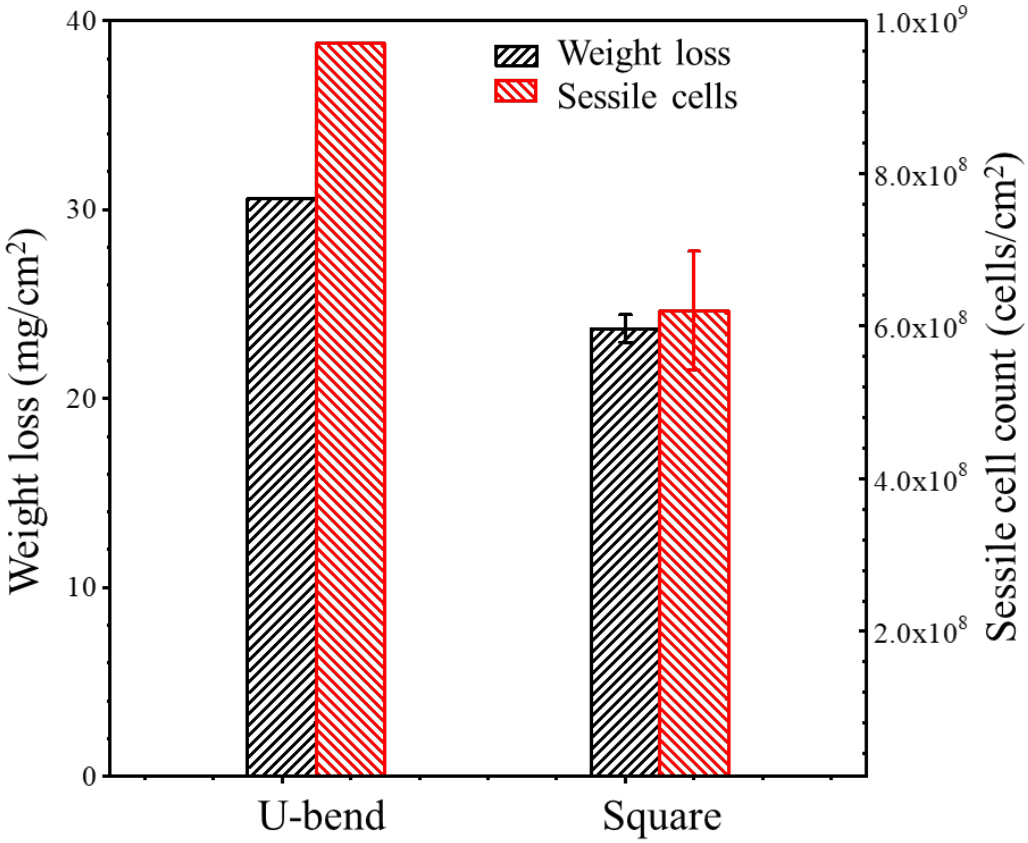

Figure 5-2. Weight losses and sessile cell counts of X80 U-bends and square coupons after 14-d incubation in EASW with *D. ferrophilus* in same anaerobic bottle. (Compare with *D. vulgaris* data in Figure 4-7(a and b)).

Table 5-2. H_2 and H_2S concentrations, total pressure, and pH value after 14-d incubation in EASW with *D. ferrophilus*. (Compare with *D. vulgaris* data in Table 4-1.)

Total pressure in headspace (bar)	H_2 in headspace (ppm) (v/v)	H_2 in headspace (M)	H_2S in headspace (ppm) (v/v)	H_2S in headspace (M)	[H_2S] in broth (M)	Broth pH
1.04	850	3.4×10^{-5}	175	7.0×10^{-6}	1.34×10^{-5}	6.9

5.3.2 Electrochemical Measurements

The variations of OCP vs. time for X80 U-bend working electrode and X80 square working electrode incubated in the *D. ferrophilus* broth for 14 d are shown in Figure 5-3. The OCP values of X80 U-bend were higher than those of X80 square coupon at the same incubation time, suggesting X80 U-bend more easily corroded. Although a higher OCP value theoretically indicates a lower corrosion tendency, the corrosion kinetics determine the actual corrosion rate (Liu et al., 2018b). In most SRB MIC systems, OCP cannot be reliably used to predict corrosion outcome due to their complexities (Wang et al., 2020). Instead, kinetic electrochemical data such as LPR and EIS, and PDP scans should be relied upon.

Figure 5-4 shows the variation of R_p vs. time for X80 U-bend working electrode and X80 square working electrode incubated in the *D. ferrophilus* broth. In corrosion kinetics, R_p is inversely proportional to the corrosion rate. At the same incubation time, the R_p values of the U-bend were lower than those of the square, indicating that the corrosion rate of the U-bend coupon was faster than that of the square coupon, which was consistent with the weight loss results. Thus, R_p data also proved that the mechanical stress applied to the U-bend promoted the *D. ferrophilus* MIC.

The R_p values of the X80 U-bend working electrode and X80 square coupon working electrode decreased gradually, reaching their maximum values on the 6 d, and then gradually increased (Figure 5-4). The reason for this trend in the corrosion rate

was that the SRB grew rather quickly initially, and the sessile cell count increased, which directly led to the increased EET rate and thus a higher MIC rate. However, at the later stage of immersion, the nutrients in the medium were depleted. Thus, the number of sessile bacteria decreased, resulting in a decrease in the corrosion rate.

The Nyquist and Bode plots of X80 U-bend and X80 square during the 14-d incubation are shown in Figure 5-5. The impedance modulus of X80 U-bend was less than that of X80 square at the same incubation time, indicating that *D. ferrophilus* was more corrosive against X80 U-bend's stressed outer bottom surface than against X80 square coupon's flat surface (not stressed). The capacitive reactance arc radius and impedance modulus of U-bend coupon and square coupon also showed a decreasing trend and then increased. A smaller capacitive reactance arc radius and an impedance modulus mean a higher corrosion rate (Dou et al., 2019). Thus, the EIS spectra here suggest that the *D. ferrophilus* MIC rate of X80 steel first increased and then decreased with the incubation time, consistent with R_p data.

The equivalent circuit model for EIS modeling is shown in Figure 5-6, in which R_s is solution resistance, and R_f and Q_f the resistance and constant-phase elements of the film consisting of biofilm and corrosion products, respectively. R_{ct} is the charge-transfer resistance, Q_{dl} the constant-phase element of the electric double layer, and the Warburg (W) element describing the diffusion process. Table 5-3 lists the electrochemical parameters obtained from fitting the EIS spectra. The (R_{ct} + R_f) values

of the X80 U-bend were lower than those of the X80 square at the same incubation time, similar to the R_p trend above, which demonstrates that the MIC rate of the X80 U-bend was higher than that of the X80 square once again. Moreover, the (R_{ct} + R_f) values of the X80 U-bend and X80 square decreased first at the early incubation stage and reached maximum values on the 7th day (22.1 Ω cm^2 for U-bend and 35 Ω cm^2 for square, respectively). Afterwards, the (R_{ct} + R_f) values of the X80 coupons increased with the incubation time, suggesting that the MIC rate of the X80 steel increased first and then decreased. The EIS parameters are consistent with the R_p results.

Figure 5-7 shows the PDP curves of the X80 U-bend and X80 square in the *D. ferrophilus* broths at end of the 14-d incubation. The fitting results of the PDP curves are shown in Table 5-4. The current density (i_{corr}) values of the X80 U-bend and X80 square were 7.9×10^{-4} A cm^{-2} and 3.0×10^{-4} A cm^{-2}, respectively, indicating that the pre-applied stress in the U-bend increased the *D. ferrophilus* MIC rate. This agrees with the sessile cell count data and all the other electrochemical data above.

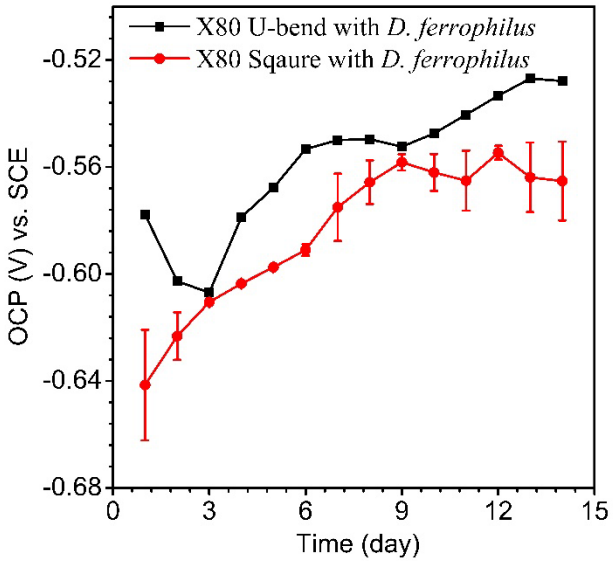

Figure 5-3. Variations of OCP vs. time for X80 U-bend and X80 square coupons incubated in EASW with *D. ferrophilus* for 14 d.

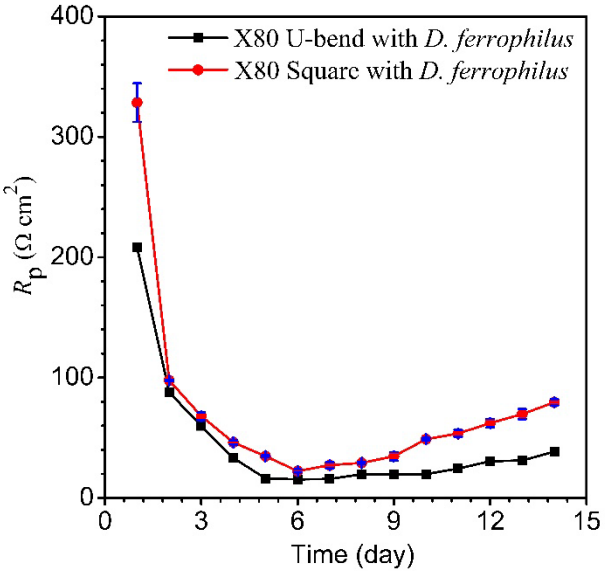

Figure 5-4. Variations of LPR vs. time for X80 U-bend and X80 square coupons incubated in EASW with *D. ferrophilus* for 14 d.

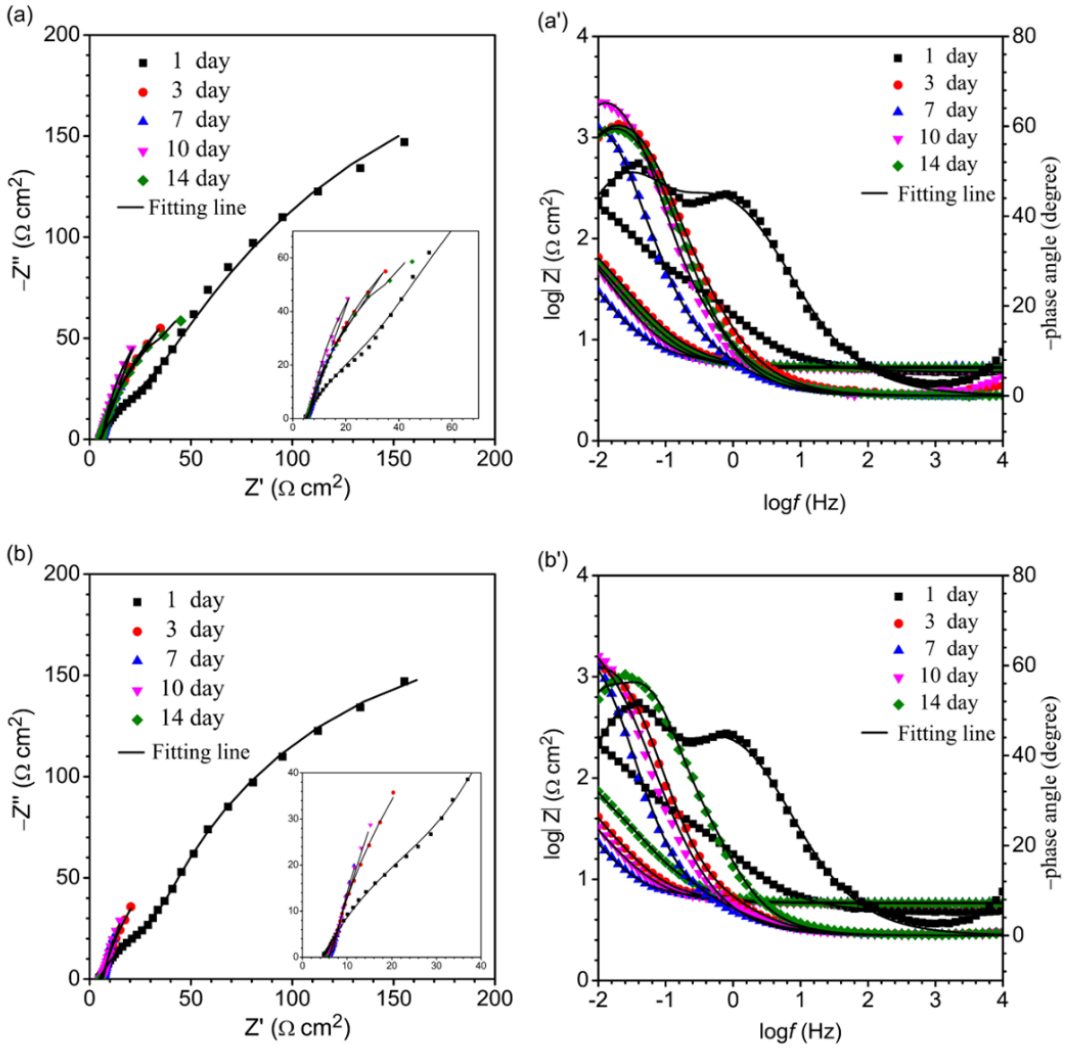

Figure 5-5. Nyquist and Bode plots of (a, a') X80 U-bend coupon and (b, b') X80 square coupon in EASW with *D. ferrophilus* for 14 d.

Table 5-3. Electrochemical parameters obtained from fitting EIS spectra in Figure 5-5.

	t (d)	R_s (Ω cm^2)	Q_{dl} (Ω^{-1} cm^{-2} s^n)	n_1	R_f (Ω cm^2)	Q_{dl} ($\times10^{-2}$ Ω^{-1} cm^{-2} s^n)	n_2	R_{ct} (Ω cm^2)	W (Ω^{-1} cm^{-2} s$^{1/2}$)	χ^2 ($\times10^{-3}$)
U-bend	1	4.83	1.92×10^{-2}	0.70	116	2.63	0.85	217	0.43	3.78
	3	5.26	1.29×10^{-1}	0.82	27	2.57	0.99	42	0.55	4.86
	7	5.39	2.33×10^{-4}	0.79	5.20	12.8.	0.99	22	0.60	2.59
	10	5.23	1.46×10^{-1}	0.96	5.80	11.3	0.97	29	0.48	2.74
	14	5.31	1.54×10^{-1}	0.84	6.12	28.6	0.98	52	0.49	1.62
Square	1	4.79	1.69×10^{-2}	0.71	92	2.64	0.99	352	0.42	5.78
	3	5.79	1.59×10^{-2}	0.84	3.22	11.2	0.87	234	0.53	2.32
	7	5.86	2.68×10^{-2}	0.78	3.53	26.5	0.97	35	0.60	4.95
	10	5.83	3.07×10^{-2}	0.84	6.53	41.9	0.99	63	0.48	3.57
	14	5.84	8.63×10^{-2}	0.95	8.53	60.7	0.99	70	0.46	7.98

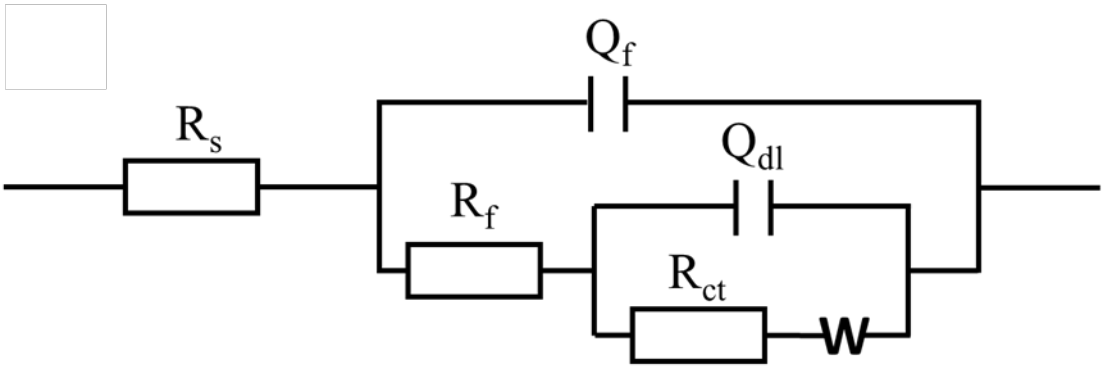

Figure 5-6. Equivalent circuit models employed in fitting EIS data.

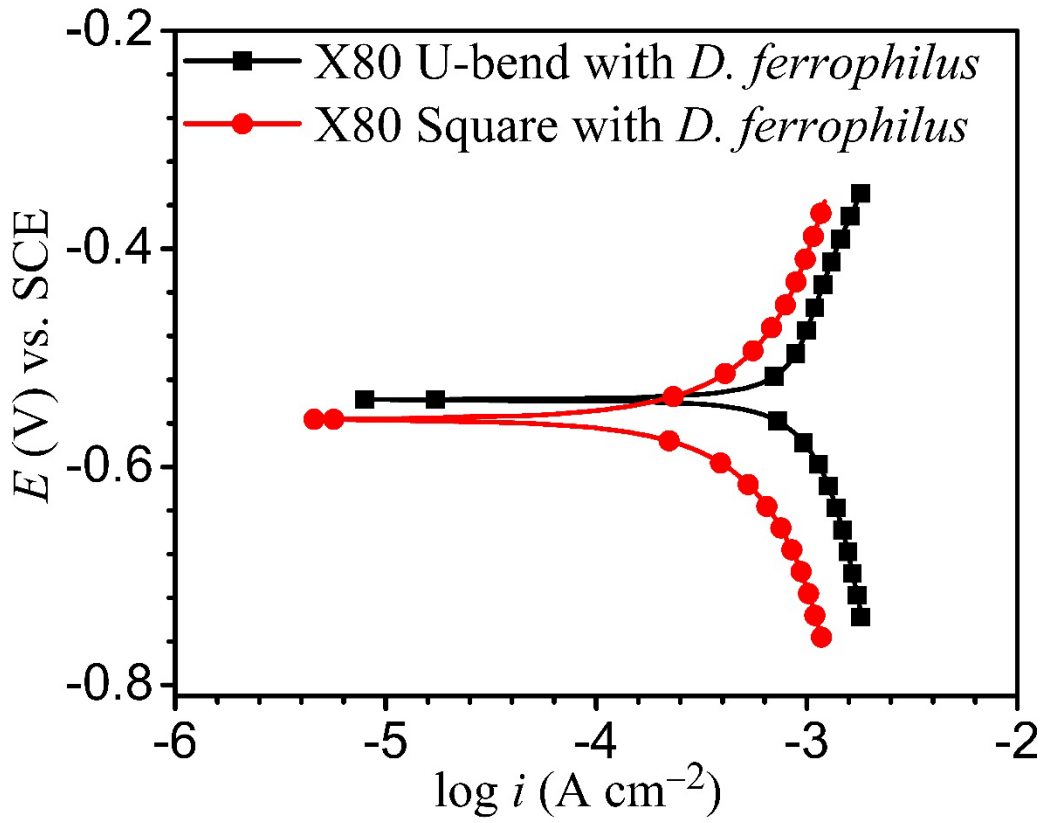

Figure 5-7. PDP curves of X80 U-bend and square coupons in EASW with *D. ferrophilus* at end of a 14-d incubation.

Table 5-4. Electrochemical parameters fitted from Tafel curves for X80 U-bend and square working electrodes in EASW with *D. ferrophilus* at end of 14-d incubation.

D. ferrophilus	i_{corr} ($\mu A\ cm^{-2}$)	E_{corr} (V) vs. SCE	β_a ($V\ dec^{-1}$)	β_c ($V\ dec^{-1}$)
U-bend	790	–0.53	0.524	–0.464
Square	300	–0.56	0.245	–0.245

5.3.3 X80 U-Bend SCC Analyses

Figure 5-8 shows the SEM images of the cross sections on the X80 U-bend coupon after the 14-d incubation in the *D. ferrophilus* broth and in the *D. vulgaris* broth. Severe uniform corrosion occurred on the work surface for the X80 U-bend coupon (with the outer bottom of the U-bend with the bottom facing upward for better viewing) exposed to *D. ferrophilus*, with a layer of metal disappearing, and the corroded surface showed wide pits. In contrast, the X80 U-bend exposed to *D. vulgaris* showed much less metal loss, but with sharper pits and some cracks. Although *D. vulgaris* caused much lower uniform corrosion than *D. ferrophilus*, *D. vulgaris* left behind harmful cracks. Figure 5-7 once again confirms that *D. ferrophilus* was more corrosive than *D. vulgaris* (Beese et al., 2013; Enning et al., 2012).

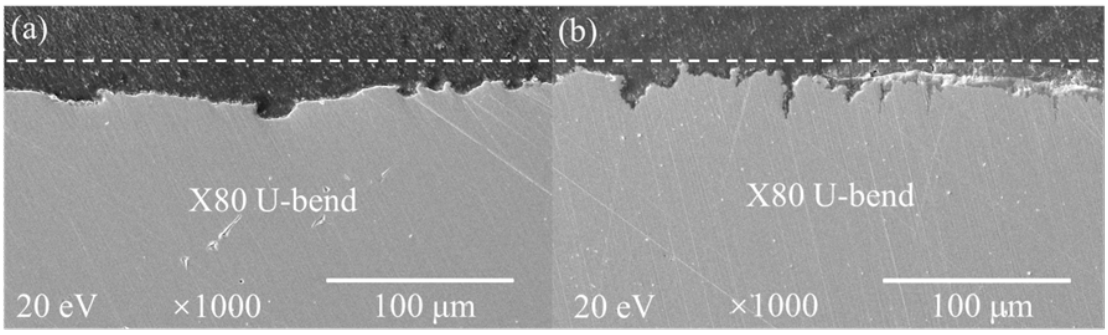

Figure 5-8. c (a) EASW with *D. ferrophilus*, and (b) ATCC 1249 culture medium with *D. vulgaris* after 14-d incubation. (The dotted line suggests the work surface of X80 U-bend coupon before SRB immersion.)

The SEM images in Figure 5-8 show that *D. vulgaris* caused significant cracks in addition to pitting, whereas *D. ferrophilus* did not. This was because *D. ferrophilus* was more corrosive, which resulted in the crack tips being prevented from forming or being dissolved by the fast-corroding biofilm. For the first time it was demonstrated for biotic corrosion that fast-corrosion actually has less SCC risk, owing to the use of a super-corrosive SRB. In contrast, the MIC rate of *D. vulgaris* was relatively slow, resulting in cracks being formed.

It is worth noting that for the first time it was demonstrated for biotic corrosion owing to the use of a highly corrosive SRB. In contrast, the MIC rate of *D. vulgaris* was relatively slow, resulting in the crack tip manifestation. Fast corrosion leads to crack tip dissolution has been observed in abiotic corrosion (Abedi et al., 2007; Wu et al., 2015). This can explain why only severe pits were observed on the coupons surface in the *D. ferrophilus* medium, whereas cracks were also observed in the presence of *D. vulgaris*.

The surface profiles of the X80 U-bend coupons exposed to *D. ferrophilus* and *D. vulgaris* for 14 d are shown in Figure 5-9. The pristine X80 U-bend coupon profile shows no pits in Figure 5-9 (e) because it was polished to 600 grits. The X80 U-bend exposed to *D. ferrophilus* for 14 d, the flat leg area (0.7 cm from U bottom) of X80 U-bend and X80 square coupon had maximum pit depths of 47.5 μm and 40.6 μm, respectively in Figures 5-9 (a, b). In the presence of *D. vulgaris*, the maximum pit

depths on the flat leg area of the X80 U-bend and X80 square coupons were 25.1 µm and 17.2 µm, respectively in Figure 5-9 (c, d). The stress in the U-bend steel increased the pit depth on the flat leg area, consistent with the weight loss data (Figure 5-1).

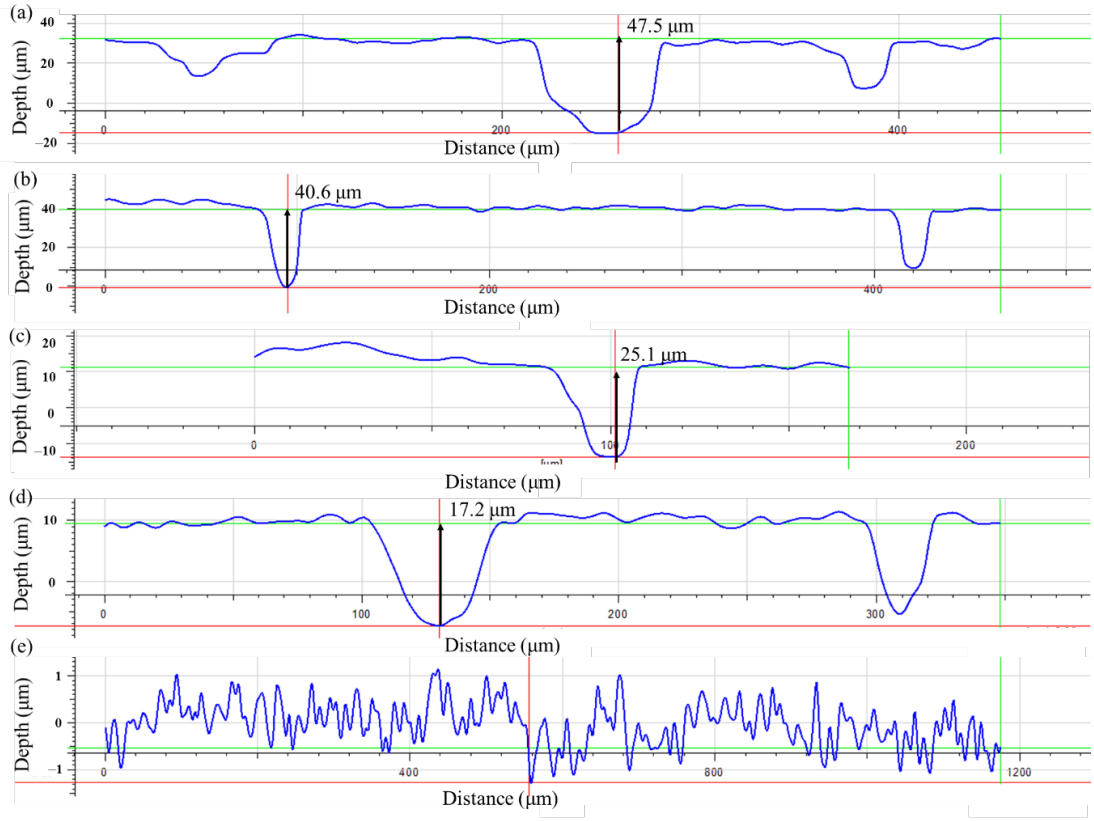

Figure 5-9. Surface profiles of X80 coupons exposed to EASW with *D. ferrophilus* for 14 d: flat leg area on (a) X80 U-bend coupon, (b) X80 square coupon, in comparison with exposure to *D. vulgaris* in ATCC 1249 culture medium: (c) flat area on X80 U-bend coupon, (d) X80 square coupon, and (e) pristine X80 U-bend coupon's flat leg area (.7 cm distance away from the U bottom).

The X80 U-bend's highest stress area was at the outer edges of the U's bottom, as illustrated by the two yellow circles in Figure 5-10 (a). The 25X magnification side views of U-bend coupons of the area after 3 months of incubation (no culture medium refreshment) are provided in Figure 5-10 (b) and (c). After 3 months exposure to *D. ferrophilus* in EASW, the X80 U-bend coupon maintained a relatively smooth curved surface despite the loss of a metal layer to uniform corrosion (Figure 5-8 (b)). It should be noted that the 25X magnification used in Figure 5-10 was insufficient to reveal micron-sized pits. The X80 U-bend coupon shows a rugged surface profile with many small cracks after the 3-month exposure to *D. vulgaris* in ATCC 1249 culture medium (Figure 5-10 (c)). The crack tips on the U-bond coupon exposed to *D. ferrophilus* were not seen (dissolved) (Figure 5-10 (b)) owing to the very fast corrosion by *D. ferrophilus*. In contrast, slower corroding *D. vulgaris* left behind numerous harmful cracks. For the first time, crack tip dissolution by fast corrosion was demonstrated in MIC which expands the abiotic SCC behavior to biotic.

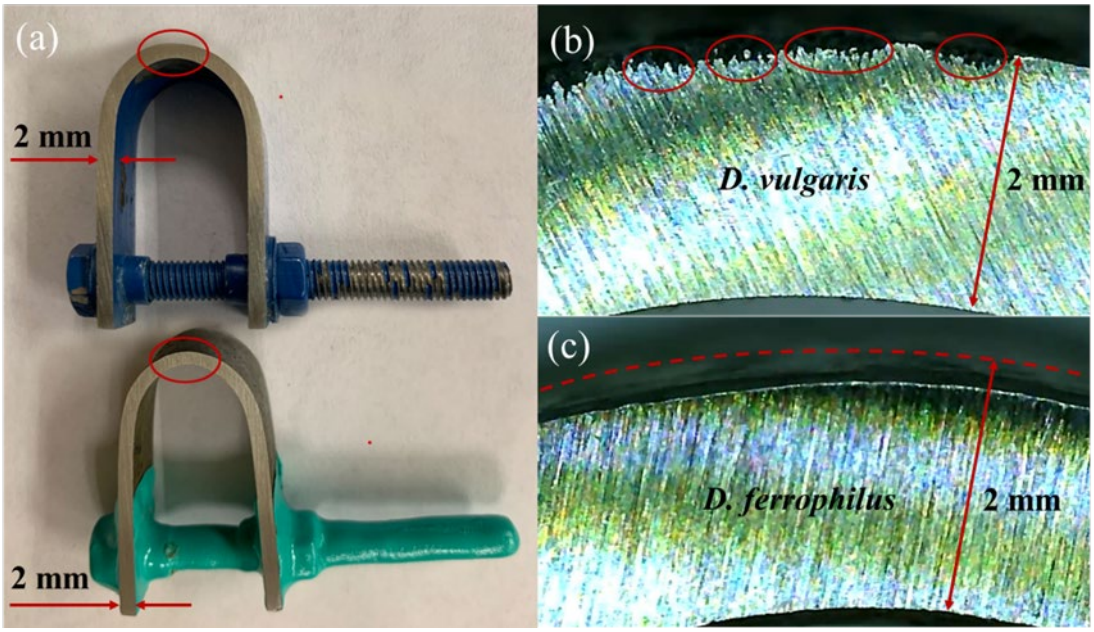

Figure 5-10. (a) X80 U-bends after 3-month immersion in EASW with *D. ferrophilus* (top) and ATCC 1249 culture medium with *D. vulgaris* (bottom) broths, (b) side view (25X magnification) of U-bend exposed to *D. vulgaris*, and (c) U-bend exposed to *D. ferrophilus*.

5.3.4 Relative Pitting Severity Analyses

Relative pitting severity (*RPS*) is more practical to use in lab tests than the classical pitting factor. The latter requires the location of an area with an intact surface such as an original pipe wall in pipeline corrosion. However, pitting factor is not convenient for lab tests in which the original surface is completely missing after being corroded. *RPS* is defined by the following equation (Dou et al., 2018):

$$RPS = \frac{\text{maximum pit growth rate}}{\text{uniform corrosion rate based on (specific) weight loss}} \quad (5\text{-}1)$$

which can be directly calculated as follows:

$$RPS = \frac{\text{maximum pit depth} \times \text{metal density}}{\text{(specific) weight loss}} \quad (5\text{-}2)$$

After the 14-d incubation with *D. vulgaris*, the weight losses of X80 U-bend coupon and X80 square coupon were 2.35 mg cm^{-2} and 3.83 mg cm^{-2} (Li et al., 2023), respectively with the square coupon having a higher weight loss, opposite to that in *D. ferrophilus* MIC discussed earlier. The maximum pit depths on the flat area of the X80 U-bend coupon and X80 square coupon were 25.1 μm and 17.2 μm, respectively. Therefore, the *RPS* values of U-bend coupon and square X80 coupon in the 14-d *D. vulgaris* incubation were 9.4 and 3.9, respectively. In comparison with *D. ferrophilus* in EASW, the weight losses of the X80 U-bend coupon and square coupon were much higher at 30.2 mg cm^{-2} and 23.9 mg cm^{-2}, respectively. The corresponding maximum pit depths were 47.5 μm and 40.6 μm, respectively. Therefore, the *RPS* values of X80 U-bend coupon and X80 square coupon in *D. ferrophilus* incubation for 14 d were 1.2 and 1.3, respectively. A higher than unity *RPS* value means localized corrosion is more severe than uniform corrosion. A near-unity *RPS* means both localized corrosion and uniform corrosion are equally important. The data in this work indicated that fast-corroding *D. ferrophilus* had much smaller *RPS* values in X80 MIC than lower-corroding *D. vulgaris*. This is reasonable because a fast uniform corrosion rate keeps removing the top layers of pits, and thus making pits less deep.

5.4 Conclusion

This study used super-corrosive *D. ferrophilus* in EASW to compare with far less corrosive *D. vulgaris* in ATCC 1249 culture medium to study the MIC impact on X80 U-bend (with largest stress at U's bottom) and flat square (without stress). The weight loss and pit depth of the X80 U-bend coupon were larger than that of the X80 square coupon after the 14-d exposure to *D. ferrophilus*, demonstrating that the mechanical stress accelerated the *D. ferrophilus* MIC of X80 pipeline steel. This was supported by LPR, EIS and PDP data. For slow-corroding *D. vulgaris*, the trend was opposite (i.e., U-bend less corroded). After the 14-d incubation, *D. vulgaris* caused significant SCC cracks in the X80 U-bend, whereas *D. ferrophilus* did not. This was attributed to the fast corrosion rate caused by *D. ferrophilus* preventing or dissolving SCC crack tips. This is the first time such a phenomenon was demonstrated in MIC. This expands the very important SCC phenomenon from abiotic corrosion to biotic corrosion.

Chapter 6: Carbon Source Starvation Elevated MIC Deterioration of Tensile Strength and Tensile Strain

6.1 Introduction

The elemental iron releases electrons extracellularly but the electrons are used in sulfate reduction inside SRB cytoplasm, which is the result of the demand of electroactive sessile cells for energy. Starved cells are more eager to harvest the extracellular electrons for energy production in order to survive, which can lead to more severe corrosion (Flemming et al., 2016; Gu & Xu, 2013; Liu et al., 2018a). In this work, carbon source starvation was used as a means to vary MIC severity in the study of the MIC impact on the degradation of X80 mechanical properties. Starvation also induced changes in dissolved H_2S and headspace H_2 levels, which were used to study their impact as well.

6.2 Materials and Methods

The composition of X80 carbon steel is listed in Table A-1, X80 square coupon (Figure A-1) and X80 dogbone coupon dimensions (Figure A-5) are shown in Appendix A. Twenty X80 square coupons (1 cm^2 exposed surface on top) were used as weight loss specimens and working electrode in electrochemical tests (Figure A-4). The preparation of the coupon surface and the chemicals used in this work were illustrated in Appendix A.

*This chapter was previously published in Frontiers in Materials (Z. Li et al., 2022). Copyright permission is not required by the journal.

D. vulgaris (ATCC 7757) was selected in this research. It is a typical pure-strain SRB. Each anerobic bottle contained 3 square coupons (at bottom) or one dogbone coupon (leaning on the wall having 30^{o} angle with the bottom as shown in Figure A-5).

The dogbone was not pulled or stressed before or during incubation. This was compatible with the field situation in which a support beam normally under no or a small load is being corroded by SRB. When a large load (e.g., a heavy truck on a bridge) finally comes, the beam fails. After the 3-d pre-growth, the square coupons including working electrode coupons (already in Epoxy resin) and dogbone coupons were covered with mature biofilms. They were transferred into other 450 mL anaerobic bottles with fresh culture media (200 mL) containing different levels of carbon source (0%, 10%, 50%, 100% vs. the carbon source in the standard ATCC 1249 medium as shown in Table A-2) for an additional 14-d carbon starvation incubation. Both lactate and citrate were adjusted to vary the carbon source levels in the ATCC 1249 medium although only lactate is utilized by *D. vulgaris* as a carbon source.

In this study, because the dogbone coupons were too heavy to obtain milligram weight losses accurately, small X80 coupons with 1 cm^2 exposed top surface were used for weight loss analysis. After the starvation incubation, the square coupons were cleaned with a fresh Clarke's solution to remove biofilms and corrosion products before weighing to obtain weight loss data.

After 14 d of starvation incubation, the X80 square coupons were retrieved. A scanning electron microscope (SEM) (FEI Quanta 250, Hillsboro, OR, USA) was used to observe the biofilm morphology on the square coupon surfaces and the process of SEM observation was explained in Appendix A (Cui et al., 2020). Subsequently, the same coupons were cleaned using Clarke's solution to remove biofilms and corrosion products before pit image analysis under the SEM and finally used for weight loss measurements. The live sessile SRB cells X80 square coupon with varied carbon source levels were visualized under a confocal laser scanning microscopy (CLSM, Zeiss LSM780, Germany).

A VersaSTAT 3 potentiostat from Princeton Applied Research (Oak Ridge, TN, USA) was used to measure the electrochemical responses of the X80 working electrodes for varied carbon source levels in *D. vulgaris* broths. Each glass cell contained 200 mL culture medium with varied carbon source (0%, 10%, 50%, 100%) and 250 mL headspace. It was inoculated with 2 mL SRB seed culture before the 3-d pre-growth incubation at 37^{o}C. The parameters of the electrochemical tests were listed in Appendix A.

The concentrations of H_2S and H_2 as well as total pressure in the headspace of each anaerobic bottle containing one dogbone coupon were measured as Appendix A. The sessile cell counting using a hemocytometer (Li et al., 2015), which follow the steps in the Appendix A. Each dogbone coupon was cleaned to obtain pit depth profiles

by IFM as shown in Appendix A. Finally, all the dogbone coupons after SRB incubation and a fresh X80 dogbone coupon did a tensile test to obtain a stress-strain curve, followed the illustration in Appendix A. The test matrix of carbon source starvation of a SRB elevated MIC deterioration of tensile strength and strain of X80 pipeline steel is described in Table 6-1.

Table 6-1. Test matrix for carbon source starvation of SRB elevating MIC deterioration of tensile strength and strain of X80 steel.

Parameter	Condition
Bacterium	*D. vulgaris*
Culture medium	ATCC 1249
Coupon	X80 square coupon and X80 dogbone coupon
Temperature	37°C
Incubation time	14 d
Anaerobic bottle volume	450 mL
Culture medium volume	200 mL
Carbon source levels	0%, 10%, 50%, 100%
Analysis	Weight loss, surface observation by SEM, CLSM biofilm imaging sessile cell, electrochemical measurements, gas measurement, sessile cell count, pit depth, tensile test.

6.3 Results and Discussion

6.3.1 Weight Losses Using Square Coupons

After the 14-d carbon starvation incubation, the coupon weight losses for carbon source levels of 0%, 10%, 50% and 100% were obtained. They are shown in Figure 6-1. The highest weight loss 4.4 mg cm^{-2} for 50% carbon source and lowest 1.9 mg cm^{-2} for 0% carbon source. The weight loss for 10% carbon source 3.3 mg cm^{-2} and weight loss for 100% carbon source 3.7 mg cm^{-2} were close. Note that 0% carbon source had the lowest weight loss instead of the highest. It was because the extreme starvation led to too much loss of sessile cells (Jia et al., 2019c; Xu & Gu, 2014). P-value = 0.0001, which means carbon source leads to statistically significant difference of the corrosion rate.

6.3.2 Surface and Biofilm Analyses Using Square Coupons

SEM images in Figure 6-2 depict the surface morphologies of the *D. vulgaris* biofilms under different carbon source after the 14-d carbon starvation incubation. The amounts of sessile cells on their surfaces were increasing with the increasing carbon source levels, from 0% carbon source level to 100% carbon source level as expected. The SEM images in Figure 6-3 are consistent with the weight loss findings that 50% carbon source level caused the most severe corrosion and 0% the least.

The CLSM images of X80 square coupons surface after the 14-d starvation incubation in anaerobic vials are shown in Figure 6-4. On the surface of the coupons,

the number of sessile cells can be clearly noticed to be counted that different carbon source levels were different. The number of sessile cells on the coupon surface were increasing with increasing carbon source level, which is consistent with the SEM result (Figure 6-2). A sufficient carbon source can provide more nutrition to maintain the SRB cells growth.

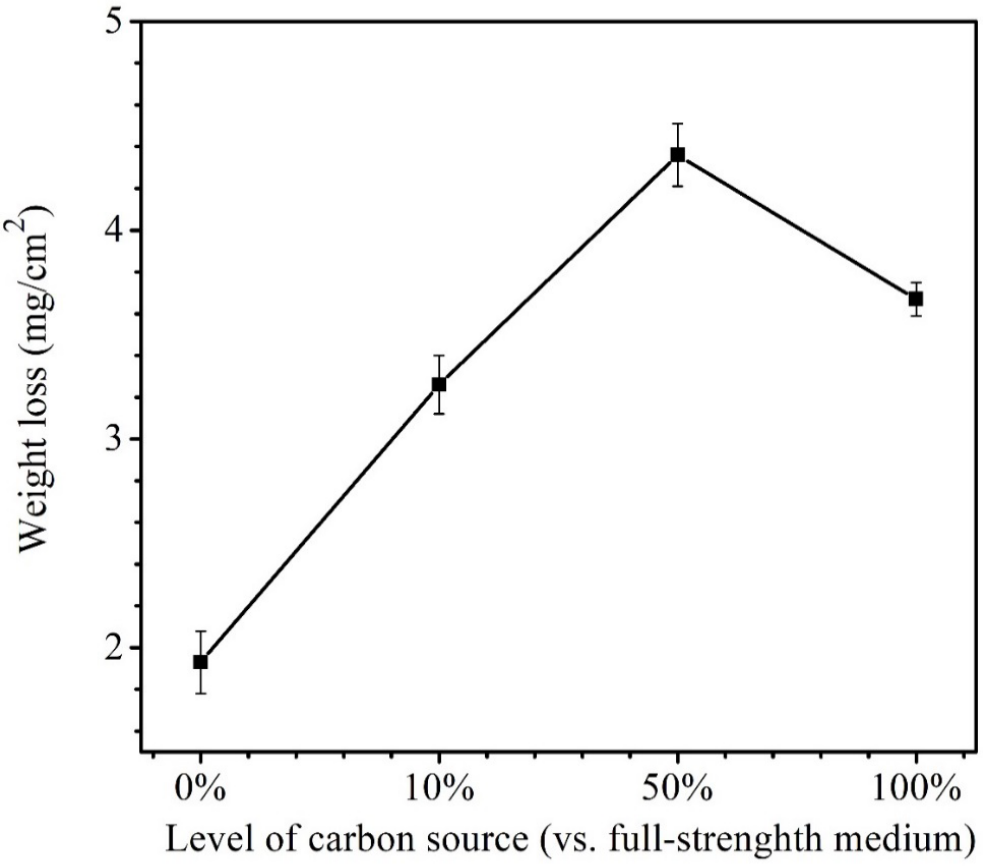

Figure 6-1. Weight losses after 14-d starvation incubation in 450 mL anaerobic bottles with varied carbon source levels. (Each error bar represents range of readings from 3 coupons in the same anaerobic bottle.)

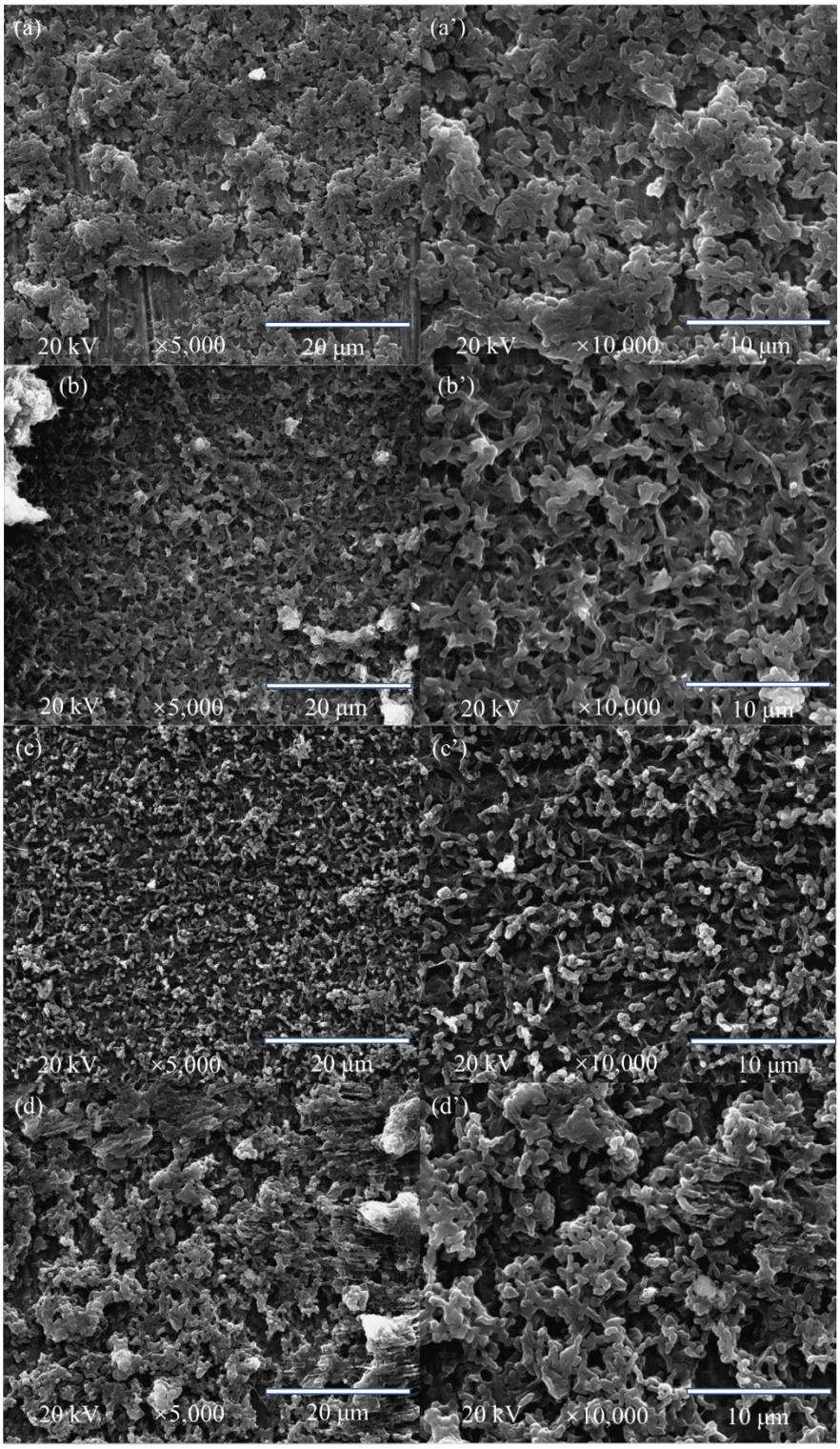

Figure 6-2. SEM of square coupon surfaces after 14-d starvation incubation in anaerobic vials with 200 mL *D. vulgaris* broth, 250 mL headspace and carbon source level of 0% (a, a'), 10% (b, b'), 50% (c, c'), and 100% (d, d').

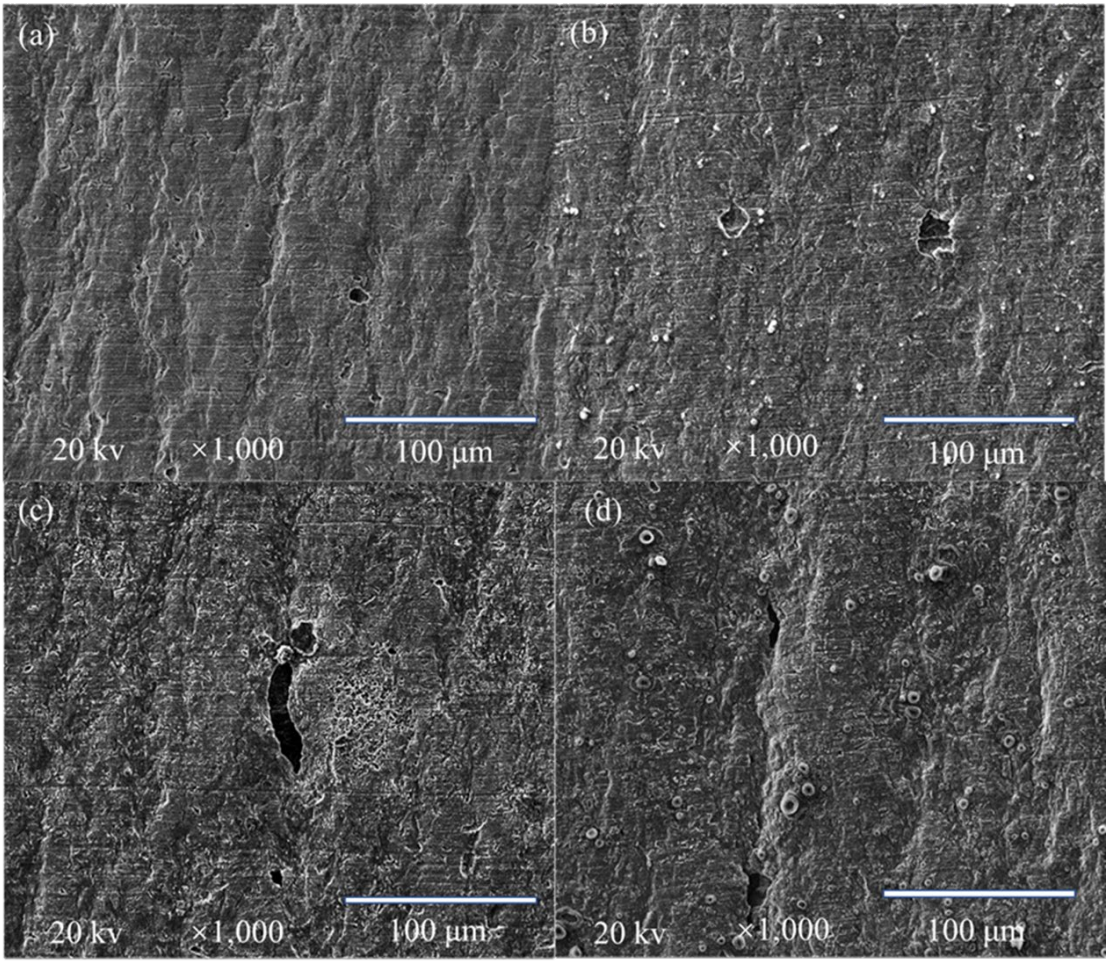

Figure 6-3. SEM images for X80 square coupons (with corrosion products removed) after 14-d starvation incubation in anaerobic vial with 200 mL *D. vulgaris* broth, 250 mL headspace and carbon source level of 0% (a), 10% (b), 50% (b), and 100% (d).

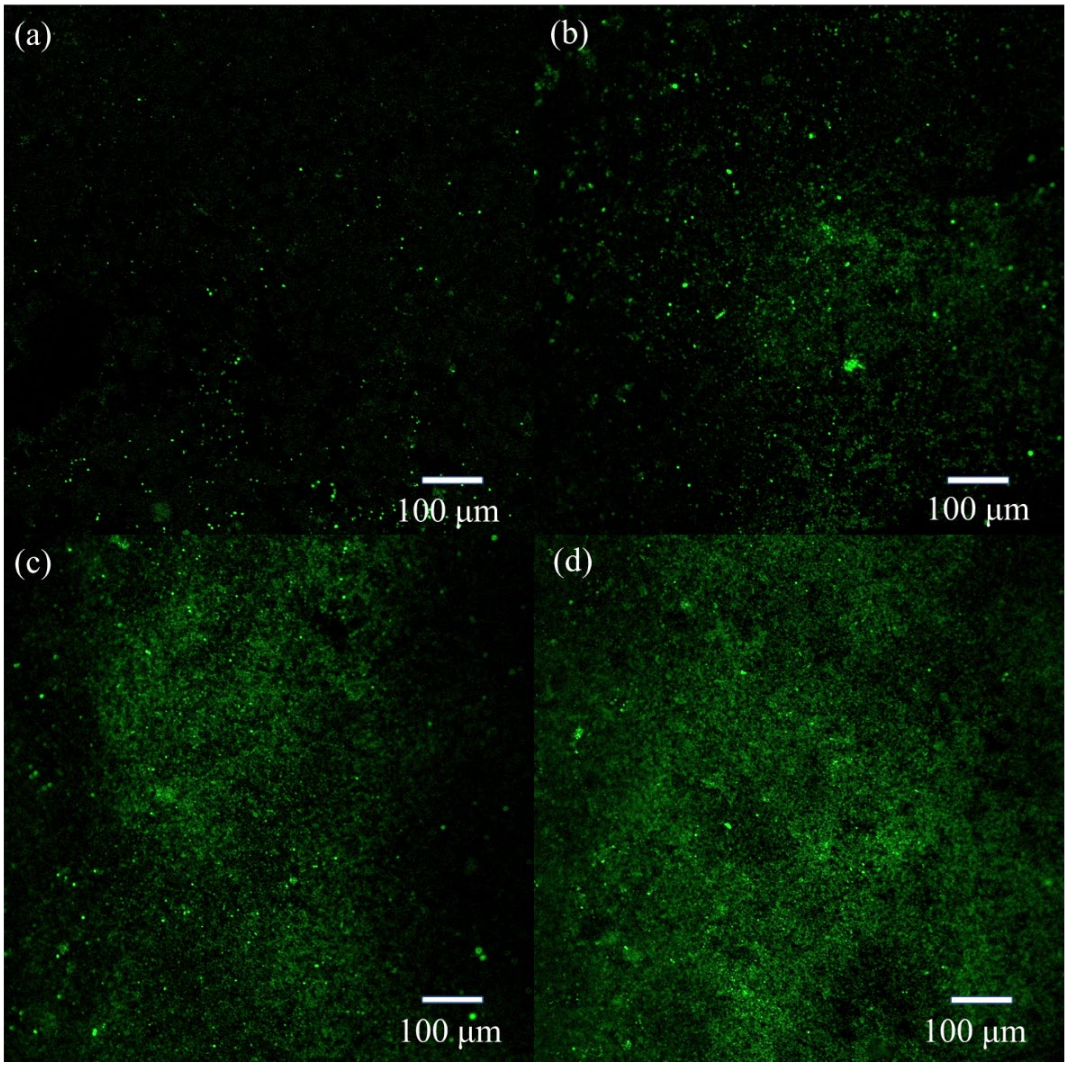

Figure 6-4. CLSM images of biofilm on X80 square coupons surface after 14-d starvation incubation in an anaerobic vial with 200 ml of *D. vulgaris* broth, 250 ml of headspace, and carbon source levels of (a) 0%, (b)10%, (c) 50%, and (d)100%.

6.3.3 Electrochemical Tests Using Square Coupons

The variations of OCP during the 14-d carbon starvation are shown in Figure 6-5. A lower OCP indicates a higher tendency for the working electrode to lose electrons (i.e., undergoing oxidation) or to be corroded. During the period, 50% carbon source

had the lowest OCP and 0% the highest, which is consistent with the weight loss trend. In MIC, sometimes, OCP trends are not always correct, because OCP only indicates a tendency without factoring in actual corrosion speed. Kinetic electrochemical data on corrosion resistance or corrosion current are more reliable (Jia et al., 2019b). In corrosion kinetics, R_p is inversely proportional to corrosion rate.

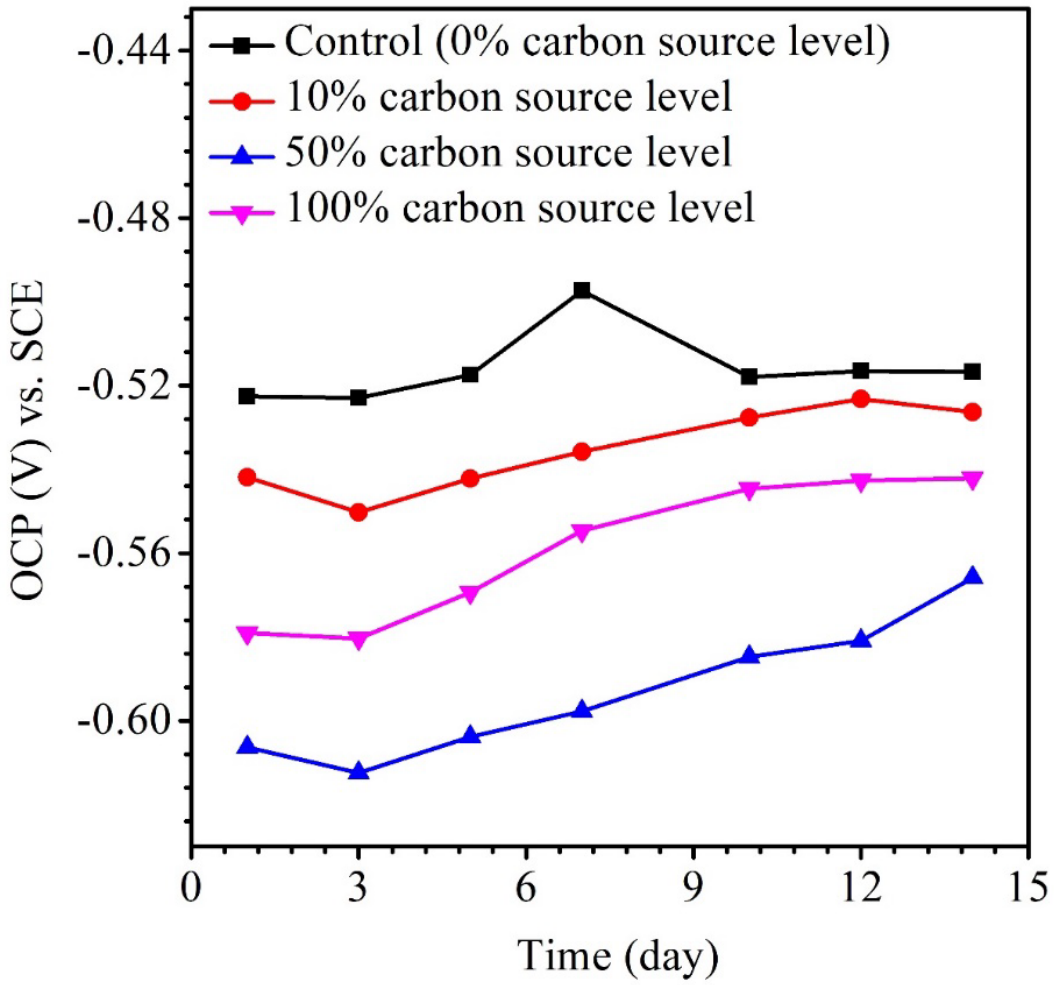

Figure 6-5. Variations of OCP vs. time for X80 during 14-d starvation incubation.

Figure 6-6 shows that the R_p for the 50% carbon source level is the lowest, corresponding to highest corrosion rate, followed by 100%, 10%, 0% carbon source levels. The $1/R_p$ here is consistent with the weight loss trend.

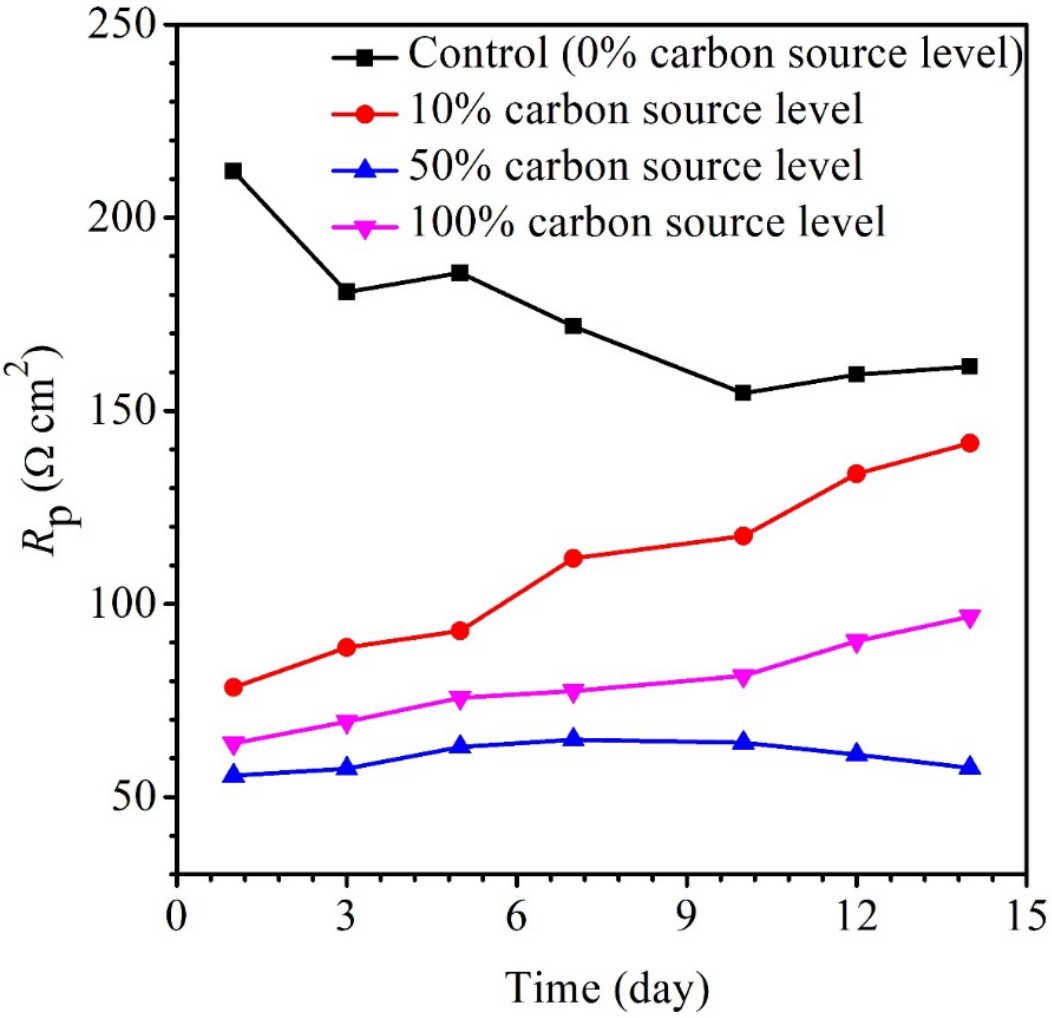

Figure 6-6. Variations of R_p vs. time for X80 during 14-d starvation incubation.

The EIS Nyquist and Bode plots of the X80 square coupons for different carbon source levels on different days during the 14-d starvation incubation are shown in

Figure 6-7. The corresponding fitted parameters are listed in Table 6-2. The Nyquist plots of the square coupons indicate a capacitive behavior and a diffusion phenomenon.

The equivalent circuit model is shown in Figure 6-8, in which Q is a constant phase element (CPE), which is derived from the following formula (Labjar et al., 2010):

$$Z_{CPE} = A^{-1}(i\omega)^{-n} \quad (6\text{-}1)$$

where A is the capacitance, and ω, i, and n are angular frequency, unit imaginary number, and CPE exponent, respectively. R_s is solution resistance, R_f and Q_f the resistance and constant-phase element of biofilm, respectively. R_{ct} is charge-transfer resistance, Q_{dl} the constant-phase element of the electric double layer, and Warburg (W) element describing the diffusion process. The presence of W in Figure 6-7 and Table 6-2 was caused by the mass transfer resistance effect exerted by biofilm and corrosion product film on the X80 working electrode (Yin et al., 2018). The impedance spectra for different carbon source levels fitted well with the two-time constant circuit model. The 50% carbon source level had the smallest diameters of the semi-circles in the Nyquist plots (Figure 6-7) and smallest value of (R_{ct} + R_b) (Table 6-2), which means that 50% carbon source level exhibited the highest corrosion rate (Jia et al., 2019c). The EIS results are consistent with LPR results (Figure 6-6), supporting weight loss trend (Figure 6-1).

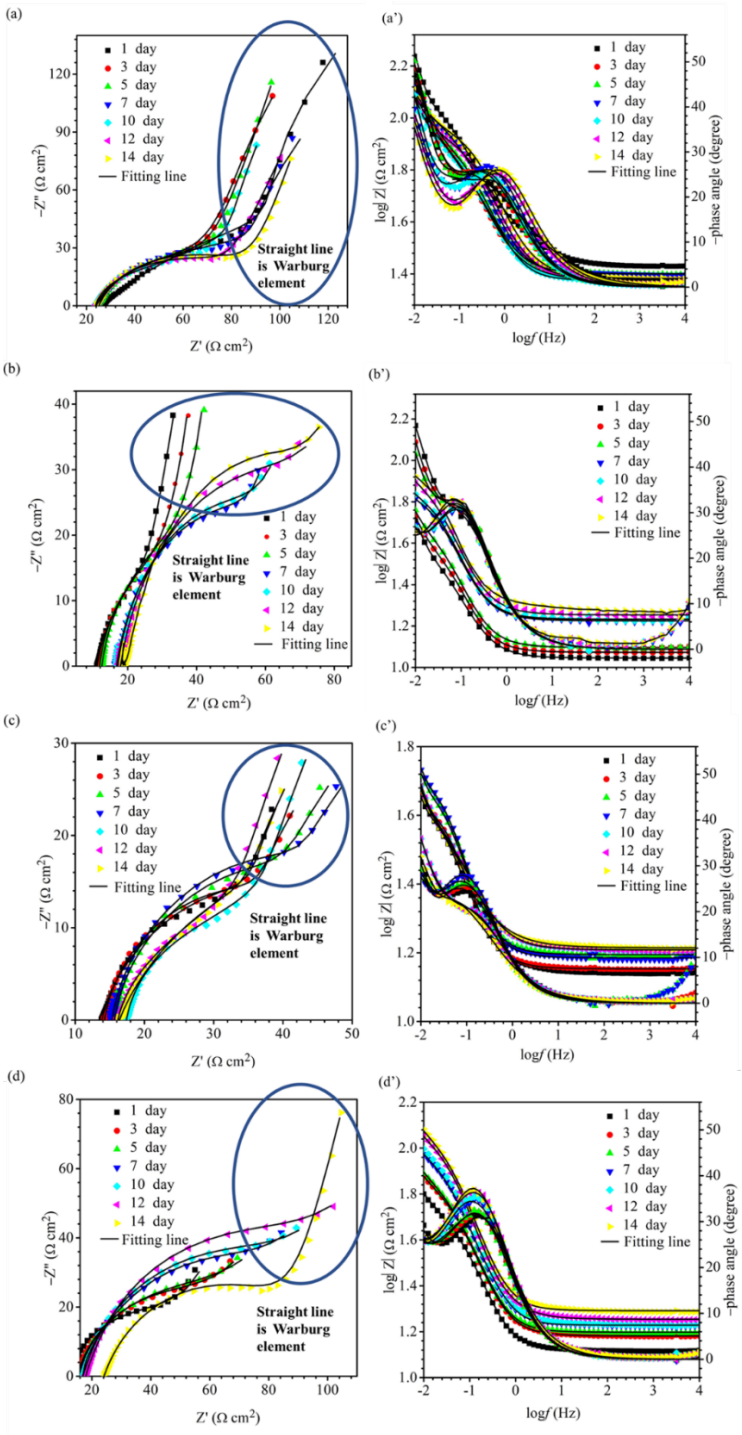

Figure 6-7. Nyquist and Bode plots for X80 during 14-d incubation in anaerobic vial with 200 mL *D. vulgaris* broth, 250 mL headspace and carbon source level of 0% (a, a'), 10% (b, b'), 50% (c, c'), 100% (d, d').

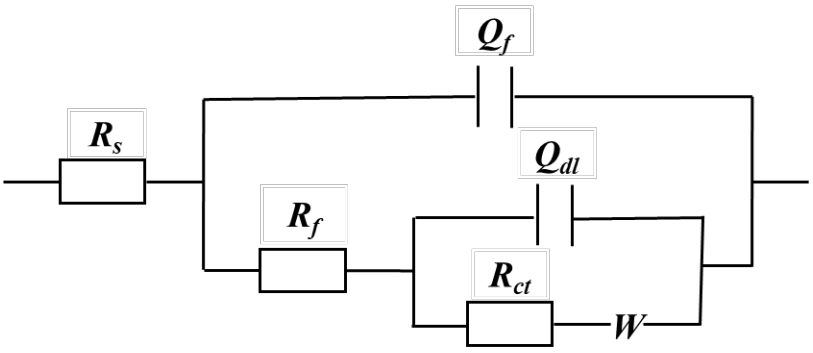

Figure 6-8. Equivalent electrical circuit model for fitting EIS data.

Table 6-2. Electrochemical parameters obtained from fitting EIS spectra.

Carbon source level	t (d)	R_s (Ω cm^2)	Q_{dl} (Ω^{-1} cm^{-2} s^n)	n_1	R_f (Ω cm^2)	Q_{dl} (Ω^{-1} cm^{-2} s^n)	n_2	R_{ct} (Ω cm^2)	*W-R* (Ω cm^2)	*W-T* (s)	*W-P*
0%	1	26.7	1.09×10^{-2}	0.63	31.2	1.03×10^{-2}	0.44	182	80.6	3.43	0.63
	3	23.8	1.61×10^{-2}	0.73	74.5	7.91×10^{-2}	0.96	110	1260	68.4	0.64
	5	25.1	1.38×10^{-2}	0.79	65.5	7.50×10^{-2}	0.90	121	309	3.51	0.35
	7	25.1	9.56×10^{-3}	0.85	44.9	3.54×10^{-2}	0.56	131	38.4	2.21	0.61
	10	23.7	1.03×10^{-2}	0.87	33.9	4.10×10^{-2}	0.63	112	76.2	4.79	0.58
	12	23.9	9.62×10^{-3}	0.78	63.5	1.01×10^{-1}	0.78	82.1	215	2.74	0.63
	14	24.1	8.41×10^{-3}	0.76	73.9	1.26×10^{-1}	0.84	79.2	145	1.01	0.71
10%	1	11.1	8.43×10^{-2}	0.83	28.8	1.51×10^{-1}	0.80	49.1	101	3.93	0.63
	3	11.2	7.82×10^{-2}	0.85	36.7	2.52×10^{-1}	0.98	53.1	148	14.4	0.43
	5	12.5	7.30×10^{-2}	0.84	44.1	2.51×10^{-1}	0.97	45.9	106	7.91	0.42
	7	16.8	6.05×10^{-2}	0.83	53.1	5.41×10^{-1}	0.95	60.6	108	8.02	0.55
	10	17.1	5.81×10^{-2}	0.84	57.7	3.77×10^{-1}	0.82	63.9	182	8.99	0.64
	12	17.9	5.21×10^{-2}	0.83	61.2	1.48×10^{-1}	0.54	76.8	198	14.2	0.62
	14	18.9	4.97×10^{-2}	0.81	68.4	1.04×10^{-1}	0.43	79.8	195	14.3	0.65
50%	1	13.9	7.20×10^{-2}	0.83	10.8	4.60×10^{-2}	0.30	45.1	56.9	11.4	0.63
	3	14.2	7.04×10^{-2}	0.88	12.2	4.60×10^{-2}	0.28	42.3	48.3	9.81	0.63
	5	15.7	6.91×10^{-2}	0.88	15.7	4.91×10^{-2}	0.30	45.7	71.9	11.2	0.62
	7	15.3	6.63×10^{-2}	0.88	17.3	4.51×10^{-2}	0.26	48.9	78.6	12.2	0.63
	10	17.4	5.57×10^{-2}	0.82	23.3	2.05×10^{-1}	0.73	35.5	63.9	4.19	0.55
	12	16.2	7.07×10^{-2}	0.78	27.3	2.92×10^{-1}	0.96	32.8	59.8	10.6	0.42
	14	16.4	8.47×10^{-2}	0.70	28.3	9.06×10^{-2}	0.52	33.5	37.8	6.03	0.66
100%	1	13.1	3.80×10^{-2}	0.90	20.5	4.19×10^{-2}	0.43	43.5	224	96.2	0.73
	3	15.2	3.56×10^{-2}	0.87	25.5	2.56×10^{-2}	0.50	44.9	241	212	0.72
	5	15.8	3.41×10^{-2}	0.89	29.3	4.15×10^{-2}	0.63	47.3	364	359	0.76
	7	16.9	2.71×10^{-2}	0.93	31.5	3.62×10^{-2}	0.83	49.1	323	415	0.70
	10	17.0	3.25×10^{-2}	0.80	37.3	3.20×10^{-3}	0.99	50.7	405	592	0.71
	12	17.9	2.74×10^{-2}	0.84	44.8	9.72×10^{-3}	0.96	51.1	376	442	0.69
	14	19.6	9.03×10^{-1}	0.90	50.8	2.74×10^{-2}	0.80	49.1	425	552	0.63

Tafel plots are shown in Figure 6-9. The potentiodynamic polarization scans use a large voltage range, which may alter the surface of a working electrode. Thus, Tafel scans are usually performed only once at the end. In this work, they were performed at the end of the 14-d starvation period after all other electrochemical measurements. The fitted Tafel parameters are listed in Table 6-3. The i_{corr} data here are consistent with the weight loss trend showing 50% carbon source having the highest value (145 μA cm^{-2}), followed by 100% carbon source (98 μA cm^{-2}), 10% carbon source (84 μA cm^{-2}) and 0% carbon source (41 μA cm^{-2}). The i_{corr} trend here is consistent with weight loss trend. This work showed that LPR, EIS and Tafel scans all confirmed weight loss trend, suggesting that electrochemical methods are valuable in MIC studies. Furthermore, weight loss only reflects cumulative corrosion outcome, but non-destructive LPR and EIS can provide transient corrosion behaviors.

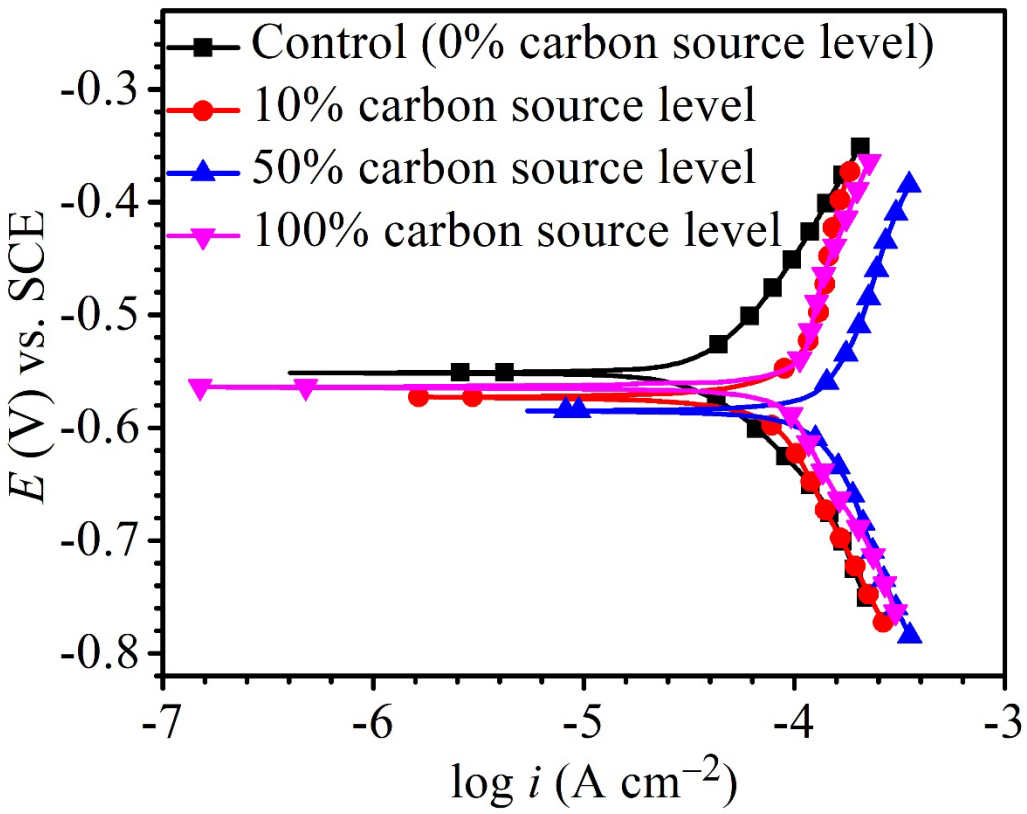

Figure 6-9. Potentiodynamic polarization curves at end of 14-d starvation incubation.

Table 6-3. Fitted electrochemical parameters from Tafel analysis.

Carbon source level	i_{corr} (μA cm^{-2})	E_{corr} (V) vs. SCE	β_a (V dec^{-1})	β_c (V dec^{-1})
0%	41	–0.56	0.294	–0.187
10%	84	–0.56	0.469	–0.348
50%	145	–0.59	0.604	–0.525
100%	98	–0.62	0.945	–0.364

Note that unlike abiotic corrosion, Tafel slopes in MIC vary a lot (Table 6-3) because the MIC system is far more complicated. This is why Tafel scan results should be used for qualitative trend analysis to support weight loss (gold standard), and they should never be used directly to calculate corrosion rate.

6.3.4 Dogbone-Bottle H_2 Concentration, H_2S Concentration, Total Pressure

Table 6-4 shows that a higher carbon source level led to a higher concentration of H_2. This H_2 trend is reasonable, because it is known that *D. vulgaris* produces H_2 during lactate oxidation, and later it consumes H_2 when there is a shortage of organic carbon (Wang et al., 2020).

$$CH_3CHOHCOO^- + H_2O \rightarrow CH_3COO^- \text{ (acetate)} + 2H_2 + CO_2 \quad (6\text{-}2)$$

$$SO_4^{2-} + 4H_2 + H^+ \rightarrow HS^- + 4H_2O \quad (6\text{-}3)$$

HS^- can absorb one proton to become H_2S or to lose one proton to become S^{2-} as shown below (Gu & Xu, 2013),

$$HS^- + H^+ \rightarrow H_2S \quad (6\text{-}4)$$

$$HS^- \rightarrow H^+ + S^{2-} \quad (6\text{-}5)$$

The H_2S data in Table 6-4 indicate that better SRB growth (as a result of a higher carbon source level) produced more H_2S from sulfate reduction. The dissolved H_2S concentrations in the liquid phases were estimated based on H_2S equilibrium at 37°C (Ning et al., 2014). [H_2S] in the culture medium data were plotted together with broth pH data at the end of the 14-d starvation incubation in Figure 6-10. Dissolved [H_2S] in culture media and broth pH after the 14-d starvation incubation in 450 mL anaerobic bottles. Figure 6-10 clearly indicates that a higher dissolved H_2S concentration corresponds to a higher pH. This contradicts conventional thinking of more H_2S in a system for more acidic liquid pH (lower pH). This is because in abiotic H_2S corrosion

testing, externally introduced H_2S acidifies the liquid phase due to H_2S dissociation, which releases protons. However, in an SRB broth, H_2S, is as a reservoir of H^+, but its H^+ originally comes from the broth itself, rather than externally introduced. Thus, it not rational to argue for acidification by biogenic H_2S in an SRB system. More H_2S in an SRB system results in higher pH, not lower.

Table 6-4. Headspace gas concentrations and total pressure as well as calculated [H_2S] after 14-d carbon starvation incubation in dogbone bottles.

Carbon source	Total pressure in headspace (bar)	H_2 concentration in headspace (10^3 ppm) (v/v)	H_2S concentration in headspace (10^3 ppm) (v/v)	Dissolved [H_2S] in broth (10^{-4} M)
0%	1.03	0.75	4.08	3.10
10%	1.07	1.16	5.08	4.01
50%	1.16	1.95	9.00	7.66
100%	1.55	2.50	12.6	14.4

It is known that sulfate respiration does not normally change scalar and vectorial protons (Peck, 1993). On the contrary, better SRB growth allows more H_2S to escape to the headspace, thus taking away more protons from the broth. This is why Figure 6-10 shows higher carbon source level led to higher broth pH (7.38 for 100% carbon source, 7.31 for 50% carbon source, 7.23 for 10% carbon source, and 7.11 for 0% carbon source). In fact, SRB are used to increase acid mine drainage's pH for exactly the same reason as demonstrated here (Bai et al., 2013). The above 7.00 pH values in

Figure 6-10 also suggest that acid attack and H_2S attached were not important contributors to the EET-MIC in this work (Wang et al., 2020).

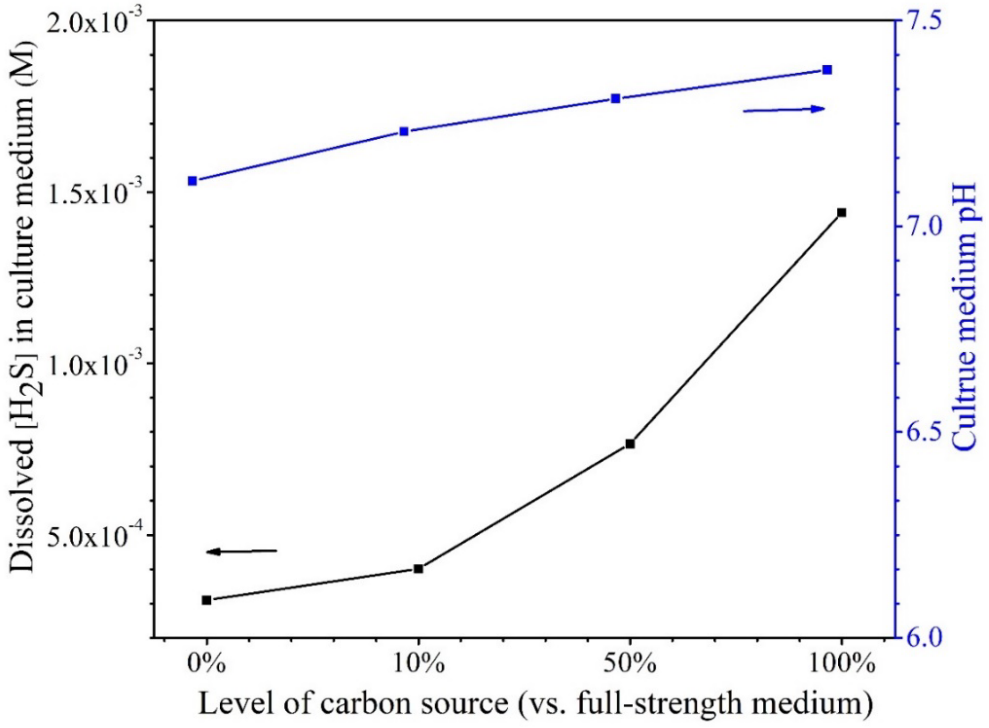

Figure 6-10. Dissolved [H_2S] in culture medium and broth pH after 14-d starvation incubation in 450 mL anaerobic bottles.

6.3.5 Sessile Cell Counts on Dogbone Coupons

After the 14-d starvation incubation, the sessile cell count was found to be higher for a larger carbon source level as expected (Figure 6-11). The cell counts on dogbone coupons in the bottles with the carbon source levels of 0%, 10%, 50% and 100% were 8.1×10^6, 3.2×10^7, 8.3×10^7 and 1.3×10^8 cells cm^{-2}, respectively. The 0% carbon source bottle had the lowest sessile cell count due to extreme starvation (Jia et al., 2019c). The

sessile cell counts on X80 dogbone coupons here are consistent with the SEM biofilm images on the X80 square coupons above.

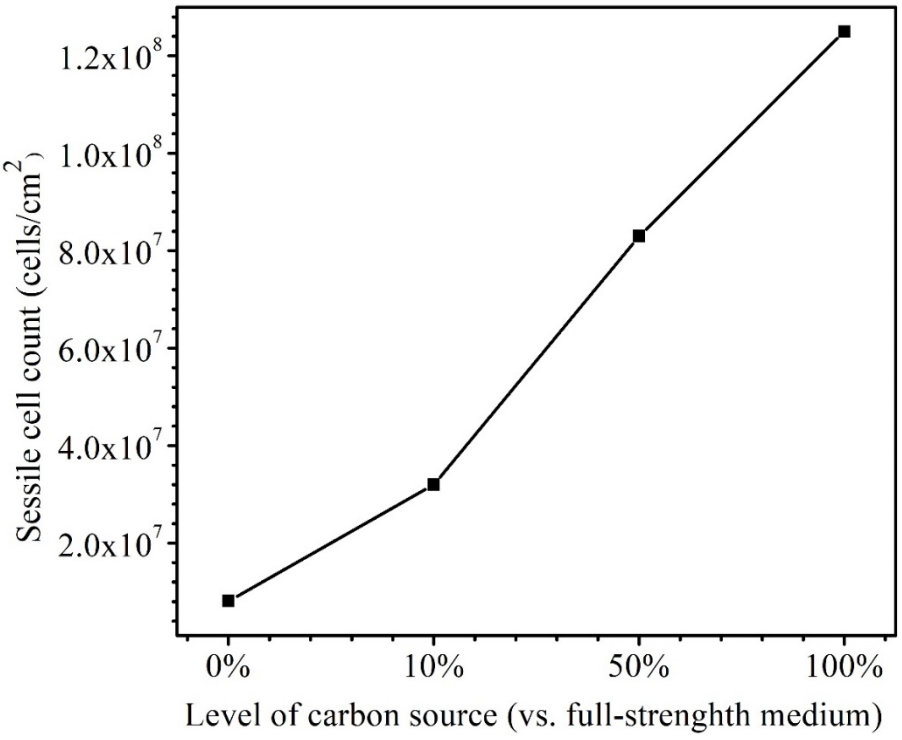

Figure 6-11. Sessile cell counts on dogbone coupons after 14-d starvation incubation in 450 mL anaerobic bottles with varied carbon source levels.

6.3.6 Pit Depths on Dogbone Coupons

Morphologies of MIC pits on the dogbone coupons after the 14-d carbon starvation incubation with biofilms and corrosion products removed were examined under IFM before tensile testing (Figure 6-12). The maximum pit depth was the highest for 50% caron source (9.1 μm) followed by 100% carbon source (6.4 μm), 10% carbon source

(4.9 µm) and 0% carbon source (1.9 µm). The pit depth trend here is consistent with the weight loss trend.

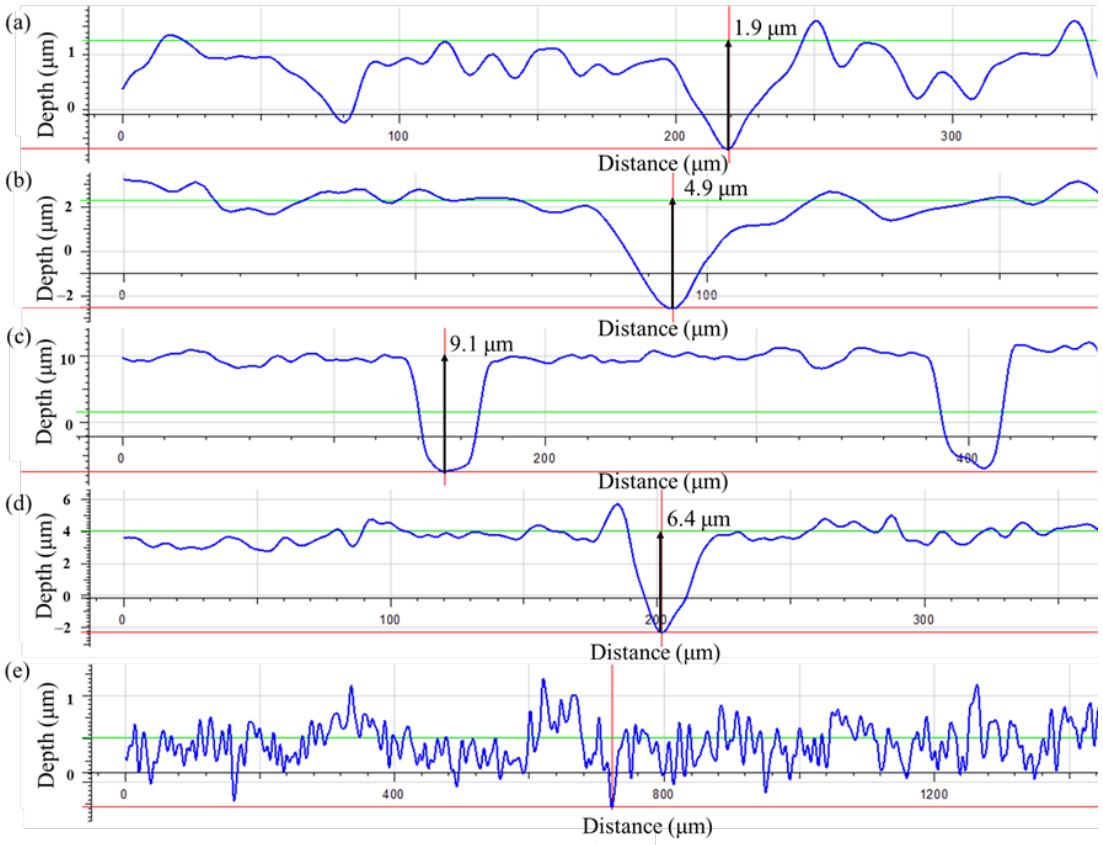

Figure 6-12. Representative pit depth profiles for dogbone coupons after 14-d starvation incubation with carbon source level of: (a) 0%, (b) 10%, (c) 50%, (d) 100%, and with (e) fresh dogbone (control).

6.3.7 Tensile Testing Using Dogbone Coupons

Figure 6-13 shows the stress-strain curves of dogbone coupons after the 14-d starvation incubation. Compared with the fresh X80 dogbone's ultimate strength of 879

MPa, all the biotic dogbone coupons had lower ultimate tensile strength and ultimate tensile strain. Table 6-5 shows a summary. It indicates that the trend of the degradation of ultimate tensile strain followed the trend of MIC severity (in terms of weight loss and pit depth) followed the following sequence (more to less): 50%, 100%, 10%, 0% carbon source levels. The degradation of ultimate strength followed the same general trend (but with 10% and 0% having practically the same value). A lower ultimate tensile strain means a less ductile metal. Thus, the tensile strain data indicated that SRB MIC made X80 more brittle in addition to weakening its mechanical strength.

The 50% carbon source led to the highest reductions in both ultimate tensile strength (22% loss) and ultimate tensile strain (23% loss) compared with the fresh dogbone data. In this work, 50% carbon source caused the biggest MIC damages in terms of weight loss and pitting depth. As a result, it led to the most severe degradation of X80 mechanical properties. This trend could not be attributed to H_2 or H_2S because 50% carbon source did not have the highest H_2 or H_2S level. In abiotic H_2S studies, externally introduced H_2S acidifies a liquid, which causes corrosion. But it was not the case in this study with biogenic H_2S production, which does not acidity the liquid phase. Thus, it was not surprising that the highest dissolved H_2S concentration (100% carbon source) did not result in the highest losses of ultimate strength and ultimate tensile strain.

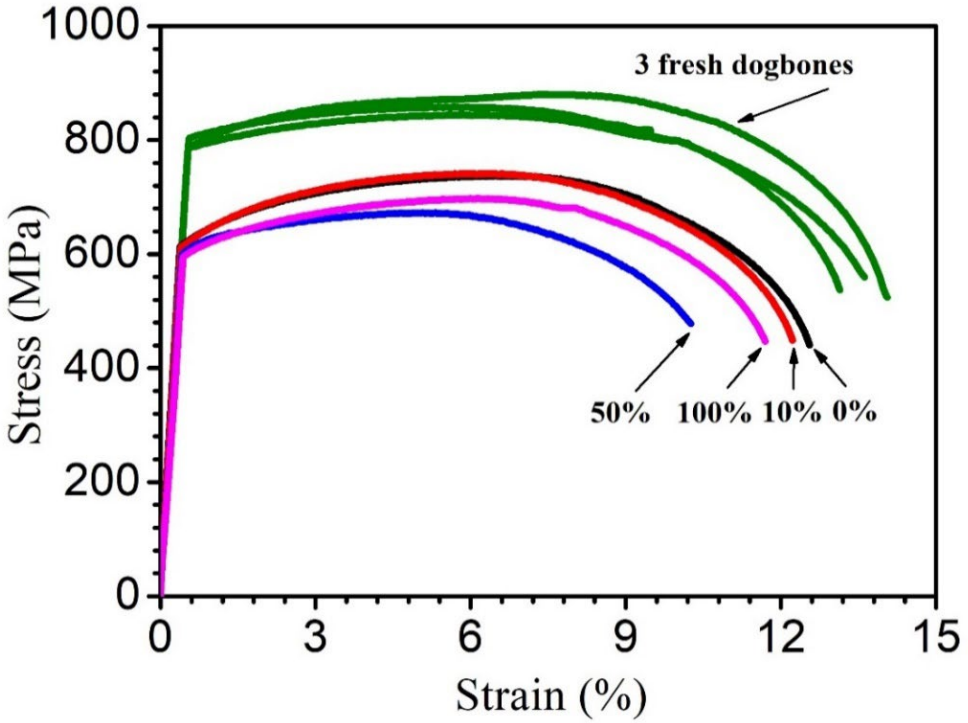

Figure 6-13. Stress–strain curves for 3 fresh X80 dogbone coupons (3 replicates) and dogbone coupons (with corrosion products removed) after 14-d starvation incubation in 450 mL anaerobic with varied carbon source levels. (The topmost fresh dogbone curve's data were from Li et al., 2021).

Table 6-5. Ultimate tensile strength and ultimate tensile strain data.

Carbon source level	Ultimate tensile strength (MPa) (and loss)	Ultimate tensile strain (%) (and loss)
(No immersion)	860 ± 17.6 (control)	13.6% ± 0.5% (control)
0%	736 (14% loss)	12.7% (7% loss)
10%	741 (14% loss)	12.2% (10% loss)
50%	672 (22% loss)	10.3% (24% loss)
100%	697 (19% loss)	11.7% (14% loss)

6.4 Conclusions

The weight loss data using square coupons indicated that 50% carbon source level resulted in the highest weight loss. This was because 50% carbon had the combination of carbon starvation without suffering too much sessile cell loss. The weight loss trend was supported by the pit depth trend. The electrochemical results, including LPR, EIS and Tafel scans all supported the weight loss trend, confirming that 50% carbon source level caused the most severe MIC. The SEM biofilm results agreed with the sessile cell count trend. The H_2S, H_2 and sessile cell count data for dogbone coupons were consistent in supporting higher carbon source levels for better growth exhibiting higher biogenic H_2S and H_2 concentrations. The tensile test results for the biotic coupons and the fresh X80 dogbone showed that more severe MIC led to larger degradations of ultimate tensile strain and ultimate tensile strength. The 50% carbon source led to the highest reductions in both ultimate tensile strength (22% loss vs. fresh dogbone) and ultimate tensile strain (23% loss). A higher dissolved H_2S concentration at non-acidic pH in this work did not result in higher losses in ultimate strength and ultimate tensile strain, because it did not provide higher weight loss and pit depth.

Chapter 7: Mechanical Property Degradation of X80 Pipeline Steel Due to MIC by *D. vulgaris*

7.1 Introduction

It has been known that in carbon steel MIC by SRB, a larger headspace allows more H_2S to escape from the broth. This reduces the H_2S cytotoxicity in the broth, allowing better planktonic and sessile SRB growth, and thus leading to more severe MIC (Jia et al., 2019b). However, the effect of headspace on MIC deterioration of tensile strength and strain of steel was unclear. Therefore, this work investigated the effects of SRB sessile cell growth on MIC and the subsequent mechanical property degradation of X80 pipeline steel.

7.2 Materials and Methods

The composition of X80 carbon steel, X80 square coupon dimensions and X80 dogbone coupon dimensions are listed in Appendix A. Three square coupons, each with a 1 cm^2 unpainted top surface (all other surfaces were covered with a polytetrafluoroethylene paint), were incubated in 450 mL anaerobic bottles containing 150 mL deoxygenated culture medium (fixed) with either 150 mL, 200 mL or 300 mL headspace (adjusted using inert glass beads or Epoxy blocks), respectively. A 2 mL 3-d old SRB seed culture was used to inoculate each biotic bottle before incubation in ATCC 1249 culture medium at 37ºC without shaking.

*This chapter was previously published in Frontiers in Bioengineering and Biotechnology (Z. Li et al., 2022). Copyright permission is not required by the journal.

D. vulgaris (ATCC 7757), a common pure SRB strain in MIC research, was selected for this research. The culture medium was ATCC 1249 medium, which is a modified Baar's medium for sulfate reducers. The culture medium preparation procedure followed the procedure in Appendix A (Dou et al., 2019).

In this research, square coupons (1 cm^2 exposed surface) were also used as working electrodes in electrochemical glass cells. Dogbone coupons were immersed in anaerobic bottles with 150 mL culture medium and varied headspace volumes (150 mL, 200 mL and 300 mL), and each anaerobic bottle contained one dogbone coupon. The headspace variation was achieved using Epoxy resin as space filler because the bottle volume and liquid culture medium volume were the same, but the headspace volume varied.

After the 14-d incubation, the X80 square coupons were retrieved. A scanning electron microscope (SEM) (FEI Quanta 250, Hillsboro, OR, USA) was used to observe the biofilm morphology on the square coupon surfaces and the process of SEM observation was explained in Appendix A (Cui et al., 2020). The live sessile SRB cells X80 square coupon with varied headspace volumes were observed by confocal laser scanning microscopy (CLSM, Zeiss LSM780, Germany).

The square coupons for weight loss data were obtained by the steps which is shown in Appendix A. The electrochemical work of X80 square coupons was tested by A potentiostat (Model VersaSTAT 3, Princeton Applied Research, Oak Ridge, TN, USA).

Each glass cell contained 150 mL deoxygenated culture medium (fixed) with either 150 mL, 200 mL or 300 mL headspace (adjusted using Epoxy resin as space filler). Each bottle was inoculated with 2 mL 3-d old SRB seed culture for static incubation at 37^{o}C.The abiotic control glass cell had 150 mL culture medium and 300 mL headspace without SRB inoculation. There was no need to vary the headspace for the abiotic control because there was no biogenic H_2S escape to the headspace. The electrochemical parameters for scans were listed in Appendix A.

The headspace concentration of H_2S, H_2, and total pressure in different anaerobic bottles were measured using a portable H_2S sensor as shown in Appendix A (Wang et al., 2020). Sessile cells on a coupon were counted using a hemocytometer under a 400X microscope as described in Appendix A (Wang et al., 2020).

The biofilms and corrosion products on the coupon surfaces were removed using a fresh Clarke's solution according to ASTM G1–03. After the removal, the maximum pit depth for each dogbone coupon was obtained under an IFM machine, which is shown in Appendix A. After the pit depth analysis, tensile tests were performed on an electromechanical universal testing machine on the same dogbone coupons, which followed the parameter described in Appendix A.

Table 7-1. Test matrix for X80 mechanical property degradation by *D. vulgaris.*

Parameter	Condition
Bacterium	*D. vulgaris*
Culture medium	ATCC 1249
Coupon	X80 square coupon and X80 dogbone coupon
Temperature	37°C
Incubation time	14 d
Culture medium volumes	200 mL
Headspace volume	150 mL, 200 mL, 300 mL
Analysis	SEM and CLSM biofilm imaging, weight loss, electrochemical measurements, gas measurement, sessile cell count, pit depth, tensile test.

7.3 Results and Discussion

7.3.1 Surface and Biofilm Analyses Using Square Coupons

The SEM biofilm images in Figure 7-1 show the surface morphologies of the *D. vulgaris* biofilms for different headspace volumes after the 14-d incubation. The short rod shape is typical for *D. vulgaris,* consistent with SEM images in other studies (Unsal et al., 2022; Wang et al., 2022a). Figure 7-1 indicates that the number of sessile cells increased with increasing headspace volume. This qualitative information is consistent with quantitative sessile cell count data on dogbone coupons discussed below. A larger headspace led to less H_2S cytotoxicity in the broth and thus better SRB growth (Jia et al., 2019b).

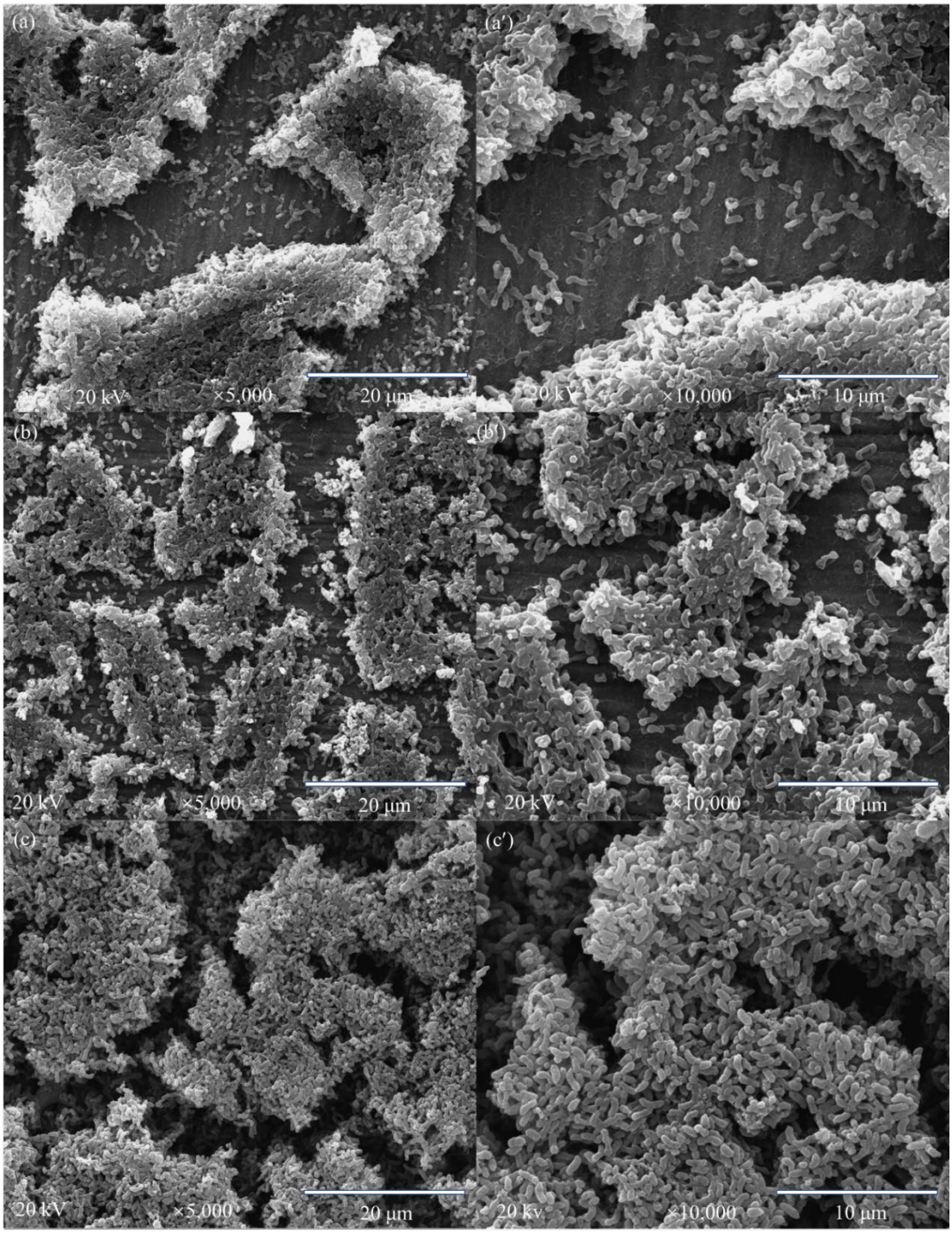

Figure 7-1. SEM biofilm images of X80 square coupon in 150 mL SRB broth with varied headspace volume after 14-d incubation: (A, A') with 150 mL headspace at two magnifications, (B, B') with 200 mL headspace, and (C, C') with 300 mL headspace.

The CLSM images of X80 square coupons surface after 14 d with varied headspace volume are shown in Figure 7-2. The number of sessile cells present on the surface of the coupons can be clearly seen to be counted that various headspace volume. The findings of the SEM (Figure 7-1) are consistent with the observation that an increased headspace volume leads to an increase in the number of sessile cells seen on the coupon surface (Figure 7-2). Larger headspace results in less dissolved H_2S (less toxicity) can provide more moderate circumstance for SRB cells growth (growth much better).

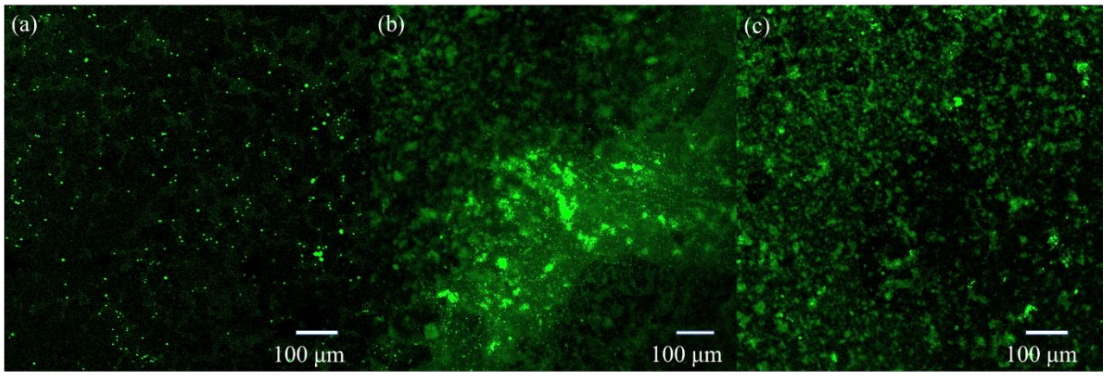

Figure 7-2. CLSM images of biofilm on X80 square coupons surface after 14-d incubation in with fixed 150 ml of *D. vulgaris* broth with varied headspace volume: (a) 150 mL headspace, (b) 200 mL headspace, and (c) 300 mL headspace.

7.3.2 Weight Losses Using Square Coupons

The weight losses for 150 mL, 200 mL and 300 headspace volumes were 1.7 ± 0.17 mg cm^{-2}, 1.9 ± 0.33 mg cm^{-2} and 2.3 ± 0.37 mg cm^{-2}, respectively (Figure 7-3).

Although the neighboring weight loss data were close with fairly wide error bars as a result of the short-term test, the 150 mL and 300 mL weight losses still had a p-value < 0.05, indicating that the weight increased with statistical significance when the headspace volume increased from 150 to 300 mL. These weight losses after SRB incubation were much larger than the 0.2 ± 0.05 mg cm^{-2} abiotic carbon steel weight loss obtained after 14 d of incubation in the deoxygenated ATCC 1249 culture medium without SRB inoculation. The increasing SRB MIC weight loss trend corresponds to the increasing sessile cell trend observed in Figure 7-1 and Figure 7-2, which is consistent with EET-MIC, in which more sessile cells harvest more electrons from elemental iron, leading to more severe corrosion (Jia et al., 2018a).

7.3.3 Electrochemical Tests Using Square Coupons

The OCP trends for different headspace volumes during the 14-d incubation of X80 electrode in the SRB culture medium are shown in Figure 7-4. A lower OCP indicates a higher tendency for the working electrode to lose electrons. Figure 7-4 does not consistently indicate that a higher headspace volume had a lower OCP. This is not surprising for complicated SRB systems (Thuy et al., 2020). After all, OCP only indicates corrosion tendency, but the actual corrosion outcome relies on corrosion kinetics. The same observation was made previously in a study on biogenic H_2S impact on carbon steel MIC by *D. vulgaris* in ATCC 1249 culture medium which included abiotic OCP (Jia et al., 2018a).

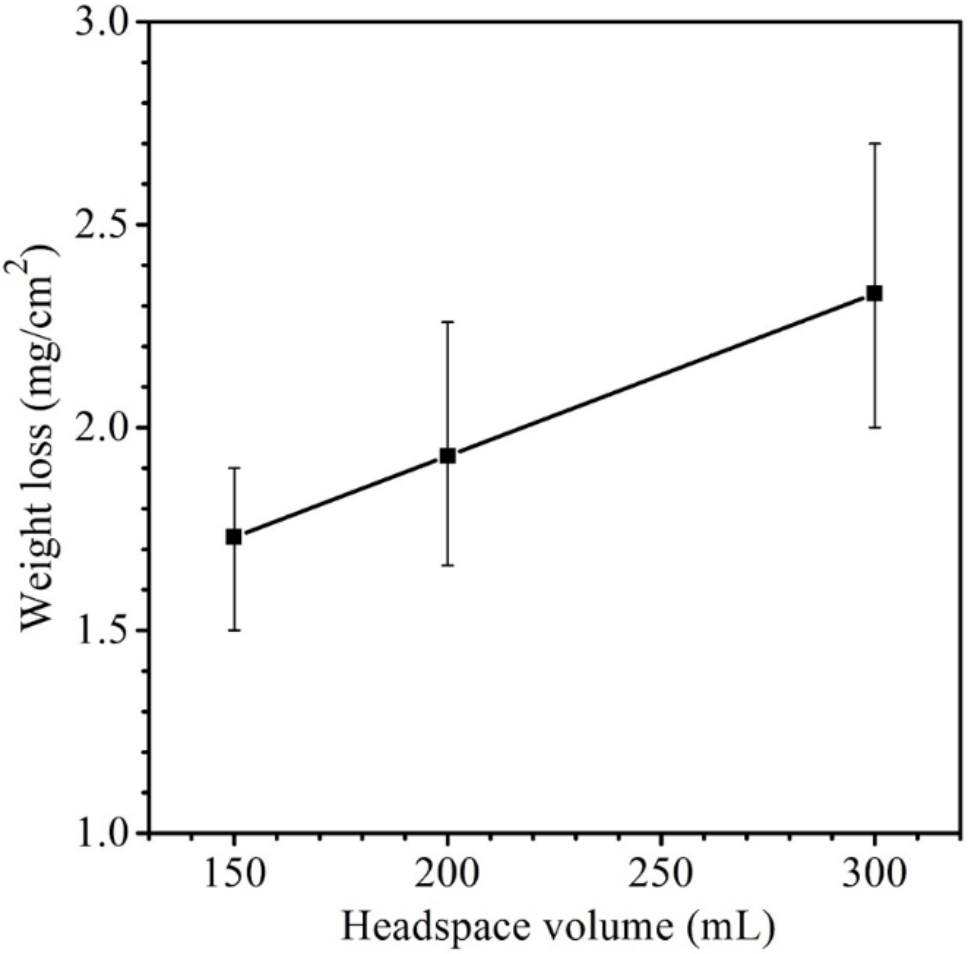

Figure 7-3. Weight losses of X80 in 150 mL SRB broth with varied headspace volume after 14-d incubation. (Each error bar represents standard deviation from 3 coupons in the same anaerobic bottle.)

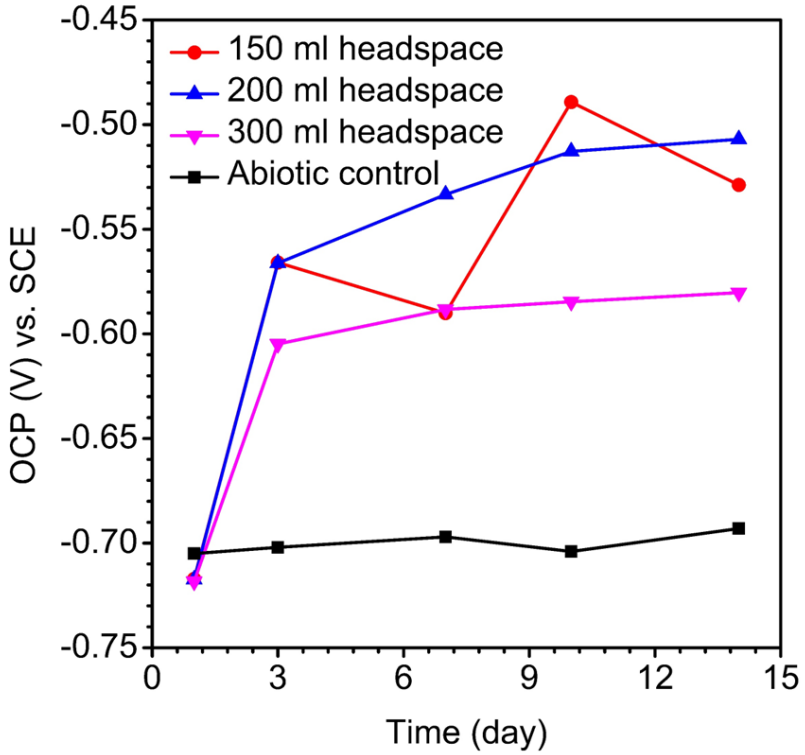

Figure 7-4. Variations of OCP vs. time for X80 in abiotic culture medium and in 150 mL SRB broth during 14-d incubation with headspace volumes of 150 mL, 200 mL and 300 mL (fixed 150 mL broth volume).

Polarization resistance (R_p, corrosion kinetics during the 14-d incubation) is inversely proportional to corrosion rate (Cai et al., 2022). Figure 7-5 shows a large drop of R_p in the first 3 d, suggesting that as biofilm established on the metal surface, corrosion rate increased. The abiotic R_p curve for X80 in the deoxygenated ATCC 1249 culture medium remained around 17~18 kΩ cm^2, much higher than the biotic R_p curves. Figure 7-5 also shows that R_p for the 300 mL headspace was the lowest, and R_p for 150

mL was the highest, indicating highest and lowest corrosion rate, respectively, which is consistent with weight loss data trend in Figure 7-3 from LPR scans in Figure 7-5 describes the transient.

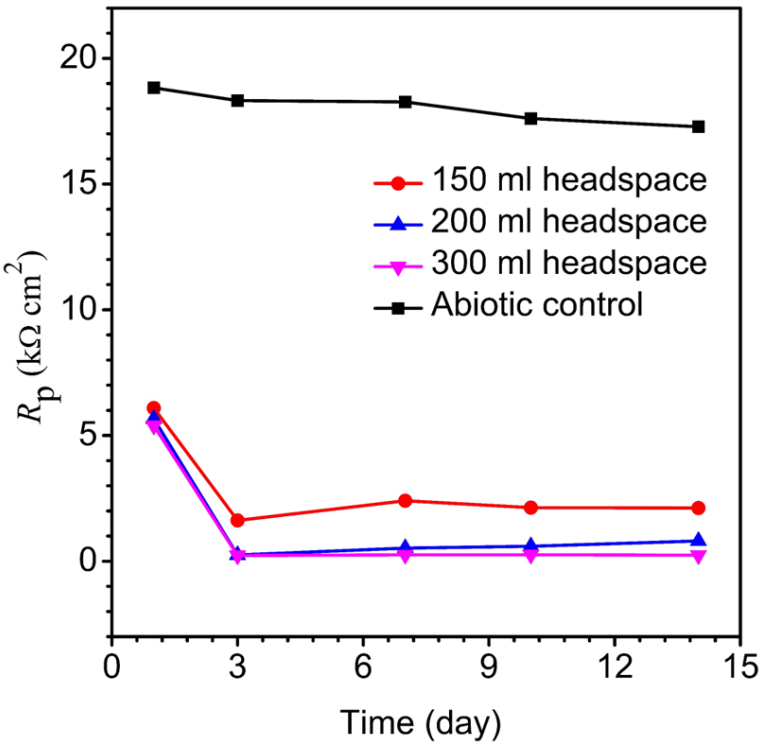

Figure 7-5. Variations of R_p vs. time for X80 in abiotic culture medium and in 150 mL SRB broth during 14-d incubation with headspace volumes of 150 mL, 200 mL and 300 mL (fixed 150 mL broth volume).

For EIS, the Nyquist and Bode plots of the abiotic and the biotic X80 coupons for different immersion times and different headspace volumes are shown in Figure 7-6. The abiotic EIS data in the deoxygenated ATCC 1249 culture medium shown the same

trend as the abiotic R_p trend. The Nyquist plots indicate capacitive behavior. A larger diameter of the semi-circle in the Nyquist plot means a higher corrosion resistance in Figure 7-6(A). The EIS data in Figure 7-6 was fitted with the equivalent electrical circuits in Figure 7-7. A simple one-time constant circuit was needed for the abiotic control EIS spectra, while the biotic EIS spectra required a two-time constant circuit. The fitted parameters are summarized in Table 7-2. The biotic impedance spectra for the three different headspace volumes (150 mL, 200 mL and 300 mL) fitted well with a two-time constant circuit model. The capacitors in the circuit model were not ideal capacitors. Thus, constant phase elements (CPE_s) were used instead with n values in Table 7-2 indicating how close the CPEs (constant phase elements) were to capacitors (n = 1). The biotic equivalent circuit in Figure 7-7 (b) contains: (1) solution resistance (R_s), (2) a parallel combination of charge transfer resistance (R_{ct}) and CPE_1 (Q_{dl}) associated with the metal surface electric double layer, (3) a parallel combination of biofilm resistance (R_f) and CPE_2 (Q_f) associated with the biofilm/corrosion product layer on the X80 steel surface. The abiotic equivalent circuit in Figure 7-7 (a) is simpler without R_f and Q_f.

Compared with charge transfer resistance (R_{ct}) values, the film resistance R_f values were quite small. However, the R_f values became larger with the increasing headspace volume due to *D. vulgaris* becoming more corrosive, which is consistent with the increased sessile cell count (Figure 7-1 and Figure 7-2). R_{ct} was rate limiting in this

study because it was much larger than R_s and R_f. (R_{ct} + R_f) is often used as the equivalent to R_p in qualitative corrosion analysis. In this work, (R_{ct} + R_f) was the smallest for 300 mL headspace in Table 7-2, indicating the highest corrosion rate.

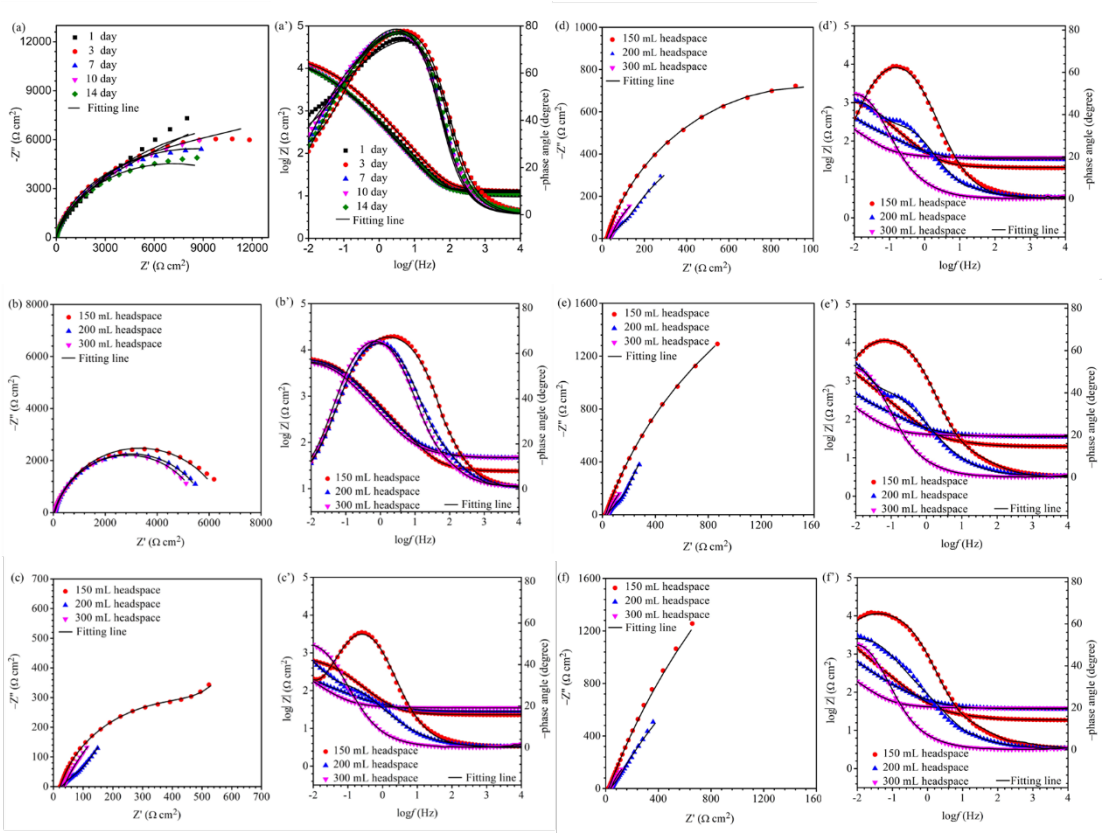

Figure 7-6. Nyquist and Bode plots for X80 in SRB broth during 14-d incubation with fixed 150 mL broth with varied headspace volume: (a, a') abiotic control, (b, b') 1st day biotic, (c, c') 3rd day biotic, (d, d') 7th day biotic, (e, e') 10th day biotic, and (f, f') 14th day biotic EIS spectra.

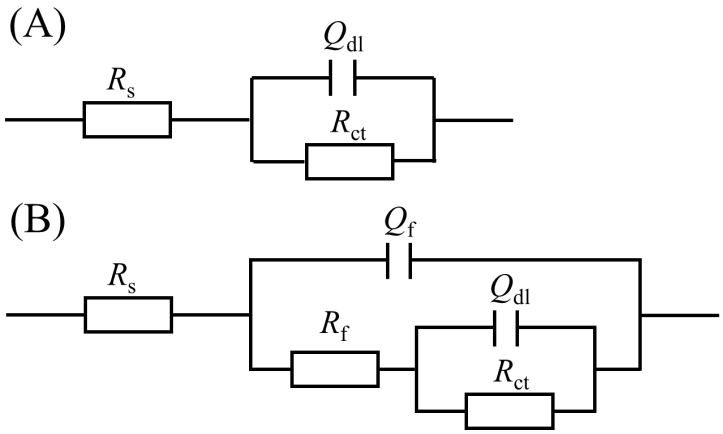

Figure 7-7. Equivalent electric circuits to model abiotic (A) and biotic (B) EIS spectra.

Table 7-2. Electrochemical parameters obtained from fitting EIS spectra.

Head-space (mL)	t (d)	R_s (Ω cm^2)	Q_f ($\times10^{-3}$ Ω^{-1} cm^{-2} s^n)	n_f	R_f (Ω cm^2)	Q_{dl} ($\times10^{-3}$ Ω^{-1} cm^{-2} s^n)	n_{dl}	R_{ct} (kΩ cm^2)	x^2 (10^{-3})
Abiotic	1	11				0.426	0.82	17.7	3.10
	3	13				0.243	0.87	16.8	1.35
	7	13				0.407	0.87	16.2	4.06
	10	12				4.17	0.88	15.7	3.24
	14	13				3.81	0.88	15.3	2.91
150	1	24	0.141	0.89	4	1.01	0.71	6.78	0.61
	3	20	4.76	0.78	11	1.14	0.97	1.91	2.32
	7	18	5.11	0.74	12	3.24	0.87	5.76	3.38
	10	19	5.24	0.73	12	2.07	0.97	9.87	7.92
	14	24	4.03	0.78	7	6.13	0.88	9.98	5.31
200	1	47	0.101	0.88	41	1.47	0.80	5.88	4.85
	3	28	1.51	0.63	121	2.40	0.68	2.21	0.43
	7	34	7.62	0.72	180	11.3	0.71	1.32	5.29
	10	36	8.07	0.68	259	9.11	0.76	4.87	4.49
	14	37	7.04	0.64	129	2.93	0.75	5.63	2.47
300	1	47	0.183	0.85	39	1.85	0.84	5.63	0.39
	3	35	4.51	0.74	152	2.36	0.93	0.94	2.29
	7	37	3.80	0.75	115	6.38	0.92	0.86	1.89
	10	37	3.73	0.74	88	7.43	0.98	1.16	10.4
	14	38	3.31	0.76	17	14.1	0.80	0.96	8.17

The Tafel plots of X80 are shown in Figure 7-8. The corrosion current densities from the Tafel analysis of the potentiodynamic polarization curves are listed in Table 7-3. After the 14-d SRB incubation, the coupon for the 300 mL headspace had the highest corrosion current density (i_{corr}) of 74.8 μA cm^{-2} (Table 7-3), compared to 19.1 μA cm^{-2} (for 200 mL) and 4.8 μA cm^{-2} (for 150 mL). The abiotic i_{corr} in the deoxygenated ATCC 1249 culture medium was 0.79 μA cm^{-2}, which was negligibly small. The corrosion current density trend here corroborates the R_p^{-1} trend in Figure 7-5 and $(R_{ct} + R_f)^{-1}$ trend in Table 7-2. Thus, all the electrochemical corrosion data trends, with the exception of OCP, are consistent with the weight loss trend, all pointing to more sessile cells for faster MIC, which is characteristic of EET-MIC.

Table 7-3. Fitted electrochemical parameters from Tafel analysis at the end of 14-d incubation.

Headspace (mL)	i_{corr} (μA cm^{-2})	E_{corr} (V) vs. SCE	β_a (V dec^{-1})	β_c (V dec^{-1})
Abiotic	0.8	–0.74	0.125	–0.675
150	4.8	–0.55	0.314	–0.299
200	19.1	–0.52	0.328	–0.322
300	74.8	–0.59	0.387	–0.279

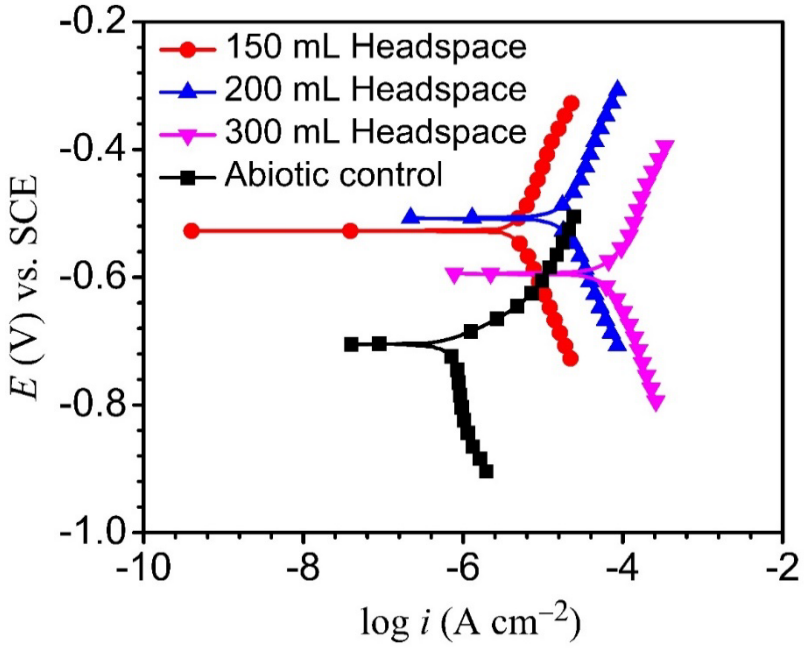

Figure 7-8. Potentiodynamic polarization curves at end of 14-d incubation with SRB, and without SRB (abiotic control).

7.3.4 H_2S Concentration and Total Gas Pressure in Headspace

Table 7-4 shows that the H_2S concentrations in the headspace gas phases for the anaerobic bottles (each containing one dogbone coupon) with headspace volumes of 150 mL, 200 mL and 300 mL were 8.50 $\times 10^3$ ppm (v/v), 7.75 $\times 10^3$ ppm, and 7.28 $\times 10^3$ ppm, respectively after the 14-d SRB incubation. The corresponding H_2S concentration in the liquid phase was estimated based on H_2S equilibrium at 37°C according to a published report (Ning et al., 2014). The dissolved [H_2S] values for the headspace volumes of 150 mL, 200 mL and 300 mL were 1.06 mM, 0.95 mM and 0.84 mM, respectively (Figure 7-9 and Table 7-4). As expected, a larger headspace allowed more

H_2S to escape from the liquid phase in order to reach a different H_2S equilibrium between the gas and liquid phases. Figure 7-9 also shows that the final broth pH values were 7.08, 7.26, and 7.54 corresponding to headspace volumes of 150 mL, 200 mL and 300 mL, respectively. The broth pH increased slightly with the increasing headspace volume, because a larger headspace allowed more H_2S to escape, and this took away more protons from the broth as shown in Reaction (7-1). According to the following reaction (Jia et al., 2019b),

$$HS^- + H^+ \leftrightharpoons H_2S \quad (7\text{-}1)$$

The dissolved [H_2S] in the broth became lower with the increasing headspace volume while the pH value became higher (Figure 7-9 and Table 7-4). All the pH values in this work were above and not far from 7. This is different from abiotic H_2S corrosion studies, in which researchers introduce exogenous H_2S to an aqueous solution, resulting in acidic pH, which is needed to cause abiotic H_2S corrosion (Sun & Nesic, 2007).

Table 7-4. Data obtained and calculated for dogbone coupons with different headspace volumes (fixed 150 mL broth volume) after 14-d incubation in anaerobic bottles.

Headspace volume (mL)	H_2S concentration in headspace (10^3 ppm) (v/v)	Total pressure in headspace (bar)	H_2S partial pressure in headspace (10^{-2} bar)	Dissolved [H_2S] broth (10^{-4} M)
150	8.50	1.70	1.32	9.73
200	7.75	1.66	0.66	4.86
300	7.28	1.58	0.26	1.92

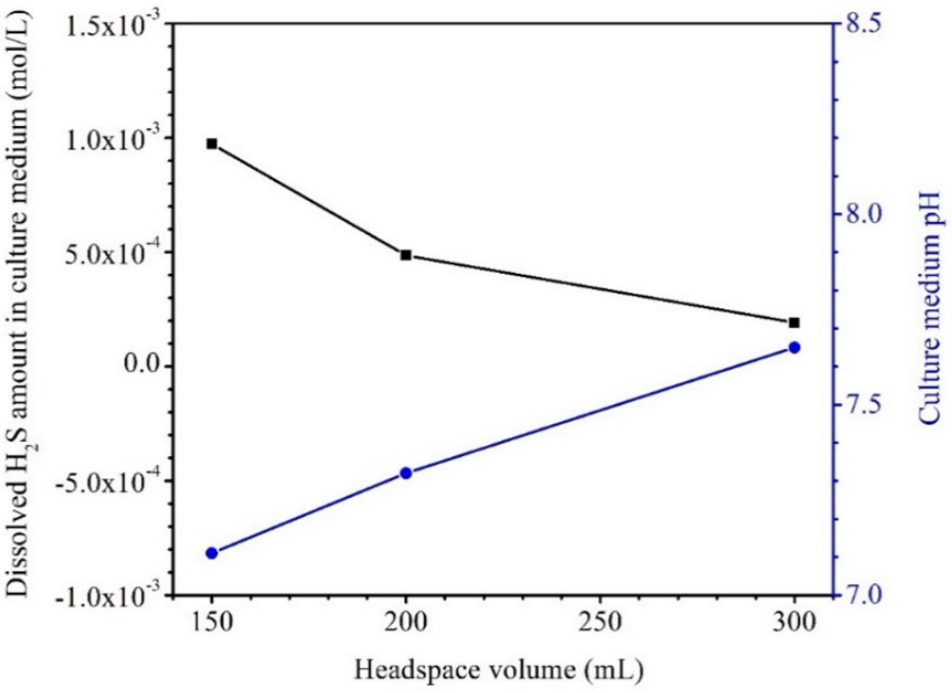

Figure 7-9. Dissolved [H_2S] in both and broth pH after 14-d incubation in bottles with fixed 150 mL broth and varied headspace volume.

7.3.5 Sessile Cell Counts on Dogbone Coupons

After the 14-d incubation, the sessile cell count was found to be higher in the anaerobic bottle with a larger headspace volume (Figure 7-10). The cell counts on coupons in the bottles with the headspace volumes of 150 mL, 200 mL and 300 mL were 6.5×10^7 cells cm^{-2}, 2.3×10^8 cells cm^{-2} and 1.4×10^9 cells cm^{-2}, respectively. The increasing sessile cell count trend agrees with the decreasing dissolved [H_2S] in Table 7-4. Decreased [H_2S] means less toxicity and thus better sessile cell growth (Jia et al., 2019c). Although the 300 mL headspace bottle had lower H_2S concentrations in both

the gas and the liquid phases, its total amount (1.47×10^{-4} mol) was higher than in the bottles with 150 mL and 200 mL headspace volumes. This was reasonable because less H_2S toxicity allowed better SRB growth and thus produced more H_2S in the total amount in the liquid and headspace of a sealed anaerobic bottle.

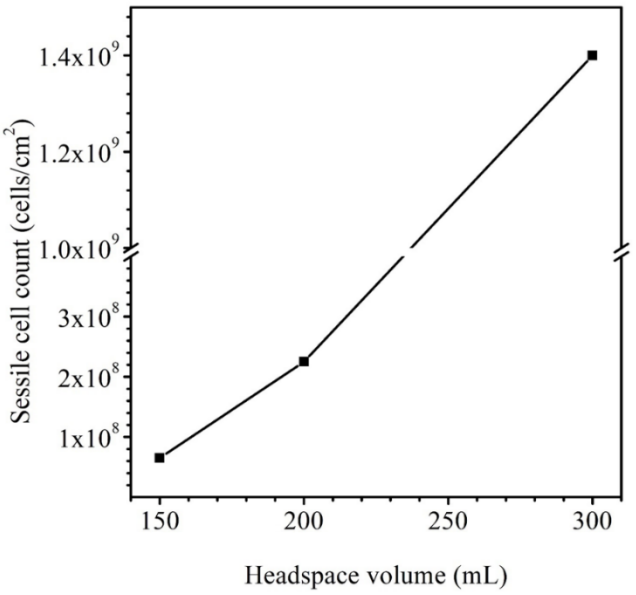

Figure 7-10. Sessile cell counts on dogbone coupons after 14-d incubation in anaerobic bottles with fixed 150 mL broth and varied headspace volume.

7.3.6 Pit Depths on Dogbone Coupons

Coupon surface morphologies on dogbone coupons after the 14-d incubation with biofilms and corrosion products removed were examined under IFM. Figure 7-11(a) shows that the abiotic coupon surface exhibited polished coupon surface roughness (y-scale enlarged to show details). For the biotic dogbone coupons, the maximum pit depth

increased with a larger headspace volume in Figure 7-11(b-d). They were 2.6 μm, 4.2 μm and 6.2 μm for headspace volumes of 150 mL, 200 mL and 300 mL, respectively. The pit depth trend here is consistent with the weight loss data trend. In future studies, pit density should be investigated as well (Javed et al., 2020a; Javed et al., 2020b). With a larger headspace, there was a lower amount of dissolved [H_2S] and more sessile cells, which led to higher weight loss and deeper pits. The maximum pit depth increased by 58% when the headspace increased from 150 mL to 300 mL, while the broth volume was fixed at 150 mL.

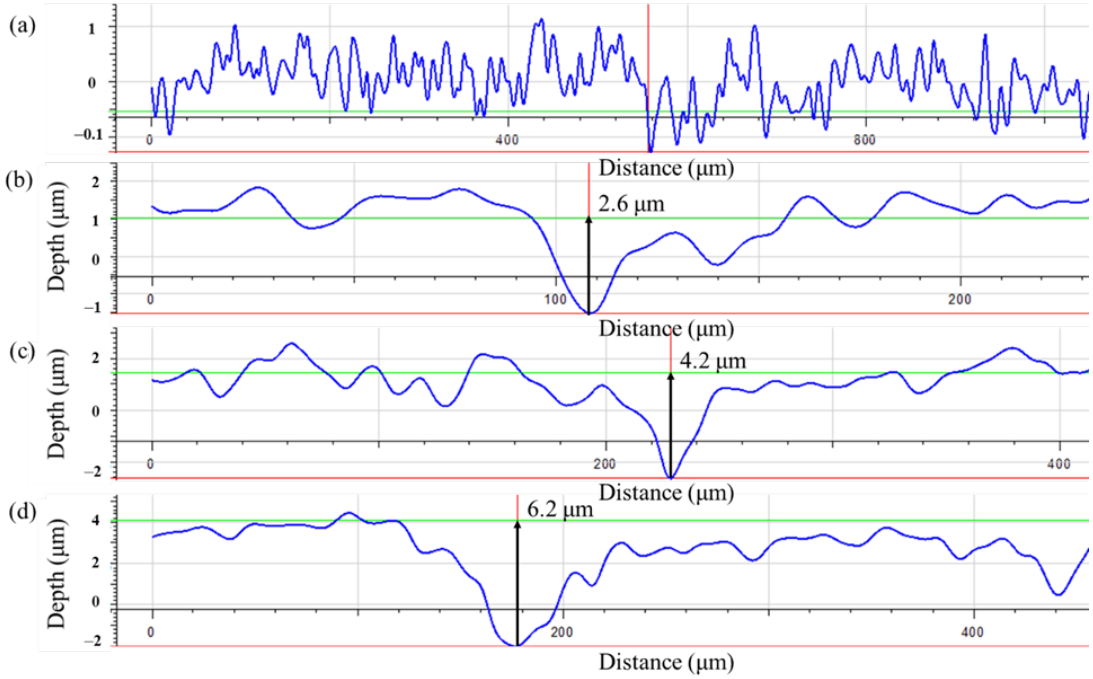

Figure 7-11. Maximum pit depths on dogbone coupons after 14-d incubation in bottles with headspace volumes of: (a) 150 mL (abiotic control), (b) 150 mL, (c) 200 mL, and (d) 300 mL, respectively.

7.3.7 Tensile Testing Using Dogbone Coupons

Figure 7-12 shows the stress-strain curves of X80 dogbone coupons. The dogbone coupons were retrieved after they had been immersed in SRB bottles with fixed 150 mL culture medium volume and varied headspace volumes (150 mL, 200 mL and 300 mL) for 14-d at 37ºC. The ultimate (tensile) strength is the maximum stress that a material can withstand before final failure (Thamma & Jantasorn, 2022). It is the highest point of the Y-axis in Figure 7-12. The ultimate strain (elongation at break) demonstrates the ability of a material to resist shape change before finally breaking (Tian et al., 2021). It is the largest value of the x-axis (strain) in Figure 7-12 (Sluzalec, 1992). The lower values of these parameters can reflect the mechanical property degradation of the material under different conditions such as different MIC severity.

The ultimate strength of abiotic control X80 carbon steel was 853 ± 3 MPa. The ultimate tensile strength values of the abiotic dogbone coupon, and biotic dogbone coupons from bottles with different headspace volumes were all quite close as shown in Figure 7-12. Compared with the abiotic dogbone, in the presence of SRB with headspace volumes of 150 mL, 200 mL 300 mL, the ultimate strength losses were 3%, 2% and 0%, respectively (Table 7-5). These values were rather small. On the other hand, ultimate strain was reduced in the presence of SRB. Compared with the abiotic dogbone, in the presence of SRB with headspace volumes of 150 mL, 200 mL 300 mL, the ultimate strain losses were 6%, 13% and 23%, respectively (Table 7-5). With an

increased headspace, MIC severity increased, making X80 steel more brittle. The corrosion damage by SRB pitting was the main factor in its mechanical property degradation study. H_2S was unlike the driving force behind the relatively large ultimate strain loss, because in this work, more severe MIC corresponded with lower [H_2S] in the broth.

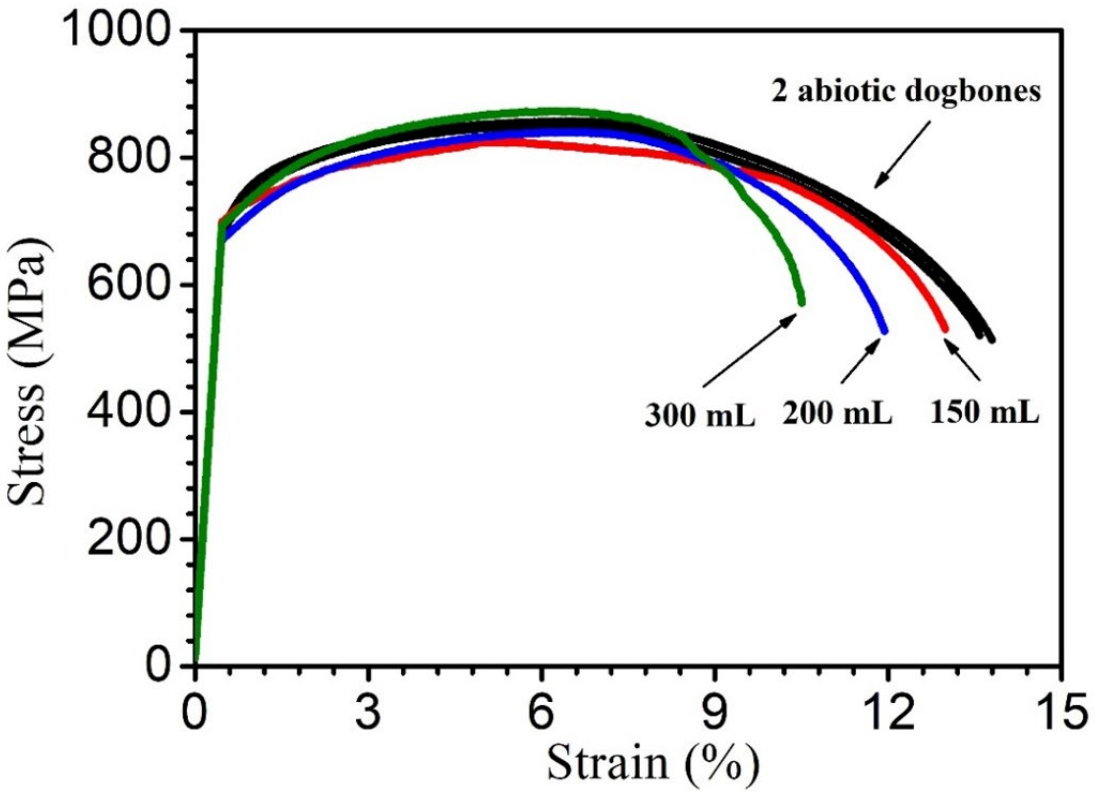

Figure 7-12. Stress–strain curves for 2 replicates abiotic X80 dogbone coupons and dogbone coupons (with corrosion products removed) obtained after 14-d incubation with SRB.

Table 7-5. Ultimate tensile strength and ultimate tensile strain data.

Headspace volume (mL)	Ultimate tensile strength (MPa) (and loss)	Ultimate tensile strain (%) (and loss)
Abiotic dogbone	853 ± 3 (control)	13.7 ± 0.1% (control)
150	824 (3% loss)	12.9% (6% loss)
200	840 (2% loss)	11.9% (13% loss)
300	872 (0% loss)	10.5% (23% loss)

7.4 Conclusions

The tensile testing results show that the presence of SRB made the X80 steel more brittle which was reflected by the relatively lower ultimate strain, compared to the abiotic control. Meanwhile, no significant ultimate strength loss (up to only 3%) for all the dogbone coupons after the 14-d incubation. More severe MIC weight loss and pitting led to more ultimate strain loss (up to 23%) in X80. This work confirms that in an anaerobic bottle with SRB, a larger headspace allows more H_2S to escape from the broth, and this reduces the H_2S toxicity in the broth and thus promoting sessile SRB growth. Increased sessile cell count leads to more severe weight loss and MIC pitting, which is consistent with EET-MIC.

Chapter 8: Impact of *D. ferrophilus* Biocorrosion Time on X80 Pipeline Steel Mechanical Property Degradation

8.1 Introduction

Many studies have demonstrated that the presence of SRB results in the failure of some engineering materials in a short time (Javaherdashti, 2011). For example, *Pseudomonas aeruginosa* biofilm coverage significantly reduced the mechanical properties of 304 SS (Li et al., 2022a). Currently, most microbiologically influenced corrosion (MIC) studies still focus on the corrosion mechanisms of microorganisms on metal materials. There are few reports on the influence of incubation time on MIC and even fewer reports on the influence of various MIC times on the mechanical properties of materials.

Therefore, in this work, *D. ferrophilus* incubated in enriched artificial seawater was employed to attack X80 pipeline steel. Three different incubation times (7, 14 and 21 d) were tested to study the impact of SRB exposure on the degradation of X80 mechanical properties. Weight loss, sessile cell count, biofilm imaging, and corrosion surface analysis were used. Electrochemical corrosion tests were employed to support weight loss and pitting data trends with extra transient corrosion information. The X80 dogbones after MIC exposures were tested using a tensile testing instrument to gauge the damage of mechanical properties.

8.2 Materials and Methods

The elemental composition of X80 pipeline steel is listed in Table A-1 in Appendix A. X80 pipeline steel was cut into square coupons and dogbone coupons. The latter was needed for tensile machine testing. The dimensions of the square coupons were 1 cm × 1 cm × 0.3 cm, and the dimensions of dogbone coupons were based on the ASTM E8/E8M standard as shown in Figure A-5(a, b) (ASTM E8, 2013). All the coupons were polished to 600 grits for the *D. ferrophilus* immersion and electrochemical tests. Each square coupon was painted with Epoxy resin, except for one 1 cm^2 top surface. Each dogbone coupon was painted at the two ends to expose a roughly 4 cm^2 middle section as shown in Figure A-5(c, d). All the coupons were cleaned with 100% isopropanol and air dried under UV light for 0.5 h (Wang et al., 2020).

D. ferrophilus (strain IS5) (DSM 15579) was originally isolated from North Sea, Wilhelmshaven, Germany. It was incubated in EASW at 28°C (optimal temperature) in this study. The chemical composition of EASW (Wang et al., 2021a) is listed in Table A-2. Before sterilization at 121°C for 20 min in an autoclave, the initial pH of the EASW was adjusted to 7.0 ± 0.1 using 1 N of NaOH and 1 N HCl solutions. EASW was deoxygenated using high-purity-filter-sterilized N_2 (> 99.999% by volume) sparging at a flow rate of 50 mL min^{-1} for more than 45 min (Eduok et al., 2019). L-cysteine which was sterilized using a sterile acetate cellulose membrane filter (0.22 μm) was added at 100 ppm final concentration to EASW as an oxygen scavenger to further

reduce the dissolved oxygen. Each anerobic bottle contained 300 mL of deoxygenated sterile EASW, 3 mL of *D. ferrophilus* seed culture, three square coupons or one dogbone coupon for incubation at 28°C for 7, 14, and 21 d, respectively.

All anaerobic manipulations were conducted in an anaerobic chamber (1029, Thermo Fisher Scientific Inc., Waltham, MA, USA) with a N_2 atmosphere (Cui et al., 2020). All chemicals in this work were purchased from Oxoid and Sinopharm Chemical Reagent Co., Ltd.

After incubation, the replicate coupons were taken out and rinsed in a pH 7.4 phosphate buffered solution (PBS) to remove loosely attached planktonic cells and culture medium. Sessile cells on each coupon were removed using a small disposable brush and transferred into a 10 mL PBS solution in a disposable plastic dish. Then, the brush, the coupon, and 10 mL PBS solution were vortexed together in a 50 mL conical tube for 30 s to make a liquid suspension (Li et al., 2021b). A hemocytometer was used to measure the liquid suspension under an optical microscope at 400× magnification (Wang et al., 2022c).

After 7, 14, and 21 d incubations, the same square coupons for weight loss measurements were cleaned with a fresh Clarke's solution to clean the coupon surfaces before weighing according to ASTM G1-03 (ASTM G1-03, 2003). Each weight loss data point was obtained from the three replicate coupons in the same anaerobic bottle.

Before biofilm observation, the coupons from replicate anaerobic bottles allocated for biofilm observation were retrieved from SRB broths and cleaned with a pH 7.40 phosphate-buffered saline (PBS) solution for 15 s, and then immersed in a 2.5% (w/w) glutaraldehyde solution for 8 h at 10°C to fix the biofilms. Thereafter, the coupons were dehydrated with 50%, 70%, 80%, 90%, 95%, and 100% ethanol (v/v) sequentially for 10 min at each concentration (Cui et al., 2020). Finally, the coupon was sputter-coated with an Au film to provide surface conductivity before observation using scanning electron microscopy (SEM) (FEI Quanta 250, Hillsboro, OR, USA) (Li et al., 2022b). Then, the same coupons were cleaned using Clarke's solution to remove biofilms and corrosion products before observation of corrosion pits under the SEM.

An X-ray photoelectron spectroscope (XPS) (AXIS Supra, Shimadzu, Kyoto, Japan) was used to analyze the chemical compounds of corrosion products on the coupon surfaces after 21 d incubation (Lu et al., 2023a).

OCP, LPR, EIS, PDP were performed using a VersaSTAT 3 potentiostat from Princeton Applied Research (Oak Ridge, TN, USA). Each working electrode used a X80 square coupon (1 cm^2). SCE was employed as the reference electrode, and a platinum plate (10 mm × 10 mm × 1 mm) was used as the counter electrode in a 450 mL electrochemical glass cells containing 300 mL EASW inoculated with 3 mL *D. ferrophilus* seed culture. LPR was scanned at a rate of 0.1667 mV s^{-1} in the range of −10 mV to +10 mV vs. OCP. Electrochemical impedance spectroscopy (EIS) was

scanned at OCP by applying a sinusoidal signal of 10 mV (amplitude) at a frequency ranging from 10^5 to 10^{-2} Hz. LPR and EIS were tested at the 1, 3, 7, 10, 14, 17, and 21 d of incubation. PDP curves were only scanned at the 7, 14, and 21 d from OCP to −200 mV vs. OCP and from OCP to +200 mV vs. OCP at a scan rate of 0.1667 mV s^{-1} using the same working electrode (Wang et al., 2022b).

A portable H_2S sensor (GAXT-H-DL, BW Technologies, Calgary, Alberta, Canada), a portable H_2 sensor (BH-90A, Forensics Detectors, Palos Verdes Peninsula, CA, USA), and a digital manometer (Xplorer GLX-PS-2002, Pasco Scientific, Roseville, CA, USA) were used to measure the concentrations of H_2S and H_2 and the total pressure in the headspace of each anaerobic bottle. The H_2 concentration in the headspace of each 450 mL vial was measured by extracting10 mL headspace gas to a sealed 250 mL vial filled with 1 atm air using a syringe. Then, 40 mL gas from the 250 mL vial was withdrawn using a syringe and directly it was injected into the H_2 detector's sampling port.

Three fresh X80 dogbone coupons and all the dogbone coupons after incubation with different time underwent tensile testing on an electromechanical universal testing machine (E44.304, MTS system, MN, USA). The strain rate used in the testing was 0.004 s^{-1}. The devices for immersion tests are shown in Figure 8-1(b, d).

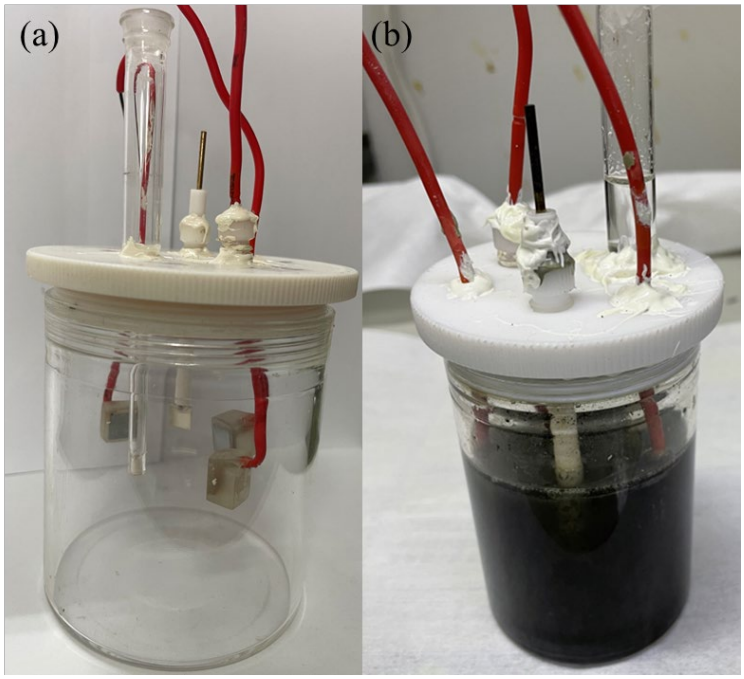

Figure 8-1. Electrochemical glass cells (three replicate X80 square coupons as working electrodes, one for 7 d, one for 14 d, and one for 21 d: (a) before and (b) after immersion in deoxygenated EASW inoculated with *D. ferrophilus*.

8.3 Results and Discussion

8.3.1 Weight Loss and Sessile Cell Count

The weight loss and corrosion rate of the X80 square coupons at different incubation times are shown in Figure 8-2(a). After the 7, 14, and 21 d incubations, the weight losses of the square coupons were 12.3, 22.3, and 24.8 mg cm^{-2}, corresponding corrosion rate 0.82, 0.74, and 0.55 mm $year^{-1}$, respectively. This indicates a corrosion rate sequence of 7 d > 14 d > 21 d. The weight loss of the X80 square coupon increased significantly as the incubation time increased. The weight loss of the coupons after 14

d incubation was 10.0 mg cm^{-2} higher than that after 7 d incubation, and the weight loss after 21 d incubation was only 2.5 mg cm^{-2} larger than that after 14 d incubation. The corrosion rate for the first 7 d was the fastest, and it decreased gradually over time. The abiotic weight loss for 7 d incubation was 0.43 mg cm^{-2}, which was negligible compared with the 12.3 mg cm^{-2} biotic weight loss for 7 d. Thus, abiotic weight loss data are not shown in Figure 8-2(a).

The sessile cell counts on the X80 square and dogbone coupons at different incubation times in deoxygenated EASW inoculated with *D. ferrophilus* are shown in Figure 8-2(b). The sessile cell counts on the surface of the square coupons after 7, 14 and 21 d incubations were 1.1×10^9, 9.2×10^8 and 7.5×10^8 cell cm^{-2}, respectively. The sessile cell counts on the dogbone coupons were 0.9×10^9, 8.5×10^8, and 6.8×10^8 cell cm^{-2}, respectively. The sessile cell count on the surface of the coupons for 7 d incubation was the highest, while 21 d lowest, indicating that the sessile cell count gradually decreased with the increased incubation time due to nutrient exhaustion and H_2S accumulation. Sessile cell counts for the dogbone coupons and the square coupons were close, indicating that the stress or curvature of the U-bend did not impact sessile cell attachment. *D. ferrophilus* corrosion of carton steel is EET-MIC (Wang et al., 2021a). The sessile bacterial cells utilize extracellular electrons from Fe^0 oxidation for biocatalytic sulfate reduction (Jia et al., 2018b). Therefore, a lower sessile cell count

would lead to a lower corrosion rate. The decreasing sessile cell count for 14 d and 21 d incubations during incubation led to a slower and slower corrosion rate.

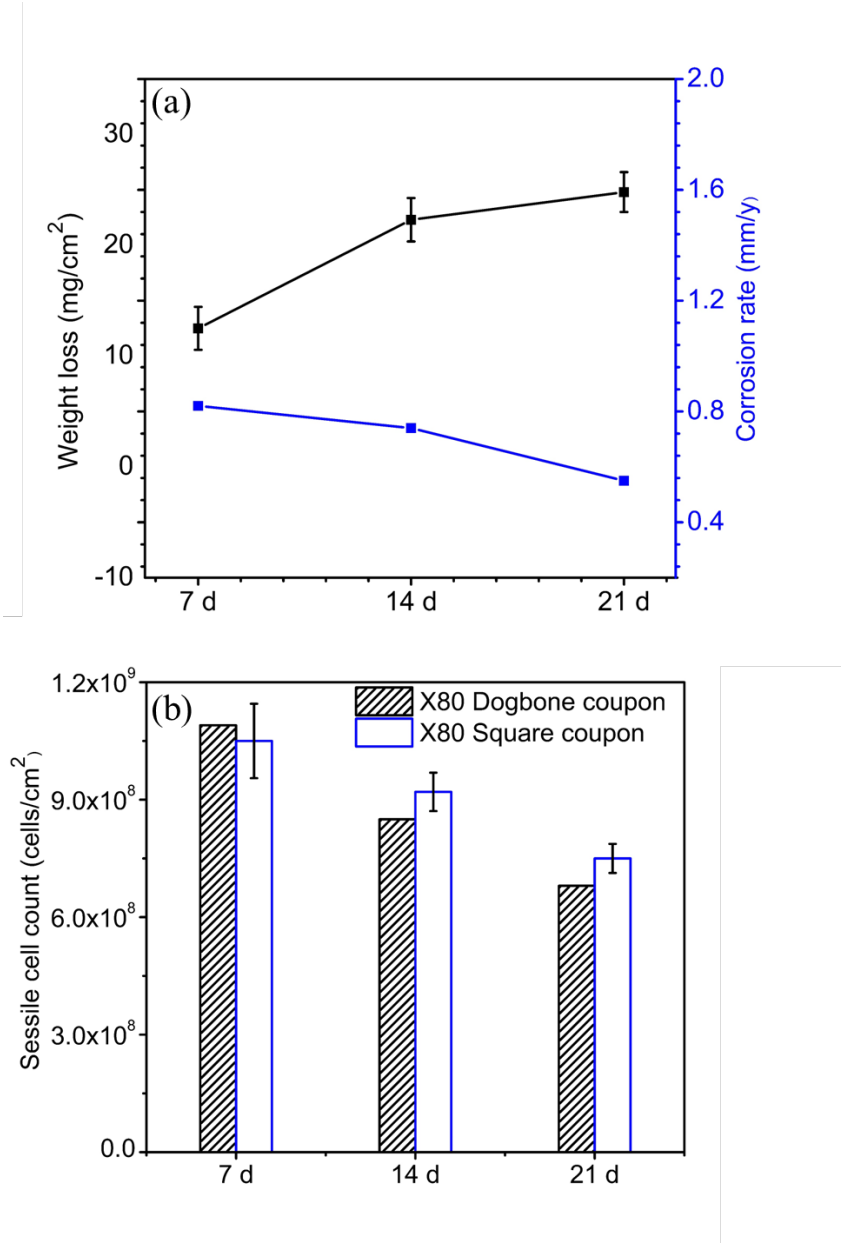

Figure 8-2. X80 square coupon weight loss and corrosion rate (a), and corresponding sessile cell counts (b) after 7, 14 and 21 d incubations in deoxygenated EASW inoculated with *D. ferrophilus*.

8.3.2 H_2 Concentration, H_2S Concentration and Surface Analysis

The dissolved H_2S concentration and pH in EASW at different incubation times are shown in Figure 8-3. After 7, 14, and 21 d of incubations, the H_2S concentrations in the medium were 9.9×10^{-5} M, 7.1×10^{-5} M, and 3.1×10^{-5} M, respectively calculated from the headspace concentrations using Henry's law (Jia et al., 2018a).

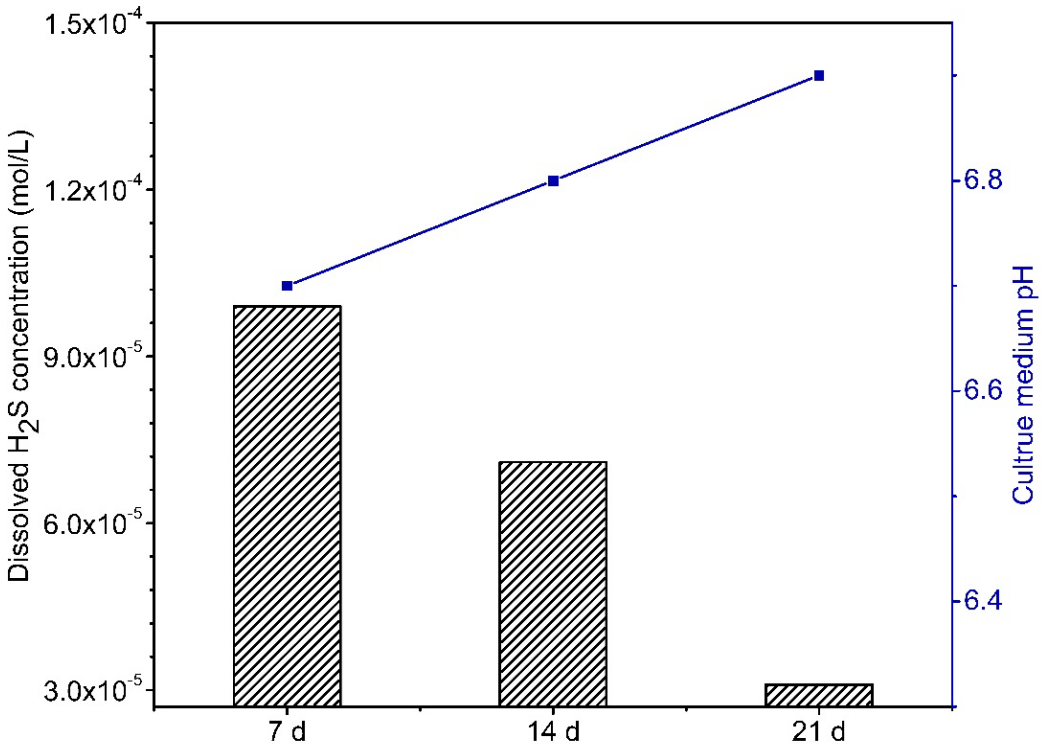

Figure 8-3. Dissolved H_2S concentration (column) and medium pH (blue line) after 7, 14 and 21 d incubations in deoxygenated EASW inoculated with *D. ferrophilus*.

Table 8-1 lists the headspace H_2S and H_2 concentrations and total pressure in the 150 mL headspace. The highest headspace H_2S concentration was 54 ppm (1.6×10^{-3} M)

for 7 d incubation, and the lowest headspace H_2S concentration was 18 ppm (5.3×10^{-4} M) for 21 d incubation. The H_2 concentrations in the headspace showed the same pattern, decreasing gradually with increased incubation time. Therefore, the total pressure in the headspace decreased with the incubation time. After 7, 14, and 21 d incubations, the total pressure in the headspace was 1.07, 1.04, and 1.01 bar, respectively. H_2S and H_2 were the metabolites of *D. ferrophilus* and were essential parameters to reflect the activity and concentration of bacteria (Jia et al., 2018a). *D. ferrophilus* can use H_2 provided by lactate oxidation (to pyruvate and then to acetate) as an energy source, as shown by Reactions (8-1) and (8-2) (Smith et al., 2019):

$$CH_3CHOHCOO^- + H_2O \rightarrow CH_3COO^- \text{(acetate)} + 2H_2 + CO_2 \quad (8\text{-}1)$$

$$SO_4^{2-} \text{(sulfate)} + 5H_2 \rightarrow H_2S + 4H_2O \quad (8\text{-}2)$$

Some H_2 is "leaked" to the headspace during SRB metabolism (Peck, 1993). The longer incubation time and lower H_2S and H_2 in the medium and headspace indicate that the number of bacteria gradually decreased with the incubation time, consistent with the sessile cell count result (Figure 8-2(b)). When there was a shortage of lactate as electron donor. SRB cells switch to H_2 dissolved in the broth as electron donor. Thus, there was a decrease in H_2 concentration in the headspace for longer incubations.

Table 8-1. Headspace gas concentrations and total pressure of anaerobic bottles after the 7, 14 and 21 d incubation in deoxygenated EASW inoculated with *D. ferrophilus*, respectively.

t (d)	Total pressure in headspace (bar)	H_2 in headspace (ppm) (v/v)	H_2 in headspace (M)	H_2S in headspace (ppm) (v/v)	H_2S in headspace (M)	[H_2S] in broth (M)
7	1.07	1250	5.1×10^{-5}	54	2.2×10^{-6}	4.2×10^{-6}
14	1.04	920	3.7×10^{-5}	30	1.2×10^{-6}	2.3×10^{-6}
21	1.01	430	1.7×10^{-5}	18	7.2×10^{-7}	1.4×10^{-6}

The pH of the medium was 6.7, 6.8, and 6.9 after 7, 14, and 21 d incubations, respectively. The pH slightly increased over time. However, [H_2S] in the headspace decreased slightly. The slightly increasing pH trend could be because some H^+ was consumed by Fe(0) oxidation over the relatively long incubation periods. This requires further investigation.

8.3.3 Biofilm, Corrosion Pit and Corrosion Product Analyses

The CLSM images on the X80 square coupons after SRB incubation are shown in Figure 8-4. There were more sessile cells after 7 d than after 14 d during the incubation. The 21-d incubation had the least sessile cells. The CLSM biofilm images indicated that the sessile cell count decreased with the incubation time, which supported sessile cell count data (Figure 8-2(b)).

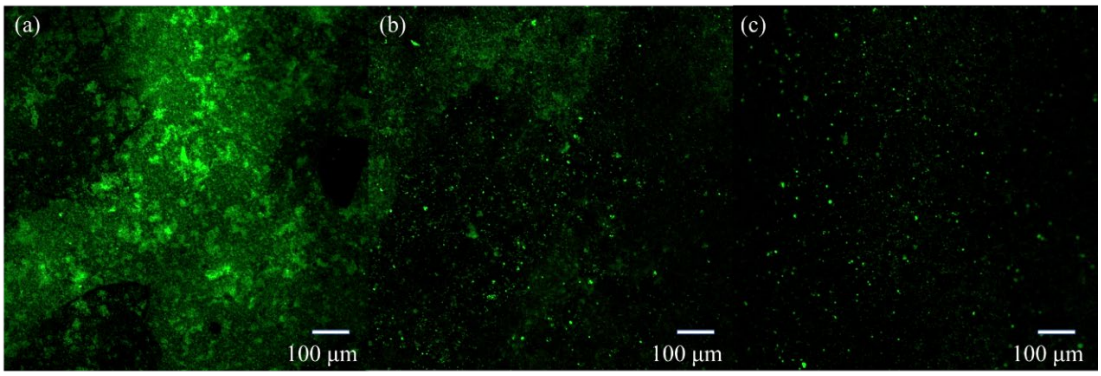

Figure 8-4. CLSM images of biofilms on X80 square coupons after: (a) 7, (b) 14, and (c) 21 d incubations in deoxygenated EASW inoculated with *D. ferrophilus*.

Figure 8-5 presents the SEM biofilm images of X80 square coupons after the 7, 14 and 21-d incubations as well as SEM pit images. After 7, 14, and 21-d incubations, a thick corrosion product film on the square coupons was observed, which means that the coupons had suffered significant corrosion. With the change in incubation time, the morphology of corrosion products changed from large particle clusters to smaller particle clusters. The corrosion products were loose and porous; therefore, the corrosion product film offered no protection to resist corrosion. After the 21 d of incubation, the number of MIC pits increased significantly (Figure 8-5). Figure 8-6 shows the maximum pit depths on the X80 coupons. Without immersion, no pits were observed. After 7, 14, and 21 d of immersion in the *D. ferrophilus* broth, the maximum pit depths were 12.3, 17.9, and 30.6 μm, respectively. This indicates that *D. ferrophilus* caused MIC of the X80, and the longer immersion time resulted in the deeper pit depth. Figure

8-7 is a schematic illustration of sessile cell count, corrosion product thickness and pitting corrosion severity for *D. ferrophilus* against X80.

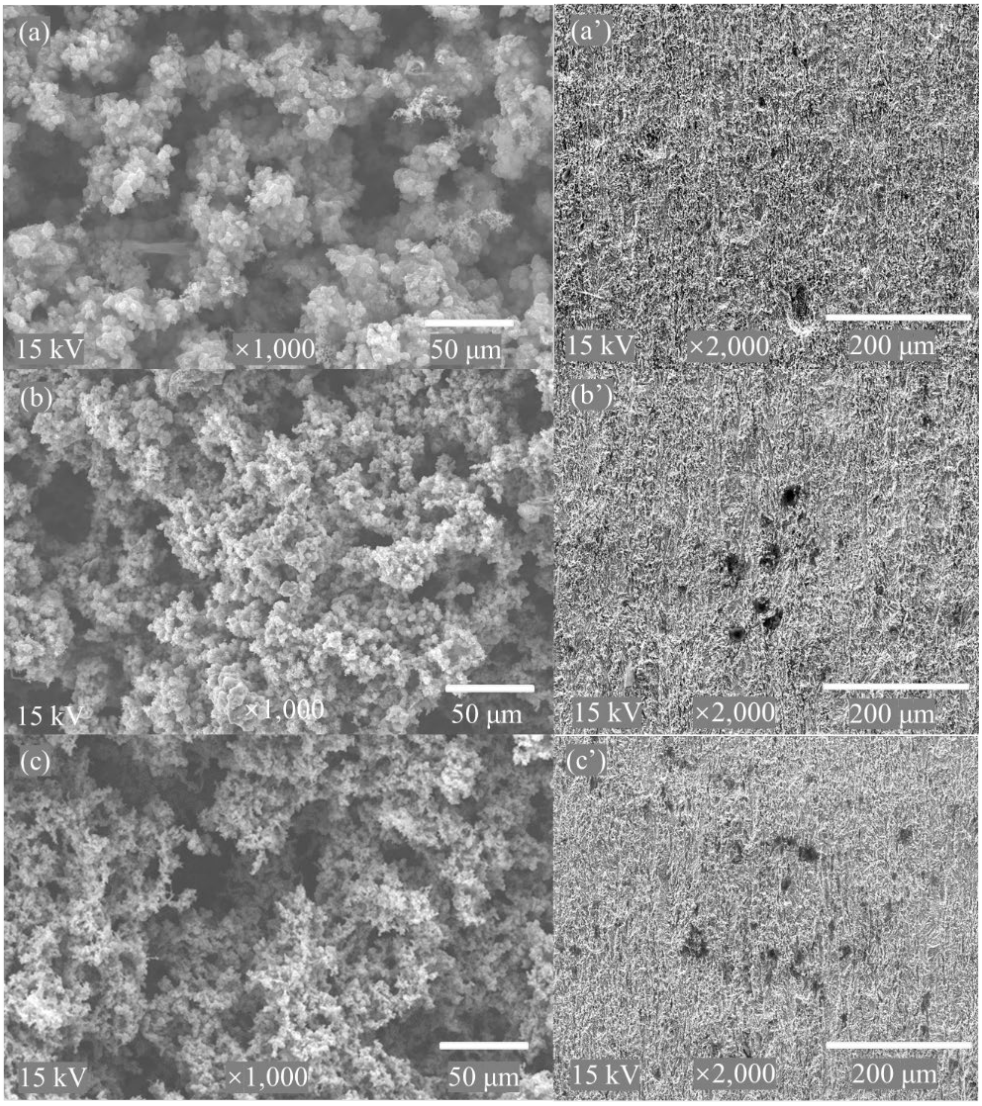

Figure 8-5. SEM images of X80 square coupons after: (a) 7, (b) 14, and (c) 21 d incubations in deoxygenated EASW inoculated with *D. ferrophilus* and corresponding surface morphologies after removing the corrosion products and biofilms (a', b', and c'), respectively.

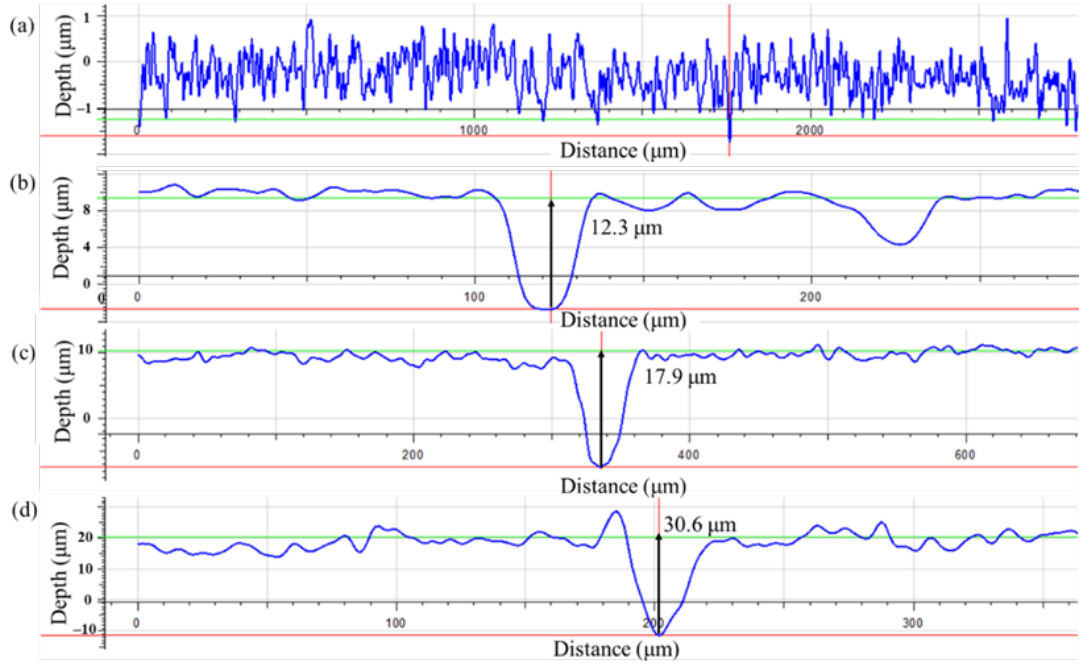

Figure 8-6. Maximum pit depths on X80 square coupons: (a) before incubation; and after: (b) 7, (c) 14, and (d) 21 d incubations in deoxygenated EASW inoculated with *D. ferrophilus.*

Figure 8-8 shows the Fe $2p_{3/2}$ XPS spectra of corrosion products of X80 steel square coupon after 21 d immersion in deoxygenated EASW inoculated with *D. ferrophilus*. The relative contents in the corrosion products are listed in Table 8-2. After 21 d incubation, the Fe 2p spectra contained five peaks located at around 710.3 eV, 711.2 eV, 709.8 eV, 712.6 eV, and 707.1 eV, respectively, corresponding to FeO, Fe_2O_3, Fe_3O_4, FeS, and FeS_2 corrosion products, respectively (Liu et al., 2018a; Yang et al., 2020).

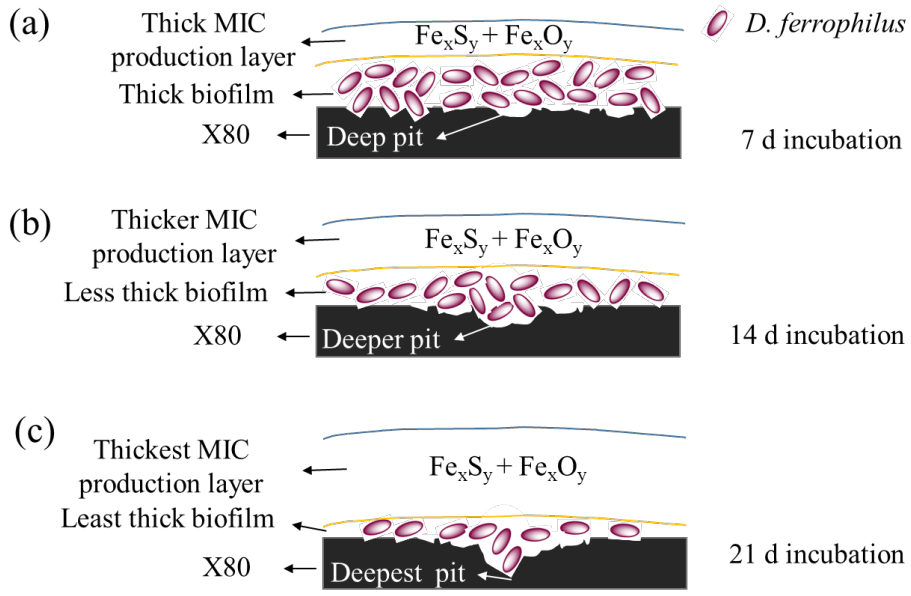

Figure 8-7. The scheme of the MIC deterioration on the X80 steel surfaces after the (a) 7, (b) 14 and (c) 21 d incubation in deoxygenated EASW inoculated with *D. ferrophilus*

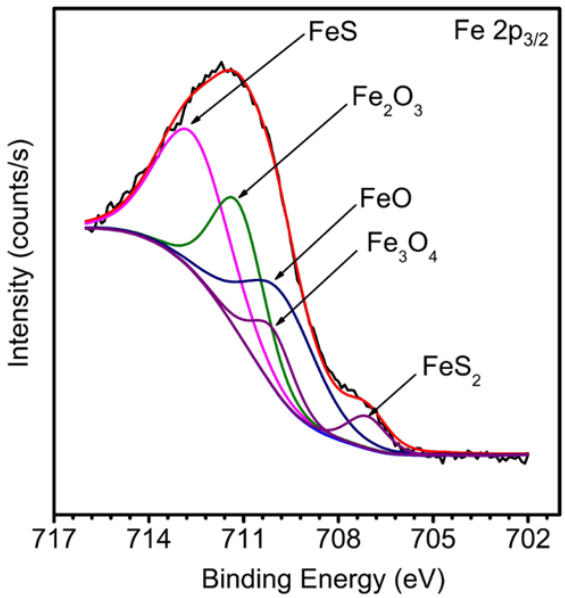

Figure 8-8. XPS spectra of X80 steel square coupon after 21 d incubation in deoxygenated EASW inoculated with *D. ferrophilus*.

Table 8-2. XPS results for relative contents of key components in corrosion products of X80 steel square coupon after 21 d immersion in deoxygenated EASW inoculated with *D. ferrophilus*.

Element	Corrosion product	Binding energy (eV)	Atom %
Fe $2p_{3/2}$	FeO	710.3±0.1	8.70
	Fe_2O_3	711.2±0.1	24.1
	Fe_3O_4	709.8±0.1	27.2
	FeS	712.6±0.1	35.4
	FeS_2	707.1±0.2	4.60

8.3.4 OCP

Figure 8-9 shows the variations of OCP and LPR vs. incubation time. Compared with the abiotic X80 square coupon, the OCP of the biotic square coupon inoculated with *D. ferrophilus* was much lower. Although a lower OCP points to a higher corrosion tendency, suggesting SRB acceleration of corrosion in this work (Wang et al., 2021b). but the corrosion outcome depends on the kinetics of the corrosion process. Thus, kinetics-based electrochemical measurements were performed.

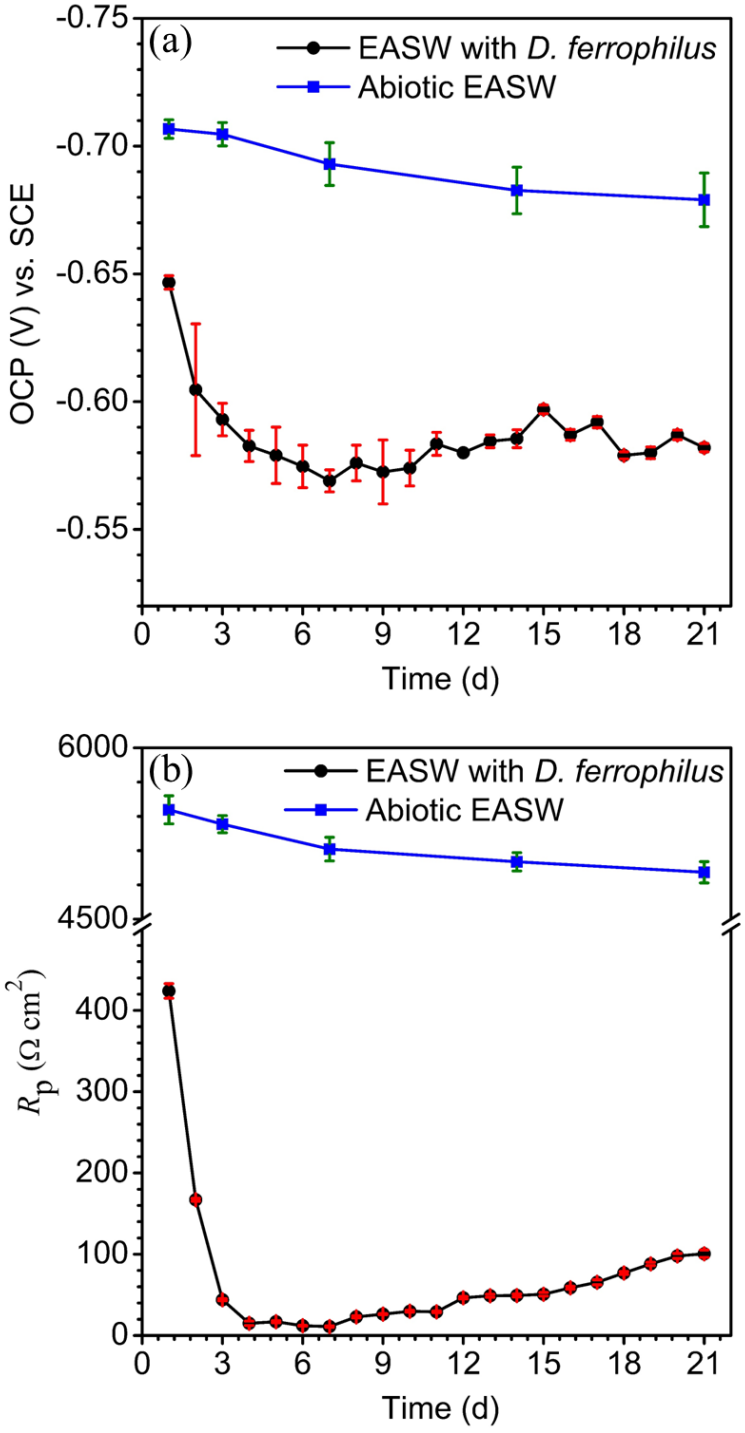

Figure 8-9. Variations of OCP vs. time (a) and LPR vs. time (b) of X80 steel square coupon during 21 d incubation in abiotic deoxygenated EASW and in deoxygenated EASW inoculated with *D. ferrophilus*.

8.3.5 LPR

Because SRB MIC systems are complicated, kinetic electrochemical measurements are needed. Compared with the abiotic X80 square coupon, the biotic LPR R_p value of the square coupon was much lower, which indicated much higher corrosion rate in the presence of *D. ferrophilus*. The biotic R_p values decreased first (1-4 d), then stabilized (4-7 d), and later increased gradually (7-12 d). The R_p value at 1 d was approximately 420 Ω cm^2, the lowest R_p value was approximately 12 Ω cm^2 (4-7 d), and the R_p value was approximately 100 Ω cm^2 at 21 d. A lower R_p value means a faster corrosion, which indicates that the X80 square coupon corrosion rate gradually increased from the 1-4 d due to the establishment of a corrosive SRB biofilm, and then remained stable until 7 d. Later, because of the decrease in sessile cells owing to nutrient depletion, the corrosion rate decreased. The corrosion trend reflected by $1/R_p$ supported the weight loss data with additional transient information (Figure 8-2(a)).

8.3.6 EIS

Figure 8-10(a, b) shows Nyquist and Bode plots of X80 square coupon working electrode during 21 d immersion in deoxygenated EASW inoculated with *D. ferrophilus*. for the 7-d scan, the diffusion resistance was detected. This was because the corrosion products and biofilm accumulated on the X80 steel coupon surface, which hindered the ion migration process (Yin et al., 2018). The equivalent circuit model for EIS modeling is presented in Figure 8-10(b, c), in which R_s, R_f, and Q_f are solution resistance, the

resistance, and the constant-phase element admittance of the biofilm/corrosion product film, respectively. R_{ct} and Q_{dl} are the charge-transfer resistance and the admittance of constant-phase element of the electric double layer, and the Warburg (W) element describes the diffusion process (Liu et al., 2019a). In the Nyquist plot, the arc radius reached maximum oat 1 d, and gradually decreased with the incubation time, then became rather stable, but later gradually increased (Figure 8-10(a)). The Bode diagram shows the same result. The impedance modulus of the samples reached its maximum at 1 d, decreased significantly, reaching its lowest value at 7 d, and later increased gradually (Figure 8-10(a')).

Table 8-3 lists the electrochemical parameters obtained from fitting the EIS spectra with the equivalent circuits. The R_{ct} value at 1 d was 522 Ω cm^2, and tit decreased to 160 Ω cm^2 at 3 d. At the 10 d the R_{ct} values increased significantly.

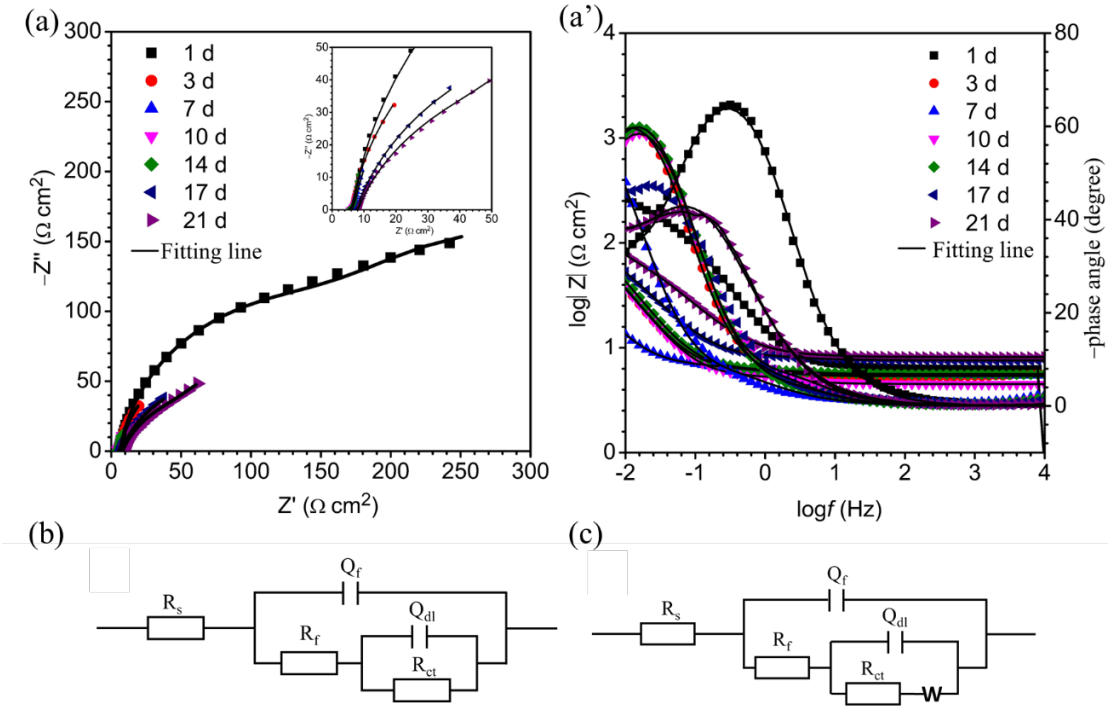

Figure 8-10. (a) Nyquist and (a') Bode plots of X80 steel square coupon during 21 d immersion in deoxygenated EASW inoculated with *D. ferrophilus*; (b) equivalent circuit model used for fitting EIS data on the 1st d and the 3rd d and (c) equivalent circuit model used for fitting EIS data on the 7th, 10th, 14th, 17th, and the 21st d, respectively.

Table 8-3. Electrochemical parameters from fitting EIS spectra in Figure 8-10.

t (d)	R_s (Ω cm^2)	Q_{dl} (Ω^{-1} cm^{-2} s^n)	n_1	R_f (Ω cm^2)	Q_{dl} (Ω^{-1} cm^{-2} s^n)	n_2	R_{ct} (Ω cm^2)	W (Ω^{-1} cm^{-2} s$^{1/2}$)
1	5.61	1.94×10^{-2}	0.90	229	1.97×10^{-1}	0.99	522	
3	5.37	9.45×10^{-2}	0.93	1.41	2.30×10^{-1}	0.88	160	
7	5.20	4.61×10^{-1}	0.82	6.14	3.68×10^{-1}	0.99	253	0.50
10	4.85	4.97×10^{-1}	0.82	4.88	4.42×10^{-1}	0.99	391	0.52
14	4.72	3.58×10^{-1}	0.82	4.20	6.49×10^{-1}	0.99	438	0.51
17	5.16	1.54×10^{-1}	0.81	4.18	6.57×10^{-1}	0.98	472	0.51
21	4.90	2.49×10^{-1}	0.75	2.19	5.39×10^{-1}	0.91	461	0.48

Similar to R_p, a higher $R_f + R_{ct}$ value suggests a lower corrosion rate (Liu et al., 2023). Thus, the variations in $R_f + R_{ct}$ values during the 21-d incubation are plotted together with R_p for LPR in Figure 8-11. The two sets of data have similar trends, except a delayed bottom at 6 d for R_p compared to 3 d for $R_f + R_{ct}$. At the initial stage, $R_f + R_{ct}$ decreased, reaching their maximum value at 3 d. This means the corrosion rate increased during the initial SRB biofilm maturation process which usually took 3 d. Then, $R_f + R_{ct}$ gradually increased with the incubation time, indicating that the corrosion rate increased first and then decreased. This could be attributed to the decrease in the sessile cell count due to nutrient depletion.

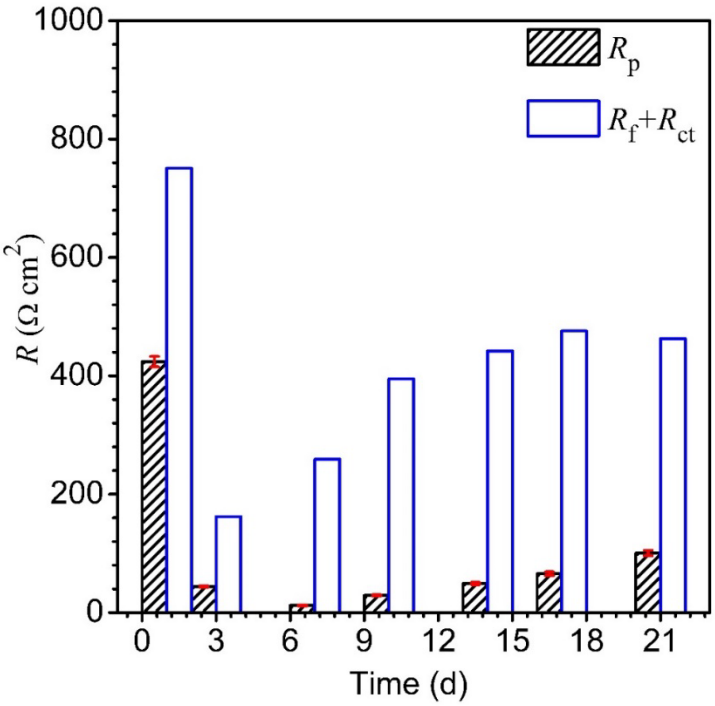

Figure 8-11. Variations of R_p and $R_f + R_{ct}$ vs. time of X80 steel square coupon during 21 d incubation in deoxygenated EASW inoculated with *D. ferrophilus*.

8.3.7 PDP

The PDP curves of the square coupon working electrodes after the 7, 14 and 21 d incubations are displayed in Figure 8-12. The corrosion current density (i_{corr}) values at 7, 14 and 21 d were 2.6×10^{-4}, 2.0×10^{-4}, and 1.6×10^{-4} A cm^{-2}, respectively (Table 8-4). This indicates a corrosion rate sequence of 7 d > 14 d > 21 d, which agreed with the weight loss data (Figure 8-2(a)).

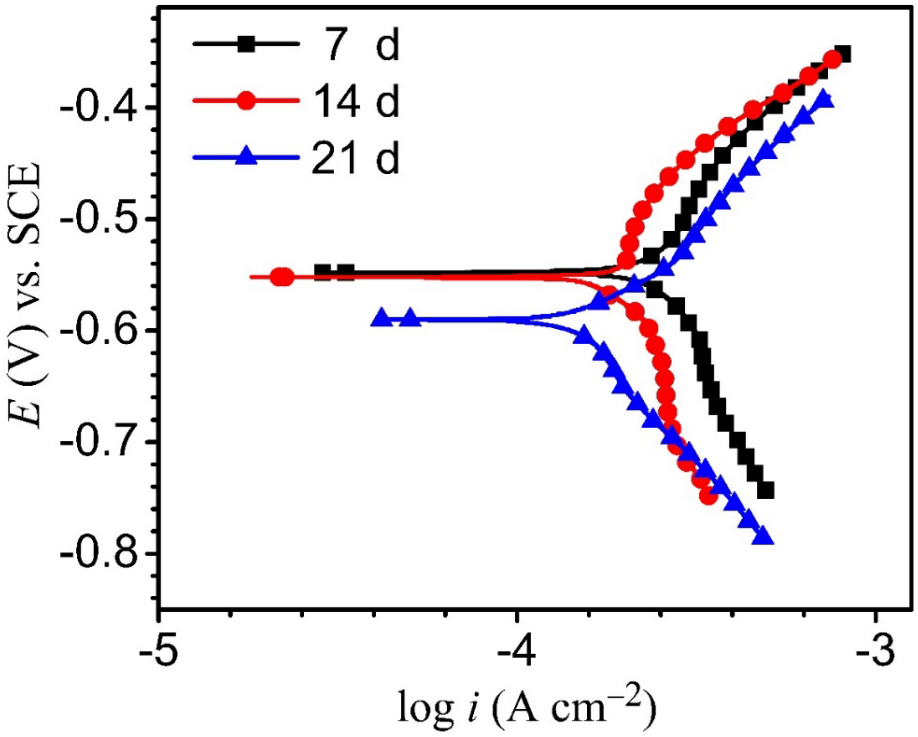

Figure 8-12. Potentiodynamic polarization curves of X80 square coupon surfaces after the 7, 14 and 21 d incubation in deoxygenated EASW inoculated with *D. ferrophilus*.

Table 8-4. Electrochemical parameters fitted from Tafel curves in Figure 8-12.

t (d)	i_{corr} ($\mu A\ cm^{-2}$)	E_{corr} (V) vs. SCE	β_a ($V\ dec^{-1}$)	β_c ($V\ dec^{-1}$)
7	260	–0.52	0.487	–0.112
14	200	–0.54	0.369	–1.32
21	160	–0.61	0.419	–0.333

8.3.8 Dogbone Tensile Testing

Figure 8-13 shows the stress-strain curves of dogbone coupons after different incubation times. Compared with the fresh dogbone's ultimate tensile strength of 884 MPa and ultimate tensile strain of 14.2%, the abiotic dogbone coupon had no obvious degradation in ultimate tensile strength and ultimate tensile strain, while the biotic dogbone coupons had lower values. Table 8-5 summarizes the stress-strain curves (Figure 8-13). After 7, 14, and 21 d incubations, the ultimate tensile strength decreased by 6%, 8%, and 11%, respectively. Moreover, after 7, 14, and 21 d incubations, the ultimate tensile strain lost 13%, 16%, and 21%, respectively. Thus, it was clear that *D. ferrophilus* caused MIC and decreased the ultimate tensile strength and ultimate tensile strain of X80. A lower ultimate tensile strain means a more brittle metal (Gou et al., 2023). Thus, *D. ferrophilus* promoted corrosion and reduced the mechanical strength and toughness of the coupons even in short-term testing.

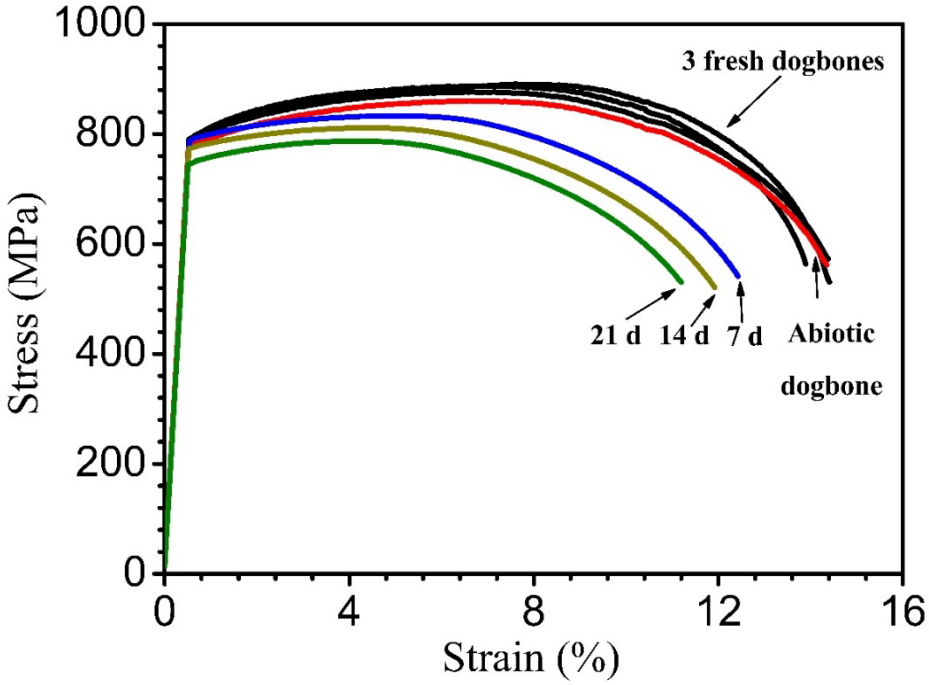

Figure 8-13. Stress-strain curves for three fresh X80 dogbone coupons (three replicates, black lines), one dogbone coupon after 21 d incubation in abiotic deoxygenated EASW (red line) and dogbone coupons (with corrosion products removed) after the 7, 14 and 21 d incubations in deoxygenated EASW inoculated with *D. ferrophilus*, respectively.

Table 8-5. Ultimate tensile strength and strain data from Figure 8-13.

Time (d)	Ultimate tensile strength (MPa) (and loss)	Ultimate tensile strain (%) (and loss)
No immersion	884 ± 6.2 (control)	14.2% ± 0.2% (control)
Abiotic control	860 (2% loss)	14.3% (0% loss)
7	830 (6% loss)	12.4% (13% loss)
14	810 (8% loss)	11.9% (16% loss)
21	787 (9% loss)	11.2% (18% loss)

8.4 Conclusion

This study revealed that *D. ferrophilus* caused MIC pitting and decreased the mechanical properties of X80 steel. The corrosion rates of X80 square coupons varied with incubation time. After the 7 d of incubation, the corrosivity of *D. ferrophilus* biofilm gradually decreased due to nutrient depletion, resulting in a gradual decrease in the corrosion rate accompanying decreasing sessile cell counts. Longer incubation times caused higher weight losses and deeper pits, leading to more severe degradations of mechanical properties reflected by lower ultimate strength and ultimate strain.

Chapter 9: Mitigation of Microbial Degradation of X80 Carbon Steel Mechanical Properties Using a Green Biocide

9.1 Introduction

Microbial corrosion widely exists in nature and various industrial environments, such as oil and gas systems, water treatment systems, and cooling water systems in power plants, leading to billions of US dollars in losses per year (Batmanghelich et al., 2017; Jin et al., 2022; Liu et al., 2022b; Wei et al., 2019; Xu et al., 2023a). Facilities in the ocean are more corroded than those in terrestrial environments, and they are more difficult to repair (Li et al., 2021d; Lu et al., 2023a; Lu et al., 2023b; Melchers, 2005; Zen, 2005). In the marine environment, microorganisms can adhere to metal surfaces, causing MIC that damages engineering facilities and even seriously threatens operators' safety (Chen et al., 2022b; Li et al., 2021c; Li et al., 2022b; Xu et al., 2023a; Xu et al., 2022b) in addition of pinhole leaks (Jacobson, 2007).

Most MIC studies focused on MIC pinhole leaks (Chandra et al., 2019; Dao et al., 2021). More attention should be paid to microbial or MIC deterioration of mechanical properties of steels, including reductions of tensile strength and strain (Li et al., 2021c; Li et al., 2022b). Such deteriorations can lead to catastrophic structural failures if not mitigated. Among the microbes that can cause serious MIC, SRB accounted for the largest number of known severe corrosion cases (Anandkumar et al., 2016; Lu et al., 2023b; Su et al., 2022). *D. ferrophilus* (strain IS5) is by far the most corrosive marine

pure-strain SRB. In lab studies, it led to a 1.6 mm year^{-1} uniform corrosion rate against C1018 carbon steel and 1.5 cm/year pitting rate against 13%Cr steel (i.e., 420 stainless steel) (Wang et al., 2021a; Xu et al., 2023b).

An effective way to reduce the degradation of mechanical properties caused by MIC is to mitigate the biofilms that are behind the MIC, and to reduce the amounts of destructive metabolites. There are many measures to mitigate MIC, such as physical, chemical, and electrochemical methods. They include the addition of alloying elements to steels, scrubbing, anti-corrosion coatings, cathodic protection, and biocides (Videla, 2002; Wang et al., 2021d; Yin et al., 2018). Among these, biocides with broad-spectrum bactericidal effects are the mainstream treatment in mitigating biofilms and MIC (Kahrilas et al., 2015; Sanchez et al., 2014; Wang et al., 2019b).

Therefore, in this study, THPS, a popular green biocide commonly used in the oil and gas industry as well as water utilities (Okoro et al., 2016; Silva et al., 2021; Xu et al., 2022a), was used to mitigate the microbial degradation of mechanical properties of X80 pipeline steel caused by *D. ferrophilus*. Bacterial sessile cell count, corrosion surface morphology, corrosion products, and X80 mechanical properties were analyzed to study the efficacy of THPS.

9.2 Materials and Methods

The composition of the X80 carbon steel, X80 square coupon dimensions, and X80 dogbone coupon dimensions (ASTM E8, 2013) are listed in Appendix A. Each

coupon was painted with Epoxy resin, leaving 1 cm^2 of exposed surface on the square coupon and 4 cm^2 total exposed surface on the dogbone coupon, as shown in Appendix A. After coating, the coupons were sterilized in 75% (v/v) alcohol and dried under a UV light for 20 min.

D. ferrophilus (strain IS5) (DSM 15579) in this work was originally isolated from an enrichment culture in North Sea, Wilhelmshaven, Germany according to its vendor (German Collection of Microorganisms and Cell Cultures) (Dinh et al., 2004). EASW culture medium (Wang et al., 2021a) was deoxygenated using N_2 sparging before it was used to incubate *D. ferrophilus* at 28°C. Each anaerobic bottle (450 mL) contained 300 mL of deoxygenated EASW, 3 mL *D. ferrophilus* seed culture, 3 square coupons, and 1 dogbone coupon (leaning against the wall at a 30° angle with respect to the bottom). One anaerobic bottle received no treatment, and another received 100 ppm (ppm) THPS added to EASW upon inoculation. The anaerobic bottles with no treatment and with 100 ppm THPS are shown in Figure 9-1. Parameters for the test matrix are presented in Table 9-1.

After a 7-d incubation, live and dead sessile cells on the X80 square coupons were examined using CLSM (confocal laser scanning microscopy) (Chen et al., 2021). The planktonic and sessile cells were enumerate using a Neubauer hemocytometer under a 400× microscope (Cheng et al., 2021). This method works well for motile cells like *D. ferrophilus* despite their small size. The concentrations of H_2S and H_2 in the headspace

and the total gas pressure in each anaerobic bottle were measured at the end of the 7-d incubation as described elsewhere (Jia et al., 2018a; Ning et al., 2015).

A freshly prepared Clarke's solution was used to remove biofilms and corrosion products before weighing each coupon adhering to ASTM G1-03 (Lu et al., 2023b). Pit depths were scanned using a different CLSM machine (VK-X250K, Keyence, Osaka, Japan).

An SEM machine (FEI Quanta 250, Hillsboro, OR, USA) was employed to examine biofilm morphology on each coupon (Cui et al., 2020). An IFM (InfiniteFocus microscope) profilometer (ALC13, Alicona Imaging GmbH, Graz, Austria) was used to scan for MIC pits on the coupons and to measure corrosion pit depth. An XPS machine (AXIS Supra, Shimadzu, Kyoto, Japan) was used to analyze the chemical composition of the corrosion products on each coupon. Before XPS analysis, the top biofilm layer on a coupon was removed using a cotton swab to reveal the bottom corrosion products.

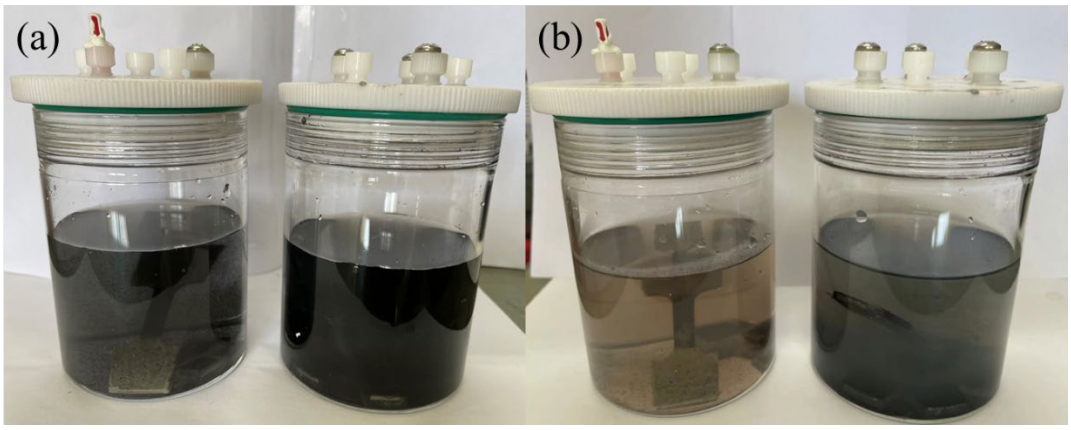

Figure 9-1. Anaerobic bottles containing X80 square coupons and X80 dogbone coupons in EASW inoculated with *D. ferrophilus*: (a) at 0 d with and without 100 ppm THPS; and (b) at 7 d with and without 100 ppm THPS; and a partially painted dogbone coupon.

After the 7-d incubation, X80 dogbone coupons were tensile tested on a Model E44.304 electromechanical universal testing machine (MTS system, MN, USA). The applied strain rate was 0.004 s^{-1} following literature (Eleiche et al., 1985).

Table 9-1. Test matrix for THPS mitigation of *D. ferrophilus* deterioration of mechanical properties of X80 steel.

Parameter	Condition
Bacterium	*D. ferrophilus*
Culture medium	EASW
Coupon	X80 square and X80 dogbone
Temperature	28ºC
Incubation time	7 d
Anaerobic bottle volume	450 mL
Culture medium volume	300 mL
Biocide	THPS
Treatment	No treatment 100 ppm THPS
Analysis	CLSM biofilm imaging, sessile cell count, planktonic cell count, gas measurement, weight loss, pit depth, surface observation of SEM, XPS, tensile test.

9.3 Results and Discussion

9.3.1 CLSM, Cell Counts, and Gas Measurements

As shown in Figure 9-2, on the X80 square coupons incubated with 100 ppm THPS and 0 ppm THPS, the *D. ferrophilus* sessile cell counts were 1.5×10^{6} cells cm^{-2} and 9.3×10^{8} cells cm^{-2}, respectively. The corresponding values on X80 dogbone surfaces were 1.6×10^{6} cells cm^{-2} and 1.1×10^{9} cells cm^{-2} for 100 ppm THPS and 0 ppm THPS, respectively. Thus, the two sets of sessile cell counts were quite close, suggesting that the square coupons could be used to obtain MIC data to save dogbone coupons. The sessile cell count data showed an approximately 3-log reduction with 100 THPS

treatment compared to the no-treatment control. As for the planktonic cells, the cell count without THPS was 6.5×10^{8} cells mL^{-1}. In the presence of 100 ppm THPS, the planktonic cell count was 1.1×10^{5} cells mL^{-1}, a reduction of approximately 3-log was observed (Figure 9-4). Thus, 100 ppm THPS yielded excellent efficacy for inhibiting both planktonic cells and sessile cells (Jia et al., 2019c).

The CLSM images of the biofilms on the X80 square coupons after the 7-d incubation are displayed in Figure 9-2. Without THPS, many live sessile cells (green dots) are seen on the coupon. However, in the presence of 100 ppm THPS, the coupon primarily shows dead sessile cells (red dots). This indicates that 100 ppm THPS was very effective for *D. ferrophilus* biofilm prevention. The same dosage was found effective against *D. vulgaris* biofilm on C1018 carbon steel (Wang et al., 2022a) , which guided the dosage selection in this work. The CLSM images here supported the sessile cell counts in Figure 9-3.

Table 9-2 lists the environmental parameters of the anaerobic bottles with and without THPS treatment. With no treatment and 100 pm THPS treatment, the headspace gas pressures were found to be 1.03 bar and 1.01 bar, respectively after the 7-d incubation. The H_2S concentrations were 450 ppm in the headspace, and 4.3×10^{-5} M in the broth (based on Henry's law calculation (Jia et al., 2018a; Ning et al., 2015) without THPS treatment, while the 100 ppm THPS treatment yielded roughly 10X lower values of 40 ppm and 3.7×10^{-6} M, respectively.

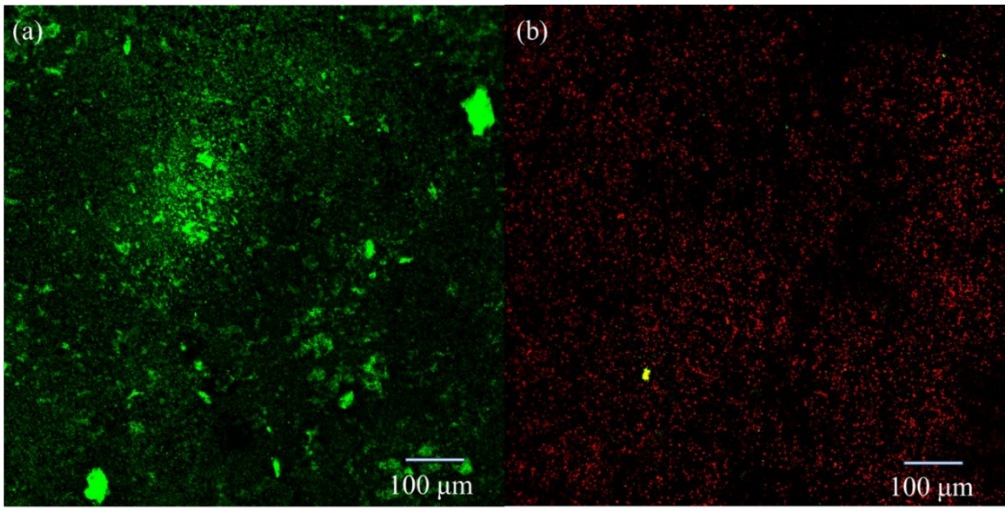

Figure 9-2. CLSM images of biofilm on X80 square coupons surface after 7-d *D. ferrophilus* incubation: (a) No treatment (b) 100 ppm THPS treatment (biocide in the culture medium upon inoculation).

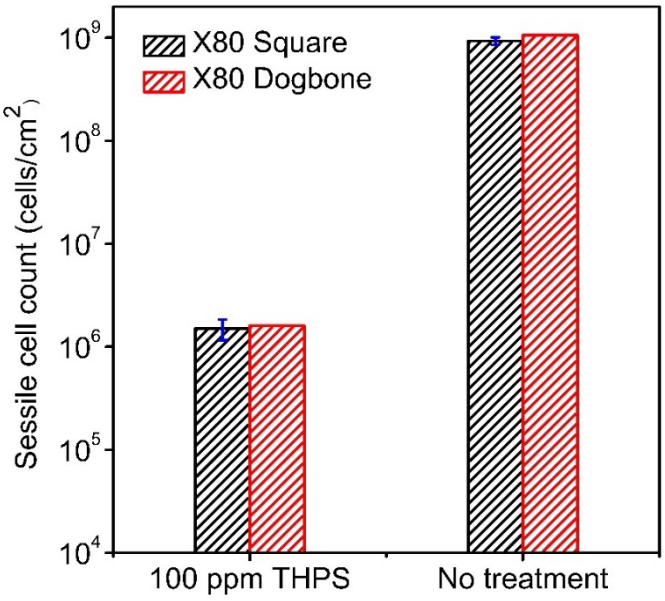

Figure 9-3. Sessile cell counts on X80 square and dogbone coupons surface after 7-d *D. ferrophilus* incubation with 100 ppm THPS treatment and no treatment.

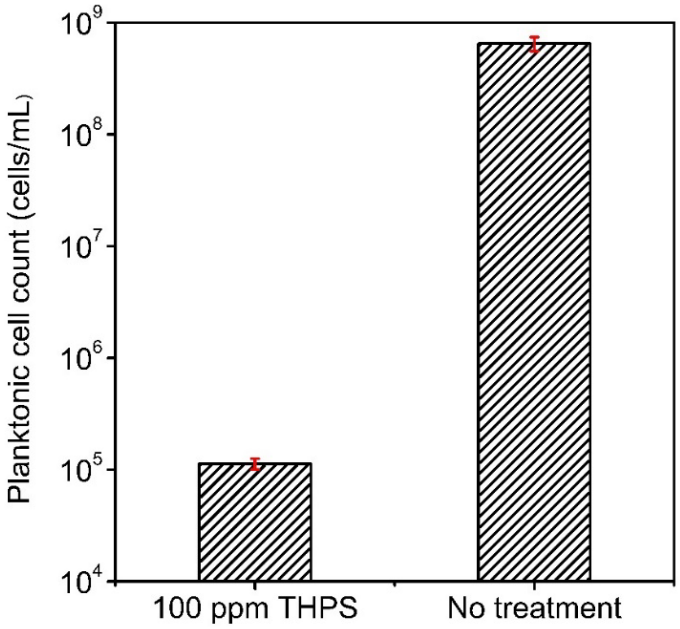

Figure 9-4. Planktonic cell counts of *D. ferrophilus* medium 7-d incubation with 100 ppm THPS treatment and no treatment.

Table 9-2. Data obtained and calculated for two anaerobic bottles containing *D. ferrophilus* medium with no treatment and 100 ppm THPS treatment.

Treatment	Total pressure in headspace (bar)	H_2 in headspace (ppm) (v/v)	H_2 in headspace (M)	H_2S in headspace (ppm) (v/v)	[H_2S] in broth (M)	pH
No treatment	1.03	280	1.2×10^{-5}	450	4.3×10^{-5}	6.9
100 ppm THPS	1.01	80	3.2×10^{-6}	40	3.7×10^{-6}	7.0

In SRB metabolism, lactate is first oxidized to pyruvate. Pyruvate is then oxidized to yield acetate with H_2 production. H_2 is used for sulfate reduction, but some of it

escapes to the headspace. When there is a shortage of lactate, some headspace H_2 is consumed as electron donor for sulfate reduction (Smith et al., 2019; Xu et al., 2023a):

$$CH_3CHOHCOO^- + H_2O \rightarrow CH_3COO^- \text{ (acetate)} + 2H_2 + CO_2 \quad (9\text{-}1)$$

$$SO_4^{2-} \text{ (sulfate)} + 5H_2 \rightarrow H_2S + 4H_2O \quad (9\text{-}2)$$

9.3.2 Weight Loss, Pit Depth, SEM, and XPS

Figure 9-5 s shows the weight loss of the X80 square coupons after the 7-d incubation. The weight losses of the X80 square coupons with and without the 100 ppm THPS treatment were 1.1 mg cm^{-2} (vs. 0.43 mg cm^{-2} weight loss for abiotic control), and 19.5 mg cm^{-2} (equivalent to 1.3 mm $year^{-1}$ uniform corrosion rate), respectively. This reflects a 94% THPS treatment efficiency in terms of uniform corrosion reduction.

The surface profiles on the X80 square coupons after the removal of the corrosion products and biofilms are shown in Figure 9-6. No obvious corrosion pits are observed when 100 ppm THPS was in EASW at the beginning of incubation. In contrast, the coupon with no treatment had a maximum pit depth of 13.5 μm (0.70 mm $year^{-1}$ pitting rate) and a maximum pit surface diameter of 36.7 μm. The weight loss and pit depth data with and without 100 ppm THPS in EASW indicate that MIC on the X80 square coupons was greatly reduced by the biocide treatment.

The rather severe MIC uniform corrosion (1.3 mm $year^{-1}$) on the coupon with no THPS treatment occurred because of a robust *D. ferrophilus* biofilm (9.3×10^8 cells cm^{-2}) formation on the X80 square coupon. *D. ferrophilus* sessile cells in the biofilm

harvested electrons for respiration in the SRB cytoplasm via extracellular electron transfer (EET) because the electron donor Fe(0) is insoluble (Wang et al., 2021a). The led to corrosion. The two half-reactions below can be adopted to illustrate the EET-MIC of carbon steel caused by *D. ferrophilus* (Wang et al., 2021a):

$$4Fe \rightarrow 4Fe^{2+} + 8e^{-} \quad (E^{o} = -447 \text{ mV}) \qquad \text{(extracellular)} \qquad (9\text{-}3)$$

$$SO_4^{2-} + 9H^{+}\ 8e^{-} \rightarrow HS^{-} + 4H_2O \quad (E^{o\prime} = -217 \text{ mV}) \quad \text{(intracellular)} \qquad (9\text{-}4)$$

The cell potential ($\Delta E^{o\prime}$) of the combined reaction consisting of Reactions (3) and (4) is +230 mV, indicating a thermodynamically favorable corrosion process with energy release that helped SRB metabolism (Wang et al., 2020).

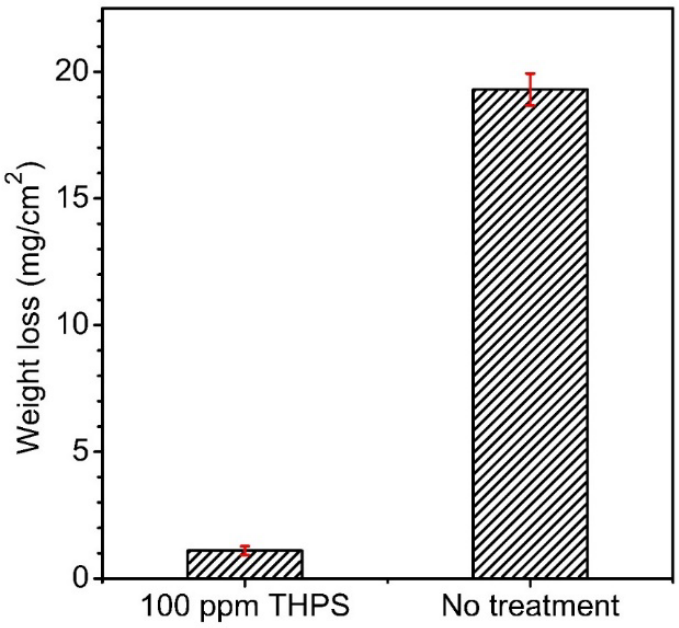

Figure 9-5. Weight losses of X80 square coupons after 7-d *D. ferrophilus* incubation with 100 ppm THPS and No treatment.

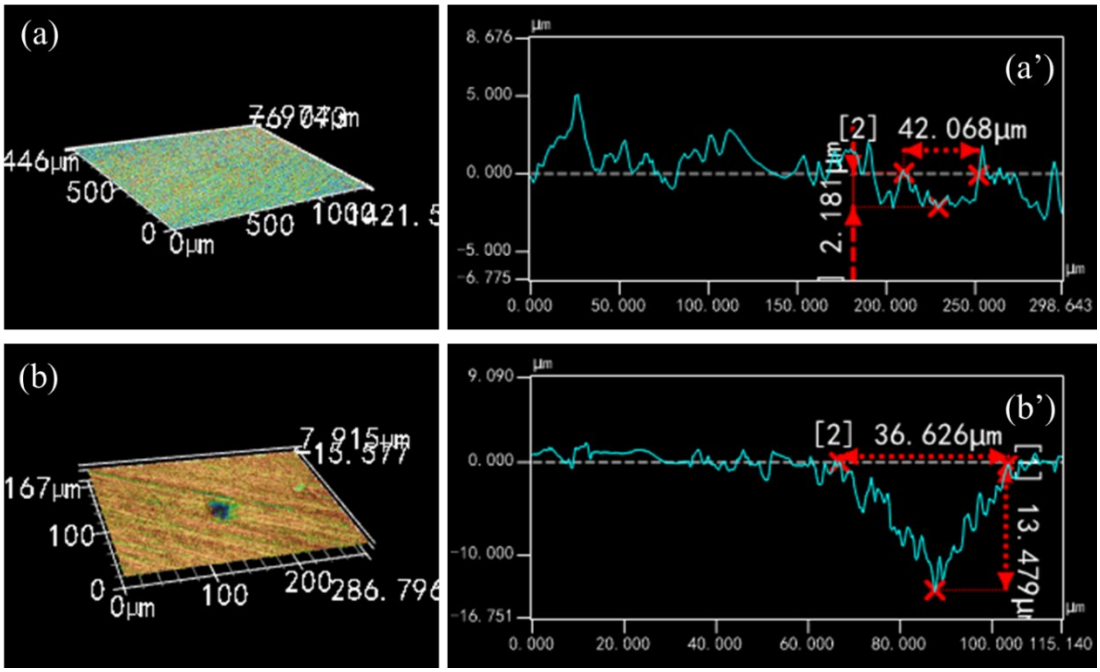

Figure 9-6. CLSM images and pit depth of X80 square coupons surface after removing the biofilms and corrosion products at the end of 7-d *D. ferrophilus* incubation with 100 ppm THPS (a, a') and no treatment (b, b').

SEM images of the X80 square coupons with 100 ppm THPS treatment and no treatment after the 7-d incubation are shown in Figure 9-7. In the presence of 100 ppm THPS, a corrosion product film with cracks is observed on the surface of the coupon in Figure 9-7(a). The cracks could be due to the dehydration procedure in the preparation of the coupon for biofilm imaging under SEM. In comparison, without treatment, the coupon was completely covered with biofilm biomass on top (Figure 9-7(b)). The difference in the surface morphologies of the X80 square coupons was caused by the difference in sessile cell counts between the two treatments. More sessile cells on the

coupons with no treatment led to severe corrosion with thicker biofilms, which produced more corrosion products.

Figure 9-8 shows the XPS spectra of Fe 2p on the surface of the X80 square coupons after the 7-d SRB incubation. The relative contents of the key components and binding energies of the corrosion products are listed in Table 9-3. In the presence of 100 ppm THPS, there were three peaks located at 710.3 eV, 711.2 eV, and 709.8 eV, corresponding to FeO, Fe_2O_3, and Fe_3O_4, respectively (Liu et al., 2018a; Yang et al., 2020). These peaks were also observed on the coupon with no treatment. The coupon with no treatment had additional FeS and FeS_2 peaks located at 712.6 eV and 707.1 eV, respectively. These additional iron sulfide peaks were typical SRB corrosion products caused by *D. ferrophilus,* which obtained the electrons from the steel substrate and then transferred the electrons into the cell membrane to bio-catalytically reduced the SO_4^{2-} to S^{2-} and S^{-}. Then, S^{2-} and S^{-} combined with Fe^{2+} to form FeS and FeS_2. As previously shown, the sessile cell count on the coupon treated with 100 ppm THPS was much lower than on those with no treatment (Figure 9-3), resulting in a lower MIC rate (Figure 9-5 and 9-6). This lower MIC rate reduced the generation of corrosion products (Figure 9-8). Notably, the H_2S concentration in the bottle with 100 ppm THPS treatment was only 8.6% of that with no treatment (Table 9-3). Therefore, the relative contents of FeS and FeS_2 were too low to be detected.

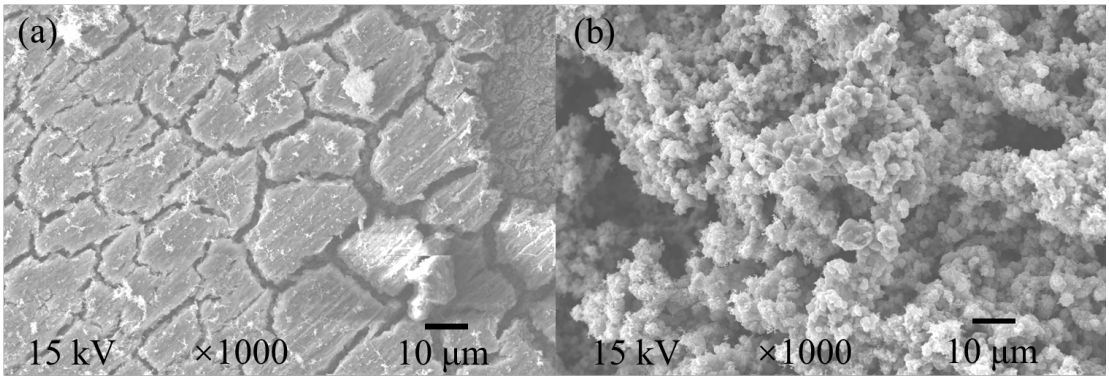

Figure 9-7. SEM images of X80 square coupons surface after 7-d *D. ferrophilus* incubation with 100 ppm THPS (a) and no treatment (b).

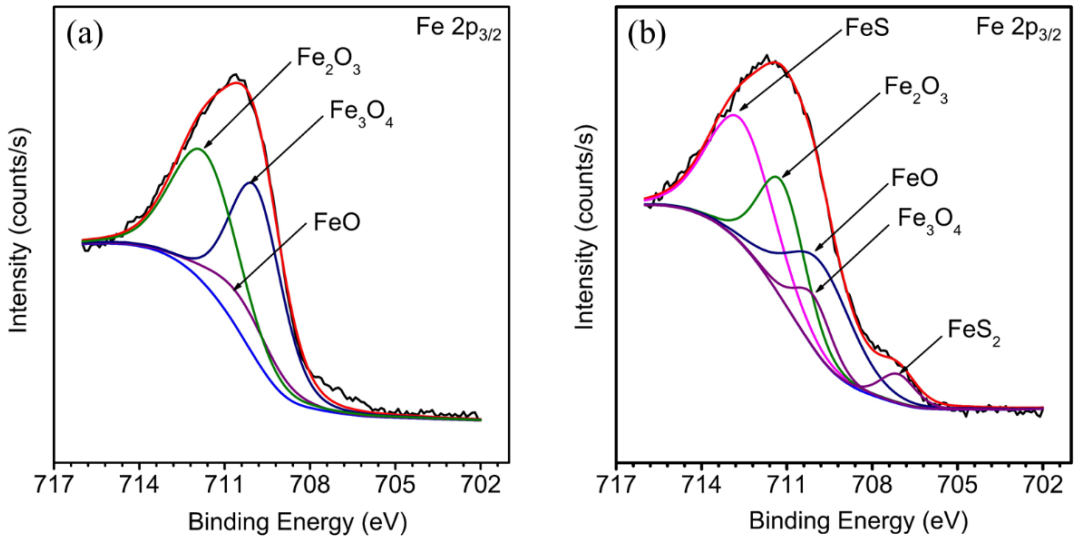

Figure 9-8. XPS spectra of corrosion production of X80 square coupons surface after 7-d *D. ferrophilus* incubation with 100 ppm THPS (a) and no treatment (b).

Table 9-3. XPS results for relative contents of key components in corrosion products of X80 steel coupon after 7-d immersion in *D. ferrophilus* medium with 100 ppm THPS treatment and no treatment.

Treatment	Corrosion product	Binding energy (eV)	At. %
No treatment	FeO	710.3 ± 0.1	21.5
	Fe_2O_3	711.2 ± 0.1	14.8
	Fe_3O_4	709.8 ± 0.1	23.6
	FeS	712.6 ± 0.1	35.4
	FeS_2	707.1 ± 0.2	4.7
100 ppm THPS	FeO	710.3 ± 0.1	36.3
	Fe_2O_3	711.2 ± 0.1	38.4
	Fe_3O_4	709.8 ± 0.1	26.3

Figure 9-9 exhibits the stress–strain curves for X80 dogbone coupons after the 7-d incubation in abiotic EASW (control) and in *D. ferrophilus* broth with no treatment and with 100 ppm THPS treatment. The abiotic curve is also shown in the figure, but it is very close to the fresh X80 dogbone coupon's curve because the deoxygenated EASW had negligible corrosion against carbon steel (Wang et al., 2021a). The ultimate tensile strength and strain data are listed in Table 9-4. A high ultimate tensile strain means that a metal is less brittle. Figure 9-9 shows that the abiotic dogbone in EASW suffered a minor degradation of mechanical properties when compared with pristine dogbone without immersion.

The abiotic dogbone's ultimate tensile strength of 867 MPa and ultimate tensile strain of 14.0% were used as the basis to calculate the microbial degradation of

mechanical properties and the 100 ppm THPS treatment effects. After the 7-d *D. ferrophilus* incubation with no treatment, the ultimate tensile strength lost 6%. In comparison, with 100 ppm THPS, the X80 dogbone suffered no loss in ultimate tensile strength. Moreover, after the 7-d *D. ferrophilus* incubation with no treatment and with 100 ppm THPS treatment, the ultimate tensile strain lost 13% and 3%, respectively. This suggests that the MIC treatment mitigated the microbial degradation of X80 mechanical properties by cutting down the losses in ultimate tensile strength and ultimate tensile strain. Therefore, to mitigate the degradation of mechanical properties caused by MIC, MIC itself must be treated Figure 9-10 graphically summarizes the main results presented in this study.

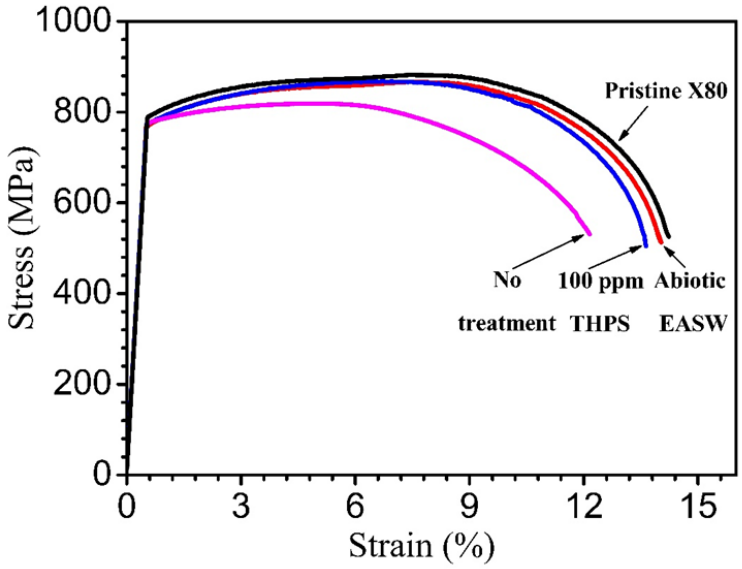

Figure 9-9. Stress–strain curves for X80 dogbone coupons after 7 d in *D. ferrophilus* broth with and without 100 ppm THPS in EASW.

Table 9-4. Ultimate tensile strength and ultimate tensile strain data.

Treatment	Ultimate tensile strength (MPa) (and loss)	Ultimate tensile strain (%) (and loss)
Abiotic EASW	867 (control)	14.0% (control)
100 ppm THPS	867 (0% loss)	13.6% (3% loss)
No treatment	819 (6% loss)	12.2% (13% loss)

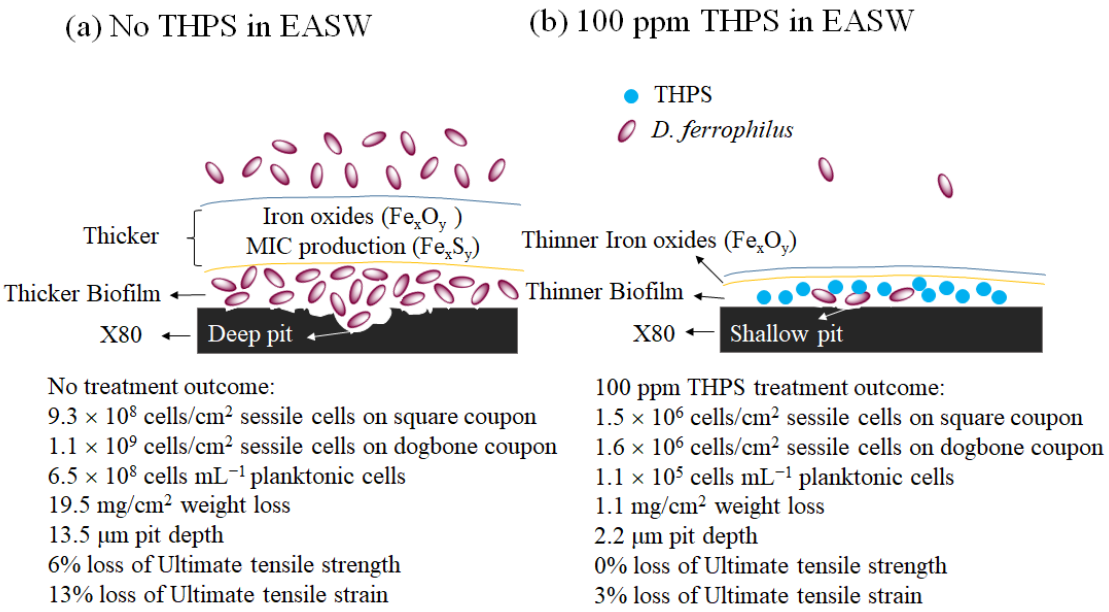

Figure 9-10. Graphic abstract for Mitigating *D. ferrophilus* MIC deterioration of Mechanical degradation of X80 Steel by no treatment (a) and 100 ppm THPS (b).

9.4 Conclusion

In this study, the significant weight loss, pitting and degradation of mechanical properties in the 7-d lab experiment were made possible by the use of a super-corrosive SRB again X80 carbon steel. The mitigation of *D. ferrophilus* biofilms on the X80 square coupons with 100 ppm THPS resulted in approximately 3-log reduction in

sessile cells compared to the no-treatment control. Because fewer sessile cells were present on the treated X80 square coupons, fewer electrons were harvested by the sessile cells from X80, leading to a much lower weight loss of 1.1 mg cm^{-2} (vs. 19.5 mg cm^{-2} for the control). The maximum pit depth dropped from 13.5 μm to 2.2 μm to practically undetectable. As a consequence, the 100 ppm THPS treatment reduced the losses of ultimate tensile strength and ultimate tensile strain. The data in this work convincingly proved the hypothesis that mitigating biofilm and MIC will reduce the microbial degradation of a carbon steel's mechanical properties.

Chapter 10: Conclusions

This work investigated biotic SCC and microbial degradation of mechanical properties using SRB which were grown in anaerobic bottles containing X80 coupons. The mechanisms of biotic SCC were investigated using two SRB strains: namely *D. vulgaris* and *D. ferrophilus* with the latter being more corrosive. X80 is a commonly used carbon steel for pipelines. The U's bottom of an X80 U-bend coupon was found to be the highest stress region according to computer simulation using FEM modeling, which was the focus of SCC. Stress was applied to X80 U-bends with a bolt. X80 (flat) square coupons were used as control for no-stress condition. The following conclusions were drawn based on the experimental data and observations in Chapter 4:

- Without a pre-crack, *D. vulgaris* MIC pitting generated tiny SCC cracks on the X80 U-bend coupon under continuous stress after only 2 weeks of incubation in ATCC 1249 culture medium.
- With a pre-crack at the bottom of the X80 U-bend coupon, *D. vulgaris* incubation caused complete SCC failure after 6 weeks of incubation, while abiotic condition did not grow the pre-crack.
- Without *D. vulgaris*, no SCC or corrosion pits were formed on the X80 U-bend coupon and X80 square coupon after 14 d of immersion in the abiotic culture medium.

- The weight loss of X80 U-bend coupon was lower than that of the square coupon (2.35 mg cm^{-2} vs. 3.83 mg cm^{-2}) after 14 d of *D. vulgaris* incubation. The corresponding sessile cell counts (2.1×10^8 cells cm^{-2} vs. 2.4×10^8 cells cm^{-2} cm^{-2}) were consistent with the weight loss trend because more sessile cells harvested more electrons released by EET-MIC caused by SRB against carbon steel. The weight loss trend was corroborated by electrochemical data. This interesting weight loss variation warrants further investigation.

In abiotic SCC, it is known that fast corrosion does not necessarily lead to fast SCC failures because fast corrosion can prevent or dissolve crack tips and convert them to less harmful corrosion pits. Chapter 5 proved the hypothesis that the same phenomenon occurs in SCC caused by MIC. This was demonstrated for the first time ever because we possessed a super-corrosive SRB, namely *D. ferrophilus*, which is several times more corrosive than *D. vulgaris.* The following conclusions were drawn based on the experimental data and observations in Chapter 5:

- Compare with *D. vulgaris* in ATCC 1249 culture medium at 37ºC, *D. ferrophilus* in EASW at 28ºC was far more corrosive, which was supported by weight loss (3.5 mg cm^{-2} vs. 23.9 mg cm^{-2}), pit depth (17.2 μm vs. 40.6 μm) data after 14 d of incubation with X80 square coupons. The weight loss data were supported by electrochemical data.

- After 12 weeks of incubation, *D. vulgaris* caused typical SCC cracks in the X80 U-bend visible easily at 25X magnifications, whereas *D. ferrophilus* did not show any cracks. *D. vulgaris* caused sharper peaks than *D. ferrophilus*, while *D. ferrophilus* led to much larger weight loss (much higher uniform corrosion rate). This was the result of fast corrosion preventing or dissolving SCC crack tips.
- Unlike in *D. vulgaris* MIC, *D. ferrophilus* had a higher weight loss (30.2 mg cm^{-2} vs. 23.9 mg cm^{-2}) and sessile cell count (8.8×10^8 cells cm^{-2} vs. 6.1×10^8 cells cm^{-2}) on X80 U-bend coupon compared to X80 square coupon. This weight loss trend was supported by electrochemical data. This interesting phenomenon warrants further investigation.

In Chapters 6 – 8, microbial degradation of mechanical properties in terms of ultimate strength and ultimate strain losses were investigated by varying SRB MIC severities against X80 coupons using three different ways. The first way was to use carbon source starvation. When pre-grown *D. vulgaris* biofilms on X80 coupons were relocated to ATCC1249 culture medium with a reduced carbon source level, carbon source starvation decreased sessile cell count, but increased the EET rate per sessile cell. The second way was to adjust the headspace to culture medium volume ratio. The more H_2S that escaped to the headspace, the less H_2S toxicity in the culture medium which promoted *D. vulgaris* growth. The third way was to increase the incubation time

from 7 d to 14 d and to 21 d. Much longer incubation time led to longer X80 exposure to *D. ferrophilus* causing more severe MIC outcome, but the MIC rate decreased because of weakened biofilm after nutrient depletion. The following conclusions were drawn from these studies:

Mechanical property degradation caused by starved D. vulgaris (Chapter 6)

- 50% carbon had the combination of carbon starvation effect without suffering too much sessile cell loss. It caused the highest weight loss and pit depth which were supported by electrochemical data.
- The H_2S, H_2 and sessile cell count data for X80 dogbone coupons were consistent in supporting higher carbon source levels for better growth exhibiting higher biogenic H_2S and H_2 concentrations in the headspace. A higher dissolved H_2S concentration at non-acidic pH in this work did not result in higher microbial degradation of mechanical properties. The data suggested that the degradation was the result of H_2S.
- The tensile test results for the biotic dogbone coupons and the fresh X80 dogbone (control) showed that more severe MIC led to larger degradation of ultimate tensile strain and ultimate tensile strength. The 50% carbon source starvation led to the highest reductions in both ultimate tensile strength (22% loss) and ultimate tensile strain (23% loss).

Mechanical property degradation caused by D. vulgaris grown with varied headspace (Chapter 7)

- The weight loss, pit depth, electrochemical results showed that a larger headspace allowed more H_2S to escape from the broth, and this reduced the H_2S toxicity in the broth, thus promoting sessile *D. vulgaris* growth. Increased sessile cell count led to more severe MIC, which is consistent with EET-MIC.
- The tensile test results for the biotic X80 dogbone coupons and the fresh X80 dogbone coupons (control) illustrated that the presence of SRB made the X80 steel less ductile as indicated by a larger ultimate strain loss (up to 23%). Meanwhile, there was no or only a small significant ultimate strength loss (no more than 3%) for all the dogbone coupons after the 14-d *D. vulgaris* incubation. More severe MIC led to more ultimate strain loss (up to 23%) in X80.

Mechanical property degradation caused by D. ferrophilus at different incubation times (Chapter 8)

- Based on the weight loss, pit depth and electrochemical results for the 21-d *D. ferrophilus* incubation test, the corrosion rates of X80 square coupons varied with incubation time. The highest cumulative weight loss (24.8 mg cm^{-2}) and pit depth (30.6 μm) occurred at 21-d of incubation. However, the highest corrosion rate (0.82 mm $year^{-1}$) and pitting rate (1.5 cm $year^{-1}$) happened at 7-

d of incubation because the biofilm was most robust without deterioration due to nutrient exhaustion at much longer incubation times.

- CLSM biofilm images and electrochemical results supported the biofilm growth and corrosion rate trends.
- *D. ferrophilus* MIC degraded the mechanical properties of X80 carbon steel. Longer incubation caused more severe MIC and led to more severe degradation of mechanical properties as reflected by ultimate strength (up to 9%) and ultimate strain (up to 18%) losses after 21 d.

This work proved the hypothesis that MIC degraded mechanical properties of X80 carbon steel. To explore a mitigation strategy, THPS, a green biocide widely used in the oil and gas industry, was used to mitigate *D. ferrophilus* MIC and to arrest the microbial degradation of mechanical properties in Chapter 9. The following conclusions were made based on the experimental data and observations:

- Compared to the no-treatment control, the mitigation of *D. ferrophilus* biofilm on the X80 square coupon with 100 ppm THPS in EASW during the 7-d incubation resulted in approximately 3-log reduction in sessile cells.
- The weight loss, pit depth, ultimate strength and ultimate strain losses were reduced with 100 ppm THPS in EASW inoculated with *D. ferrophilus*. The weight loss reduction was 94% compared to the no-treatment control. With

THPS the treatment, no pitting was detected, and the ultimate strength was higher (867 MPa vs. 819 MPa), and the ultimate strain was (13.6% vs.12.2%) compared with the no-treatment X80 dogbone after the 7-d incubation.

- Mitigating MIC will result in the prevention of microbial degradation mechanical properties. THPS was an effective biocide to mitigate SRB degradation of X80 mechanical properties.

References

Abedi, S. S., Abdolmaleki, A., & Adibi, N. (2007). Failure analysis of SCC and SRB induced cracking of a transmission oil products pipeline. *Engineering Failure Analysis, 14*(1), 250-261. https://doi.org/10.1016/j.engfailanal.2005.07.024

Abu Bakar, M., McKimm, J., Haque, S. Z., Majumder, M. A. A., & Haque, M. (2018). Chronic tonsillitis and biofilms: a brief overview of treatment modalities. *Journal of Inflammation Research, 11*, 329-337. https://doi.org/10.2147/JIR.S162486

Al-Abbas, F. M., Williamson, C., Bhola, S. M., Spear, J. R., Olson, D. L., Mishra, B., & Kakpovbia, A. E. (2013). Microbial corrosion in linepipe steel under the influence of a sulfate-reducing consortium isolated from an oil field. *Journal of Materials Engineering and Performance, 22*, 3517-3529. https://doi.org/10.1007/s11665-013-0627-7

Alpkvist, E., Picioreanu, C., van Loosdrecht, M. C., & Heyden, A. (2006). Three-dimensional biofilm model with individual cells and continuum EPS matrix. *Biotechnology and Bioengineering, 94*(5), 961-979. https://doi.org/10.1002/bit.20917

Anandkumar, B., George, R. P., Maruthamuthu, S., Parvathavarthini, N., & Mudali, U. K. (2016). Corrosion characteristics of sulfate-reducing bacteria (SRB) and the

role of molecular biology in SRB studies: an overview. *Corrosion Reviews, 34*(1-2), 41-63. https://doi.org/10.1515/corrrev-2015-0055

Araujo-Jorge, T. C. d., Coutinho, C. M., & Aguiar, L. E. V. d. (1992). Sulphate-reducing bacteria associated with biocorrosion: a review. *Memórias do Instituto Oswaldo Cruz, 87*, 329-337. https://doi.org/10.1590/S0074-02761992000300001

Asahi, H., Kushida, T., Kimura, M., Fukai, H., & Okano, S. (1999). Role of microstructures on stress corrosion cracking of pipeline steels in carbonate-bicarbonate solution. *Corrosion, 55*(7), 644-652. https://doi.org/10.5006/1.3284018

Asawa, M., Devasenapathi, A., & Fujisawa, M. (2004). Effect of corrosion product layer on SCC susceptibility of copper containing type 304 stainless steel in 1 M H_2SO4. *Materials Science and Engineering: A, 366*(2), 292-298. https://doi.org/10.1016/j.msea.2003.08.112

Ashcroft, I.A., Mubashar, A. (2011). Numerical Approach: Finite Element Analysis. In: da Silva, L.F.M., Öchsner, A., Adams, R.D. (eds) Handbook of Adhesion Technology. Springer, Berlin, Heidelberg. https://doi.org/10.1007/978-3-642-01169-6_25

Aslan, C., Aulia, N. I., Devianto, H., & Harimawan, A. (2022). Influence of axenic culture of *Bacillus clausii* and mixed culture on biofilm formation, carbon steel corrosion, and methyl ester degradation in B30 storage tank system. *Journal of*

Environmental Chemical Engineering, 10(3), 108013. https://doi.org/10.1016/j.jece.2022.108013

ASTM-E8/E8M-13a (2013). Standard Test Methods for Tension Testing of Metallic Materials, *West Conshohocken, PA: ASTM International*, https://doi.org/10.1520/E0008_E0008M-22

ASTM E9. (2000). Standard Test Methods of Compression Testing of Metallic Materials at Room Temperature. *West Conshohocken, PA: ASTM International*, 98-105. https://doi.org/10.1520/E0009-09

ASTM G1-03. (2003). Standard Practice for Preparing, Cleaning, and Evaluating Corrosion Test Specimens. Paper presented at the American Society for Testing and Materials. http://dx.doi.org/10.1520/G0001-03R11

ASTM G30. (2000). Standard practice for making and using U-bend stress-corrosion test specimens. https://doi.org/10.1520/G0030-22

Aulenta, F., Catervi, A., Majone, M., Panero, S., Reale, P., & Rossetti, S. (2007). Electron transfer from a solid-state electrode assisted by methyl viologen sustains efficient microbial reductive dechlorination of TCE. *Environmental Science & Technology, 41*(7), 2554-2559. https://doi.org/10.1021/es0624321

Bade, K., Manz, W., & Szewzyk, U. (2000). Behavior of sulfate reducing bacteria under oligotrophic conditions and oxygen stress in particle-free systems related to

drinking water. *FEMS Microbiology Ecology, 32*(3), 215-223. https://doi.org/10.1111/j.1574-6941.2000.tb00714.x

Bai, H., Kang, Y., Quan, H., Han, Y., Sun, J., & Feng, Y. (2013). Treatment of acid mine drainage by sulfate reducing bacteria with iron in bench scale runs. *Bioresource Technology, 128*, 818-822. https://doi.org/10.1016/j.biortech.2012.10.070

Ballantyne, B., & Jordan, S. L. (2003). Biocides: *Pesticide Toxicology and International Regulation* (pp. 365-409).

Barton, L. L., & Fauque, G. D. (2009). Biochemistry, physiology and biotechnology of sulfate-reducing bacteria. *Advances in Applied Microbiology, 68*, 41-98. https://doi.org/10.1016/S0065-2164(09)01202-7

Basafa, M., & Hawboldt, K. (2019). Reservoir souring: sulfur chemistry in offshore oil and gas reservoir fluids. *Journal of Petroleum Exploration and Production Technology, 9*(2), 1105-1118. https://doi.org/10.1007/s13202-018-0528-2

Batmanghelich, F., Li, L., & Seo, Y. (2017). Influence of multispecies biofilms of *Pseudomonas aeruginosa* and *Desulfovibrio vulgaris* on the corrosion of cast iron. *Corrosion Science, 121*, 94-104. https://doi.org/10.1016/j.corsci.2017.03.008

Batte, A., Fessler, R., Marr, J., & Rapp, S. (2012). *Managing the threat of SCC in gas transmission pipelines.* Paper presented at the International Pipeline Conference.

Beavers, J., & Bubenik, T. A. (2017). Stress corrosion cracking. In A. M. El-Sherik (Ed.), *Trends in Oil and Gas Corrosion Research and Technologies* (pp. 295-314). Boston: Woodhead Publishing.

Beavers, J. A., & Thompson, N. G. (2006). External corrosion of oil and natural gas pipelines. *ASM Handbook,* 05145, (pp. 1015-1024).

Beese, P., Venzlaff, H., Srinivasan, J., Garrelfs, J., Stratmann, M., & Mayrhofer, K. J. J. (2013). Monitoring of anaerobic microbially influenced corrosion via electrochemical frequency modulation. *Electrochimica Acta, 105*, 239-247. https://doi.org/10.1016/j.electacta.2013.04.144

Biezma, M. V. (2001). The role of hydrogen in microbiologically influenced corrosion and stress corrosion cracking. *International Journal of Hydrogen Energy, 26*(5), 515-520. https://doi.org/10.1016/S0360-3199(00)00091-4

Booth, G., & Tiller, A. (1960). Polarization studies of mild steel in cultures of sulphate-reducing bacteria. *Transactions of the Faraday Society, 56*, 1689-1696. https://doi.org/10.1039/TF9605601689

Borlee, B. R., Goldman, A. D., Murakami, K., Samudrala, R., Wozniak, D. J., & Parsek, M. R. (2010). *Pseudomonas aeruginosa* uses a cyclic-di-GMP-regulated adhesin to reinforce the biofilm extracellular matrix. *Molecular Microbiology, 75*(4), 827-842. https://doi.org/10.1111/j.1365-2958.2009.06991.x

Brandal, G., & Lawrence Yao, Y. (2017). Material influence on mitigation of stress corrosion cracking via laser shock peening. *Journal of Manufacturing Science and Engineering, 139*(1). https://doi.org/10.1115/1.4034283

Brileya, K. A., Camilleri, L. B., Zane, G. M., Wall, J. D., & Fields, M. W. (2014). Biofilm growth mode promotes maximum carrying capacity and community stability during product inhibition syntrophy. *Frontiers in Microbiology, 5*, 693. https://doi.org/10.3389/fmicb.2014.00693

Burt, V. (2015). Stress-Corrosion Cracking: *Corrosion in the Petrochemical Industry*. https://doi.org/10.31399/asm.tb.cpi2.t55030126

Cai, Z., Xu, J., Wei, B., & Sun, C. (2022). A comparative study of sulfate-reducing *Desulfovibrio desulfuricans* induced corrosion behaviors in Q235, X65, X70, and X80 pipeline steels. *International Journal of Pressure Vessels and Piping, 195*, 104599. https://doi.org/10.1016/j.ijpvp.2021.104599

Černoušek, T., Ševců, A., Shrestha, R., Steinová, J., Kokinda, J., & Vizelková, K. (2021). Microbially influenced corrosion of container material. *The Microbiology of Nuclear Waste Disposal* (pp. 119-136): Elsevier. https://doi.org/10.1016/B978-0-12-818695-4.00006-X

Cesiulis, H., Tsyntsaru, N., Ramanavicius, A., & Ragoisha, G. (2016). The study of thin films by electrochemical impedance spectroscopy. *Nanostructures and Thin*

Films for Multifunctional Applications: Technology, Properties and Devices, 3-42. https://doi.org/10.1007/978-3-319-30198-3_1

Chandra, K., Mahanti, A., Singh, A. P., Kain, V., & Gujar, H. G. (2019). Microbiologically influenced corrosion of 70/30 cupronickel tubes of a heat-exchanger. *Engineering Failure Analysis, 105*, 1328-1339. https://doi.org/10.1016/j.engfailanal.2019.08.005

Chatterjee, M., Fan, Y., Cao, F., Jones, A. A., Pilloni, G., & Zhang, X. (2021). Proteomic study of *Desulfovibrio ferrophilus* IS5 reveals overexpressed extracellular multi-heme cytochrome associated with severe microbiologically influenced corrosion. *Scientific Reports, 11*(1), 1-11. https://doi.org/10.1038/s41598-021-95060-0

Chen, H., Kimyon, Ö., Ramandi, H. L., Craig, P., Gunawan, C., Wu, S., Manefield, M., Crosky, A., & Saydam, S. (2022a). Microbiologically influenced stress corrosion cracking responsible for catastrophic failure of cable bolts. *Engineering Failure Analysis, 131*, 105884. https://doi.org/10.1016/j.engfailanal.2021.105884

Chen, S., Deng, H., Zhao, Y., Lu, S., Zhao, Y., Cheng, X., Liu, G., Dou, W., & Chen, J. (2021). The effects of *Methanococcus maripaludis* on the corrosion behavior of EH40 steel in seawater. *Bioelectrochemistry, 140*, 107824. https://doi.org/10.1016/j.bioelechem.2021.107824

Chen, Y., Tang, Q., Senko, J. M., Cheng, G., Newby, B.-m. Z., Castaneda, H., & Ju, L.-K. (2015). Long-term survival of *Desulfovibrio vulgaris* on carbon steel and associated pitting corrosion. *Corrosion Science, 90*, 89-100. https://doi.org/10.1016/j.corsci.2014.09.016

Chen, Z., Dou, W., Chen, S., Pu, Y., & Xu, Z. (2022b). Influence of nutrition on Cu corrosion by *Desulfovibrio vulgaris* in anaerobic environment. *Bioelectrochemistry, 144*, 108040. https://doi.org/10.1016/j.bioelechem.2021.108040

Cheng, A., & Chen, N.-Z. (2017). Corrosion fatigue crack growth modelling for subsea pipeline steels. *Ocean Engineering, 142*, 10-19. https://doi.org/10.1016/j.oceaneng.2017.06.057

Cheng, X., Shi, J., Wang, W., Liao, H., Chen, S., Liu, G., & Chen, J. (2021). Constructing nanostructured functional film on EH40 steel surface for anti-adhesion of *pseudomonas aeruginosa*. *Surface and Coatings Technology, 405*, 126683. https://doi.org/10.1016/j.surfcoat.2020.126683

Cheng, Y., Liu, P., & Yang, M. (2022). Effects of Temperature and Applied Potential on the Stress Corrosion Cracking of X80 Steel in a Xinzhou Simulated Soil Solution. *Materials, 15*(7), 2560. https://doi.org/10.3390/ma15072560

Cheng, Y. (2013). *Stress corrosion cracking of pipelines*: John Wiley & Sons. http://dx.doi.org/10.1002/9781118537022

Cheng, Y., & Niu, L. (2007). Mechanism for hydrogen evolution reaction on pipeline steel in near-neutral pH solution. *Electrochemistry Communications, 9*(4), 558-562. https://doi.org/10.1016/j.elecom.2006.10.035

Choung, J., & Cho, S. (2008). Study on true stress correction from tensile tests. *Journal of Mechanical Science and Technology, 22*, 1039-1051. https://doi.org/10.1007/s12206-008-0302-3

Coetser, S., & Cloete, T. E. (2005). Biofouling and biocorrosion in industrial water systems. *Critical Reviews in Microbiology, 31*(4), 213-232. https://doi.org/10.1080/10408410500304074

Costerton, J. W., Lewandowski, Z., Caldwell, D. E., Korber, D. R., & Lappin-Scott, H. M. (1995). Microbial biofilms. *Annual Review of Microbiology, 49*(1), 711-745. https://www.annualreviews.org/doi/pdf/10.1146/annurev.mi.49.100195.003431

Courtney, T. H. (2005). *Mechanical Behavior of Materials*: Waveland Press. https://doi.org/10.1002/crat.2170270407

CPUC & DOGGR (2019). California public utilities commission (CPUC) and department of conservation's division of oil, gas, and geothermal resources (DOGGR). Available at: https://docs.cpuc.ca.gov/PublishedDocs/Published/G000/M292/K947/292947433.PDF.

Cui, L., Liu, Z., Xu, D., Hu, P., Shao, J., Du, C., & Li, X. (2020). The study of microbiologically influenced corrosion of 2205 duplex stainless steel based on high-resolution characterization. *Corrosion Science, 174*, 108842. https://doi.org/10.1016/j.corsci.2020.108842

Cui, T., Qian, H., Lou, Y., Chen, X., Sun, T., Zhang, D., & Li, X. (2022). Single-cell level investigation of microbiologically induced degradation of passive film of stainless steel via FIB-SEM/TEM and multi-mode AFM. *Corrosion Science, 206*, 110543. https://doi.org/10.1016/j.corsci.2022.110543

Cui, Z., Liu, Z., Wang, L., Du, C., & Li, X. (2015). Effect of pH value on the crack growth behavior of X70 pipeline steel in the dilute bicarbonate solutions. *Materials Transactions, 56*(6), 777-780. https://doi.org/10.2320/matertrans.M2015096

Dao, V. H., Ryu, H. K., & Yoon, K. B. (2021). Leak failure at the TP316L welds of a water pipe caused by microbiologically influenced corrosion. *Engineering Failure Analysis, 122*, 105244. https://doi.org/10.1016/j.engfailanal.2021.105244

Deng, X., Nakamura, R., Hashimoto, K., & Okamoto, A. (2015). Electron extraction from an extracellular electrode by *Desulfovibrio ferrophilus* strain IS5 without using hydrogen as an electron carrier. *Electrochemistry, 83*(7), 529-531. https://doi.org/10.5796/electrochemistry.83.529

Dinh, H. T., Kuever, J., Mußmann, M., Hassel, A. W., Stratmann, M., & Widdel, F. (2004). Iron corrosion by novel anaerobic microorganisms. *Nature, 427*(6977), 829-832. https://doi.org/10.1038/nature02321

Djukic, M. B., Sijacki Zeravcic, V., Bakic, G. M., Sedmak, A., & Rajicic, B. (2015). Hydrogen damage of steels: A case study and hydrogen embrittlement model. *Engineering Failure Analysis, 58*, 485-498. https://doi.org/10.1016/j.engfailanal.2015.05.017

Dong, Y., Jiang, B., Xu, D., Jiang, C., Li, Q., & Gu, T. (2018). Severe microbiologically influenced corrosion of S32654 super austenitic stainless steel by acid producing bacterium *Acidithiobacillus caldus* SM-1. *Bioelectrochemistry, 123*, 34-44. https://doi.org/10.1016/j.bioelechem.2018.04.014

Dou, W., Jia, R., Jin, P., Liu, J., Chen, S., & Gu, T. (2018). Investigation of the mechanism and characteristics of copper corrosion by sulfate reducing bacteria. *Corrosion Science, 144*, 237-248. https://doi.org/10.1016/j.corsci.2018.08.055

Dou, W., Liu, J., Cai, W., Wang, D., Jia, R., Chen, S., & Gu, T. (2019). Electrochemical investigation of increased carbon steel corrosion via extracellular electron transfer by a sulfate reducing bacterium under carbon source starvation. *Corrosion Science, 150*, 258-267. https://doi.org/10.1016/j.corsci.2019.02.005

Dubey, R. S., Dubey, R., & Upadhyay, S. (1999). A review of electrochemical techniques applied to microbiologically influenced corrosion in recent studies. http://10.1016/S0378-3820(99)00038-7

Eduok, U., Ohaeri, E., & Szpunar, J. (2019). Accelerated corrosion of pipeline steel in the presence of *Desulfovibrio desulfuricans* biofilm due to carbon source deprivation in CO_2 saturated medium. *Materials Science and Engineering: C, 105*, 110095. https://doi.org/10.1016/j.msec.2019.110095

El Hosary, A., & Saleh, R. (1993). Progress in understanding and prevention of corrosion, vol. 2. *The Institute of Materials, London, 911.*

Elboujdaini, M., & Revie, R. (2009). Metallurgical factors in stress corrosion cracking (SCC) and hydrogen-induced cracking (HIC). *Journal of Solid State Electrochemistry, 13*(7), 1091-1099. https://doi.org/10.1007/s10008-009-0799-0

Eleiche, A. M., Albertini, C., & Montagnani, M. (1985). The influence of strain-rate history on the ambient tensile-strength of AISI type-316 stainless-steel. *Nuclear Engineering and Design, 88*(2), 131-141. https://doi.org/10.1016/0029-5493(85)90056-1

Enning, D., & Garrelfs, J. (2014). Corrosion of iron by sulfate-reducing bacteria: new views of an old problem. *Applied and Environmental Microbiology, 80*(4), 1226-1236. https://doi.org/10.1128/AEM.02848-13

Enning, D., Venzlaff, H., Garrelfs, J., Dinh, H. T., Meyer, V., Mayrhofer, K., Hassel, A. W., Stratmann, M., & Widdel, F. (2012). Marine sulfate-reducing bacteria cause serious corrosion of iron under electroconductive biogenic mineral crust. *Environmental Microbiology, 14*(7), 1772-1787. https://doi.org/10.1111/j.1462-2920.2012.02778.x

Etube, L. S., Brennan, F. P., & Dover, W. D. (2000). A new method for predicting stress intensity factors in cracked welded tubular joints. *International Journal of Fatigue, 22*(6), 447-456. https://doi.org/10.1016/S0142-1123(00)00024-4

Flemming, H. C., Neu, T. R., & Wozniak, D. J. (2007). The EPS matrix: the "house of biofilm cells". *Journal of Bacteriology, 189*(22), 7945-7947. https://doi.org/10.1128/JB.00858-07

Flemming, H. C., & Wingender, J. (2010). The biofilm matrix. *Nature Reviews Microbiology, 8*(9), 623-633. https://doi.org/10.1038/nrmicro2415

Flemming, H. C., Wingender, J., Szewzyk, U., Steinberg, P., Rice, S. A., & Kjelleberg, S. (2016). Biofilms: an emergent form of bacterial life. *Nature Reviews Microbiology, 14*(9), 563-575. https://doi.org/10.1038/nrmicro.2016.94

Ford, F. (1982). Mechanisms of stress corrosion cracking. *Aspects of Fracture Mechanics in Pressure Vessels and Piping*, 229-269

Ford, F. (1996). Quantitative prediction of environmentally assisted cracking. *Corrosion, 52*(5), 375-395. https://doi.org/10.5006/1.3292125

Funari, R., & Shen, A. Q. (2022). Detection and characterization of bacterial biofilms and biofilm-based sensors. *ACS Sensors, 7*(2), 347-357. https://doi.org/10.1021/acssensors.1c02722

Gabrielli, C., Keddam, M., Takenouti, H., Kinh, V. Q., & Bourelier, F. (1979). The relationship between the impedance of corroding electrode and its polarization resistance determined by a linear voltage sweep technique. *Electrochimica Acta, 24*(1), 61-65. https://doi.org/10.1016/0013-4686(79)80042-0

Galvele, J. R. (1995). Electrochemical aspects of stress corrosion cracking. *Modern Aspects of Electrochemistry*, 233-358. https://doi.org/10.1007/978-1-4899-1724-9_3

Gerchakov, S. M., Udey, L. R., & Mansfeld, F. (1981). An Improved Method for Analysis of Polarization Resistance Data. *Corrosion, 37*(12), 696-700. https://doi.org/10.5006/1.3577560

Ghiasi, V., Omar, H., Yusoff, Z. B. M., Huat, B. K., Muniandy, R., & Alias, M. N. (2010). A New Model of Microcracks Propagation in Granite Rock. *Australian Journal of Basic and Applied Sciences, 1*(1), 1-23. https://www.ajbasweb.com/old/ajbas/2010/5830-5851.pdf

Gopi, D., Govindaraju, K. M., Manimozhi, S., Ramesh, S., & Rajeswari, S. (2007). Inhibitors with biocidal functionalities to mitigate corrosion on mild steel in

natural aqueous environment. *Journal of Applied Electrochemistry, 37*(6), 681-689. https://doi.org/10.1007/s10800-007-9300-x

Gou, J., Nie, R., Xing, X., Li, Z., Cui, G., Liu, J., Deng, X., & Cheng, Y. F. (2023). Hydrogen-induced cracking of welded X80 steel studies by experimental testing and molecular dynamics modeling. *Corrosion Science, 214*, 111027. https://doi.org/10.1016/j.corsci.2023.111027

Gu, T., Jia, R., Unsal, T., & Xu, D. (2019). Toward a better understanding of microbiologically influenced corrosion caused by sulfate reducing bacteria. *Journal of Materials Science & Technology, 35*(4), 631-636. https://doi.org/10.1016/j.jmst.2018.10.026

Gu, T., & Xu, D. (2013). *Why are some microbes corrosive and some not?* Paper presented at the CORROSION 2013.

Gu, T., Zhao, K., & Nesic, S. (2009). *A new mechanistic model for MIC based on a biocatalytic cathodic sulfate reduction theory.* Paper presented at the CORROSION 2009.

Hagarová, M., Cervová, J., & Jas, F. (2015). Selected types of corrosion degradation of pipelines. *Koroze a Ochrana Materiálu, 59*(1), 30. https://doi.org/10.1515/kom-2015-0010

Hall-Stoodley, L., Costerton, J. W., & Stoodley, P. (2004). Bacterial biofilms: from the natural environment to infectious diseases. *Nature Reviews Microbiology, 2*(2), 95-108. https://doi.org/10.1038/nrmicro821

Hall-Stoodley, L., & Stoodley, P. (2005). Biofilm formation and dispersal and the transmission of human pathogens. *Trends in Microbiology, 13*(1), 7-10. https://doi.org/10.1016/j.tim.2004.11.004

Huang, F., Liu, J., Deng, Z., Cheng, J., Lu, Z., & Li, X. (2010). Effect of microstructure and inclusions on hydrogen induced cracking susceptibility and hydrogen trapping efficiency of X120 pipeline steel. *Materials Science and Engineering: A, 527*(26), 6997-7001. https://doi.org/10.1016/j.msea.2010.07.022

Hwang, W., Bae, S., Kim, J., Kang, S., Kwag, N., & Lee, B. (2015). Acoustic emission characteristics of stress corrosion cracks in a type 304 stainless steel tube. *Nuclear Engineering and Technology, 47*(4), 454-460. https://doi.org/10.1016/j.net.2015.04.001

Iverson, W., & Olson, G. (1983). Anaerobic corrosion by sulfate-reducing bacteria due to highly reactive volatile phosphorus compound. *Microbial Corrosion*, 46-53. https://www.osti.gov/biblio/5175515

Iverson, W. P. (2001). Research on the mechanisms of anaerobic corrosion. *International Biodeterioration & Biodegradation, 47*(2), 63-70. https://doi.org/10.1016/S0964-8305(00)00111-6

Jack, T. R., Krist, K., Erno, B., & Fessler, R. R. (2000). *Generation of near neutral pH and high pH SCC environments on buried pipelines.* Paper presented at the CORROSION 2000.

Jacobson, G. A. (2007a). Corrosion at Prudhoe Bay: A lesson on the line. *Materials Performance*, *46*(8), 26–35.

Jakubowski, M. (2015). Influence of pitting corrosion on fatigue and corrosion fatigue of ship and offshore structures, part II: load - pit - crack interaction. *Polish Maritime Research, 22*(3), 57-66. https://doi.org/10.1515/pomr-2015-0057

Javaherdashti, R. (2011). Impact of sulphate-reducing bacteria on the performance of engineering materials. *Applied Microbiology and Biotechnology, 91*(6), 1507. https://doi.org/10.1007/s00253-011-3455-4

Javed, M. A., Neil, W. C., McAdam, G., Moreau, J. W., & Wade, S. A. (2020a). Microbiologically Influenced Corrosion of Stainless Steel by Sulfate Reducing Bacteria: A Tale of Caution. *Corrosion, 76*(7), 639-653. https://doi.org/10.5006/3467

Javed, M. A., Rieders, N., Beech, I., Avci, R., Neil, W. C., & Wade, S. A. (2020b). The influence of chemical cleaning methods on pitting morphology attributed to microbially influenced corrosion of stainless steels. *Corrosion, 77*(3), 276-286. https://doi.org/10.5006/3707

Jia, R., Tan, J. L., Jin, P., Blackwood, D. J., Xu, D., & Gu, T. (2018a). Effects of biogenic H_2S on the microbiologically influenced corrosion of C1018 carbon steel by sulfate reducing *Desulfovibrio vulgaris* biofilm. *Corrosion Science, 130*, 1-11. https://doi.org/10.1016/j.corsci.2017.10.023

Jia, R., Unsal, T., Xu, D., Lekbach, Y., & Gu, T. (2019a). Microbiologically influenced corrosion and current mitigation strategies: A state of the art review. *International Biodeterioration & Biodegradation, 137*, 42-58. https://doi.org/10.1016/j.ibiod.2018.11.007

Jia, R., Wang, D., Jin, P., Unsal, T., Yang, D., Yang, J., Xu, D., & Gu, T. (2019b). Effects of ferrous ion concentration on microbiologically influenced corrosion of carbon steel by sulfate reducing bacterium *Desulfovibrio vulgaris*. *Corrosion Science, 153*, 127-137. https://doi.org/10.1016/j.corsci.2019.03.038.

Jia, R., Yang, D., Al-Mahamedh, H. H., & Gu, T. (2017a). Electrochemical testing of biocide enhancement by a mixture of D-amino acids for the prevention of a corrosive biofilm consortium on carbon steel. *Industrial & Engineering Chemistry Research, 56*(27), 7640-7649. https://doi.org/10.1021/acs.iecr.7b01534

Jia, R., Yang, D., Xu, D., & Gu, T. (2017b). Electron transfer mediators accelerated the microbiologically influence corrosion against carbon steel by nitrate reducing

Pseudomonas aeruginosa biofilm. *Bioelectrochemistry (Amsterdam, Netherlands), 118*, 38-46. https://doi.org/10.1016/j.bioelechem.2017.06.013

Jia, R., Yang, D., Xu, D., & Gu, T. (2018b). Carbon steel biocorrosion at 80 °C by a thermophilic sulfate reducing archaeon biofilm provides evidence for its utilization of elemental iron as electron donor through extracellular electron transfer. *Corrosion Science, 145*, 47-54. https://doi.org/10.1016/j.corsci.2018.09.015

Jia, R., Yang, D., Dou, W., Liu, J., Zlotkin, A., Kumseranee, S., Punpruk, S., Li, X. G., & Gu, T. Y. (2019c). A sea anemone-inspired small synthetic peptide at sub-ppm concentrations enhanced biofilm mitigation. *International Biodeterioration & Biodegradation, 139*, 78-85. https://doi.org/10.1016/j.ibiod.2018.11.009

Jin, Z., Liu, H., Wang, Z., Zhang, W., Chen, Y., Zhao, T., Meng, G., Liu, H., & Liu, H. (2022). Enhancement of anticorrosion and antibiofouling performance of self-healing epoxy coating using nano-hydrotalcite materials and bifunctional biocide sodium pyrithione. *Progress in Organic Coatings, 172*, 107121. https://doi.org/10.1016/j.porgcoat.2022.107121

Jurelevicius, D., Ramos, L., Abreu, F., Lins, U., de Sousa, M. P., dos Santos, V. V. C. M., Penna, M., & Seldin, L. (2021). Long-term souring treatment using nitrate and biocides in high-temperature oil reservoirs. *Fuel, 288*, 119731. https://doi.org/10.1016/j.fuel.2020.119731

Kahrilas, G. A., Blotevogel, J., Stewart, P. S., & Borch, T. (2015). Biocides in hydraulic fracturing fluids: A critical review of their usage, mobility, degradation, and toxicity. *Environmental Science & Technology, 49*(1), 16-32. https://doi.org/10.1021/es503724k

Khalifeh, A. (2019). Stress Corrosion Cracking Damages. *Failure Analysis*. https://doi.org/10.5772/INTECHOPEN.80826

Khan, A. J. (2016). Detecting Pipeline Stress Corrosion Cracking through Direct Assessment., from http://www.materialsperformance.com/articles/material-selection-design/2016/06/detecting-pipeline-stress-corrosion-cracking-through-direct-assessment

Khan, M. S., Liang, T., Liu, Y., Shi, Y., Zhang, H., Li, H., Guo, S., Pan, H., Yang, K., & Zhao, Y. (2022). Microbiologically Influenced Corrosion Mechanism of Ferrous Alloys in Marine Environment. *Metals, 12*(9), 1458. https://doi.org/10.3390/met12091458

King, R., & Miller, J. (1971). Corrosion by the sulphate-reducing bacteria. *Nature, 233*(5320), 491-492. https://doi.org/10.1038/233491a0

Kostakioti, M., Hadjifrangiskou, M., & Hultgren, S. J. (2013). Bacterial biofilms: development, dispersal, and therapeutic strategies in the dawn of the postantibiotic era. *Cold Spring Harbor Perspectives in Medicine, 3*(4), a010306. https://doi.org/10.1101/cshperspect.a010306

Labjar, N., Lebrini, M., Bentiss, F., Chihib, N. E., El Hajjaji, S., & Jama, C. (2010). Corrosion inhibition of carbon steel and antibacterial properties of aminotris-(methylenephosphonic) acid. *Materials Chemistry and Physics, 119*(1-2), 330-336. https://doi.org/10.1016/j.matchemphys.2009.09.006

Lazzari, L. (2019). Mechanistic model for stress corrosion cracking-anodic dissolution mechanism. *Metallurgia Italiana* (11-12), 21-25. http://www.aimnet.it/la_metallurgia_italiana/2019/novembredicembre/lazzari.pdf

Leis, B., Bubenik, T., & Nestleroth, J. (1996). Stress-corrosion cracking in pipelines. *Pipeline and Gas Journal, 223*(8). https://doi.org/10.3390/ma13245771

Li, H., Xu, D., Li, Y., Feng, H., Liu, Z., Li, X., Gu, T., & Yang, K. (2015). Extracellular electron transfer is a bottleneck in the microbiologically influenced corrosion of C1018 carbon steel by the biofilm of sulfate-reducing bacterium *Desulfovibrio vulgaris*. *PloS one, 10*(8), e0136183. https://doi.org/10.1371/journal.pone.0136183

Li, K., Zeng, Y., & Luo, J. L. (2021a). Influence of H_2S on the general corrosion and sulfide stress cracking of pipelines steels for supercritical CO_2 transportation. *Corrosion Science, 190*, 109639. https://doi.org/10.1016/j.corsci.2021.109639

Li, L., Mahmoodian, M., Li, C. Q., & Robert, D. (2018a). Effect of corrosion and hydrogen embrittlement on microstructure and mechanical properties of mild

steel. *Construction and Building Materials, 170*, 78-90. https://doi.org/10.1016/j.conbuildmat.2018.03.023

Li, Q., Wang, J., Xing, X., & Hu, W. (2018b). Corrosion behavior of X65 steel in seawater containing sulfate reducing bacteria under aerobic conditions. *Bioelectrochemistry, 122*, 40-50. https://doi.org/10.1016/j.bioelechem.2018.03.003

Li, X., Xie, F., Wang, D., Xu, C., Wu, M., Sun, D., & Qi, J. (2018c). Effect of residual and external stress on corrosion behaviour of X80 pipeline steel in sulphate-reducing bacteria environment. *Engineering Failure Analysis, 91*, 275-290. https://doi.org/10.1016/j.engfailanal.2018.04.016

Li, Y., Feng, S., Liu, H., Tian, X., Xia, Y., Li, M., Xu, K., Yu, H., Liu, Q., & Chen, C. (2020). Bacterial distribution in SRB biofilm affects MIC pitting of carbon steel studied using FIB-SEM. *Corrosion Science, 167*, 108512. https://doi.org/10.1016/j.corsci.2020.108512

Li, Y., Jia, R., Al-Mahamedh, H. H., Xu, D., & Gu, T. (2016). Enhanced Biocide Mitigation of Field Biofilm Consortia by a Mixture of D-Amino Acids. *Frontiers in Microbiology, 7*. https://doi.org/10.3389/fmicb.2016.00896

Li, Y., & Ning, C. (2019). Latest research progress of marine microbiological corrosion and bio-fouling, and new approaches of marine anti-corrosion and anti-fouling.

Bioactive Materials, 4, 189-195. https://doi.org/10.1016/j.bioactmat.2019.04.003

Li, Y., Xu, D., Chen, C., Li, X., Jia, R., Zhang, D., Sand, W., Wang, F., & Gu, T. (2018d). Anaerobic microbiologically influenced corrosion mechanisms interpreted using bioenergetics and bioelectrochemistry: a review. *Journal of Materials Science & Technology, 34*(10), 1713-1718. https://doi.org/10.1016/j.jmst.2018.02.023

Li, Z., Huang, L., Hao, W., Yang, J., Qian, H., & Zhang, D. (2022a). Accelerating effect of pyocyanin on microbiologically influenced corrosion of 304 stainless steel by the *Pseudomonas aeruginosa* biofilm. *Bioelectrochemistry, 146*, 108130. https://doi.org/10.1016/j.bioelechem.2022.108130

Li, Z., Yang, J., Lu, S., Dou, W., & Gu, T. (2023). Stress corrosion cracking failure of X80 carbon steel U-bend caused by *Desulfovibrio vulgaris* biocorrosion. *Journal of Materials Science & Technology*. (Submitted to a journal).

Li, Z., Yang, J., Guo, H., Kumseranee, S., Punpruk, S., Mohamed, M. E., Saleh, M. A., & Gu, T. (2021b). Carbon source starvation of a sulfate-reducing bacterium-elevated MIC deterioration of tensile strength and strain of X80 pipeline steel. *Frontiers in Materials, 8*, 536. https://doi.org/10.3389/fmats.2021.794051

Li, Z., Yang, J., Guo, H., Kumseranee, S., Punpruk, S., Mohamed, M. E., Saleh, M. A., & Gu, T. (2022b). Mechanical property degradation of X80 pipeline steel due

to microbiologically influenced corrosion caused by *Desulfovibrio vulgaris*. *Frontiers in Bioengineering and Biotechnology, 10*, 1028462. https://doi.org/10.3389/fbioe.2022.1028462

Li, Z., Zhou, J., Yuan, X., Xu, Y., Xu, D., Zhang, D. , Feng, D., & Wang, F. (2021d). Marine biofilms with significant corrosion inhibition performance by secreting extracellular polymeric substances. *ACS Applied Materials & Interfaces, 13*(39), 47272-47282. https://doi.org/10.1021/acsami.1c14746

Lim, H., & Hoag, S. W. (2013). Plasticizer Effects on Physical–Mechanical Properties of Solvent Cast Soluplus® Films. *AAPS PharmSciTech, 14*(3), 903-910. https://doi.org/10.1208/s12249-013-9971-z

Little, B. J., & Lee, J. S. (2007). *Microbiologically Influenced Corrosion* (Vol. 3): John Wiley & Sons. https://doi.org/10.1002/9783527610426.bard040603

Liu, H., Chen, C., Asif, M., Zhao, T., Lei, B., Meng, G., & Liu, H. (2022a). Mechanistic investigations of corrosion and localized corrosion of X80 steel in seawater comprising sulfate-reducing bacteria under continuous carbon starvation. *Corrosion Communications, 8*, 70-80. https://doi.org/10.1016/j.corcom.2022.08.002

Liu, H., & Cheng, Y. F. (2020). Corrosion of initial pits on abandoned X52 pipeline steel in a simulated soil solution containing sulfate-reducing bacteria. *Journal*

of Materials Research and Technology, 9(4), 7180-7189. https://doi.org/10.1016/j.jmrt.2020.04.090

Liu, H., Meng, G., Li, W., Gu, T., & Liu, H. (2019a). Microbiologically Influenced Corrosion of Carbon Steel Beneath a Deposit in CO2-Saturated Formation Water Containing Desulfotomaculum nigrificans. *Frontiers in Microbiology, 10*. https://doi.org/10.3389/fmicb.2019.01298

Liu, H. W., Gu, T. , Zhang, G. , Liu, H. , & Cheng, Y. (2018a). Corrosion of X80 pipeline steel under sulfate-reducing bacterium biofilms in simulated CO_2-saturated oilfield produced water with carbon source starvation. *Corrosion Science, 136*, 47-59. https://doi.org/10.1016/j.corsci.2018.02.038

Liu, H. , Jin, Z. , Liu, H. , Meng, G. , & Liu, H. (2022b). Microbiological corrosion acceleration of N80 steel in shale gas field produced water containing *Citrobacter amalonaticus* at 60 ℃. *Bioelectrochemistry, 148*, 108253. https://doi.org/10.1016/j.bioelechem.2022.108253

Liu, H. X., Jin, Z. , Wang, Z., Liu, H. , Meng, G. , & Liu, H. (2023). Corrosion inhibition of deposit-covered X80 pipeline steel in seawater containing *Pseudomonas stutzeri*. *Bioelectrochemistry, 149*, 108279. https://doi.org/10.1016/j.bioelechem.2022.108279

Liu, J., Jia, R., Zhou, E., Zhao, Y., Dou, W., Xu, D., Yang, K., & Gu, T. (2018b). Antimicrobial Cu-bearing 2205 duplex stainless steel against MIC by nitrate

reducing *Pseudomonas aeruginosa* biofilm. *International Biodeterioration & Biodegradation, 132*, 132-138. https://doi.org/10.1016/j.ibiod.2018.03.002

Liu, Z., Li, Q., Cui, Z., Wu, W., Li, Z., Du, C., & Li, X. (2017). Field experiment of stress corrosion cracking behavior of high strength pipeline steels in typical soil environments. *Construction and Building Materials, 148*, 131-139. https://doi.org/10.1016/j.conbuildmat.2017.05.058

Liu, Z., Wang, X., Tang, J., Deng, C., Zhao, H., & Chen, X. (2019b). The effects of in-plane and out-of-plane constraints on J-R curves for X80 steel: A study using clamped SENT specimens. *Engineering Fracture Mechanics, 206*, 342-358. https://doi.org/10.1016/j.engfracmech.2018.12.004

Liu, Z. Y., Li, X. G., & Cheng, Y. (2012). Mechanistic aspect of near-neutral pH stress corrosion cracking of pipelines under cathodic polarization. *Corrosion Science, 55*, 54-60. https://doi.org/10.1016/j.corsci.2011.10.002

López-Celvera, S. A., Orozco-Cruz, R., Mejía-Sánchez, E., Contreras-Cuevas, A., & Galván-Martínez, R. (2018). Corrosion of API X80 steel Immersed in seawater: Application of Electrochemical Noise Technique. *ECS Transactions, 84*(1), 117. https://doi.org/10.1149/08401.0117ecst

Loto, C. A. (2017). Stress corrosion cracking: characteristics, mechanisms and experimental study. *The International Journal of Advanced Manufacturing Technology, 93*(9), 3567-3582. https://doi.org/10.1007/s00170-017-0709-z

Lou, Y., Chang, W., Cui, T., Wang, J., Qian, H., Ma, L., Hao, X., & Zhang, D. (2021). Microbiologically influenced corrosion inhibition mechanisms in corrosion protection: A review. *Bioelectrochemistry, 141*, 107883. https://doi.org/10.1016/j.bioelechem.2021.107883

Lovley, D. R., & Phillips, E. J. (1994). Novel processes for anaerobic sulfate production from elemental sulfur by sulfate-reducing bacteria. *Applied and Environmental Microbiology, 60*(7), 2394-2399. https://doi.org/10.1128/aem.60.7.2394-2399.1994

Lu, S., Dou, W., Gu, T., Chen, S., Cheng, X., Hou, R., Wang, Y., Zhang, Y., & Liu, G. (2023a). Extracellular electron transfer corrosion mechanism of two marine structural steels caused by nitrate reducing *Halomonas titanicae*. *Corrosion Science, 217*, 111125. https://doi.org/10.1016/j.corsci.2023.111125

Lu, S., He, Y., Xu, R., Wang, N., Chen, S., Dou, W., Cheng, X., & Liu, G. (2023b). Inhibition of microbial extracellular electron transfer corrosion of marine structural steel with multiple alloy elements. *Bioelectrochemistry, 151*, 108377. https://doi.org/10.1016/j.bioelechem.2023.108377

Luecke, W. E., Luecke, W. E., McColskey, J. D., McCowan, C. N., Banovic, S. W., Fields, R. J., Foecke, T., Siewert, T. A., & Gayle, F. W. (2005). *Mechanical properties of structural steels*: National Institute of Standards and Technology, Technology Administration.

Mainier, F. B., Almeida, P. C. F., Nani, B., Fernandes, L. H., & Reis, M. F. (2015). Corrosion caused by sulfur dioxide in reinforced concrete. *Open Journal of Civil Engineering, 5*(04), 379. https://doi.org/10.4236/ojce.2015.54038

Manfredi, C., & Otegui, J. L. (2002). Failures by SCC in buried pipelines. *Engineering Failure Analysis, 9*(5), 495-509. https://doi.org/10.1016/S1350-6307(01)00032-2

Materials Performance. (2020). Stress Corrosion Cracking Led to Canadian Pipeline Rupture, Fire. from https://www.materialsperformance.com/articles/coating-linings/2020/04/stress-corrosion-cracking-led-to-canadian-pipeline-rupture-fire

McCafferty, E. (2005). Validation of corrosion rates measured by the Tafel extrapolation method. *Corrosion Science, 47*(12), 3202-3215. https://doi.org/10.1016/j.corsci.2005.05.046

Megson, T. H. G. (2016). *Aircraft structures for engineering students*: Butterworth-Heinemann. https://doi.org/10.1016/C2009-0-61214-9

Melchers, R. E. (2005). The effect of corrosion on the structural reliability of steel offshore structures. *Corrosion Science, 47*(10), 2391-2410. https://doi.org/10.1016/j.corsci.2005.04.004

Mohammed, I., Isah, A., Al Shehri, D., Mahmoud, M., Arif, M., Kamal, M. S., & Patil, S. (2022). Effect of sulfate-based scales on calcite mineral surface chemistry:

Insights from zeta-potential experiments and their implications on wettability. *ACS Omega, 7*(2470-1343 (Electronic)), 28571-28587. https://doi.org/10.1021/acsomega.2c03403

Mori, K., Tsurumaru, H., & Harayama, S. (2010). Iron corrosion activity of anaerobic hydrogen-consuming microorganisms isolated from oil facilities. *Journal of Bioscience and Bioengineering, 110*(4), 426-430. https://doi.org/10.1016/j.jbiosc.2010.04.012

Mukhopadhyay, N. K., Sridhar, G., Parida, N., Tarafder, S., & Ranganath, V. R. (2001). Hydrogen embrittlement failure of hot dip galvanised high tensile wires. *Failure Analysis Case Studies II*, 393-405. https://doi.org/10.1016/B978-0-08-043959-4.50040-7

Niazi, H., Eadie, R., Chen, W., & Zhang, H. (2021). High pH stress corrosion cracking initiation and crack evolution in buried steel pipelines: A review. *Engineering Failure Analysis, 120*, 105013. https://doi.org/10.1016/j.engfailanal.2020.105013

Ning, J., Zheng, Y., Young, D., Brown, B., & Nešić, S. (2014). Thermodynamic study of hydrogen sulfide corrosion of mild steel. *Corrosion, 70*(4), 375-389. https://doi.org/10.5006/0951

Ning, J., Zheng, Y. G., Brown, B., Young, D., & Nesic, S. (2015). *Construction and verification of pourbaix diagrams for hydrogen sulfide corrosion of mild steel*. Paper presented at the CORROSION 2015.

Nyrkova, L. (2020). Stress-corrosion cracking of pipe steel under complex influence of factors. *Engineering Failure Analysis, 116*, 104757. https://doi.org/10.1016/j.engfailanal.2020.104757

Obuekwe, C., Westlake, D., Plambeck, J., & Cook, F. (1981). Corrosion of Mild Steel in Cultures of Ferric Iron Reducing Bacterium Isolated from Crude Oil. *Corrosion, 37*(11), 632-637. https://doi.org/10.5006/1.3577551

Odom, J. M., & Singleton, R. (1993). *The Sulfate-Reducing Bacteria: Contemporary Perspectives*: Springer. https://doi.org/10.1007/978-1-4613-9263-7

Ohaeri, E., Eduok, U., & Szpunar, J. (2018). Hydrogen related degradation in pipeline steel: A review. *International Journal of Hydrogen Energy, 43*(31), 14584-14617. https://doi.org/10.1016/j.ijhydene.2018.06.064

Okoro, C. C., Samuel, O., & Lin, J. (2016). The effects of Tetrakis-hydroxymethyl phosphonium sulfate (THPS), nitrite and sodium chloride on methanogenesis and corrosion rates by methanogen populations of corroded pipelines. *Corrosion Science, 112*, 507-516. https://doi.org/10.1016/j.corsci.2016.08.018

Ollivier, B., Cayol, J. L., & Fauque, G. (2007). Sulphate-reducing bacteria from oil field environments and deepsea hydrothermal vents. *Barton L, Hamilton W.,*

Sulphate-reducing Bacteria: Environmental and Engineered Systems. https://doi.org/10.1017/CBO9780511541490

Pal, S., Bhadauria, S. S., & Kumar, P. (2022). Corrosion pit to crack transition behavior of 304 stainless steel in a chloride solution. *Journal of Bio- and Tribo-Corrosion, 8*(1), 33. https://doi.org/10.1007/s40735-022-00633-9

Parkins, R. N. (1980). Predictive approaches to stress corrosion cracking failure. *Corrosion Science, 20*(2), 147-166. https://doi.org/10.1016/0010-938X(80)90128-6

Peck, H. D. (1993). Bioenergetic strategies of the sulfate-reducing bacteria. *The Sulfate-Reducing Bacteria: Contemporary Perspectives*, 41-76. https://doi.org/10.1007/978-1-4613-9263-7_3

Quej-Ake, L. M., Rivera-Olvera, J. N., Domínguez-Aguilar, Y. D., Avelino-Jiménez, I. A., Garibay-Febles, V., & Zapata-Peñasco, I. (2020). Analysis of the physicochemical, mechanical, and electrochemical parameters and their impact on the internal and external SCC of carbon steel pipelines. *Materials, 13*(24). https://doi.org/10.3390/ma13245771

Rahimi, S., Mehrez, K., & Marrow, T. (2016). Effect of surface machining on intergranular stress corrosion cracking (IGSCC) in sensitised type 304 austenitic stainless steel. *Corrosion Engineering, Science and Technology, 51*(5), 383-391. https://doi.org/10.1080/1478422X.2015.1122295

Raja, V. (2011). *Stress corrosion cracking: theory and practice*: Elsevier. https://doi.org/10.1201/9780203909188

Raman, R. K. S. (2003). Interplay of microbiological corrosion and alloy microstructure in stress corrosion cracking of weldments of advanced stainless steels. *Sadhana, 28*(3), 467-473. https://doi.org/10.1007/BF02706444

Ramesh, S., Rajeswari, S., & Maruthamuthu, S. (2003). Effect of inhibitors and biocide on corrosion control of mild steel in natural aqueous environment. *Materials Letters, 57*(29), 4547-4554. https://doi.org/10.1016/S0167-577X(03)00360-4

Ren, S., & Ren, X. (2018). Studies on laws of stress-magnetization based on magnetic memory testing technique. *Journal of Magnetism and Magnetic Materials, 449*, 165-171. https://doi.org/10.1016/j.jmmm.2017.09.050

Reza, J. (2008). Microbiologically influenced corrosion an engineering insight: Springer-Verlag London Limited. https://doi.org/10.1007/978-1-84800-074-2

Rokkam, S., Gunzburger, M., Brothers, M., Phan, N., & Goel, K. (2019). A nonlocal peridynamics modeling approach for corrosion damage and crack propagation. *Theoretical and Applied Fracture Mechanics, 101*, 373-387. https://doi.org/10.1016/j.tafmec.2019.03.010

Rosenfeld, M. J., & Kiefner, J. F. (2006). Basics of metal fatigue in natural gas pipeline systems–A primer for gas pipeline operators. *Pipeline Research Council*

International, Houston, TX. Available at: https://ingaa.org/wp-content/uploads/2016/07/29880.pdf

Rosnes Jan, T., Torsvik, T., & Lien, T. (1991). Spore-forming thermophilic sulfate-reducing bacteria isolated from North Sea oil field waters. *Applied and Environmental Microbiology, 57*(8), 2302-2307. https://doi.org/10.1128/aem.57.8.2302-2307.1991

Roylance, D. (2001). *Introduction to fracture mechanics* (Cambridge, MA: Massachusetts Institute of Technology) 1–17.

Rumbaugh, K. P., & Sauer, K. (2020). Biofilm dispersion. *Nature Reviews Microbiology, 18*(10), 571-586. https://doi.org/10.1038/s41579-020-0385-0

Sadananda, K., & Vasudevan, A. K. (2020). Analysis of pit to crack transition under corrosion fatigue & the safe-life approach using the modified Kitagawa-Takahashi diagram. *International Journal of Fatigue, 134*, 105471. https://doi.org/10.1016/j.ijfatigue.2020.105471

Salgar-Chaparro, S. J., Darwin, A., Kaksonen, A. H., & Machuca, L. L. (2020). Carbon steel corrosion by bacteria from failed seal rings at an offshore facility. *Scientific Reports, 10*(1), 1-15. https://doi.org/10.1038/s41598-020-69292-5

Sanchez, C. J., Akers, K. S., Romano, D. R., Woodbury, R. L., Hardy, S. K., Murray, C. K., & Wenke, J. C. (2014). D-Amino acids enhance the activity of antimicrobials against biofilms of clinical wound isolates of *Staphylococcus*

aureus and *Pseudomonas aeruginosa*. *Antimicrobial Agents and Chemotherapy, 58*(8), 4353-4361. https://doi.org/10.1128/Aac.02468-14

Sasser, J., Fieldhouse, D., & Carter, C. (1984). *Computer-assisted Identification of Bacteria Based on Fatty-acid Analysis.* Paper presented at the Phytopathology.

Sharma, M., Liu, H., Chen, S., Cheng, F., Voordouw, G., & Gieg, L. (2018). Effect of selected biocides on microbiologically influenced corrosion caused by *Desulfovibrio ferrophilus* IS5. *Scientific Reports, 8*(1), 16620. https://doi.org/10.1038/s41598-018-34789-7

Sherar, B., Power, I., Keech, P., Mitlin, S., Southam, G., & Shoesmith, D. (2011). Characterizing the effect of carbon steel exposure in sulfide containing solutions to microbially induced corrosion. *Corrosion Science, 53*(3), 955-960. https://doi.org/10.1016/j.corsci.2010.11.027

Shi, C., Gong, Y., Yang, Z.-G., & Tong, Q. (2019). Peridynamic investigation of stress corrosion cracking in carbon steel pipes. *Engineering Fracture Mechanics, 219*, 106604. https://doi.org/10.1016/j.engfracmech.2019.106604

Shiraz, H. G., Crispin, X., & Berggren, M. (2021). Transition metal sulfides for electrochemical hydrogen evolution. *International Journal of Hydrogen Energy, 46*(47), 24060-24077. https://doi.org/10.1016/j.ijhydene.2021.04.194

Silva, P., Oliveira, S. H., Vinhas, G. M., Carvalho, L. J., Barauna, O. S., Urtiga Filho, S. L., & Lima, M. A. G. (2021). Tetrakis hydroxymethyl phosphonium sulfate

(THPS) with biopolymer as strategy for the control of microbiologically influenced corrosion in a dynamic system. *Chemical Engineering and Processing-Process Intensification, 160*, 108272. https://doi.org/10.1016/j.cep.2020.108272

Skovhus, T. L., Eckert, R. B., & Rodrigues, E. (2017). Management and control of microbiologically influenced corrosion (MIC) in the oil and gas industry—Overview and a North Sea case study. *Journal of biotechnology, 256*, 31-45. https://doi.org/10.1016/j.jbiotec.2017.07.003

Skovhus, T. L., Enning, D., ,& Lee, J. S. (2017). Microbiologically influenced corrosion in the upstream oil and gas industry. *CRC press*. https://doi.org/10.1201/9781315157818-17

Sluzalec, A. (1992). Introduction to Nonlinear Thermomechanics: Theory and finite-element solutions. *NASA STI/Recon Technical Report A, 92*, 48425. https://doi.org/10.1007/978-1-4471-1906-7

Smith, N. W., Shorten, P. R., Altermann, E., Roy, N. C., & McNabb, W. C. (2019). A mathematical model for the hydrogenotrophic metabolism of sulphate-reducing bacteria. *Frontiers in Microbiology, 10*, 1652. https://doi.org/10.3389/fmicb.2019.01652

Song, F. (2010). Predicting the effect of soil seasonal change on stress corrosion cracking susceptibility of buried pipelines at high pH. *Corrosion, 66*(9), 095004-095004-095014. https://doi.org/10.5006/1.3490309

Sridhar, N., Beavers, J., Rollins, B., Chawla, S., Evans, K., & Li, X. (2016). Stress corrosion cracking and localized corrosion of carbon steel in nitrate solutions. *Corrosion, 72*(7), 927-942. https://doi.org/10.5006/2035

Su, W., Tian, Y., & Peng, S. (2014). The influence of sodium hypochlorite biocide on the corrosion of carbon steel in reclaimed water used as circulating cooling water. *Applied Surface Science, 315*, 95-103. https://doi.org/10.1016/j.apsusc.2014.07.095

Su, Z., Li, X., Xi, Y., Xie, T., Liu, Y., Liu, B., Liu, H., Xu, W., & Zhang, C. (2022). Microbe-mediated transformation of metal sulfides: Mechanisms and environmental significance. *Science of the Total Environment, 825*, 153767. https://doi.org/10.1016/j.scitotenv.2022.153767

Sun, D., Wang, D., Li, L., Gong, K., Ren, S., Xie, F., & Wu, M. (2023). Study on stress corrosion behavior and mechanism of X70 pipeline steel with the combined action of sulfate-reducing bacteria and constant load. *Corrosion Science, 213*, 110968. https://doi.org/10.1016/j.corsci.2023.110968

Sun, W., & Nesic, S. (2007). *A mechanistic model of H_2S corrosion of mild steel.* Paper presented at the CORROSION 2007.

Syah Putri, E. D. W., Triyono, T., & Prabowo, A. R. (2022). Estimating failure mechanism of steel specimens using stress corrosion-cracking (SCC) testing methods: state and development. *Procedia Structural Integrity, 41*, 266-273. https://doi.org/10.1016/j.prostr.2022.05.031

Tang, H. Y.,Yang, C., Ueki, T., Pittman, C. C., Xu, D., Woodard, T. L., Holmes, D. E., Gu, T., Wang, F., & Lovley, D. R. (2021). Stainless steel corrosion via direct iron-to-microbe electron transfer by *Geobacter* species. *The ISME Journal, 15*(10), 3084-3093. https://doi.org/10.1038/s41396-021-00990-2

Tang, X., & Cheng, Y. F. (2009). Micro-electrochemical characterization of the effect of applied stress on local anodic dissolution behavior of pipeline steel under near-neutral pH condition. *Electrochimica Acta, 54*(5), 1499-1505. https://doi.org/10.1016/j.electacta.2008.09.037

Terzopoulos, D., & Fleischer, K. (1988). *Modeling inelastic deformation: viscolelasticity, plasticity, fracture.* Paper presented at the Proceedings of the 15th annual conference on Computer graphics and interactive techniques.

Thamma, U., & Jantasorn, P. (2022). Effects of shear deformation via torsion on tensile strain-hardening behavior of SCM415 low-alloy steel. *Materials Today: Proceedings, 52*, 2496-2500. https://doi.org/10.1016/j.matpr.2021.10.437

Thauer, R. K., Stackebrandt, E., & Hamilton, W. A. (2007). Energy metabolism and phylogenetic diversity of sulphate-reducing bacteria. *Sulphate-reducing Bacteria*, 1-38. https://doi.org/10.1017/CBO9780511541490

Thomas, W. E., Nilsson, L. M., Forero, M., Sokurenko, E. V., & Vogel, V. (2004). Shear-dependent 'stick-and-roll'adhesion of type 1 fimbriated Escherichia coli. *Molecular Microbiology, 53*(5), 1545-1557. https://doi.org/10.1111/j.1365-2958.2004.04226.x

Tian, J., Li, C., & Xian, G. (2021). Reciprocating friction and wear performances of nanometer sized-TiO_2 filled epoxy composites. *Polymer Composites, 42*(4), 2061-2072. https://doi.org/10.1002/pc.25959

Tran Thi Thuy, T., Kannoorpatti, K., Padovan, A., & Thennadil, S. (2020). Effect of alkaline artificial seawater environment on the corrosion behaviour of duplex stainless steel 2205. *Applied Sciences, 10*(15), 5043. https://doi.org/10.3390/app10155043

Uhlig, H., & Cook, E. (1969). Mechanism of inhibiting stress corrosion cracking of 18-8 stainless steel in $MgCl_2$ by acetates and nitrates. *Journal of The Electrochemical Society, 116*(2), 173. https://doi.org/10.1149/1.2411789

Unsal, T., Wang, D., Kijkla, P., Kumseranee, S., Punpruk, S., Mohamed, M. E., Saleh, M. A., & Gu, T. (2022). Food-grade D-limonene enhanced a green biocide in the mitigation of carbon steel biocorrosion by a mixed-culture biofilm

consortium. *Bioprocess and Biosystems Engineering, 45*(4), 669-678. https://doi.org/10.1007/s00449-021-02685-6

Unsal, T., Xu, L., Jia, R., Kijkla, P., Kumseranee, S., Punpruk, S., Mohamed, M. E., Saleh, M. A., & Gu, T. (2023). Microbiologically influenced corrosion of titanium by *Desulfovibrio vulgaris* biofilm under organic carbon starvation. *Bioelectrochemistry, 149*, 108307. https://doi.org/10.1016/j.bioelechem.2022.108307

Uppuluri, P., & Lopez-Ribot, J. L. (2016). Go forth and colonize: dispersal from clinically important microbial biofilms. *PLoS Pathogens, 12*(2), e1005397. https://doi.org/10.1371/journal.ppat.1005397

Usher, K., Kaksonen, A., & MacLeod, I. (2014). Marine rust tubercles harbour iron corroding archaea and sulphate reducing bacteria. *Corrosion Science, 83*, 189-197. https://doi.org/10.1016/j.corsci.2014.02.014

Venezuela, J., Liu, Q., Zhang, M., Zhou, Q., & Atrens, A. (2016). A review of hydrogen embrittlement of martensitic advanced high-strength steels. *Corrosion Reviews*, *34*(3), 153-186. https://doi.org/10.1515/corrrev-2016-0006

Videla, H. A. (2002). Prevention and control of biocorrosion. *International Biodeterioration & Biodegradation, 49*(4), 259-270. Pii S0964-8305(02)00053-7. https://doi.org/10.1016/S0964-8305(02)00053-7

Videla, H. A. (2018). *Manual of biocorrosion*: Routledge. https://doi.org/10.1201/9780203748190

Virpiranta, H., Sotaniemi, V. H., Leiviskä, T., Taskila, S., Rämö, J., Johnson, D. B., & Tanskanen, J. (2022). Continuous removal of sulfate and metals from acidic mining-impacted waters at low temperature using a sulfate-reducing bacterial consortium. *Chemical Engineering Journal, 427*, 132050. https://doi.org/10.1016/j.cej.2021.132050

Wang, D., Ivanova, S. A., Hahn, R., & Gu, T. (2022a). Evaluation of trehalase as an enhancer for a green biocide in the mitigation of *Desulfovibrio vulgaris* biocorrosion of carbon steel. *Bioprocess and Biosystems Engineering, 45*(4), 659-667. https://doi.org/10.1007/s00449-021-02684-7

Wang, D., Kijkla, P., Mohamed, M. E., Saleh, M. A., Kumseranee, S., Punpruk, S., & Gu, T. (2021a). Aggressive corrosion of carbon steel by *Desulfovibrio ferrophilus* IS5 biofilm was further accelerated by riboflavin. *Bioelectrochemistry, 142*, 107920. https://doi.org/10.1016/j.bioelechem.2021.107920

Wang, D., Kijkla, P., Saleh, M. A., Kumseranee, S., Punpruk, S., & Gu, T. (2022b). Tafel scan schemes for microbiologically influenced corrosion of carbon steel and stainless steel. *Journal of Materials Science & Technology, 130*, 193-197. https://doi.org/10.1016/j.jmst.2022.05.018

Wang, D., Liu, J., Jia, R., Dou, W., Kumseranee, S., Punpruk, S., Li, X., & Gu, T. (2020). Distinguishing two different microbiologically influenced corrosion (MIC) mechanisms using an electron mediator and hydrogen evolution detection. *Corrosion Science, 177*, 108993. https://doi.org/10.1016/j.corsci.2020.108993

Wang, D., Unsal, T., Kumseranee, S., Punpruk, S., Mohamed, M. E., Saleh, M. A., & Gu, T. (2021b). Sulfate reducing bacterium *Desulfovibrio vulgaris* caused severe microbiologically influenced corrosion of zinc and galvanized steel. *International Biodeterioration & Biodegradation, 157*, 105160. https://doi.org/10.1016/j.ibiod.2020.105160

Wang, D., Yang, C., Saleh, M. A., Alotaibi, M. D., Mohamed, M. E., Xu, D., & Gu, T. (2022c). Conductive magnetite nanoparticles considerably accelerated carbon steel corrosion by electroactive *Desulfovibrio vulgaris* biofilm. *Corrosion Science, 205*, 110440. https://doi.org/10.1016/j.corsci.2022.110440

Wang, J., Du, M., Li, G., & Shi, P. (2022d). Research progress on microbiological inhibition of corrosion: A review. *Journal of Cleaner Production, 373*, 133658. https://doi.org/10.1016/j.jclepro.2022.133658

Wang, J., Hou, B., Xiang, J., Chen, X., Gu, T., & Liu, H. (2019a). The performance and mechanism of bifunctional biocide sodium pyrithione against sulfate reducing bacteria in X80 carbon steel corrosion. *Corrosion Science, 150*, 296-308. https://doi.org/10.1016/j.corsci.2019.01.037

Wang, J., Li, C., Zhang, X., Asif, M., Zhang, T., Hou, B., Li, Y., Xia, W., Wang, H., & Liu, H. (2019b). Corrosion behavior of *Aspergillus niger* on 7075 aluminum alloy and the inhibition effect of zinc pyrithione biocide. *Journal of The Electrochemical Society, 166*(8), G39-G46. https://doi.org/10.1149/2.0061908jes

Wang, Y. Z., Li, G. Q., Wang, Y. B., & Lyu, Y. F. (2021c). Simplified method to identify full von Mises stress-strain curve of structural metals. *Journal of Constructional Steel Research, 181*, 106624. https://doi.org/10.1016/j.jcsr.2021.106624

Wang, Y., Wu, J., Zhang, D., Li, E., & Zhu, L. (2021d). The inhibition effects of Cu and Ni alloying elements on corrosion of HSLA steel influenced by *Halomonas titanicae*. *Bioelectrochemistry, 141*, 107884. https://doi.org/10.1016/j.bioelechem.2021.107884

Wang, Z., Xie, F., Wang, D., & Liu, J. (2021e). Effect of applied potential on stress corrosion cracking behavior of X80 steel in alkaline soil simulated solution with sulfate-reducing bacteria. *Engineering Failure Analysis, 121*, 105109. https://doi.org/10.1016/j.engfailanal.2020.105109

Wasim, M., & Djukic, M. B. (2020). Long-term external microbiologically influenced corrosion of buried cast iron pipes in the presence of sulfate-reducing bacteria (SRB). *Engineering Failure Analysis, 115*, 104657. https://doi.org/10.1016/j.engfailanal.2020.104657

Wasim, M., & Djukic, M. B. (2022). External corrosion of oil and gas pipelines: A review of failure mechanisms and predictive preventions. *Journal of Natural Gas Science and Engineering, 100*, 104467. https://doi.org/10.1016/j.jngse.2022.104467

Wasim, M. (2018). External corrosion and its effects on mechanical properties of buried metal pipes (Doctoral dissertation, RMIT University). https://researchrepository.rmit.edu.au/esploro/outputs/doctoral/External-corrosion-and-its-effects-on/9921864144401341#file-0

Wei, B. X., Qin, Q. Y., Bai, Y. L., Yu, C. K., Xu, J., Sun, C., & Ke, W. (2019). Short-period corrosion of X80 pipeline steel induced by AC current in acidic red soil. *Engineering Failure Analysis, 105*, 156-175. https://doi.org/10.1016/j.engfailanal.2019.07.014

Weng, S., Huang, Y., Lin, S., & Xuan, F. Z. (2022). Stress corrosion crack propagation affected by microstructures for nuclear steam turbine rotor steels in the simulated environment. *Journal of Materials Research and Technology, 17*, 725-742. https://doi.org/10.1016/j.jmrt.2022.01.020

Wolodko, J., Haile, T., Khan, F., Taylor, C., Eckert, R., Hashemi, S. J., Ramirez, A. M., & Skovhus, T. L. (2018). *Modeling of Microbiologically Influenced Corrosion (MIC) in The Oil and Gas Industry-Past, Present and Future.* Paper presented at the CORROSION 2018.

Woodard Trevor, L., Ueki, T., & Lovley Derek, R. (2023). H_2 Is a major intermediate in *Desulfovibrio vulgaris* corrosion of iron. *mBio, 14*(2), e00076-00023. https://doi.org/10.1128/mbio.00076-23

Wool, R. P. (2005). FUNDAMENTALS OF FRACTURE IN BIO-BASED POLYMERS. In R. P. Wool & X. S. Sun (Eds.), *Bio-Based Polymers and Composites* (pp. 149-201). Burlington: Academic Press. https://doi.org/10.1016/B978-012763952-9/50007-1

Wu, T., Xu, J., Yan, M., Sun, C., Yu, C., & Ke, W. (2014). Synergistic effect of sulfate-reducing bacteria and elastic stress on corrosion of X80 steel in soil solution. *Corrosion Science, 83*, 38-47. https://doi.org/10.1016/j.corsci.2014.01.017

Wu, T., Yan, M., Zeng, D., Xu, J., Sun, C., Yu, C., & Ke, W. (2015). Stress Corrosion Cracking of X80 Steel in the Presence of Sulfate-reducing Bacteria. *Journal of Materials Science & Technology, 31*(4), 413-422. https://doi.org/10.1016/j.jmst.2014.08.012

Xie, Q., Lu, Y., Tang, L., Zeng, G., Yang, Z., Fan, C., Wang, J., & Atashgahi, S. (2021). The mechanism and application of bidirectional extracellular electron transport in the field of energy and environment. *Critical Reviews in Environmental Science and Technology, 51*(17), 1924-1969. https://doi.org/10.1080/10643389.2020.1773728

Xu, D., & Gu, T. (2011). Bioenergetics explains when and why more severe MIC pitting by SRB can occur. Paper presented at the CORROSION 2011.

Xu, D., & Gu, T. (2014). Carbon source starvation triggered more aggressive corrosion against carbon steel by the *Desulfovibrio vulgaris* biofilm. *International Biodeterioration & Biodegradation, 91*, 74-81. https://doi.org/10.1016/j.ibiod.2014.03.014

Xu, D., Jia, R., Li, Y., & Gu, T. (2017). Advances in the treatment of problematic industrial biofilms. *World Journal of Microbiology & Biotechnology, 33*(5). https://doi.org/10.1007/s11274-016-2203-4

Xu, D., Lovley, D. R., & Gu, T. (2023a). Microbially mediated metal corrosion. *Nature Review Microbiology*. (In press).

Xu, L., Kijkla, P., Kumseranee, S., Punpruk, S., & Gu, T. (2023b). "Corrosion-resistant" chromium steels for oil and gas pipelines can suffer from very severe pitting corrosion by a sulfate-reducing bacterium. *Journal of Materials Science & Technology*. https://doi.org/10.1016/j.jmst.2023.01.008

Xu, L., Guan, F., Ma, Y., Zhang, R., Zhang, Y., Zhai, X., Dong, X., Wang, Y., Duan, J., & Hou, B. (2022a). Inadequate dosing of THPS treatment increases microbially influenced corrosion of pipeline steel by inducing biofilm growth of *Desulfovibrio hontreensis* SY-21. *Bioelectrochemistry, 145*, 108048. https://doi.org/10.1016/j.bioelechem.2021.108048

Xu, Z., Dou, W., Chen, S., Pu, Y., & Chen, Z. (2022b). Limiting nitrate triggered increased EPS film but decreased biocorrosion of copper induced by *Pseudomonas aeruginosa*. *Bioelectrochemistry, 143*, 107990. https://doi.org/10.1016/j.bioelechem.2021.107990

Yan, M., Sun, C., Xu, J., Wu, T., Yang, S., & Ke, W. (2015). Stress corrosion of pipeline steel under occluded coating disbondment in a red soil environment. *Corrosion Science, 93*, 27-38. https://doi.org/10.1016/j.corsci.2015.01.001

Yang, C., Feng, H., Chen, X., Han, Y., Li, H., Xu, D., & Wang, F. (2023). Enhanced pitting corrosion resistance of CoCrFeMnNi high entropy alloy in the presence of *Desulfovibrio vulgaris* via nitrogen doping. *Journal of Materials Science & Technology, 139*, 92-102. https://doi.org/10.1016/j.jmst.2022.08.021

Yang, X., Shao, J., Liu, Z., Zhang, D., Cui, L., Du, C., & Li, X. (2020). Stress-assisted microbiologically influenced corrosion mechanism of 2205 duplex stainless steel caused by sulfate-reducing bacteria. *Corrosion Science, 173*, 108746. https://doi.org/10.1016/j.corsci.2020.108746

Yavas, D., Alshehri, A., Mishra, P., Shrotriya, P., Bastawros, A. F., & Hebert, K. R. (2018). Morphology and stress evolution during the initial stages of intergranular corrosion of X70 steel. *Electrochimica Acta, 285*, 336-343. https://doi.org/10.1016/j.electacta.2018.07.207

Yin, K., Liu, H., & Cheng, Y. (2018). Microbiologically influenced corrosion of X52 pipeline steel in thin layers of solution containing sulfate-reducing bacteria trapped under disbonded coating. *Corrosion Science, 145*, 271-282. https://doi.org/10.1016/j.corsci.2018.10.012

Z Zeitvogel, D. T., Matlack, K. H., Kim, J. Y., Jacobs, L. J., Singh, P. M., & Qu, J. (2014). Characterization of stress corrosion cracking in carbon steel using nonlinear Rayleigh surface waves. *NDT & E International, 62*, 144-152. https://doi.org/10.1016/j.ndteint.2013.12.005

Zen, K. (2005). Corrosion and life cycle management of port structures. *Corrosion Science, 47*(10), 2353-2360. https://doi.org/10.1016/j.corsci.2005.04.003

Zeng, Q., Fu, Z., Yang, B., Gou, G., Chen, H., & Zhu, S. (2020). SCC behavior and susceptibility prediction mode of SMA490BW weathering steel under cathodic potential. *Materials Research Express, 7*(7), 076523. https://doi.org/10.1088/2053-1591/aba808

Zhang, C., Ran, M., Wang, Y., & Zheng, W. (2022a). Microstructural effects in the development of near-neutral pH stress corrosion cracks in pipelines. *Materials, 15*(13), 4372. https://doi.org/10.3390/ma15134372

Zhang, P., Xu, D., Li, Y., Yang, K., & Gu, T. (2015). Electron mediators accelerate the microbiologically influenced corrosion of 304 stainless steel by the

Desulfovibrio vulgaris biofilm. *Bioelectrochemistry, 101*, 14-21. https://doi.org/10.1016/j.bioelechem.2014.06.010

Zhang, S., Zheng, H., Chang, W., Lou, Y., & Qian, H. (2023). Microbiological deterioration of epoxy coating on carbon steel by *Pseudomonas aeruginosa*. *Coatings, 13*(3), 606. https://doi.org/10.3390/coatings13030606

Zhang, Y., He, J., Zheng, L., Jin, Z., Liu, H., Liu, L., Gao, Z., Meng, G., Liu, H., & Liu, H. (2022b). Corrosion of aluminum alloy 7075 induced by marine aspergillus terreus with continued organic carbon starvation. *npj Materials Degradation, 6*(1), 27. https://doi.org/10.1038/s41529-022-00236-2

Zhang, Z., Zheng, Y., Li, J., Liu, W., Liu, M., Gao, W., & Shi, T. (2019). Stress corrosion crack evaluation of super 13Cr tubing in high-temperature and high-pressure gas wells. *Engineering Failure Analysis, 95*, 263-272. https://doi.org/10.1016/j.engfailanal.2018.09.030

Zheng, W., Elboujdaini, M., & Revie, R. W. (2011). Stress corrosion cracking in pipelines. In V. S. Raja & T. Shoji (Eds.), *Stress Corrosion Cracking* (pp. 749-771): Woodhead Publishing. https://doi.org/10.1533/9780857093769.4.749

Zhou, E., Zhang, M., Huang, Y., Li, H., Wang, J., Jiang, G., Jiang, C., Xu, D., Wang, Q., & Wang, F. (2022a). Accelerated biocorrosion of stainless steel in marine water via extracellular electron transfer encoding gene phzH of *Pseudomonas*

aeruginosa. *Water research, 220*, 118634. https://doi.org/10.1016/j.watres.2022.118634

Zhou, E., Li, F., Zhang, D., Xu, D., Li, Z., Jia, R., Jin, Y., Song, H., Li, H., Wang, Q., Wang, J. J., Li, X., Gu, T., Homborg, A. M., Mol, J. M. C., Smith, J. A., Wang, F. H., & Lovley, D. R. (2022b). Direct microbial electron uptake as a mechanism for stainless steel corrosion in aerobic environments. *Water research, 219*, 118553. https://doi.org/10.1016/j.watres.2022.118553

Zhu, L. (2022). Probing intergranular mixed transgranular stress corrosion cracking under the high constant load. *Scientific Reports, 12*(1), 12390. https://doi.org/10.1038/s41598-022-16390-1

Zhu, L., Yan, Y., Li, J., Qiao, L. J., & Volinsky, A. A. (2014a). Stress corrosion cracking under low stress: Continuous or discontinuous cracks? *Corrosion Science, 80*, 350-358. https://doi.org/10.1016/j.corsci.2013.11.057

Zhu, M., Du, C., Li, X., Liu, Z., Li, H., & Zhang, D. (2014b). Effect of AC on stress corrosion cracking behavior and mechanism of X80 pipeline steel in carbonate/bicarbonate solution. *Corrosion Science, 87*, 224-232. https://doi.org/10.1016/j.corsci.2014.06.028

Zuo, R. (2007). Biofilms: strategies for metal corrosion inhibition employing microorganisms. *Applied Microbiology and Biotechnology, 76*(6), 1245-1253. https://doi.org/10.1007/s00253-007-1130-6

Zvirko, O. I., Savula, S. F., Tsependa, V. M., Gabetta, G., & Nykyforchyn, H. M. (2016). Stress corrosion cracking of gas pipeline steels of different strength. *Procedia Structural Integrity, 2*, 509-516. https://doi.org/10.1016/j.prostr.2016.06.066

Appendix A: Experimental Methods

A.1 Metal materials and methods

The elemental composition of X80 steel is listed in Table A-1. X80 square coupons with 1.0 cm × 1.0 cm exposed surface were used for electrochemical testing in 450 mL anaerobic bottles. X80 U-bend coupons were also prepared for use as the working electrode in electrochemical testing. These X80 U-bend coupons were painted with Epoxy resin, leaving a 1.0 cm^2 exposed surface area at the outer bottom of the U-shape.

For the anaerobic bottle incubation tests, all surfaces of the X80 coupons, except the top-exposed surface, were coated with inert polytetrafluoroethylene (Teflon) paint or Epoxy resin. The coupon surface painted with Teflon was air dried for 1 h in ambient conditions, then baked in an oven at 90ºC for 2 h to cure the paint. Surfaces painted with the Epoxy resin were dried at ambient condition for 24 h. All coupons were abraded progressively to a final finish of 600 grit and cleaned with 100% isopropanol before being air dried under UV light for more than 20 min.

Table A-1. Elemental composition of X80 steel (mass%) (Fe balance).

Element	C	Mn	Ni	Cu	Si	Mo	Cr	Nb	Ti
Amount (wt%)	0.050	1.850	0.285	0.246	0.228	0.307	0.016	0.065	0.013

A.2 Square coupon preparation for immersion tests

The X80 square coupons were embedded in inert Epoxy resin, leaving an exposed top surface area of 1 cm × 1 cm., This unpainted area was used for MIC during SRB immersion (Figure A-1). Before testing, the exposed surface was abraded by 180, 400, and 600 grit emery papers sequentially, then cleaned with 100 % isopropanol, and air dried under a UV lamp for 0.5 h.

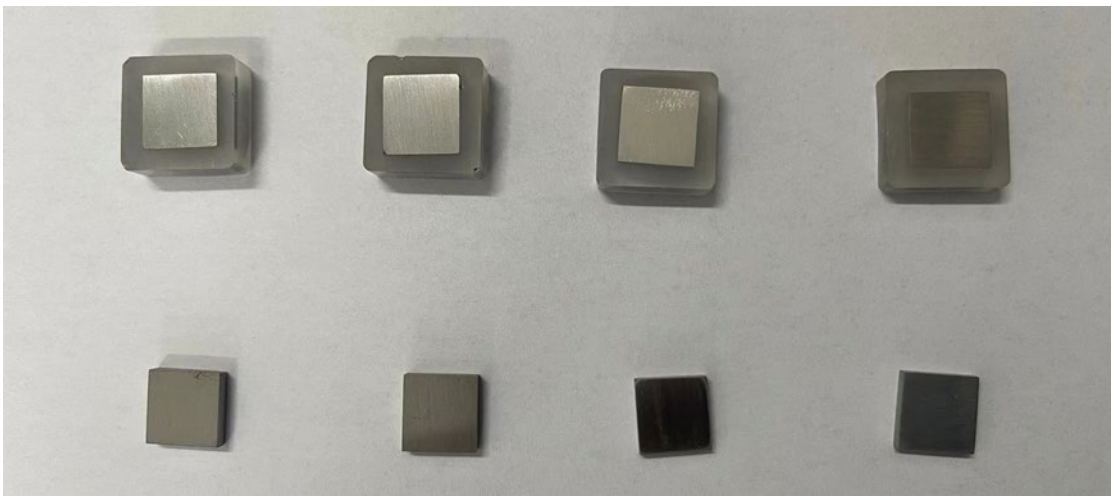

Figure A-1. X80 square coupon (1 cm^2) with and without Epoxy resin.

A.3 Square coupon preparation for electrochemical tests

To prepare an X80 square coupon for use as the working electrode in electrochemical tests, each coupon was embedded in Epoxy resin leaving 1 cm^2 of exposed surface area (default in electrochemical tests) as shown in Figure A-2. Before

use, the working electrode was cleaned with pure isopropanol and dried under UV light for 20 min.

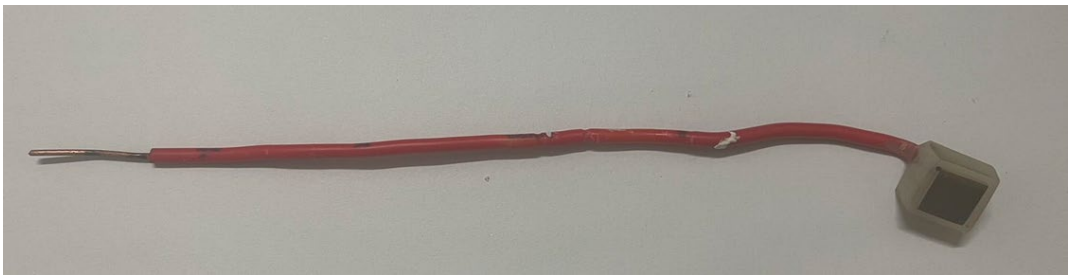

Figure A-2. Image of working electrode set up using X80 square coupon.

A.4 U-bend preparation for immersion tests

X80 U-bend coupons were prepared by a vendor based on the ASTM G30-97 standard, as shown in Figure A-3. For the immersion tests, bolts and nuts were painted. Each X80 U-bend had a total of 12 cm^2 of exposed surface (Figure A-3(c)). Before use, the U-bend coupons were cleaned with pure isopropanol and dried under UV light for 20 min.

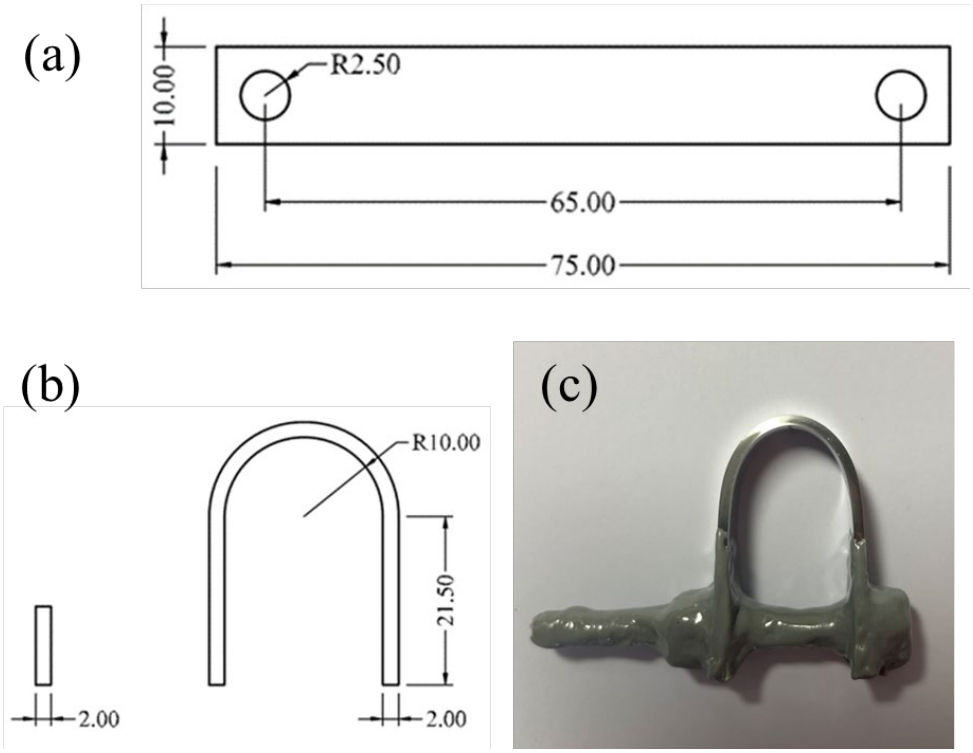

Figure A-3. Schematic of X80 U-bend coupons: (a) dimensions of unpainted X80 U-bend coupon before bending (in mm), (b) dimensions of X80 U-bend coupon after bending (mm), and (c) X80 U-bend after coating for immersion testing.

A.5 U-bend working electrode preparation for electrochemical tests

Each X80 U-bend coupon was completely painted, except for 1 cm^2 of exposed surface area on the outer bottom, as shown in Figure A-4. Before use, the coupons were cleaned with pure isopropanol and dried under UV light for 20 min.

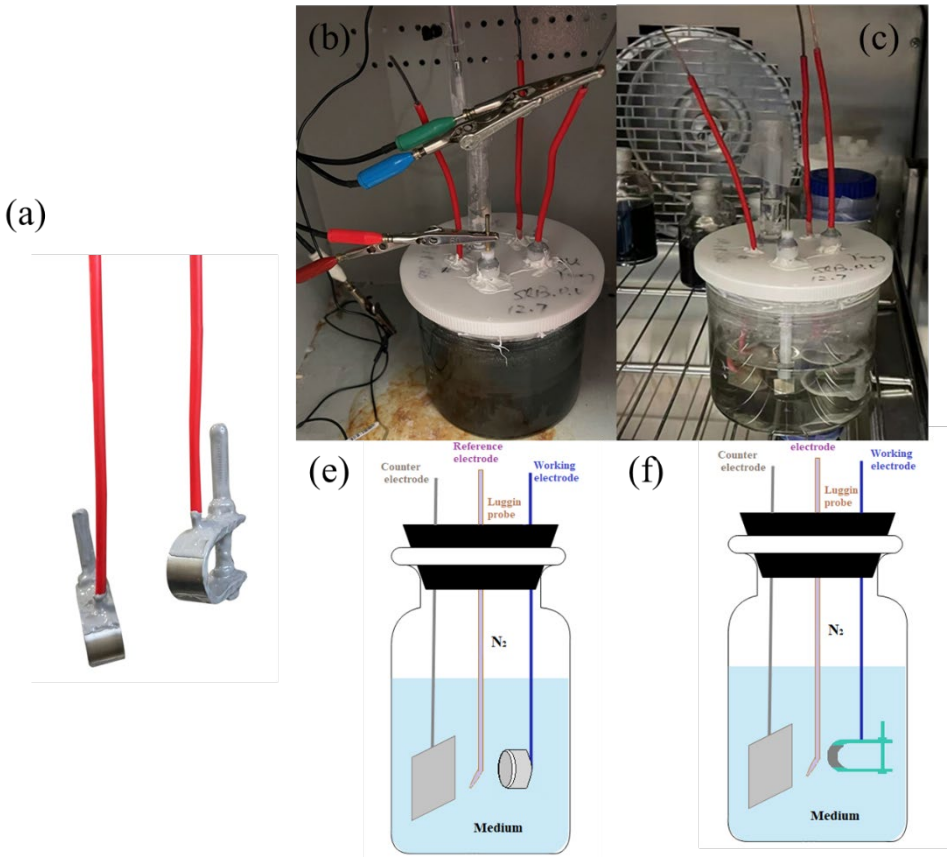

Figure A-4. Schematic illustration of coupons and devices: (a) X80 U-bend coupon after Epoxy painting with 1 cm^2 on the outer bottom surface, (b) 450 mL electrochemical glass cells containing coupons (one X80 U-bend and two X80 square coupons) and SRB, (c) abiotic control for (b), (d) X80 square coupon working electrode, and (e) X80 U-bend working electrode, with a platinum sheet as counter electrode and SCE as reference electrode.

A.6 Dogbone coupon preparation for immersion tests

Dogbone specimens were used in tensile testing to evaluate the mechanical properties of the X80 steel after SRB exposure. The dimensions of the dogbone coupons

(Figure A-5) were based on the ASTM E8/E8M standards (ASTM E8, 2013). The dog bone coupons were polished to 1200 grit by the supplier. Each dogbone coupon was painted with Teflon, except for the middle 2.5 cm section (four sides unpainted) with a total exposed area of 4 cm^2 based on the following calculations:

$$\text{Exposed area} = 2 \times 25\ \text{mm}((20\ \text{mm} - 7\ \text{mm} \times 2) + 2\ \text{mm}) = 4\ \text{cm}^2 \quad \text{(A-1)}$$

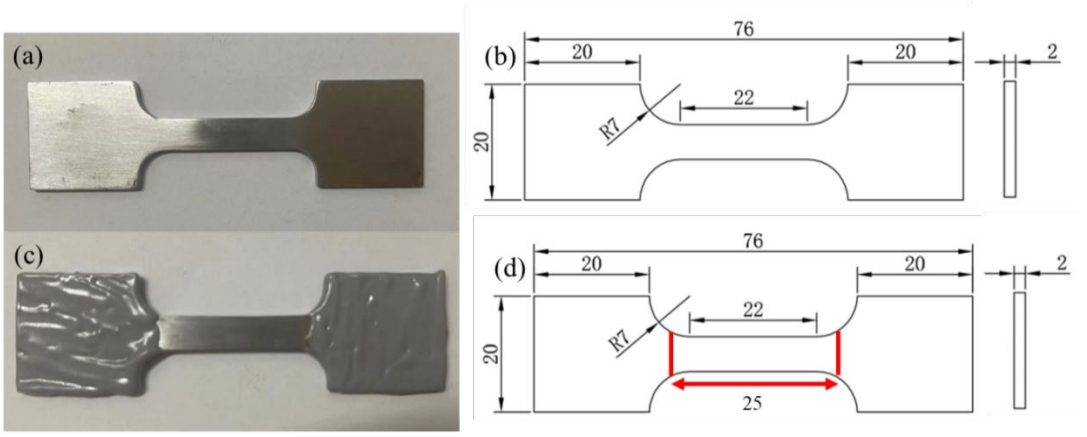

Figure A-5. Image of dogbone coupon of X80 carbon steel and, dimensions in mm with (a, b) and without Epoxy resin coating (exposed area approximately 4 cm^2) (c, d).

A.7 Chemicals and materials

Unless otherwise indicated, all chemicals used in this work were purchased from either Fisher Scientific (Pittsburgh, PA, USA) or Sigma-Aldrich (St. Louis, MO, USA). Anaerobic bottles (450 mL) were purchased from Wheaton Industries Inc. (Millville, NJ, USA).

A.8 Culture medium and inoculum for *D. vulgaris*

For *D. vulgaris* incubation, ATCC 1249 was used as the culture medium. The composition of the ATCC 1249 medium is shown in Table A-2. Yeast extract (1 g/L) was in the standard ATCC 1249 medium for optimal SRB growth. Trisodium citrate is the chelator to enhance Fe^{2+} (a key enzyme co-factor) bioavailability during SRB growth to mitigate its precipitation by sulfide. Sodium lactate serves as the carbon source. Each anaerobic bottle with 200 mL culture medium was inoculated with 2 mL of 3-d-old *D. vulgaris* seed culture before static incubation at 37ºC.

Table A-2. Chemical composition of ATCC 1249 medium.

Component	Chemical	Amount
Component I	$MgSO_4 \cdot 7H_2O$	4.1 g
	Sodium citrate	5.0 g
	$CaSO_4 \cdot 2H_2O$	1.0 g
	NH_4Cl	1.0 g
Component II	Distilled water	400 mL
	K_2HPO_4	0.5 g
Component III	Distilled water	200 mL
	Sodium lactate	4.5 mL
	Yeast extract	1.0 g
Component IV	Distilled water	400 mL
	$Fe(NH_4)_2(SO_4)_2$	1.0 g

A.9 Culture medium and inoculum for *D. ferrophilus*

The culture medium for *D. ferrophilus* used in this study was EASW, as recommended for the SRB. The composition of EASW was (g/L): $NaHCO_3$ 0.192, KBr 0.096, KCl 0.664, H_3BO_3 0.026, $SrCl_2 \cdot 6H_2O$ 0.040, $MgCl_2 \cdot 6H_2O$ 10.610, $CaCl_2 \cdot 2H_2O$ 1.469, yeast extract 1, tri-sodium citrate ($Na_3C_6H_5O_7$) 0.5, sodium lactate ($C_3H_5NaO_3$)

3.5, $CaSO_4 \cdot 0.5H_2O$ 0.1, NH_4Cl 0.1, $MgSO_4 \cdot 7H_2O$ 0.71, $Fe(NH_4)_2(SO_4)_2 \cdot 6H_2O$ 1.38, K_2HPO_4 0.05. Each anaerobic bottle containing 200 mL EASW was inoculated with 2 mL 3-d-old *D. ferrophilus* seed culture before static incubation at 28°C (optimal for growth).

A.10 Sterilization and culture medium deoxygenation

Before conducting the experiments, all the culture media and laboratory equipment, including anaerobic bottles, electrochemical glass cells, aluminum caps, rubber septa, rubber stopper, tweezers, N_2 spargers, pipette tips, and gas filters, were sterilized in an autoclave (Panasonic model MLS-3751L, Osaka, Japan) at 121°C. After sterilization, the initial pH of the medium was adjusted to 7.0 ± 0.1 using 1 M NaOH and HCl solutions as required. The culture medium was then deoxygenated using high-purity, filter-sterilized N_2 (> 99.999% by vol.) sparging at a flow rate of 50 mL min^{-1} for more than45 min, as shown in Figure A-6. L-cysteine (100 ppm in the culture medium) sterilized using a sterile acetate cellulose membrane (0.22 μm) was added to the medium to further reduce dissolved oxygen.

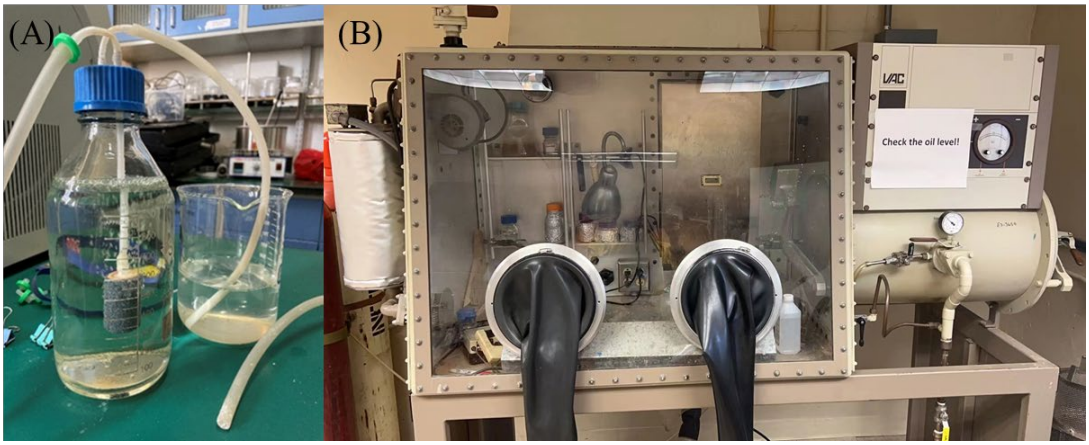

Figure A-6. (a) A nitrogen sparging bottle of ATCC 1249 medium with a stainless-steel nitrogen gas bubble distributor, and (b) an anaerobic chamber filled with N_2.

A.11 Headspace gas and liquid-phase pH measurements

The concentrations of H_2S and H_2 in the headspace and the total pressure in an anaerobic bottle were measured at the end of the incubation using a portable H_2S sensor (GAXT-H-DL, BW Technologies, Calgary, Alberta, Canada) and a portable H_2 sensor (BH-90A, Forensics Detectors, Palos Verdes Peninsula, CA, USA), respectively, as shown in Figure A-7. The H_2S sensor has an upper limit of 100 ppm (v/v). Headspace samples with concentrations above this limit required dilution. A sealed 125 mL bottle with 1 atm air pressure was injected with 10 mL of headspace gas for a 12.5X dilution. After mixing, a syringe was used to flush and flood the sensor port with 40 mL of headspace gas before the meter was read. The H_2 sensor had an upper limit of 1,000 ppm. The dilution method was the same as that for H_2S. It is recommended that the H_2

sensor should be calibrated from time to time with bottled H_2 standard gas because H_2S may skew the reading.

A portable pH meter (Thermo Fisher, Star A2210) was used to measure the pH in the culture medium. It is recommended that the meter should be calibrated each time because H_2S exposure can skew the reading.

Figure A-7. (a) H_2S sensor, (b) H_2 sensor, and (c) gas dilution syringe and bottles.

A.12 Cell count using the hemocytometer methods

A hemocytometer was used to count cells in a cell suspension under a 400X microscope (Figure A-8). Normally, bacterial cells are too small to be distinguished from artifact particles. However, *D. vulgaris and D. ferrophilus* cells are motile and thus easily identified. Non-motile cells would need staining as in CLSM imaging. A minimum cell count of 5×10^4 cells mL^{-1} is needed for accurate counting of a cell suspension. Using a hemocytometer is far more accurate than MPN (most probable number) enumeration (Jia et al., 2019b).

To get a sessile cell count, sessile cells on a coupon (typically 1 cm^2 working surface) rinsed with a pH 7.4 PBS (phosphate buffered saline) buffer to remove the culture medium and loose planktonic cells. Then, the biofilm on the coupon surface was scraped off using a sterile brush into a 10 mL PBS solution. The cells and the brush were transferred to a 50 mL conical tube, and vortexed for 30 s to suspend the cells evenly in the solution.

The 400X microscope view area is just sufficient to view a 0.2 mm × 0.2 mm square. The cell count (cells mL^{-1}) of a cell suspension deposited on the hemocytometer can be calculated using the following formula:

$$\text{Cell count} = (\text{Number of cells in 0.2 mm} \times \text{0.2 mm square}) \times 2.5 \times 10^5 \text{ cells mL}^{-1} \qquad \text{(A-1)}$$

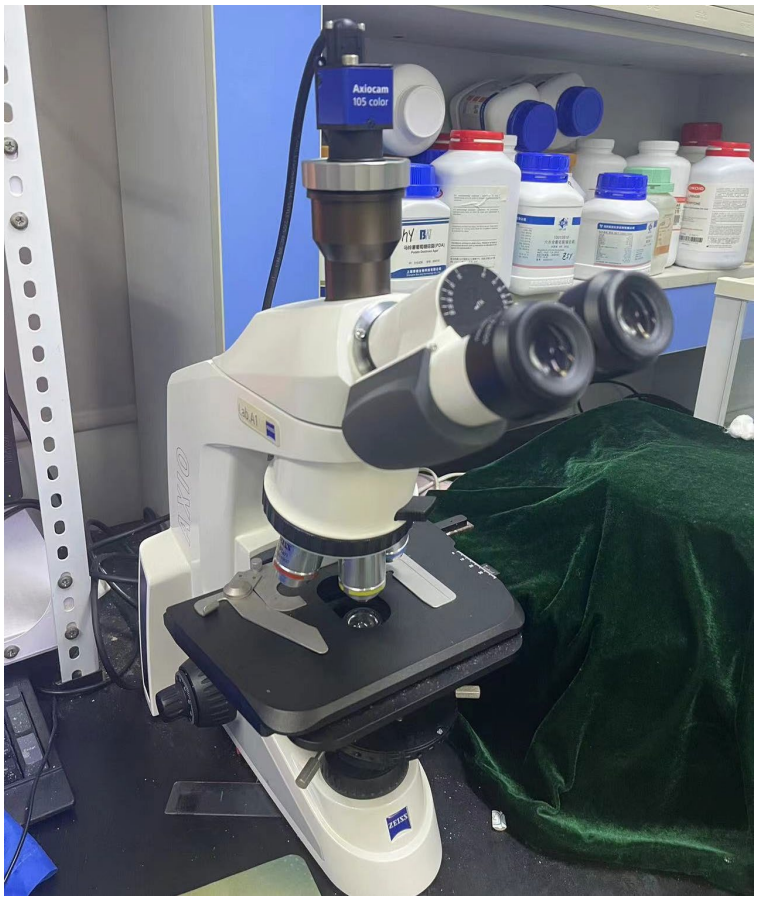

Figure A-8. An optical microscope (PrimoStar, Zeiss, Carl Zeiss, Oberkochen, Germany)

A.13 Biofilm observation under FESEM

The biofilm morphology on the surface of a coupon was observed using field-emission scanning electron microscopy (FESEM) (Carl Zeiss Ultra Plus, Carl Zeiss, Oberkochen, Germany) (Figure A-9). Before the SEM observation, the coupon covered with biofilm was rinsed with pH 7.4 PBS buffer for 15 s and then soaked in 2.5% (w/w) glutaraldehyde biocide solution for 8 h at 10˚C to immobilize the biofilm on the coupon. Then, the coupon was sequentially dehydrated with 50% (v/v), 70%, 80%, 90%, and

95% ethanol for 10 min at each concentration, and finally with 100% ethanol for 30 min. Subsequently, the coupon surface was sputter coated with an Au film to provide electrical conductivity before the FESEM observation.

Figure A-9. FESEM (Carl Zeiss Ultra Plus, Carl Zeiss, Oberkochen, Germany)

A.14 Biofilm observation under CLSM

Confocal laser scanning microscopy (CLSM) (Zeiss LSM780, Carl Zeiss, Oberkochen, Germany) was used to observe live and dead cells in a biofilm on a coupon (Figure A-10). After incubation, the coupon was rinsed with pH 7.4 PBS buffer to remove the culture medium and loosely attached planktonic cells. The biofilm was stained using the LIVE/DEAD™ BacLight™ Bacterial Viability Kit (Life

Technologies, Grand Island, NY). In the kit, SYTO-9 is a green stain under fluorescence light, and it penetrates both live cells and dead cells, while propidium iodide (PI) (red) can only stain dead cells. Under CLSM, SYTO-9 makes live cells appear as green dots while PI makes dead cells appear as red dots at excitation wavelengths of 488 nm and 559 nm, respectively.

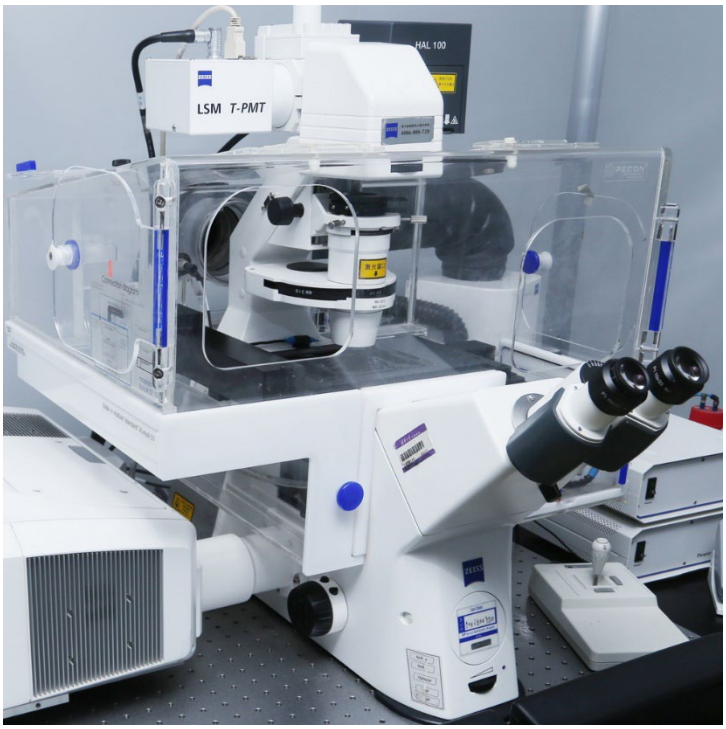

Figure A-10. CLSM machine (Zeiss LSM780, Carl Zeiss, Oberkochen, Germany).

A.15 Corrosion pits observed under SEM

After SRB incubation, the X80 square coupons were retrieved. A scanning electron microscope (SEM) (FEI Quanta 250, Hillsboro, OR, USA) was used to observe the corrosion pits on the square coupon surfaces (Figure A-11). The X80 square

coupons were cleaned using a fresh Clarke's solution to remove biofilms and corrosion products before pit image analysis under SEM. The chemical composition of Clarke's solution consisted of 50 g of stannous chloride and 20 g of antimony chloride in 1 L of hydrochloric acid solution (specific gravity: 1.19). These cleaned coupons were also used for weight loss measurements, and to scan for pit profiles.

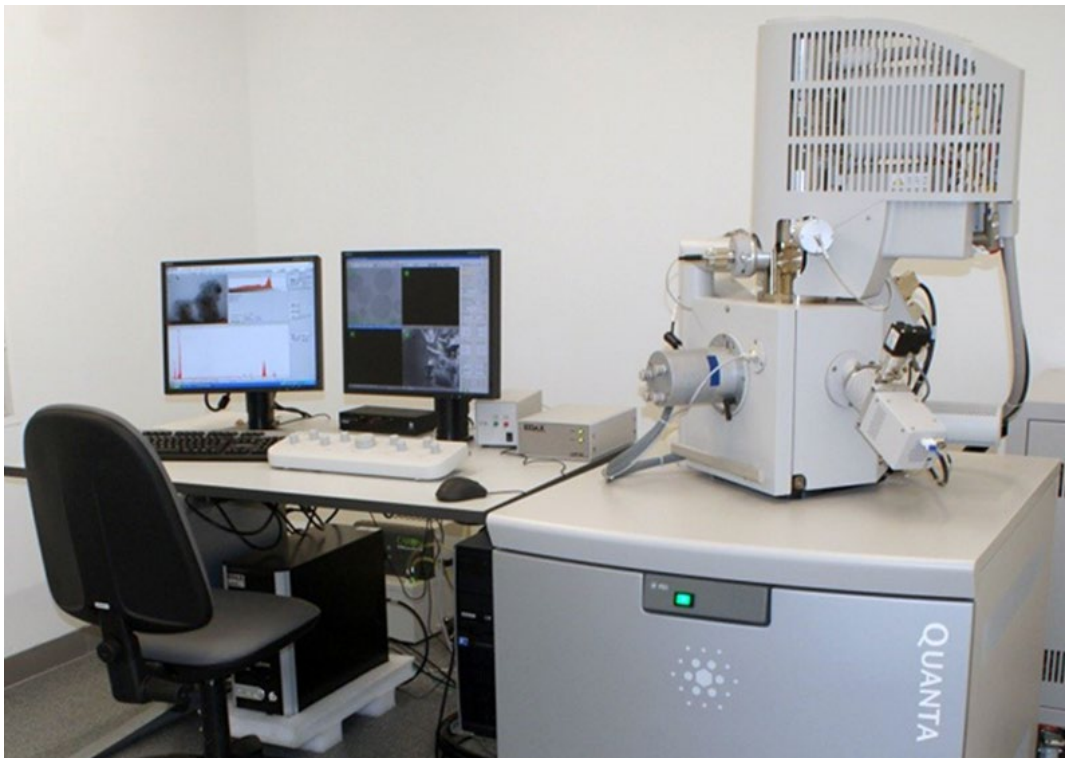

Figure A-11. SEM machine (FEI Quanta 250, Hillsboro, OR, USA).

A.16 Corrosion pit depth profile scans using IFM and CLSM

The pit depth profiles of a cleaned coupon surface were scanned using IFM (Model ALC13, Alicona Imaging GmbH, Graz, Austria) at 400X magnification in Chapters 5

to 7 (Figure A-12(a)). CLSM (VK-X250K, KEYENCE, Japan) was used in Chapters 8 and 9 for logistic reasons (Figure A-12(b)). The profile with the deepest pit was chosen as the representative profile to indicate the severity of the pitting corrosion.

Figure A-12. IFM Model ALC13 machine (a), and CLSM VK-X250K machine (b).

A.17 Corrosion product analysis using XRD and XPS

Chemical compositions of the corrosion products were analyzed using XRD and XPS with the latter providing more information. The X80 square coupon was removed from the anaerobic bottle after SRB incubation. The top biofilm was removed using a cotton swab to reveal corrosion products underneath. It was then dried under N_2 for approximately 10 min before being placed under XRD and XPS.

A.18 SCC Observation under SEM

X80 U-bend coupons were retrieved from anaerobic bottles after SRB incubation. Each U-bend coupon was too large for the SEM machine, so the U bottom section was cut off and molded into an Epoxy cake (2 cm diameter), as shown in Figure A-13.

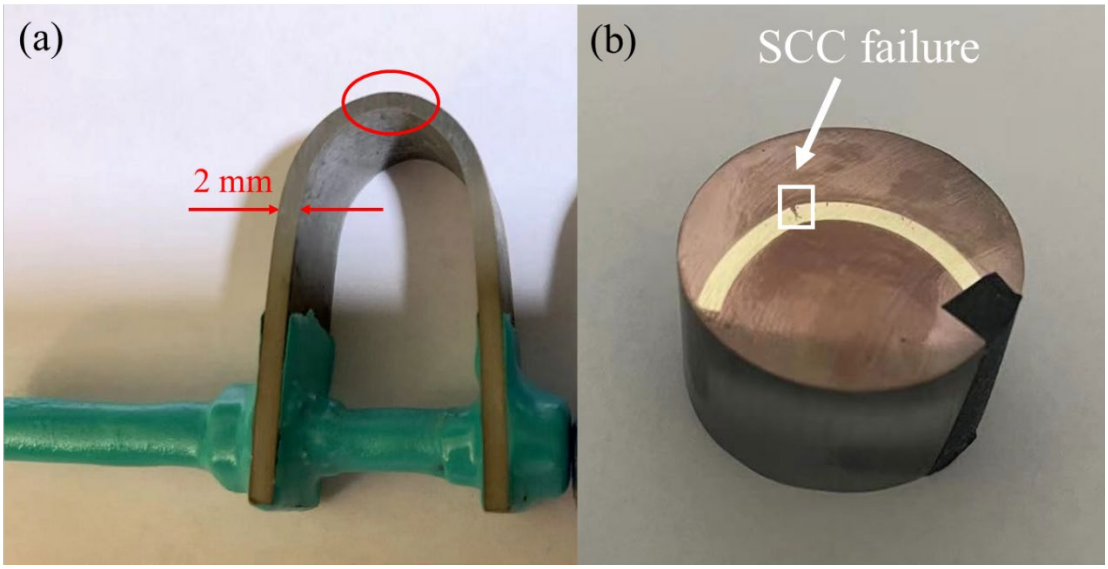

Figure A-13. (a) The pre-crack X80 U-bend by immersed in NS4 solution for 2-week. (b) The SCC failure of X80 U-bend after pre-crack that induced by 6-weeks incubated in *D. vulgaris*.

After removing the corrosion products using fresh Clarke's solution, the surface and cross-sectional morphologies of the coupon were observed under SEM to see cracks and pits.

A.19 Weight loss measurement

After the immersion tests, biofilms and corrosion products on the coupons were removed using a fresh Clarke's solution for approximately 1 min, according to ASTM G1−03 (ASTM G1-03, 2003). After dying, the samples were weighed using an electronic analytical balance (0.1 mg readability). The square coupons were weighed in triplicates (three coupons from each bottle) to provide error bars based on 95% confidence interval. The X80 U-bend coupons were too large to place multiple in the anaerobic bottles and they were in short supply, so there was no replicate.

A.20 Electrochemical measurements

A classical three-electrode system was constructed using an electrochemical workstation. A VersaSTAT 3 potentiostat with VersaStudio version 2.44.4 (Princeton Applied Research, Oak Ridge, TN, USA) was used in Chapters 4 and 5. A Gamry potentiostat (Reference 600 Plus with Framework version 7.04) was used for Chapters 6 and 7. The electrochemical tests were conducted in 450 mL glass cells with 200 mL culture medium, except in the headspace variation work which used 150-, 200-, and 300-mL culture medium. Two types of working electrodes were used in this work. One was a square coupon and the other a U-bend coupon. The square coupon working electrode was an X80 square coupon embedded in Epoxy with 1 cm^2 exposed surface. The X80 U-bend working electrode was completely painted, except for the 1 cm^2 surface (default in electrochemical tests) on the outer bottom, as shown in Figure A-14.

Before use, the coupons were cleaned with pure isopropanol and air dried under UV light for 20 min. The counter electrode was a platinum plate (Chapters 4, 5, 8, and 9) or a mesh plate (Chapters 4 and 5). The reference electrode was a saturated calomel electrode (SCE) fitted with a Vycor tip facing the working electrode. Each electrochemical glass cell (an anerobic bottle with electrodes) in the anaerobic chamber was sealed with a 2.44 inch-diameter rubber stopper.

LPR was scanned at stable OCP with a potential range of −10 to +10 mV (vs. OCP) at a rate of 0.1667 mV s^{-1}. EIS was conducted at stable OCP between 10^{-2} and 10^{5} Hz with a sinusoidal voltage signal (10 mV amplitude).

PDP curves were measured at the end of incubation from OCP to OCP – 200 mV using one working electrode and from OCP to OCP + 200 mV using another working electrode in a replicate glass cell at a rate of 0.1667 mV s^{-1}. The Tafel curves were analyzed to obtain Tafel slopes (β_α and β_c), corrosion current densities (i_{corr}), and corrosion potentials (E_{corr}).

In Chapters 4 and 5, EIS spectra were analyzed using the Zview software (Version 2), while the LPR and Tafel scans were analyzed using the Cview software (Version 2). For Chapters 6 and 7, EIS was performed using the ZSimpWin software version 3.60, and the LPR and Tafel scans were analyzed using Gamry Echem Analyst Version 7.04. The electrochemical setup of the X80 square coupon and X80 U-bend for the OCP, LPR, EIS, and Tafel scans in the SRB test are shown in Figure A-14.

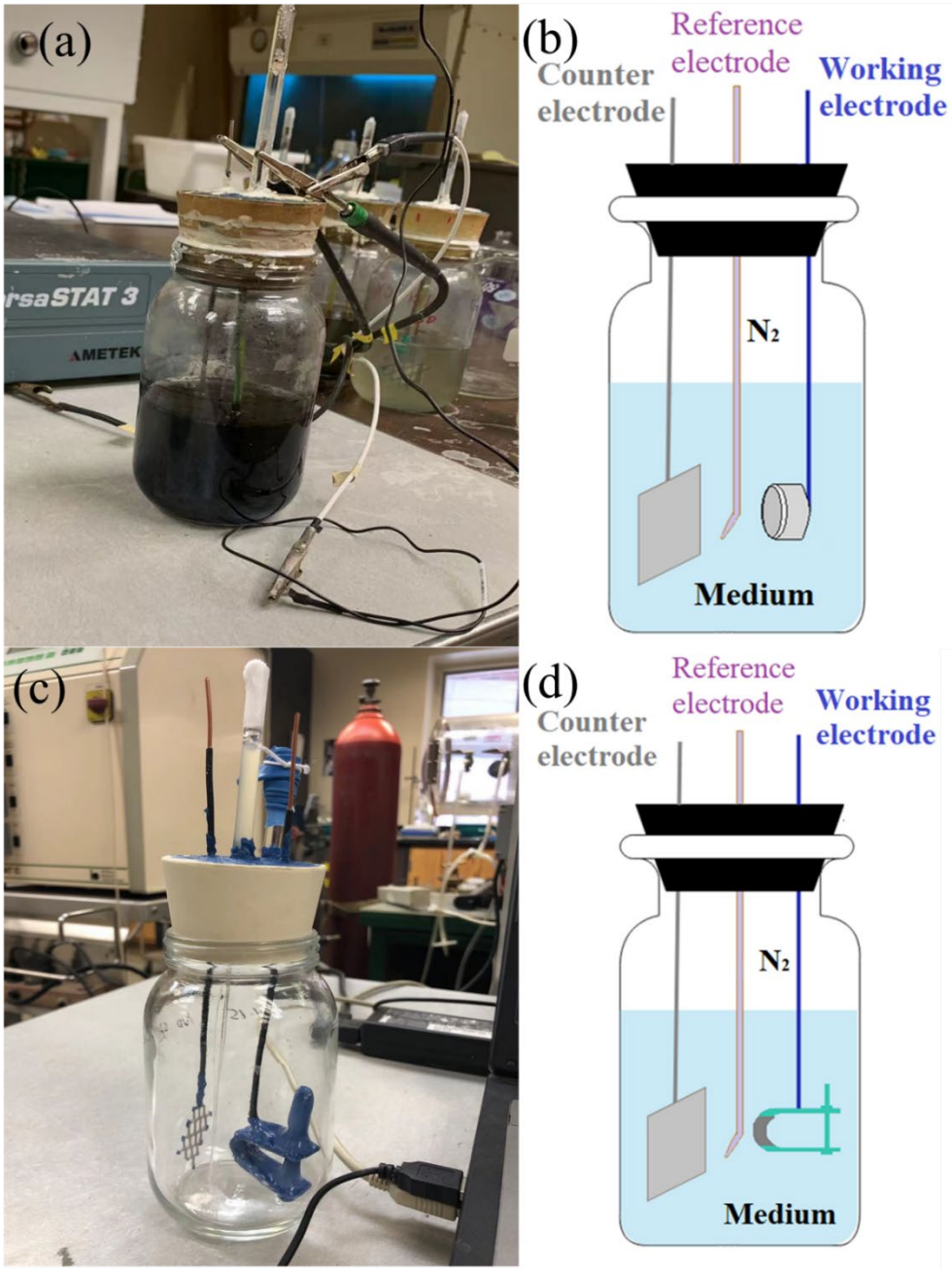

Figure A-14. Electrochemical setup for OCP, LPR, EIS, and Tafel scans: (a) X80 square coupon electrochemical anaerobic bottle, (b) schematic illustration of X80 square coupon working electrode in electrochemical glass cell, (c) X80 U-bend working electrode in electrochemical glass cell, and (d) schematic illustration of X80 U-bend working electrode in electrochemical glass cell.

A.21 Tensile testing of dogbone coupons

After SRB exposure, the dogbone coupons were cleaned using a fresh Clarke's solution for 1 min to remove biofilms and corrosion products based on ASTM G1-03. They were then tested on an electromechanical universal testing machine (E44.304, MTS system, MN, USA for Chapters 6 and 7; LandMark 370, MTS system, MN, USA for Chapter 8) to obtain the stress-strain curves (Figure A-15). The strain rate of the extensometer accessory used in the testing was 0.004 s^{-1} based on literature (Eleiche et al., 1985). Testing was complete when the dogbone coupon broke into two pieces completely.

Figure A-15. Tensile testing machine: (a) MTS E44 universal testing machine, and (b) MTS LandMark 370 universal testing machine.

Appendix B: FEM Simulation

ABAQUS 2022 software was used to calculate the stress distribution of the X80 U-bend coupon. To perform the calculations, ABAQUS 2022 requires the basic mechanical properties of a material to be provided along with a stress-strain curve and the density. The density of X80 steel is 7.86 g cm^{-3}. Figure B-1 shows the X80 (in pristine condition) stress-strain curve that was fed to the software for Chapter 4's FEM simulation. Using the input data information, the software calculates a theoretical stress-strain curve, which can provide the material properties of fresh X80 steel. A screenshot of the software for inputting the material properties is shown in Figure B-2.

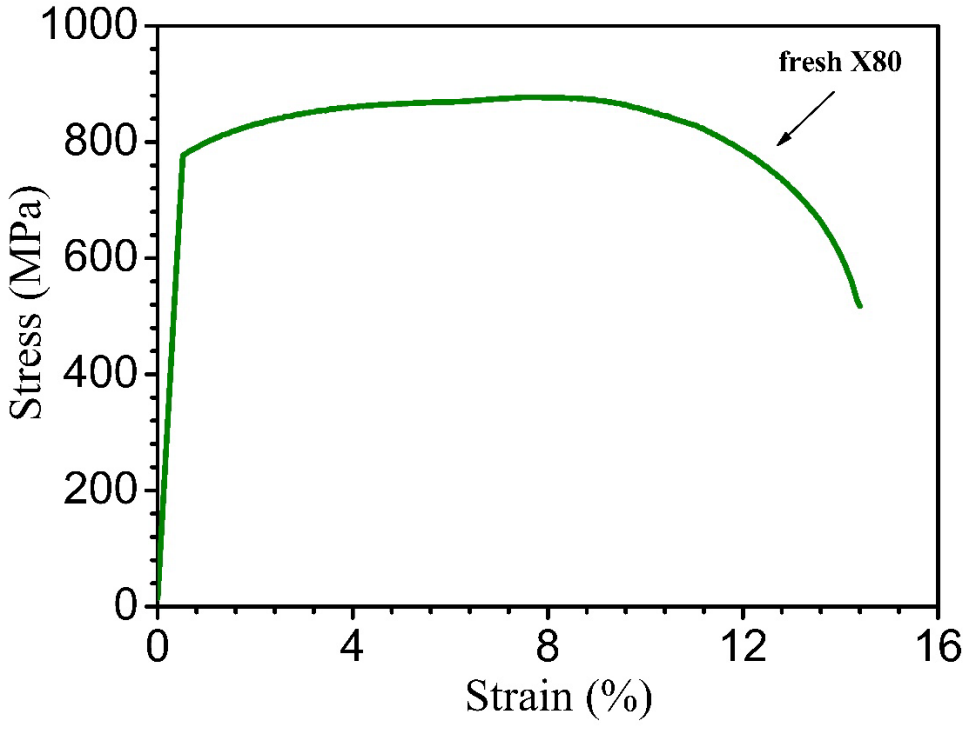

Figure B-1. The X80 stress-strain curve that was fed to the FEM software simulation.

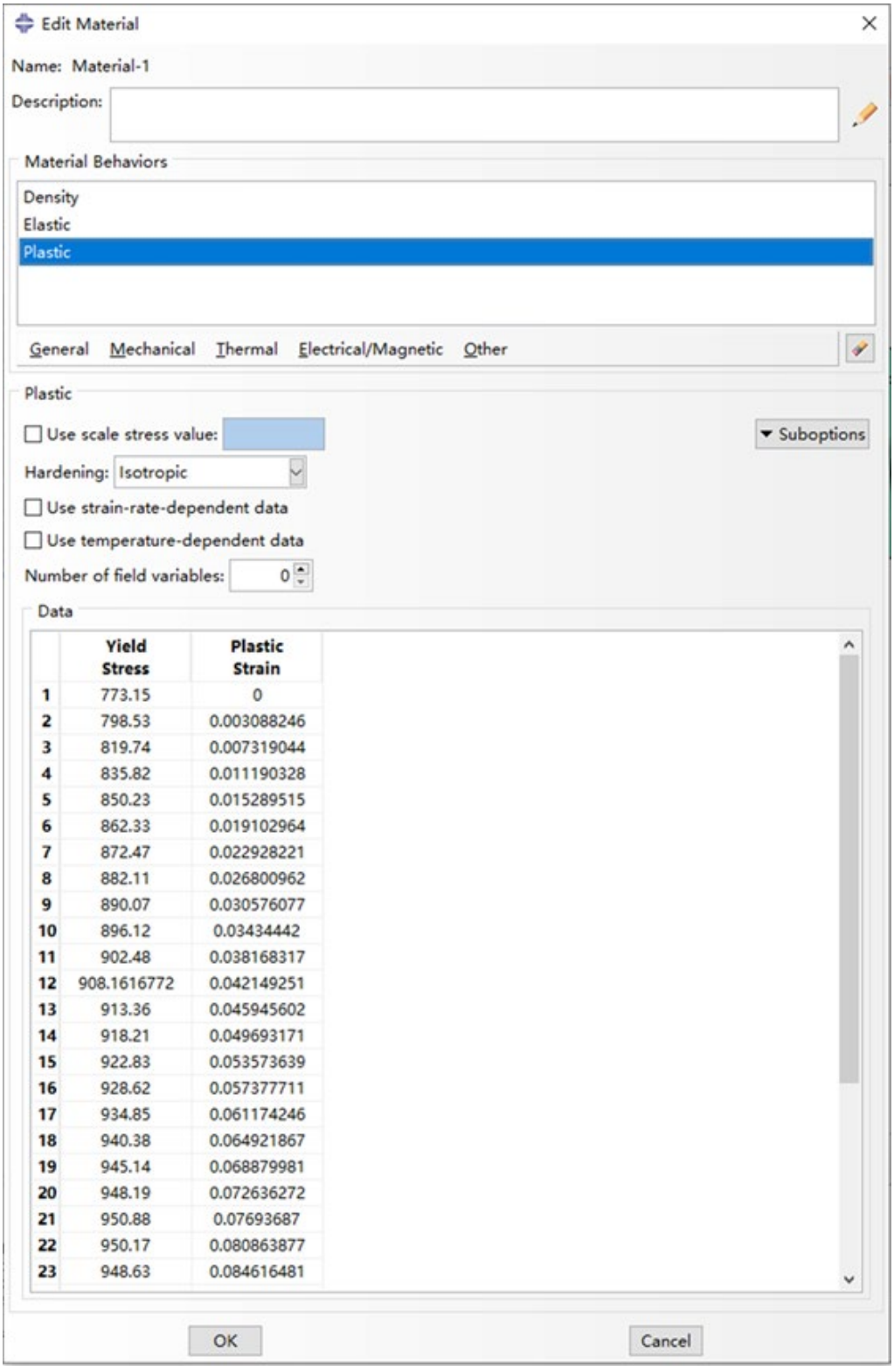

	Yield Stress	Plastic Strain
1	773.15	0
2	798.53	0.003088246
3	819.74	0.007319044
4	835.82	0.011190328
5	850.23	0.015289515
6	862.33	0.019102964
7	872.47	0.022928221
8	882.11	0.026800962
9	890.07	0.030576077
10	896.12	0.03434442
11	902.48	0.038168317
12	908.1616772	0.042149251
13	913.36	0.045945602
14	918.21	0.049693171
15	922.83	0.053573639
16	928.62	0.057377711
17	934.85	0.061174246
18	940.38	0.064921867
19	945.14	0.068879981
20	948.19	0.072636272
21	950.88	0.07693687
22	950.17	0.080863877
23	948.63	0.084616481

Figure B-2. Screenshot of the ABAQUS 2022 that can provide the X80 properties parameters.

Additionally, a U-bend model was established using ABAQUS 2022. With the given X80 U-bend dimensions, there were 9924 units and 13280 nodes on the X80 U-bend, as shown in Figure B-3.

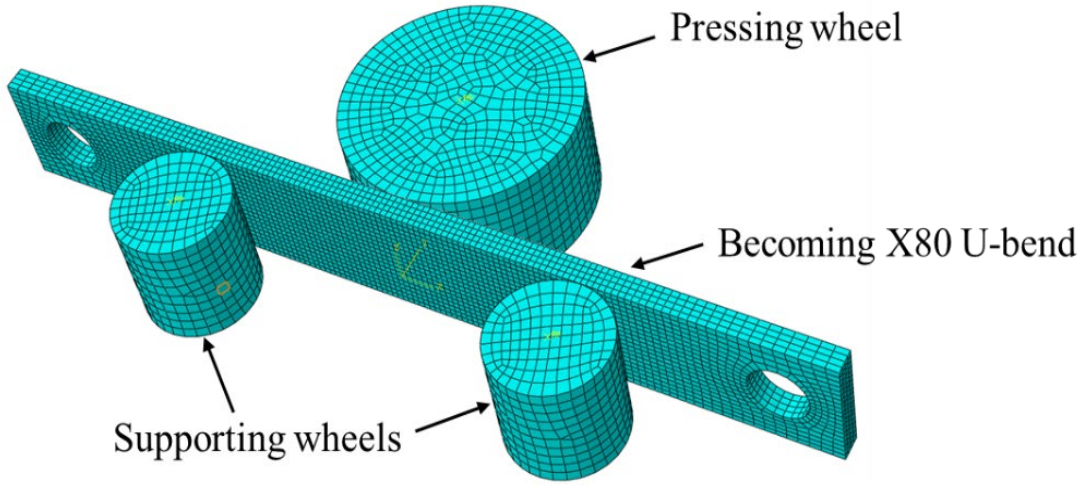

Figure B-3. FEM model for machining X80 U-bend with units and nodes.

The displacement of the boundary must be set up as shown in Figure B-4. Because the diameter of the X80 U-bend on the curved part was 20 mm, the displacements were set to 20 mm and −10 mm.

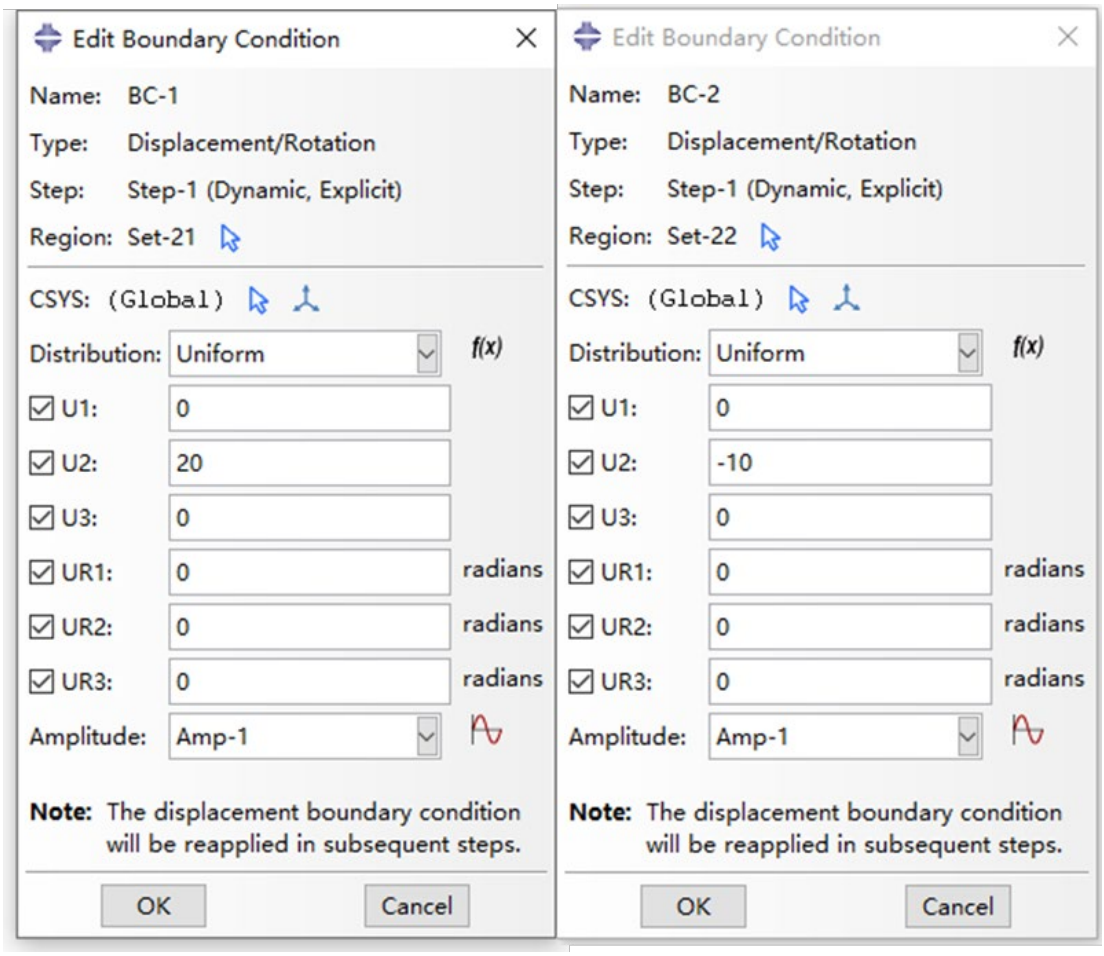

Figure B-4. Screenshot of ABAQUS 2022 defining boundary conditions.

The ABAQUS software was then able to calculate the stress distribution shown in Figure 4-2 in Chapter 4. The simulation results were 3D images that could be rotated for closer examination.

Appendix C: Impact-Factor Journal Publications (Based on Dissertation Work)

1. **Li, Z.**, Yang, J., Guo, H., Kumseranee, S., Punpruk, S., Mohamed, M. E., Gu, T. (2022). Mechanical property degradation of X80 pipeline steel due to microbiologically influenced corrosion caused by *Desulfovibrio vulgaris*. *Frontiers in Bioengineering and Biotechnology*, 10:1028462. https://doi.org/10.3389/fbioe.2022.1028462

2. **Li, Z.,** Yang, J., Guo, H., Kumseranee, S., Punpruk, S., Mohamed, M. E., Gu, T. (2021). Carbon source starvation of a sulfate-reducing bacterium–elevated mic deterioration of tensile strength and strain of X80 pipeline steel. *Frontiers in Materials*, 8:794051. https://doi.org/10.3389/fmats.2021.794051

Manuscripts Under Review by Journals

3. **Li, Z.,** Yang J., Lu S., Dou W., & Gu T. (2023). Stress corrosion cracking failure of X80 carbon steel U-bend caused by *Desulfovibrio vulgaris* biocorrosion.

4. **Li, Z.,** Yang J., Lu S., Dou W., & Gu T. (2023). Impact of *Desulfovibrio ferrophilus* biocorrosion time on X80 pipeline steel mechanical property degradation.

5. **Li, Z.,** Yang J., Lu S., Dou W., & Gu T. (2023). Mitigation of microbial degradation of X80 carbon steel mechanical properties using a green biocide.

6. **Li, Z.,** Yang J., Lu S., & Gu T. (2023). X80 U-bend stress corrosion cracking (SCC) crack tip dissolution by fast corroding *Desulfovibrio ferrophilus* biofilm.

Appendix D: List of Acronyms

ATCC	American Type Culture Collection
BCSR	Biocatalytic cathodic sulfate reduction
CGR	Crack growth rate
CLSM	Confocal laser scattering microscopy
CPR	Crack propagation rate
DET	Direct electron transfer
EET	Extracellular electron transfer
EASW	Enriched artificial seawater
EET-MIC	Extracellular electron transfer MIC
EIS	Electrochemical impedance spectrometry
FEM	Finite element method
FESEM	Field emission scanning electron microscopy
IFM	InfiniteFocus microscopy
IGSCC	Intergranular stress corrosion cracking
LPR	Linear polarization resistance
M-MIC	Metabolite MIC
MET	Mediated electron transfer
MIC	Microbiologically influenced corrosion
MICORP	MIC corrosion prediction software created by Ohio University
NRB	Nitrate reducing bacteria
OCP	Open circuit potential
PBS	Phosphate buffered saline
PDP	Potentiodynamic polarization
RPS	Relative pitting severity
SCC	Stress corrosion cracking

SCE	Saturated calomel electrode
SEM	Scanning electron micrograph
SIF	Stress intensity factor
SRB	Sulfate reducing bacteria
SS	Stainless steel
TGSCC	Transgranular stress corrosion cracking
THPS	Tetrakis hydroxymethyl phosphonium sulfate
XRD	X-ray diffraction
XPS	X-ray photoelectron spectroscopy

Thesis and Dissertation Services